

# **P and S Wave Velocity Structure of the Crust and Upper Mantle China and Surrounding Areas From Body and Surface Wave Tomography**

**M. Nafi Toksöz  
Youshun Sun**

**Earth Resources Laboratory  
Department of Earth, Atmospheric and Planetary Sciences  
Massachusetts Institute of Technology  
77 Massachusetts Avenue, 54-1814  
Cambridge, MA 02139**

**Final Report**

**31 March 2008**

<b>APPROVED FOR PUBLIC RELEASE; DISTRIBUTION UNLIMITED.</b>
---



**AIR FORCE RESEARCH LABORATORY  
Space Vehicles Directorate  
29 Randolph Road  
AIR FORCE MATERIEL COMMAND  
Hanscom AFB, MA 01731-3010**

---

## NOTICE AND SIGNATURE PAGE

Using Government drawings, specifications, or other data included in this document for any purpose other than Government procurement does not in any way obligate the U.S. Government. The fact that the Government formulated or supplied the drawings, specifications, or other data does not license the holder or any other person or corporation; or convey any rights or permission to manufacture, use, or sell any patented invention that may relate to them.

This report was cleared for public release and is available to the general public, including foreign nationals. Qualified requestors may obtain additional copies from the Defense Technical Information Center (DTIC) (<http://www.dtic.mil>). All others should apply to the National Technical Information Service.

AFRL-RV-HA-TR-2008-1091 HAS BEEN REVIEWED AND IS APPROVED FOR  
PUBLICATION IN ACCORDANCE WITH ASSIGNED DISTRIBUTION STATEMENT.

//Signed//

---

ROBERT RAISTRICK  
Contract Manager

//Signed//

---

PAUL TRACY, Acting Chief  
Battlespace Surveillance Innovation Center

This report is published in the interest of scientific and technical information exchange, and its publication does not constitute the Government's approval or disapproval of its ideas or findings.

REPORT DOCUMENTATION PAGE				Form Approved OMB No. 0704-0188	
Public reporting burden for this collection of information is estimated to average 1 hour per response, including the time for reviewing instructions, searching existing data sources, gathering and maintaining the data needed, and completing and reviewing this collection of information. Send comments regarding this burden estimate or any other aspect of this collection of information, including suggestions for reducing this burden to Department of Defense, Washington Headquarters Services, Directorate for Information Operations and Reports (0704-0188), 1215 Jefferson Davis Highway, Suite 1204, Arlington, VA 22202-4302. Respondents should be aware that notwithstanding any other provision of law, no person shall be subject to any penalty for failing to comply with a collection of information if it does not display a currently valid OMB control number. <b>PLEASE DO NOT RETURN YOUR FORM TO THE ABOVE ADDRESS.</b>					
1. REPORT DATE (DD-MM-YYYY) 31-03-2008		2. REPORT TYPE Scientific Report - Final		3. DATES COVERED (From - To) 15-09-2004 to 10-01-2008	
4. TITLE AND SUBTITLE P and S Wave Velocity Structure of the Crust and Upper Mantle Under China and Surrounding Areas From Body and Surface Wave Tomography				5a. CONTRACT NUMBER FA8718-04-C-0018	
				5b. GRANT NUMBER N/A	
				5c. PROGRAM ELEMENT NUMBER N/A	
6. AUTHOR(S) M. Nafi Toksöz Youshun Sun				5d. PROJECT NUMBER	
				5e. TASK NUMBER	
				5f. WORK UNIT NUMBER	
7. PERFORMING ORGANIZATION NAME(S) AND ADDRESS(ES) Earth Resources Laboratory Dept. of Earth, Atmospheric, and Planetary Sciences Massachusetts Institute of Technology 77 Massachusetts Avenue, 54-1814 Cambridge, MA 02139				8. PERFORMING ORGANIZATION REPORT NUMBER	
9. SPONSORING / MONITORING AGENCY NAME(S) AND ADDRESS(ES)  Air Force Research Laboratory 29 Randolph Rd. Hanscom AFB, MA 01731-3010				10. SPONSOR/MONITOR'S ACRONYM(S) AFRL/VSBYA	
				11. SPONSOR/MONITOR'S REPORT NUMBER(S)	
12. DISTRIBUTION / AVAILABILITY STATEMENT  Approved for Public Release; Distribution Unlimited.					
13. SUPPLEMENTARY NOTES					
14. ABSTRACT We have used a combination of travel-time and surface wave tomography to obtain compressional and shear wave velocity distributions in the crust and upper mantle under China and surrounding areas. We first determined 3-D P- and S-wave velocity structures for the crust and uppermost mantle using local and regional arrival time data. Travel-time data from the Annual Bulletin of Chinese Earthquakes (ABCE) and the International Seismological Centre (ISC/EHB) were used. We then extended the model deeper into the mantle through the upper mantle transition zone using ISC/EHB data for P and PP phases combined with the ABCE data. We also used surface wave data from broadband stations to determine the S-velocity structure. Multi-mode surface wave tomography was employed for the whole region of China and surrounding areas and ambient noise interferometry was used in Tibet.					
15. SUBJECT TERMS Travel-time tomography, Surface wave tomography, Ambient noise interferometry					
16. SECURITY CLASSIFICATION OF:			17. LIMITATION OF ABSTRACT	18. NUMBER OF PAGES  106	19a. NAME OF RESPONSIBLE PERSON Robert J. Raistrick
a. REPORT UNCLASSIFIED	b. ABSTRACT UNCLASSIFIED	c. THIS PAGE UNCLASSIFIED			19b. TELEPHONE NUMBER (include area code) 781-377-3726





## Table of Contents

1. Summary	1
2. Introduction	1
3. Methods and Results	3
3.1. Data of Travel-Time Tomography	3
3.2. P and S Wave 3-D Velocity Models From Travel-Time Tomography	3
3.3. Surface Wave Tomography	10
3.4. Validation of P and S Wave Velocity Models	13
4. Conclusions	15
References	21
List of Publications	24
Appendix: Publications	25
A. Crustal structure of China and surrounding regions from P wave travel-time tomography	
B. The layered shear-wave velocity structure of the crust and uppermost mantle in China	
C. Upper mantle seismic velocities and anisotropy in China determined through Pn and Sn tomography	
D. M <sub>1</sub> amplitude tomography in North China	
E. Constraining P-wave velocity variations in the upper mantle beneath Southeast Asia	
F. Surface-wave array tomography in SE Tibet from ambient seismic noise and two-station analysis—I. Phase velocity maps	



## Figures

1. Shown are 25,000 earthquakes ( $M > 3.0$  from 1990 to 2004), 220 stations, active faults and major tectonic boundaries in China and the surrounding area. Earthquake epicenters are shown in red dots and stations are shown in red triangles. The yellow line shows the boundary of China. Active faults in the China area are shown in purple lines and tectonic sutures are shown in blue lines, where SoB: Songliao Basin; OB: Ordos Basin; SB: Sichuan Basin; KB: Khorat Basin; STB: Shan Thai Block; IB: Indochina Block. 2
2. (a) 25,000 earthquakes, 220 stations, and 450,000 ray paths in China and the surrounding area. Earthquake epicenters are shown in black circles and stations are shown in red triangles. The green line shows the boundary of China. (b) The distribution of stations and events in the Tibetan Plateau and surrounding regions. 3
3. Imaged Pn lateral velocity variations. Average Pn velocity is 8.05 km/s and variation corresponds with color. Red represents velocities lower than the average 4
4. Tomographic image of Pn velocity anisotropy. Line segments are drawn parallel to the direction of highest velocity, with their length proportional to the magnitude of anisotropy. 5
5. Tomographic image of Sn lateral velocity variations. Blue corresponds to high velocity and red to low velocity. The average Sn velocity is 4.55 km/s. The black thin lines represent active faults. 7
6. Horizontal slices of three-dimensional (a) Vp and (b) Vs models for China and surrounding regions at 10, 20, 30, 40, 60, and 80 km depths. 8
7. Pn (left) and Sn (right) velocities in China and surrounding regions. 1: Tarim Basin; 2: Ordos Basin; 3: Songliao Basin; 4: Sichuan Basin; 5: Shan Thai Block; 6: Khorat Basin. 9
8. Lateral P wavespeeds perturbation at 60 km, 100 km, 200 km, and 400 km depths. 10
9. West-east vertical cross-sections (a), (b), and (c) through the 3-D P-wave velocity model (indicated as white lines in the upper left hand image). 11
10. Lateral variations in S wave velocity at selected depths from the automated multi-mode surface wave tomography. The depths and limits of the color scales are given next to the frames. The reference model is the (3-D) CRUST2.0 in the crust and a (1-D) AK135 in the mantle. Circles show seismicity at each of the depths. (After Lebedev et al., 2006). 12
11. Inter-station ray paths (upper left corner) from ambient noise interferometry study for M.I.T. and Lehigh University arrays in southeastern Tibet. Shear wavespeeds at four cross-sections through the Sichuan and Yunnan provinces of China from the combined results of ambient noise interferometry study and two-station dispersion analysis. 13

12. The selected four profiles in west and east China. 47 stations of the China Digital Broadband Network (CDBN) are plotted in red triangles.	15
13. The observed and calculated seismograms along Profile A.	17
14. The observed and calculated seismograms along Profile B.	18
15. The observed and calculated seismograms along Profile C.	19
16. The observed and calculated seismograms along Profile D.	20

## 1. SUMMARY

The objective of this project is to use a combination of travel-time and surface wave tomography to obtain compressional and shear wave velocity distributions in the crust and upper mantle under China and surrounding areas.

For travel-time tomography, we took a two-step approach. First, we determined 3-D P- and S-wave velocity structures for the crust and uppermost mantle using local and regional arrival time data. Travel data from the Annual Bulletin of Chinese Earthquakes (ABCE) and the International Seismological Centre (ISC/EHB) are used. A total of 345,000 P-wave and a similar number of S-wave arrival times are used for the tomographies. Tomographic inversions provide 3-D P- and S-wave velocities in the crust, P<sub>n</sub> and S<sub>n</sub> velocities, and Moho depths under China.

To extend the model deeper into the mantle through the upper mantle transition zone, ISC/EHB data for P and PP phases are combined with the ABCE data. To counteract the “smearing effect,” the crust and upper mantle velocity structure, derived from regional travel-times, are used. An adaptive grid method based on ray density is used in the inversion. A P-wave velocity model extending down to a depth of 1700 km is obtained. The combined regional-teleseismic tomography provides a high-resolution, 3-D P-wave velocity model for the crust, upper mantle, and the transition zone. The crustal models correlate well with geologic and tectonic features. The mantle models show the images of current and past subduction zones. A surprising result is that the “roots” of some geologic features, such as the Sichuan Basin and Ordos Plateau, extend deep into the upper mantle.

Using surface wave data from broadband stations, the S-velocity structure was determined. Multi-mode surface wave tomography was employed for the whole region of China and surrounding areas. In Tibet, where data from dense networks deployed by MIT and Lehigh University arrays are available, 3-D S-wave velocity structure for the crust and uppermost mantle were obtained using ambient noise interferometry.

## 2. INTRODUCTION

China and the surrounding area is a seismically active and geologically complex region (Figure 1). More than 500 earthquakes with magnitudes (M) greater than 6.0 occurred in this region between January 1978 and May 2004 (Sun and Töksöz, 2006). In this paper we present a 3-D compressional and shear wave velocity structure for the crust and upper mantle under China and surrounding regions obtained using local and regional travel times and surface waves.

The available P- and S-wave velocity models of the crust and upper mantle in China and the surrounding area have been obtained using different approaches. Global models such as CUB 1.0 (Shapiro and Ritzwoller, 2002) and the SAIC 1° x 1° model (Stevens et al., 2001) were constructed from group and phase velocity dispersion measurements of surface waves. The global model CRUST 2.0 (Laske et al., 2001) was constructed from

seismic refraction data and developed from the CRUST 5.1 model (Mooney, 1998) and a  $1^\circ \times 1^\circ$  sediment map (Laske and Masters, 1997). Only P-wave velocities are inverted by travel-time tomography. The S-wave velocities in the model are obtained by empirical  $V_p/V_s$  ratios or compiled from other sources. For East Asia, mantle S-velocity models were obtained from shear and surface waveforms (Friederich, 2003). Lateral spatial resolution of the models is larger than 200 km.

Regional models were constructed by Sn and/or Pn tomography (Ritzwoller et al., 2002; Hearn and Ni, 2001; Pei et al., 2007), and from surface waves (e.g., Wu et al., 1997, Lebedev and Nolet, 2003; Huang et al., 2003). P- and S-wave tomographies have been performed in several local regions in China (e.g. Huang and Zhao, 2004). All these models provide detailed crustal structures in specific regions. A detailed map for the whole China area remains to be developed.

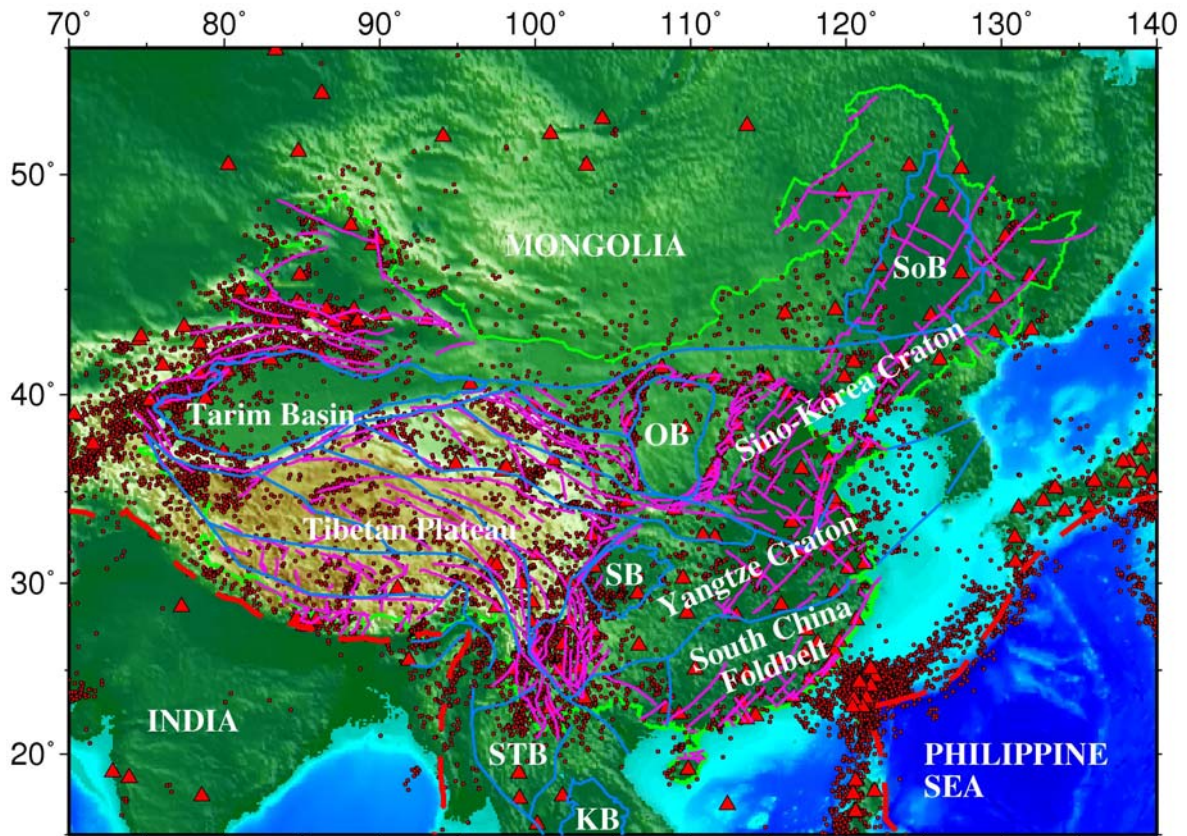


Figure 1. Shown are 25,000 earthquakes ( $M > 3.0$  from 1990 to 2004), 220 stations, active faults and major tectonic boundaries in China and the surrounding area. Earthquake epicenters are shown in red dots and stations are shown in red triangles. The yellow line shows the boundary of China. Active faults in the China area are shown in purple lines and tectonic sutures are shown in blue lines, where SoB: Songliao Basin; OB: Ordos Basin; SB: Sichuan Basin; KB: Khorat Basin; STB: Shan Thai Block; IB: Indochina Block.

In this study, using both travel-time body and surface wave tomography, we produce multi-scale, 3-D P- and S-wave velocity models for the crust, upper mantle, and transition

zone. In the following sections we describe the data, P and S travel-time tomography, long wavelength surface wave tomography, and array tomography, respectively.

### 3. METHODS AND RESULTS

#### 3.1. Data for Travel-Time Tomography

The P and S wave arrival times from local, regional and global stations come from four sources: (1) ABCE Phase readings from about 220 stations of the Chinese Seismograph Network (CSN) during the period 1990-2004 (IG-CSB, 1990-2004) (Figures 1 and 2); (2) EHB (Engdahl, van der Hilst, and Buland, 1998) data reprocessed from the International Seismological Centre (ISC) bulletins (1964-2004); (3) PP-P differential times, used to image the upper mantle beneath regions with few earthquakes and stations; and (4) Broadband waveform data, used for surface wave tomography and for model validation using synthetic seismograms.

Combining the global, regional and local seismic network data from various sources requires careful processing in order to avoid internal inconsistencies. The travel time picks from the above source 1 have been integrated and processed along with data from source 2 (i.e., the existing EHB data) using a non-linear process of earthquake relocation and phase re-identification (Engdahl et al., 1998). Most baseline inconsistencies can simply be removed, however, by recalculating all new picks relative to EHB hypocenters using ak135 travel time.

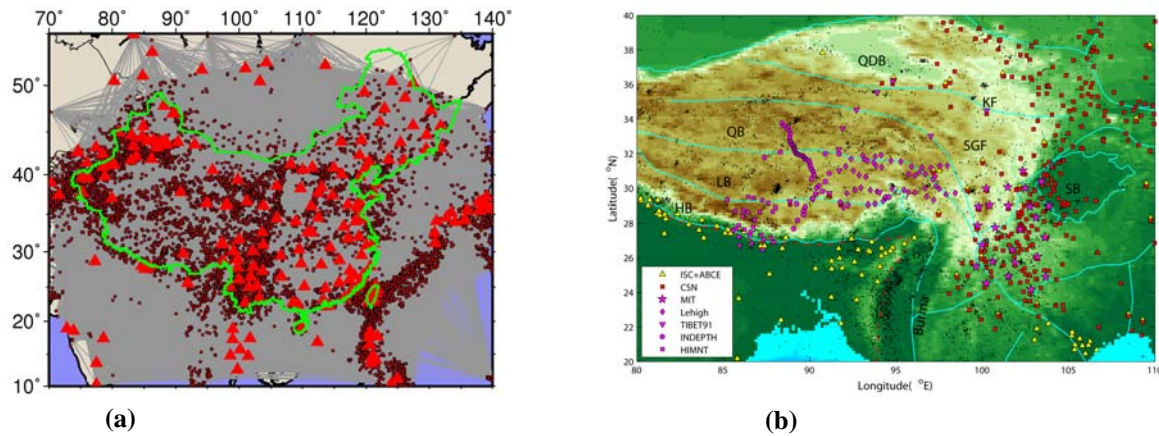


Figure 2. (a) 25,000 earthquakes, 220 stations, and 450,000 ray paths in China and the surrounding area. Earthquake epicenters are shown in black circles and stations are shown in red triangles. The green line shows the boundary of China. (b) The distribution of stations and events in the Tibetan Plateau and surrounding regions.

#### 3.2. P and S Wave 3-D Velocity Models From Travel-Time Tomography

The tomography research used here builds on our team's extensive experience in travel-time tomography for the crust and mantle (van der Hilst et al., 1991; Káráson and van der



Hilst, 2001; Sun et al., 2004; Li et al., 2006; Sun and Toksöz, 2006; Li, 2007; Sun et al., 2007). We took a two-step approach. First, we determined 3-D velocity structures for the crust and uppermost mantle (Pn, Sn). Second, we conducted the mantle tomography with the travel-times calculated from crustal models used as inputs, in order to reduce the “smearing” effect of shallow velocity structure on steep rays. In the proposed project we will follow a similar approach.

### 3.2.1. Crust and uppermost mantle P and S wave velocities

A high-resolution tomographic model for the heterogeneous crust is constructed by iterative, non-linear tomography. To generate adequate starting models for the nonlinear inversion we combine pertinent information from global (Mooney, 1998; Bassin et al., 2000; Stevens et al., 2001; Ritzwoller et al., 2002), regional, and local crust and uppermost mantle models (Wang et al., 2003; Sun et al., 2004; Huang and Zhao, 2006; Li et al., 2006; Reiter and Rodi, 2006; Sun and Toksöz, 2006; Yao et al., 2006), in addition to Pn or Sn studies (Hearn and Ni, 2001; Hearn et al., 2004; Liang et al., 2004; Phillips et al., 2005; Rowe et al., 2005) and seismic refraction profiles (Morozov et al., 2005; Li, Mooney and Fan, 2006). We first obtain upper mantle seismic velocities and anisotropy in China determined through Pn and Sn tomography.

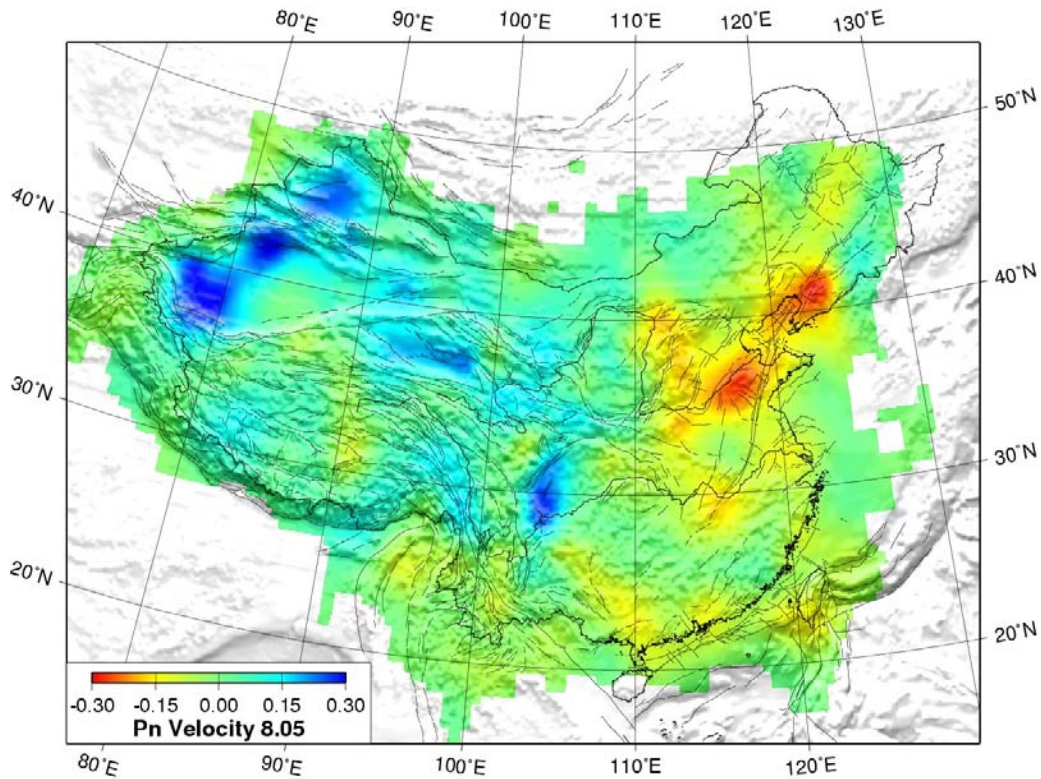


Figure 3. Imaged Pn lateral velocity variations. Average Pn velocity is 8.05 km/s and variation corresponds with color. Red represents velocities lower than the average and blue denotes higher velocities. The black thin lines represent active faults.



Pn and Sn arrival times were selected for events located between 12°N - 52°N and 65°E - 132°E from the 1985 to 1998 Annual Bulletin of Chinese Earthquakes (ABCE) compiled by IGCEA, and from the 1999 to 2001 Temporary Report of Chinese Earthquakes compiled also by IGCEA. In addition, more than 50,000 Pn travel times were collected from regional seismic networks of 26 provinces, the temporary network of project INDEPTH2 (Nelson et al., 1996) and the Sino-US Joint Seismological Survey (Ding, 1992) in Tibet. Finally, we refined the data set by removing repeated and unreliable records and using only the event parameters given in ABCE, which are more precise than the parameters in provincial reports.

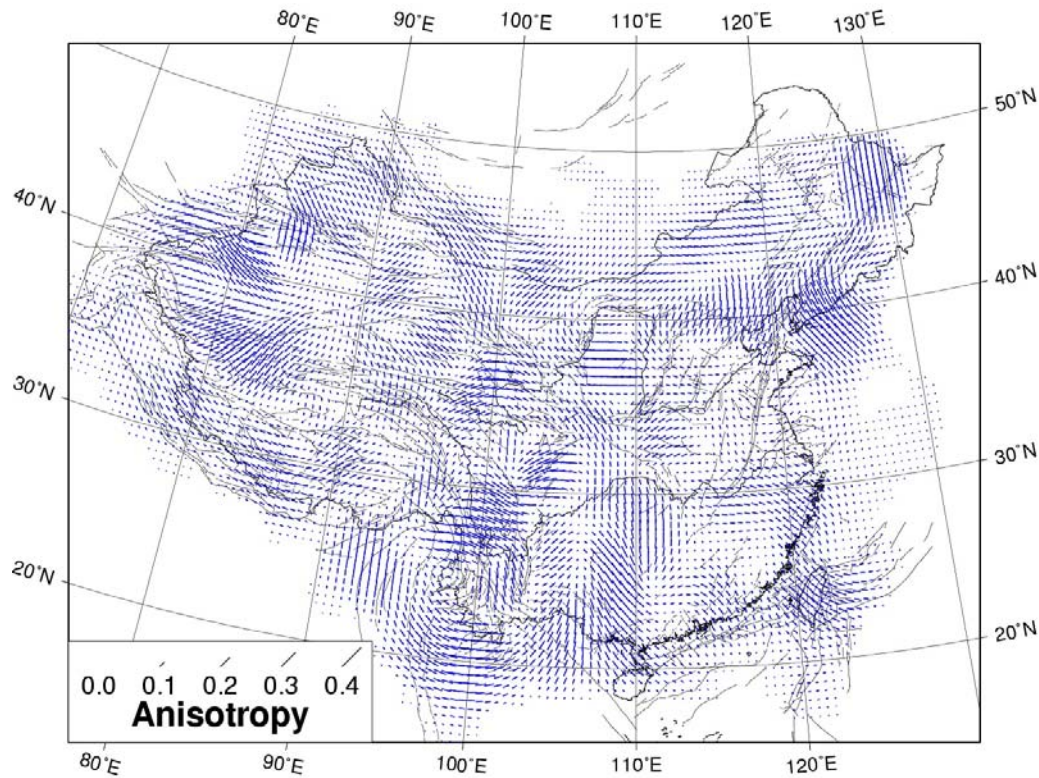


Figure 4. Tomographic image of Pn velocity anisotropy. Line segments are drawn parallel to the direction of highest velocity, with their length proportional to the magnitude of anisotropy.

Following Hearn's approach and computation method (Hearn and Ni, 1994; Hearn, 1996), Pn and Sn travel time residuals are inverted for lateral velocity variation and anisotropy within the mantle lid. Within the epicentral distances considered in this study, the Pn and Sn ray paths can be modeled as refracted rays traveling along the Moho discontinuity. The variation of seismic velocity within the uppermost mantle is parameterized by subdividing the surface of the uppermost mantle into a 2-D grid of square cells with size of 30'×30'. The Pn travel-time residuals are described as the sum of three time terms:

$$t_{ij} = a_i + b_j + \sum d_{ijk} (s_k + A_k \cos 2\varphi + B_k \sin 2\varphi)$$

where  $t_{ij}$  is the travel time residual for the ray from event  $j$  to station  $i$ ;  $a_i$  is the static delay for station  $i$ , depending on the crustal thickness and velocity beneath the station;  $b_j$  is the static delay for event  $j$ , not only depending on the crustal thickness and velocity beneath the event, but also on the event focal depth;  $d_{ijk}$  is the distance traveled by ray  $ij$  in mantle cell  $k$ ;  $s_k$  is the slowness perturbation for cell  $k$ ;  $A_k$  and  $B_k$  are the anisotropic coefficients for cell  $k$ ; and  $\varphi$  is the back azimuth angle. The unknown quantities in the equation are  $a_i$ ,  $b_j$ ,  $s_k$ ,  $A_k$  and  $B_k$ . As a first approximation, seismic anisotropy in the uppermost mantle is assumed to be described by a  $2\varphi$  azimuthal variation. The magnitude of anisotropy for cell  $k$  is given by  $(A_k^2 + B_k^2)^{1/2}$  and the azimuthal angle  $\theta$  of the fast direction of Pn propagation is given by  $1/2 \arctan(B_k/A_k)$ . The sum is calculated over all cells through which the ray travels in the uppermost mantle.

A set of Laplacian damping equations regularizes the solution, and two damping constants are separately applied to the unknown slowness and anisotropic coefficients. A proper pair of damping constants is chosen to balance the error size and the resolution width. In this approach the trade-off between velocity and anisotropy variations is a crucial issue, which has been examined by using different combinations of damping parameters for both velocity and anisotropy. In this study the main features of the velocity and anisotropy fields are observed to be significantly stable, even though the extent of the velocity anomalies and the amount of anisotropy vary slightly for different combinations of the damping constants. The method of Sn tomography applied in this study is the same to that of Pn tomography, except we do not incorporate the anisotropy into the inversion.

Pn lateral velocity variations (Figure 3) and anisotropy (Figure 4) were obtained by tomographically inverting the Pn travel-time residuals. Relative to the mean value of 8.05 km/s, the Pn velocity perturbations range from  $-0.29$  km/s ( $-3.6\%$ ) to  $0.31$  km/s ( $3.9\%$ ).

Figure 5 shows lateral variation of Sn velocity. Relative to the mean value of 4.55 km/s, the Sn velocity perturbations range from  $-0.14$  km/s ( $-3.1\%$ ) to  $0.15$  km/s ( $3.3\%$ ). By 100 bootstrap inversions the errors in velocity perturbations for all cells are found to be less than 0.026 km/s. For 71% of the studied region the errors are less than 0.01 km/s.

Next, we use the adaptive moving window (AMW) approach (Sun et al., 2004) to obtain crustal velocities and Pn and Sn models from a 1-D Monte Carlo inversion of local ( $\leq 20^\circ$ ) arrival time data in the whole region, building these into the next model (Model #2). The third step is a tomographic inversion of the local and regional arrival time data for 3-D variations in the P and S wave speed, using Model #2 as the initial input model.

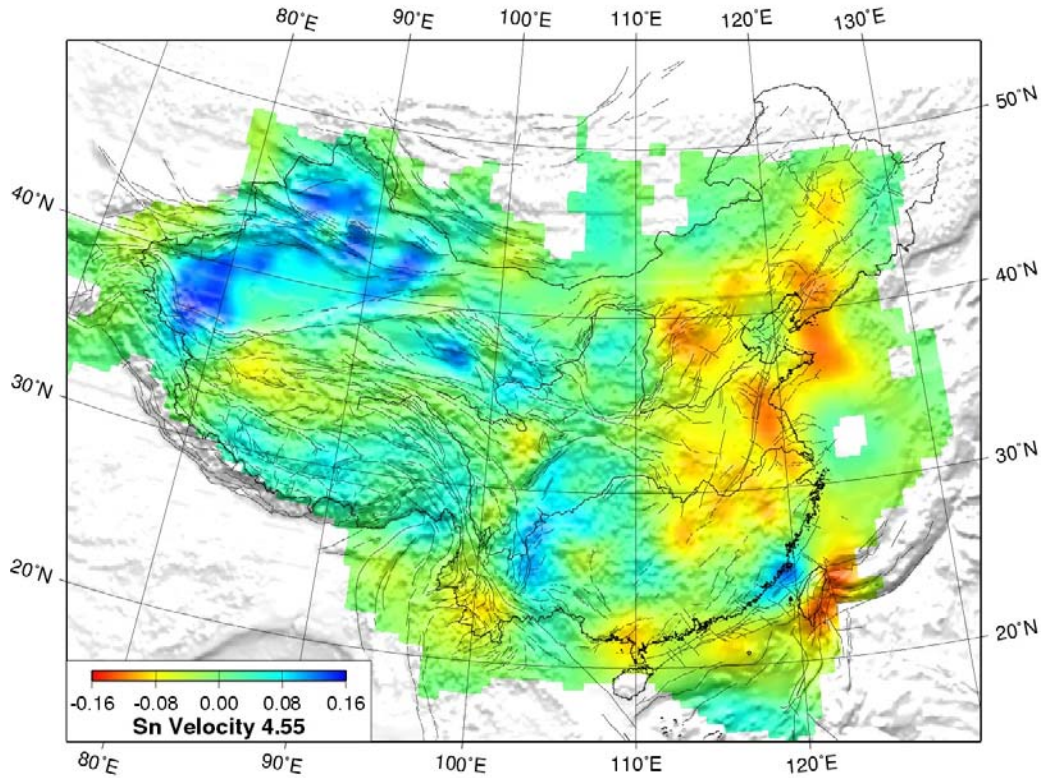


Figure 5. Tomographic image of Sn lateral velocity variations. Blue corresponds to high velocity and red to low velocity. The average Sn velocity is 4.55 km/s. The black thin lines represent active faults.

For this purpose we use a modified version of Zhao's tomographic method (Zhao et al., 1992; Sun and Toksöz, 2006), which allows for 3-D velocity variations everywhere in the model and can accommodate velocity discontinuities. The velocity structure is discretized using a 3-D grid. The velocity perturbation at each point is calculated by linear interpolation of the velocity perturbations at surrounding (adjacent) grid nodes. The velocity perturbations at grid nodes are the unknown parameters for the inversion procedure. To calculate travel-times and ray paths accurately and rapidly, the pseudo-bending technique (Um and Thurber, 1987) and Snell's law are used iteratively. We correct for station elevations by including station correction terms in the inversion. The LSQR algorithm (Paige and Saunders, 1982), with regularization, is used to solve the large and sparse system of equations. The nonlinear tomographic problem is solved by repeated linear inversions. At each iteration, perturbations to hypocentral parameters and velocity structure are determined simultaneously.

P and S wave velocity tomograms obtained for China and surrounding areas, using this method, are shown in Figures 6 and 7. The 3-D velocity model reduces the residuals and event location errors. For example, for 11 explosions at the Lop Nor site, relocation with our 3-D models reduced hypocenter errors to 1 km or less (Sun and Toksöz, 2006, Table 2).



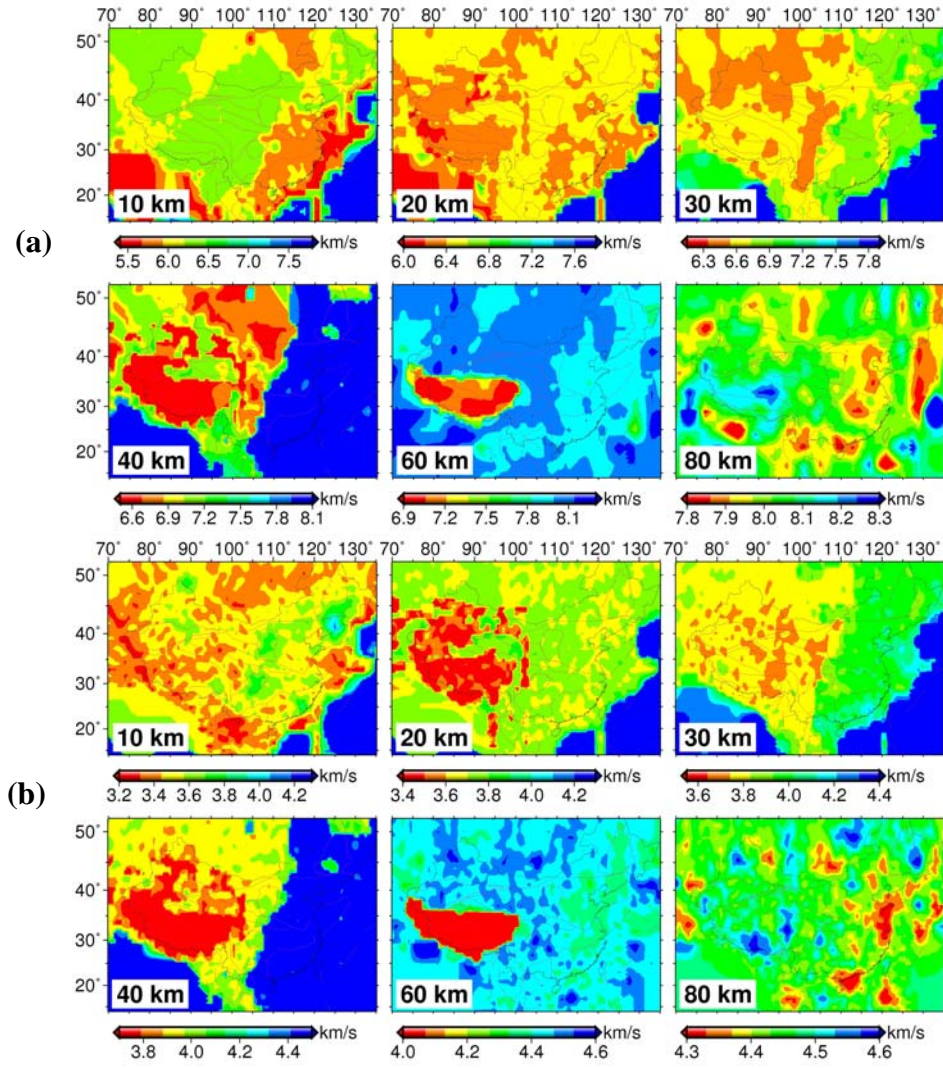


Figure 6. Horizontal slices of three-dimensional (a) Vp and (b) Vs models for China and surrounding regions at 10, 20, 30, 40, 60, and 80 km depths.

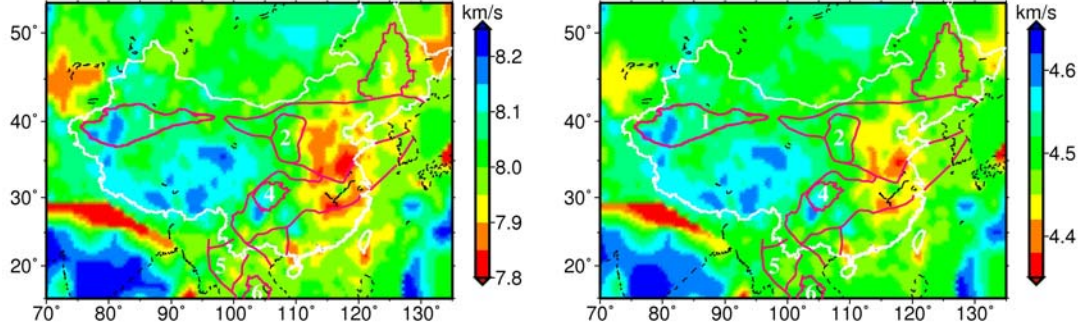


Figure 7. Pn (left) and Sn (right) velocities in China and surrounding regions. 1: Tarim Basin; 2: Ordos Basin; 3: Songliao Basin; 4: Sichuan Basin; 5: Shan Thai Block; 6: Khorat Basin.

### 3.2.2. Mantle tomography

For the upper mantle tomography, we use the multi-scale travel-time methodology we developed and improved over 15 years (e.g., Van der Hilst et al., 1991; Káráson and Van der Hilst, 2001; Li et al., 2006). Even though we focus on accurate imaging of mantle structure beneath East Asia, we perform global inversions in order to avoid artifacts created by wave propagation through the structure outside the mantle volume that is of interest here. To mitigate effects of uneven data coverage, we adapt the size of the grid block to the sampling density of the high frequency data (Káráson and van der Hilst, 2000). The size of the blocks is a multiple of  $45 \text{ km} \times 0.35^\circ \times 0.35^\circ$  (in depth, latitude, and longitude) beneath the study region (down to 800 km depth) and  $45 \text{ km} \times 0.7^\circ \times 0.7^\circ$  elsewhere. To reduce artifacts created by strong crust heterogeneity that cannot be resolved upon linearized inversion for mantle structure, we apply a crust correction using the crust models resulting from the non-linear tomography described in the previous section.

We use, again, the iterative LSQR algorithm to minimize an objective function combining a measure of data misfit and regularization terms:

$$\varepsilon = \|\mathbf{G}\mathbf{m} - \mathbf{d}\|^2 + \lambda_1 \|\mathbf{m}\|^2 + \lambda_2 \|\mathbf{L}\mathbf{m}\|^2 + \lambda_3 \|\mathbf{C} - \mathbf{m}_c\|^2. \quad (1)$$

In the first term,  $\mathbf{m}$  represents the model vector, including the constant slowness perturbation in each grid cell as well as hypocenter perturbation terms.  $\mathbf{G}$  is the sensitivity matrix, calculated using ray theory for the short period data and 3-D finite frequency kernels estimated from single scattering for long period data measured by waveform cross-correlation (Káráson, 2002). The data vector  $\mathbf{d}$  represents the travel-time residuals. The second and third terms are traditional Tikhonov regularizations that produce “minimum structure” models consistent with the data. The second term represents “norm damping” and favors a result that is close to the reference model (it minimizes the amplitude of the model). The third term reduces the difference between

adjacent cells and thus produces smooth variations;  $L$  is a first order differential operator.  $\lambda_1$  and  $\lambda_2$  are the weights of Tikhonov regularization.

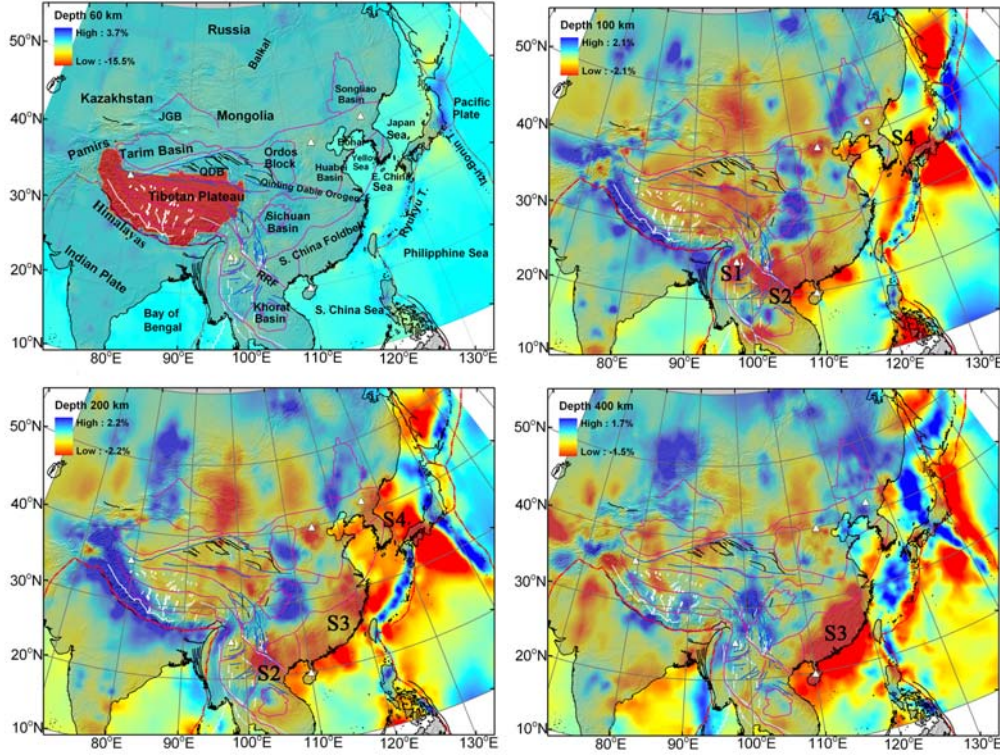


Figure 8. Lateral P wavespeeds perturbation at 60 km, 100 km, 200 km, and 400 km depths.

The last term in (1) is used to prevent time delays accrued in highly heterogeneous crust from producing artifacts in the mantle model (Li et al., 2006), with  $\mathbf{C}$  representing a best a priori estimate of the crust model and  $\mathbf{m}_c$  representing the crustal part in the model vector  $\mathbf{m}$ . The weight  $\lambda_3$  is determined through synthetic tests (Li et al., 2006). P wave velocity models obtained for China and surrounding areas by applying this method to a preliminarily assembled data set are shown in Figures 8 and 9.

### 3.3. Surface Wave Tomography

In addition to estimating S wave velocities beneath East Asia from tomographic inversion of S wave travel-time data, we use surface waves to further constrain the S velocity models.



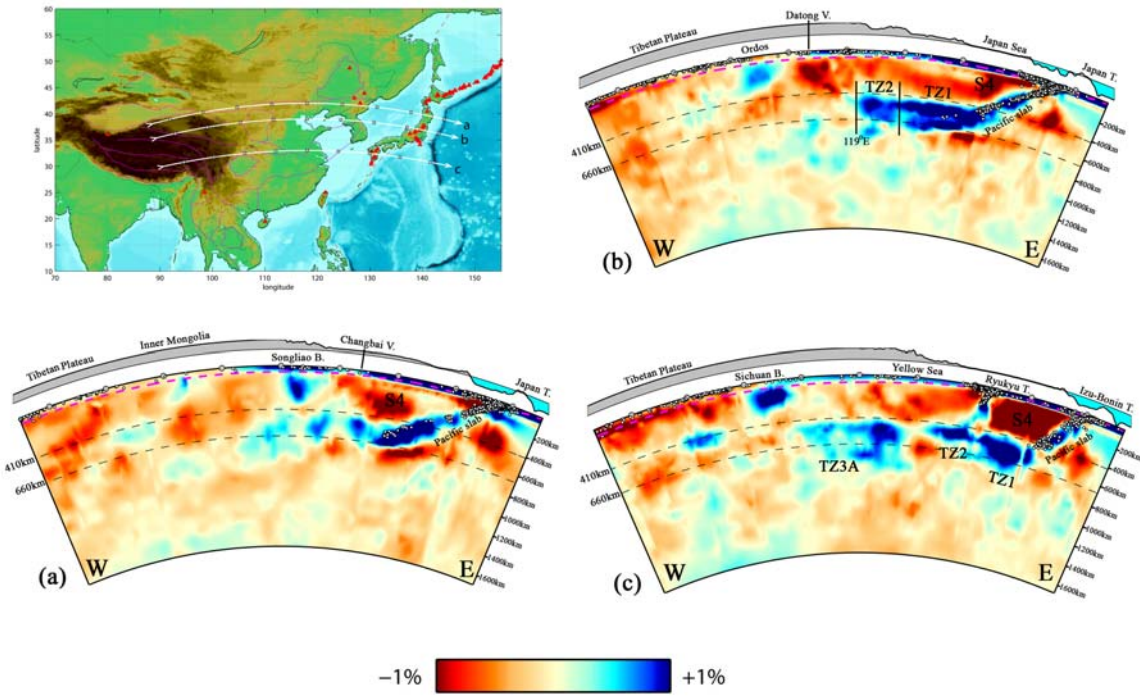


Figure 9. West-east vertical cross-sections (a), (b), and (c) through the 3-D P-wave velocity model (indicated as white lines in the upper left hand image).

### 3.3.1. Automated multi-mode surface wave tomography

Using multi-mode inversion technology we resolve long wavelength structures in the upper mantle (Lebedev and van der Hilst, 2007). To enable application to the massive volumes of earthquake data now available through international data repositories, Lebedev's multi-mode inversion procedure is almost fully automated. The velocity model for East Asia is shown in Figure 10 from Lebedev and van der Hilst (2007). The dense data coverage in China would enable the construction of shear wave velocity models at a substantially higher resolution.

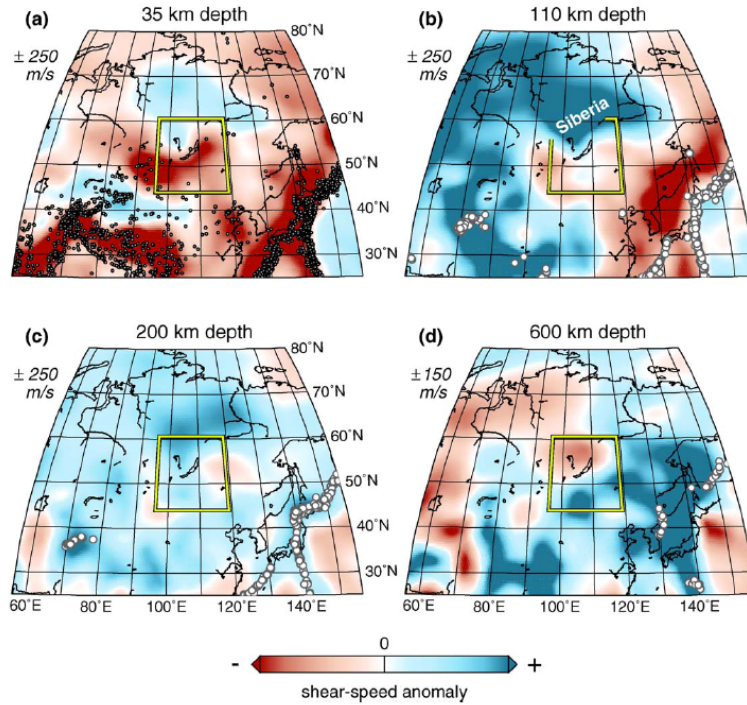


Figure 10. Lateral variations in S wave velocity at selected depths from the automated multi-mode surface wave tomography. The depths and limits of the color scales are given next to the frames. The reference model is the (3-D) CRUST2.0 in the crust and a (1-D) AK135 in the mantle. Circles show seismicity at each of the depths. (After Lebedev et al., 2006).

### 3.3.2. Array tomography based on ambient noise interferometry

Where we have dense station coverage we use cross-correlation and ambient noise tomography to obtain shear wave velocity (Campillo and Paul, 2003). We have developed a surface wave array tomography technique that uses phase velocity measurements from the empirical Green's functions (EGF) estimated from the ambient noise interferometry (Yao et al., 2006). Yao et al. (2006) shows, for broadband arrays in SE Tibet, the dense path coverage that can be achieved with this technique and the phase velocity at the period of 30 seconds from EGF analysis. Resolution tests suggest that with this data coverage one can resolve shallow mantle structure on length scales as small as  $\sim 100$  km. Figure 11 shows the dense path coverage and lateral variations in S wave velocity along several cross sections beneath the arrays.

Because of the relatively short periods involved, using data from ambient noise interferometry alone would only constrain structure in the top half of the continental lithosphere. Therefore, we combine dispersion analysis of the empirical Green's functions from interferometry with constraints from traditional inter-station dispersion analysis; together they allow spectral analysis over a wide frequency band (8–100 mHz), which allows resolution of structure between  $\sim 10$  to 150 km depth (Yao et al., 2006, 2007).



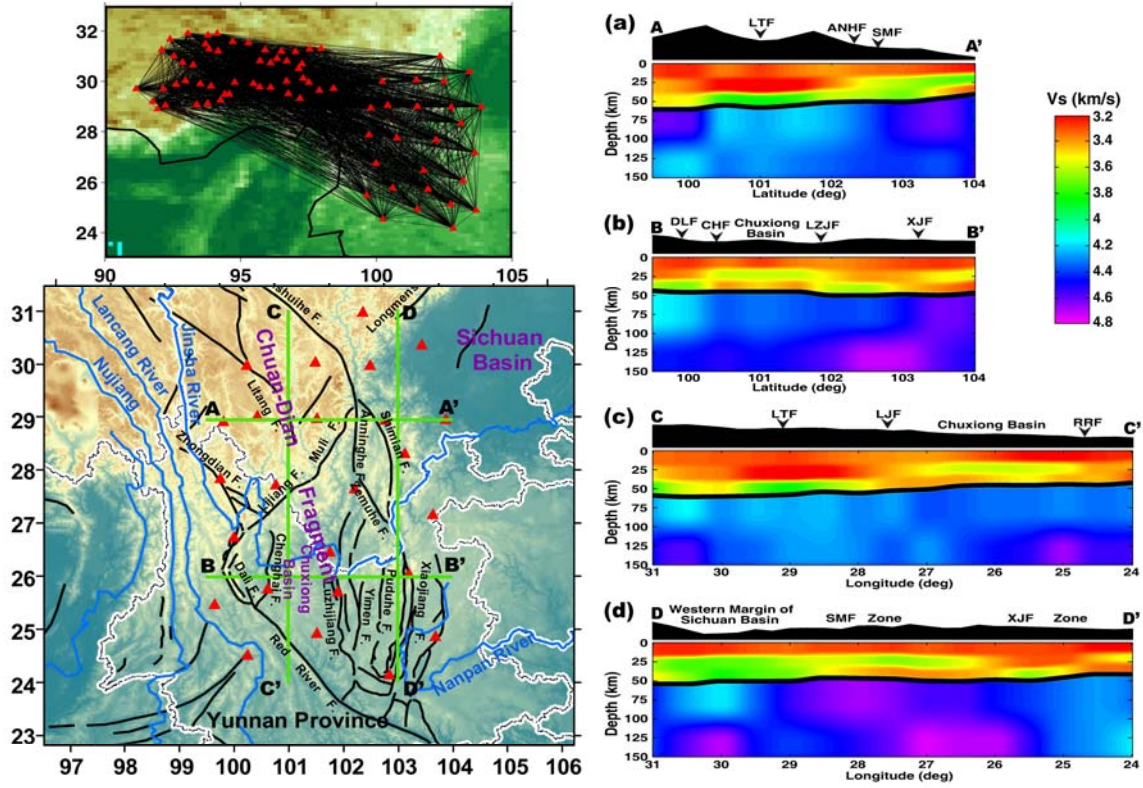


Figure 11. Inter-station ray paths (upper left corner) from ambient noise interferometry study for M.I.T. and Lehigh University arrays in southeastern Tibet. Shear wavespeeds at four cross-sections through the Sichuan and Yunnan provinces of China from the combined results of ambient noise interferometry study and two-station dispersion analysis.

### 3.4. Validation of P and S wave velocity models

Our tomographic study of the crust and uppermost mantle in China and the surrounding area generated 3-D P- and S-wave velocity models for a large continental region. Validation and interpretation of these models are part of this thesis.

#### 3.4.1. Relocation of GT events

We test our 3-D model by relocating the GT events (which were excluded from the inversion) and comparing the results with known locations. Eleven GT events are the nuclear explosions in northwestern China from 1990 to 1996, recorded by stations in China and the surrounding area. Only P-wave arrival-times are available in the dataset. These events are determined independently using both satellite imagery (Fisk, 2002) and seismic data recorded by stations in China and the surrounding area.

The explosions are closely clustered. Table 1 shows the parameters for these nuclear explosions. With our final P-wave velocity model for the crust and upper mantle in China

and the surrounding area, we relocate the GT events using arrival-time data recorded at stations within 20° epicentral distance. The relocation errors are also listed in Table 1. The three columns under “Error” are the hypocentral difference in kilometers between the reference hypocenters and relocations using the new 3-D P-wave model, 1-D average China model obtained from the 3-D model, and the AK135 global model.

Table 1: The eleven GT events in northwest China. The relocation errors (hypocentral) are listed in km. Events are relocated using our new P-wave model, the averaged 1-D model in China and the surrounding area and the standard AK135 (global).

<i>Event No.</i>	<i>Date (Y/M/D)</i>	<i>Time (H/M/S)</i>	<i>Latitude (degree)</i>	<i>Longitude (degree)</i>	<i>Error (km)</i>		
					3D	1D	AK135
<b>1</b>	1990/05/06	07:59:59.25	41.562	88.718	0.3	6.2	18.9
<b>2</b>	1990/08/16	04:59:59.26	41.539	88.745	0.9	9.5	23.0
<b>3</b>	1992/05/21	04:59:59.06	41.542	88.768	0.6	8.7	18.4
<b>4</b>	1992/09/25	08:00:00.02	41.717	88.377	0.8	9.1	17.8
<b>5</b>	1993/10/05	01:59:57.92	41.592	88.704	1.0	9.3	19.1
<b>6</b>	1994/06/10	06:25:59.46	41.527	88.707	0.9	8.1	18.4
<b>7</b>	1994/10/07	03:25:59.44	41.574	88.726	0.7	7.7	19.6
<b>8</b>	1995/05/15	04:05:59.38	41.555	88.752	0.6	8.8	24.9
<b>9</b>	1995/08/17	00:59:59.35	41.540	88.753	0.7	9.2	18.8
<b>10</b>	1996/06/08	02:55:59.37	41.578	88.688	0.9	9.3	20.1
<b>11</b>	1996/07/29	01:48:59.62	41.716	88.376	0.4	8.4	21.5

The averaged hypocentral error of relocation is only 0.7 km with a standard deviation of 0.2 km for our new 3-D P-wave model. The mean hypocentral misfit is about 10 km if the averaged 1-D velocity in China is used, and the misfit is about 20 km if the global AK135 model is used. Even though the GT events are located in northwestern China with most stations distributed in southern and eastern China, the small relocation errors clearly suggest that an accurate P-wave velocity model gives good event locations with limited azimuthal coverage.

### 3.4.2. Waveform validation

To validate P- and S-velocity models, we compare recorded seismograms with synthetics generated through the new models. Both P- and S-wave velocities can be tested by fitting body waves and surface waves. We have collected seismograms for six events (M5.0 to M6.0) recorded by the China Digital Broadband Network (CDBN) between 2001 and 2003, in different areas of China. We select three events and four profiles in eastern and southern China for seismogram fitting (Figure 12). Each event was recorded by up to 47 broadband stations in the CDBN. For each event, we select waveforms recorded by stations at different azimuths and at distances ranging from 50 km to 1000 km. Since the areas where the profiles were selected are laterally uniform we used the discrete wavenumber method (DWM) (Bouchon, 2003) to generate seismograms based on the 1-

D averaged velocity profile between the source and the station. The mechanism parameters are provided by the Harvard CMT (Centroid-Moment-Tensor) Project.

Figures 13 through 16 show the radial, transverse and vertical components for both synthetic and observed seismograms. In eastern China, the agreement between observed and calculated seismograms is good for all profiles (A, B, C and D) for both body waves and surface waves. The first arrivals of P and S waves match very well the observed arrival times and the directions of the particle motion are consistent. This good agreement suggests that our P- and S-wave models are accurate in eastern and southern China. The best agreement has been observed in the transverse component for all four profiles. The amplitude and polarity of both Rayleigh and Love waves are correctly matched. Discrepancies between transverse and radial and vertical components are primarily due to the inaccurate source mechanism, the presence of anisotropy, and the reflections of scattered waves, converted waves and multiples.

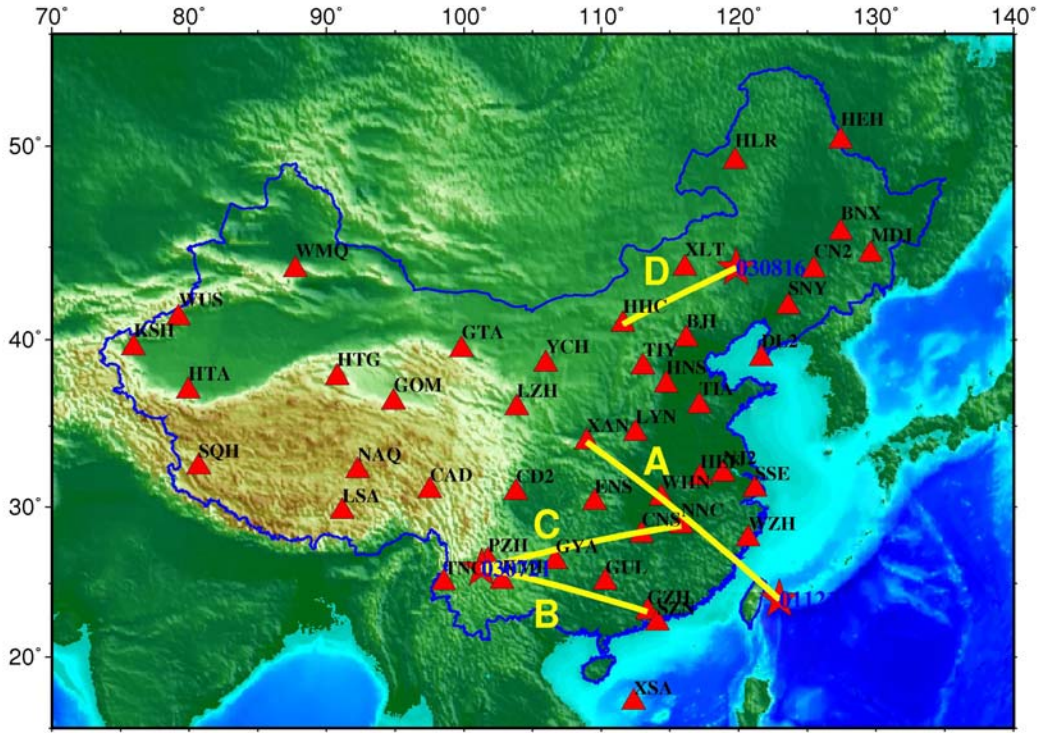


Figure 12. The selected four profiles in west and east China. 47 stations of the China Digital Broadband Network (CDBN) are plotted in red triangles.

#### 4. CONCLUSIONS

The 3-D compressional and shear-wave velocity models of the crust and upper mantle, obtained by travel-time and surface wave tomography, reveals pronounced lateral heterogeneities under China and surrounding regions. The velocity models exhibit the following features.

1. At the upper crust, down to 20 km depth, velocity variations strongly correlate with the major geological features.
2. There is a strong contrast between the regions to the east of 110°E longitude and the west. In eastern China, where crustal thickness is about 35 km or less, velocity variations are relatively small. Lower velocities delineate the rift structure of NE China. In the region to the west of 110°E longitude the crustal velocities are much more variable. Crustal thickness varies between 35 km and 78 km. The roots of prominent features such as the Tibet, Tarim, Sichuan and Ordos basins, dominate the subsurface velocity structures.
3. There is a prominent low velocity zone in the middle crust (around 40 km depth) under central Tibet. Shear velocity decreases by as much as 6% relative to the values north of Tibet and Tarim basin.
4. In general, there is good correlation between the P-wave and S-wave velocity variations. However, relative magnitudes of the variations (i.e. percentage velocity changes) are different in different regions. For example, the shear velocity decrease in the mid-crust under Tibet is twice as large as that of P-velocity, percentage wise.
5. In the upper mantle, the percentage variation of shear velocities is greater than those of P velocities.

Picking of shear wave arrivals is more prone to error than the picking of first arriving P waves, but previous studies have demonstrated the value of the reprocessed (EHB) S travel-time residuals for seismic tomography (e.g., Kennett et al., 1998; Widiyantoro et al., 1998). Encouraged by those results, we will attempt travel-time tomography for S velocity beneath East Asia. For this purpose we will augment the EHB data with S picks from the 1200 stations of the Chinese Seismograph Network and the networks in Russia.

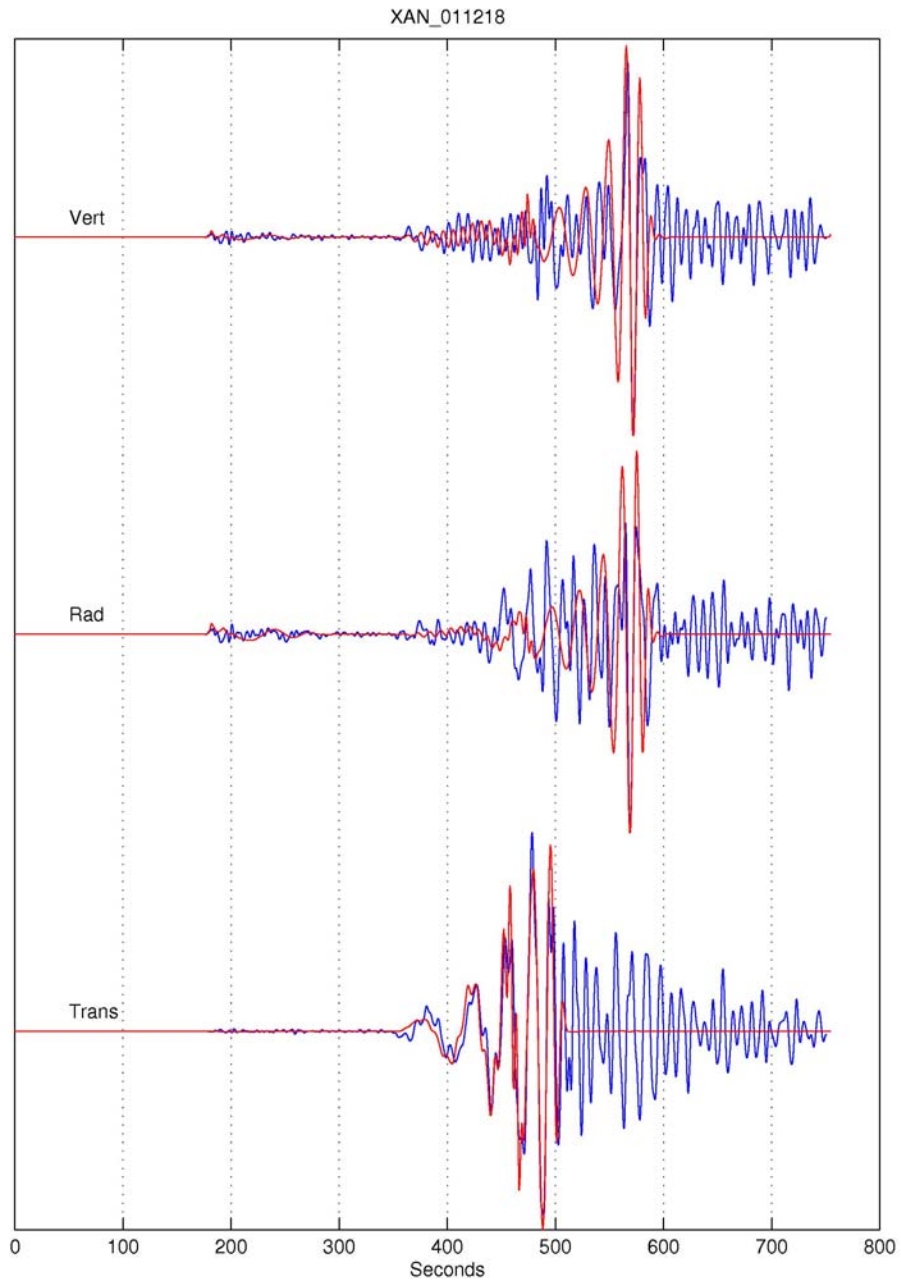


Figure 13. The observed and calculated seismograms along Profile A.



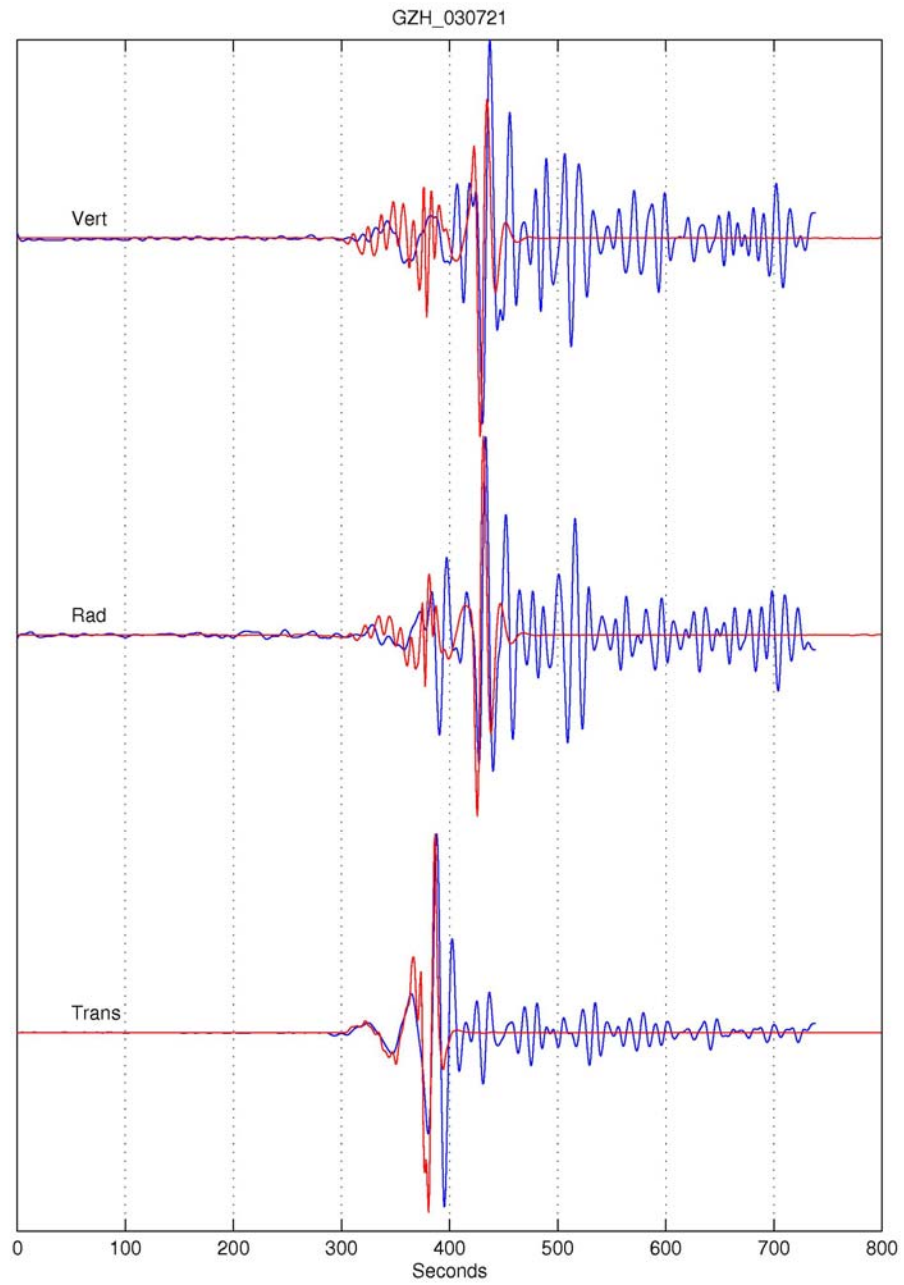


Figure 14. The observed and calculated seismograms along Profile B.

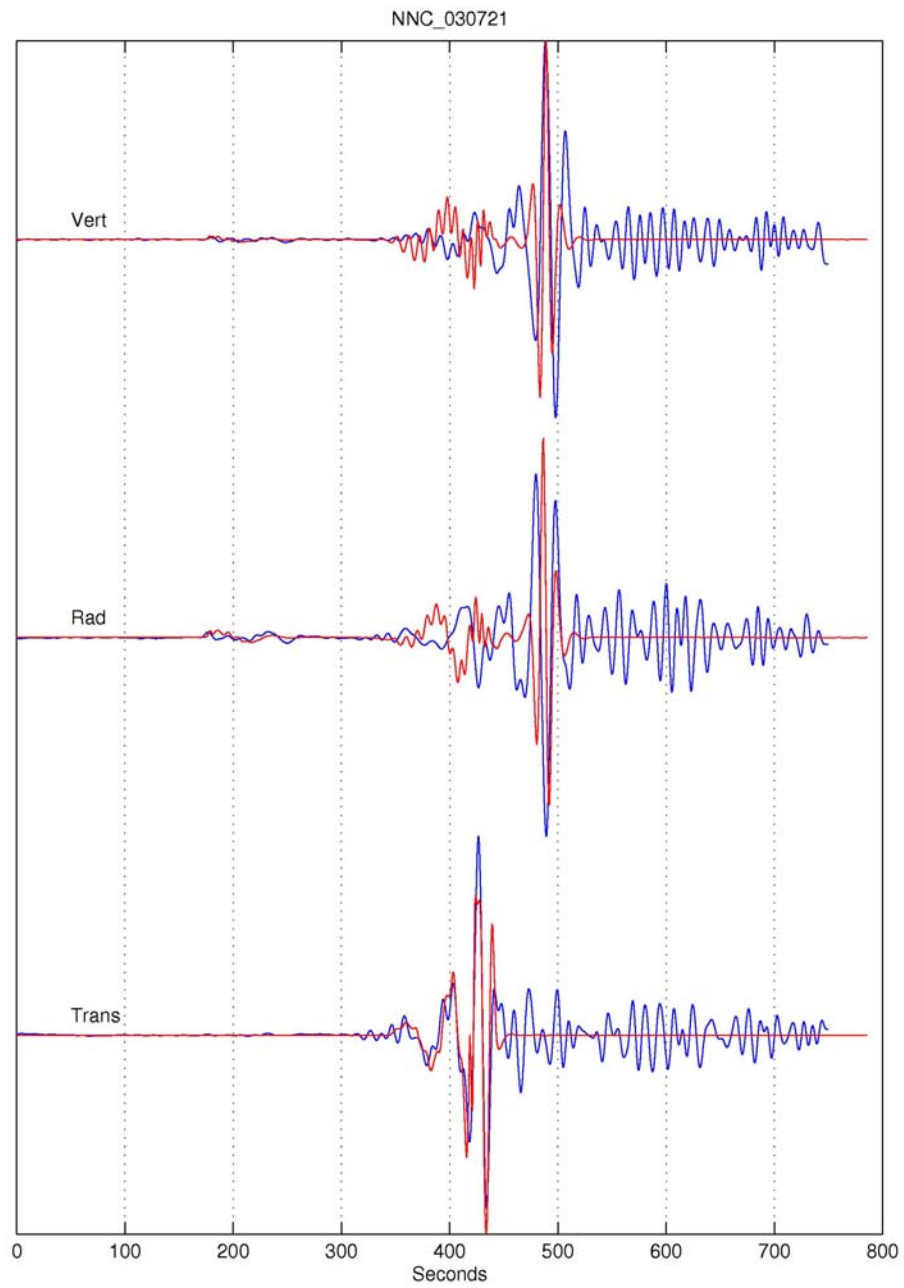


Figure 15. The observed and calculated seismograms along Profile C.

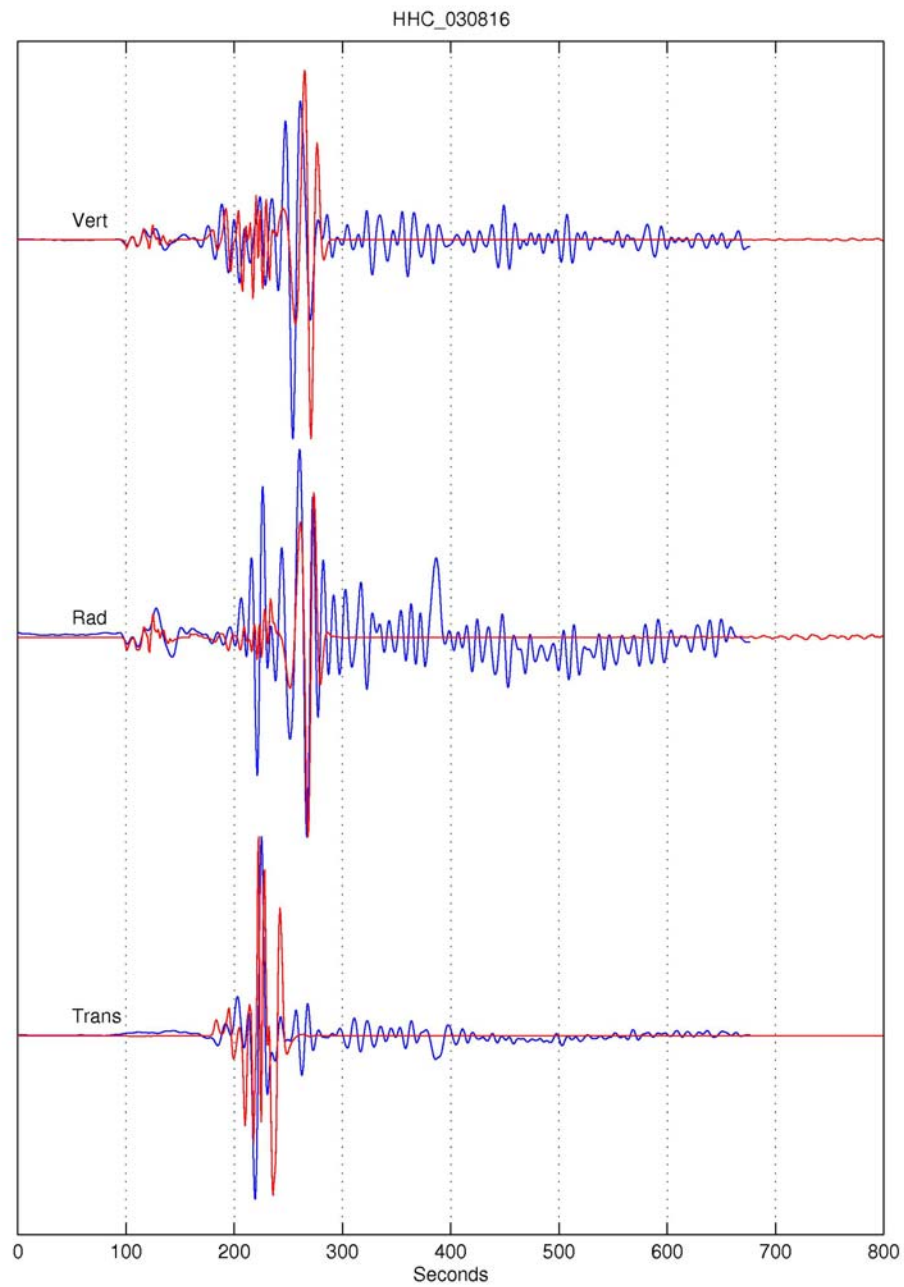


Figure 16. The observed and calculated seismograms along Profile D.



## REFERENCES

- Bassin, C., Laske, G., and Masters, G., 2000, The Current Limits of Resolution for Surface Wave Tomography in North America. *EOS Trans AGU*, 81, F897.
- Bouchon, M., 2003, A review of the discrete wavenumber method. *Pure and Applied Geophysics* 160(3-4), 445-465.
- Campillo, M. and A. Paul, 2003, Long-Range correlations in the diffuse seismic coda, *Science*, 299, 547-549.
- Ding, Z. F., R. S. Zeng, and F. T. Wu, 1993, The Pn wave velocities and the relief of Moho in the Tibetan Plateau, *Acta Seismologica Sinica*, 6, 317-325.
- Engdahl, E.R., van der Hilst, R.D., and Buland, R., 1998, Global teleseismic earthquake relocation with improved travel times and procedures for depth determination. *Bull. Seism. Soc. Am.*, 88, 722-743.
- Fisk, M. D., 2002, Accurate locations of nuclear explosions at the Lop Nor test site using alignment of seismograms and IKONOS satellite imagery. *Bull. Seismol. Soc. Am.*, 92, 2911-2925.
- Friederich, W., 2003, The S-velocity structure of the East Asian mantle from inversion of shear and surface waveforms, *Geophys. J. Int.*, 153, 88-102.
- Hearn, T.M. and J.F. Ni, 2001, Tomography and location problems in China using regional travel-time data, in the Proceedings of 23<sup>rd</sup> Seismic Research Review: Worldwide Monitoring of Nuclear Explosions, 27-45.
- Hearn, T. M., S. Wang, J. F. Ni, Z. Xu, Y. Yu, and X. Zhang, 2004, Uppermost mantle velocities beneath China and surrounding regions, *J. Geophys. Res.* 109, doi:10.1029/2003JB002874.
- Huang, J., and D. Zhao, 2004, Crustal heterogeneity and seismotectonics of the Chinese capital region. *Tectonophysics*, 385, 159-180.
- Huang, J. and D. Zhao, 2006, High-resolution mantle tomography of China and surrounding regions, *J. Geophys. Res.*, 111, B09305, doi:10.1029/2005JB004066.
- Huang, Z., W. Su, Y. Peng, Y. Zheng, and H. Li, 2003, Rayleigh wave tomography of China and adjacent regions, *J. Geophys. Res.*, 108(B2), 2073, doi:10.1029/2001JB001696.
- Kárason, H., and Van der Hilst, R.D., 2000, Constraints on mantle convection from seismic tomography. In M.A. Richards, R. Gordon and R.D. van der Hilst (Editors). *History and Dynamics of Plate Motion*. Am. Geophys. Union, *Geophys. Monogr. Ser.*, 121, 277-288.
- Kárason, H., and van der Hilst, R.D., 2001, Tomographic imaging of the lowermost mantle with differential times of refracted and diffracted core phases (PKP, Pdiff). *J. Geophys. Res.*, 106, 6569-6587.
- Kárason, H., 2002, Constraints on mantle convection from seismic tomography and flow modeling, Ph.D. thesis, Massachusetts Institute of Technology, Cambridge, MA.
- Kennett, B.L.N., Widiyantoro, S., and Van der Hilst, R.D., 1998, Joint seismic tomography for bulk-sound and shear wavespeed, *J. Geophys. Res.*, 103, p. 12469-12493.
- Laske, G., and G. Masters, 1997, A global digital map of sediments thickness (abstract), *EOS* 78, F483.

- Laske, G., G. Masters, and C. Reif, 2001, CRUST 2.0: a new global crustal model at 2x2 degrees, <http://mafi.ucsd.edu/Gabi/rem.dir/crust/crust2.html> (last accessed July 2005).
- Lebedev, S., and G. Nolet, 2003, Upper mantle beneath southeast Asia from S velocity tomography. *J. Geophys. Res.* 108, doi 10.1029/2000JB000073.
- Lebedev, S., and Van der Hilst, R.D., 2007, Global upper-mantle tomography with the automated multi-mode surface and S waveforms, *Geophys. J. Int.* (under review).
- Li, C., 2007, Evolution of upper mantle beneath East Asia and the Tibetan Plateau from P-wave tomography, Ph.D. thesis, Massachusetts Institute of Technology, Cambridge, MA.
- Li, C., R.D. van der Hilst, and M. N. Toksoz, 2006, Constraining P-wave velocity variations in the upper mantle beneath Southeast Asia, *Phys. Earth Planet. Inter.*, 154, 180 - 195.
- Li, S.L., W.D. Mooney, and J. Fan, 2006, Crustal structure of mainland China from deep seismic sounding data, *Tectonophysics*, 420, 239-252.
- Liang, C., X. Song, and J. Huang, 2004, Tomographic inversion of Pn traveltimes in China, *J. Geophys. Res.*, 109, B11304, doi:10.1029/2003JB002789.
- Mooney, W. D., 1998, CRUST 5.1: a global crustal model at 5° x 5°. *J. Geophys. Res.* 103, 727-747.
- Morozov, I.B., E.A. Morozova, S.B. Smithson, P.G. Richards, V.I. Khalturin, and L.N. Solodilov, 2005, 3D first-arrival regional calibration model of northern Eurasia, *Bull. Seism. Soc. Am.*, 95, 951-964.
- Nelson, K. D., et al., 1996, Partially molten middle crust beneath southern Tibet: Synthesis of project INDEPTH results, *Science*, 274, 1684-1688.
- Paige, C., and M. Saunders, 1982, LSQR: An algorithm for sparse linear equations and sparse least squares. *ACM Trans. Math. Software*, 8, 471.
- Pei, S., J. Zhao, Y. Sun, Z. Xu, S. Wang, H. Liu, C. A. Rowe, M. N. Toksoz, and X. Gao, 2007, Upper mantle seismic velocities and anisotropy in China determined through Pn and Sn tomography. *J. Geophys. Res.*, 112, B05312, doi:10.1029/2006JB004409.
- Phillips, W. S., C. A. Rowe, and L. K. Steck, 2005, The Use of interstation arrival time differences to account for regional path variability, *Geophys. Res. Letts.*, 32, L11301, doi:10.1029/2005GL022558.
- Reiter D. and Rodi W., 2006, Crustal and Upper-mantle P- and S- velocity structure in central and southern Asia from joint body -and surface- wave inversion, 28th Seismic Research Review: Ground-Based Nuclear Explosion Monitoring Technologies, 209-218.
- Ritzwoller, M. H., M. P. Barmin, A. Villasenor, A. L. Levshin, and E. R. Engdahl, 2002, Pn and Sn tomography across Eurasia to improve regional seismic event locations. *Tectonophysics* 358, 39-55.
- Rowe, C, Steck, L.K., W. S. Phillips, M. Begnaud, R. Stead and H. Hartse, 2005, Pn tomography and location in Eurasia, 2005 IASPEI Meeting, Santiago, Chile.
- Shapiro, N. M., and M. H. Ritzwoller, 2002, Monte Carlo inversion for a global shear velocity model of the crust and upper mantle. *Geophys. J. Int.* 151, 88-105.
- Stevens, J. L., D. A. Adams, and G. E. Baker, 2001, Improved surface wave detection and measurement using phase-matched filtering with a global one-degree dispersion

- model, in *Proceedings of 23rd Seismic Research Review: Worldwide Monitoring of Nuclear Explosions*, 420-430.
- Sun, Y. and M.N. Toksoz, 2006, Crustal structure of China and surrounding regions from P wave traveltime tomography, *J. Geophys. Res.*, 111, B03310, doi:10.1029/2005JB003962.
- Sun, Y., X. Li, S. Kuleli, F. D. Morgan, and M. N. Toksöz, 2004, Adaptive moving window method for 3-D P-velocity tomography and its application in China. *Bull. Seism. Soc. Am.* 94, 740-746.
- Sun, Y., M.N. Toksöz, S. Pei, and D. Zhao, 2007, S-wave Tomography of the Crust and uppermost mantle in China. In preparation for submission to *J. Geophys. Res.*
- Um, J., and C. Thurber, 1987, A fast algorithm for two-point seismic ray tracing. *Bull. Seism. Soc. Am.* 77, 972-986.
- Van der Hilst, R.D., Engdahl, E.R., Spakman, W., and Nolet, G., 1991, Tomographic imaging of subducted lithosphere below northwest Pacific island arcs, *Nature*, v. 353, p. 37-42.
- Wang, C.-Y., W. W. Chan, and W. D. Mooney, 2003, Three-dimensional velocity structure of crust and upper mantle in southwestern China and its tectonic implications, *J. Geophys. Res.*, 108(B9), 2442, doi:10.1029/2002JB00.
- Widiyantoro, S., Kennett, B.L.N., and Van der Hilst, R.D., 1998, Extending shear-wave tomography for the lower mantle using S and SKS arrival-time data, *Earth, Planets, and Space*, v. 50, p. 999-1012.
- Wu, F. T., A. L. Levshin, and V. M. Kozhevnikov, 1997, Rayleigh wave group velocity tomography of Siberia, China, and vicinity. *Pure Appl. Geophys.* 149, 447-473.
- Yao, H., van der Hilst, R.D., and De Hoop, M.V., 2006, Surface-wave array tomography in SE Tibet from ambient seismic noise and two-station analysis: I - Phase velocity maps, *Geophys. J. Int.*, 166, 732-744, doi: 10.1111/j.1365-246X.2006.03028.x.
- Zhao, D., A. Hasegawa, and S. Horiuchi, 1992, Tomographic imaging of P and S wave velocity structure beneath northeastern Japan. *J. Geophys. Res.*, 97, 19909-19928.

## LIST OF PUBLICATIONS

- Li, C., R. D. van der Hilst, and M. N. Toksoz, 2006. Constraining P-wave velocity variation in the upper mantle beneath southeast Asia. *Physics Earth and Planetary Interiors*, 154, 180-195.
- Pei, S., Z. Cui, Y. Sun, C. A. Rowe, X. Gao, J. Zhao, and H. Liu, 2008, S-wave Attenuation Structure of Upper Crust from Amplitude Tomography in Japan. *Bull. Seism. Soc. Am.*, submitted.
- Pei, S., J. Zhao, Y. Sun, Z. Xu, S. Wang, H. Liu, C. A. Rowe, M. N. Toksoz, and X. Gao, 2007. Upper mantle seismic velocities and anisotropy in China determined through Pn and Sn tomography. *J. Geophys. Res.*, 112, B05312, doi:10.1029/2006JB004409.
- Pei, S., J. Zhao, C. A. Rowe, S. Wang, T. M. Hearn, Z. Xu, H. Liu, and Y. Sun, 2006, ML Amplitude Tomography in North China. *Bull. Seism. Soc. Am.*, Vol. 96, No. 4A, pp. 1560-1566, August 2006, doi: 10.1785/0120060021.
- Sun, Y., M. N. Toksoz, S. Pei, D. Zhao, and A. Rosca, 2008. S-wave tomography of the crust and uppermost mantle in China. *J. Geophys. Res.*, submitted.
- Sun, Y., M. N. Toksoz, S. Pei, and F. D. Morgan, 2008. The layered shear wave velocity structure of the crust and uppermost mantle in China. *Bull. Seism. Soc. Am.*, vol. 98, No. 2, 746-755, doi: 10.1785/0120050222.
- Sun, Y., and M. N. Toksoz, 2006. Crustal structure of China and surrounding regions from P wave traveltimes tomography. *J. Geophys. Res.*, 111, B03310, doi:10.1029/2005JB003962.
- Yao, H., R. D. van der Hilst, and M. V. De Hoop, 2006, Surface-wave array tomography in SE Tibet from ambient seismic noise and two-station analysis: I - Phase velocity maps, *Geophys. J. Int.*, 166, p.732-744, doi: 10.1111/j.1365-246X.2006.03028.x.

**APPENDIX**

**PUBLICATIONS**



## Crustal structure of China and surrounding regions from *P* wave traveltime tomography

Youshun Sun<sup>1</sup> and M. Nafi Toksöz<sup>1</sup>

Received 26 July 2005; revised 30 November 2005; accepted 19 December 2005; published 21 March 2006.

[1] A three-dimensional (3-D) *P* wave velocity model is developed for the crust and uppermost mantle of China and the surrounding area by applying the tomography method of Zhao et al. using 500,000 high-quality *P* wave first arrivals extracted from the *Annual Bulletin of Chinese Earthquakes* (ABCE). This tomographic method can accommodate velocity discontinuities such as the Moho in addition to smooth velocity variations. The spatial resolution is  $1^\circ \times 1^\circ$  in the horizontal direction and 10 km in depth. The velocity images of the upper crust correspond well with the surface geologic features such as basins and the Tibetan Plateau. High-velocity anomalies are found in the lower crust beneath the Precambrian regions (Tarim Basin, Ordos Basin, Sichuan Basin, and western half of Songliao Basin). The highest-velocity anomaly is beneath the Sichuan Basin. High- and low-velocity anomalies imaged beneath the Bohai Gulf are associated with the presence of a major Cenozoic rift system. In the lower crust beneath the South China Block, *P* wave velocities are lower in the north than in the south. The Indochina Block shows low velocities both in the crust and in the uppermost mantle due to volcanism. The *P<sub>n</sub>* velocities in the Tibet area are higher than those in other areas largely due to thicker crust. Tomographic model significantly reduces the traveltime residuals. Tests conducted by relocating large explosions and earthquakes validate the 3-D velocity model.

**Citation:** Sun, Y., and M. N. Toksöz (2006), Crustal structure of China and surrounding regions from *P* wave traveltime tomography, *J. Geophys. Res.*, *111*, B03310, doi:10.1029/2005JB003962.

### 1. Introduction

[2] China and the surrounding area is a seismically active and geologically complex region (Figures 1 and 2). More than 500 earthquakes with magnitudes (*M*) greater than 6.0 occurred in this region between January 1978 and May 2004 (Figure 1). Historically large and destructive earthquakes took place frequently both in east and west China. Most large earthquakes in this region are located at depths of 10 to 20 km. A detailed investigation of the crustal structure is important for understanding the seismotectonics of the region and for assessing and mitigating seismic hazard.

[3] From a geological point of view, there are four Precambrian platforms (Figure 1) in China and the surrounding area [Lebedev and Nolet, 2003]: the North China Block, the South China Block, the Tarim Basin, and the Indochina Block. The North China Block, also known as the Sino-Korean Craton, consists of two major Archean (older than 2.5 Ga) continental nuclei surrounded by Paleoproterozoic (about 1.8 Ga) orogenic belts. One nucleus is approximately within the boundaries of the Ordos Basin (Ordos Plateau), and the other, larger one, is beneath and

around the Bohai Gulf. Younger orogenic belts are located along the margins of the block. The South China Block includes two major Precambrian elements: the Yangtze Craton and the Cathaysia Block. The Archean nucleus of the Yangtze Craton is approximately within the boundaries of the Sichuan Basin. The Paleoproterozoic basement is found in the vicinity of the basin and to the southwest; the rest of the basement is probably Grenville age (about 1.0 Ga). The Cathaysia Block is situated along the coast (partly in the South China Fold Belt and partly underwater to the east) and is separated from the Yangtze Craton by orogenic belts of different ages, from about 1000 to 150 Ma. The Tarim Basin consists of a nucleus of Archean through Proterozoic age covered by thick Cenozoic sediments. The Indochina Block also has a Precambrian core and probably extends to the northwest as the Shan Thai (Simao) Block.

[4] The available *P* wave velocity models of the crust and upper mantle in China and the surrounding area have been obtained using a variety of approaches. Global models such as CUB 1.0 [Shapiro and Ritzwoller, 2002] and the SAIC  $1^\circ \times 1^\circ$  model [Stevens et al., 2001] were constructed from group and phase velocity dispersion measurements of surface waves. The models based on surface waves are generally large-scale and intended to map the deep structure of the earth. The global model CRUST 2.0 (G. Laske et al., CRUST 2.0: A new global crustal model at  $2^\circ \times 2^\circ$  degrees, 2001, available at <http://mafi.ucsd.edu/Gabi/rem.dir/crust/crust2.html>, last accessed July 2005) was constructed from seismic refraction data and developed from the CRUST 5.1

<sup>1</sup>Earth Resources Laboratory, Department of Earth, Atmospheric, and Planetary Sciences, Massachusetts Institute of Technology, Cambridge, Massachusetts, USA.

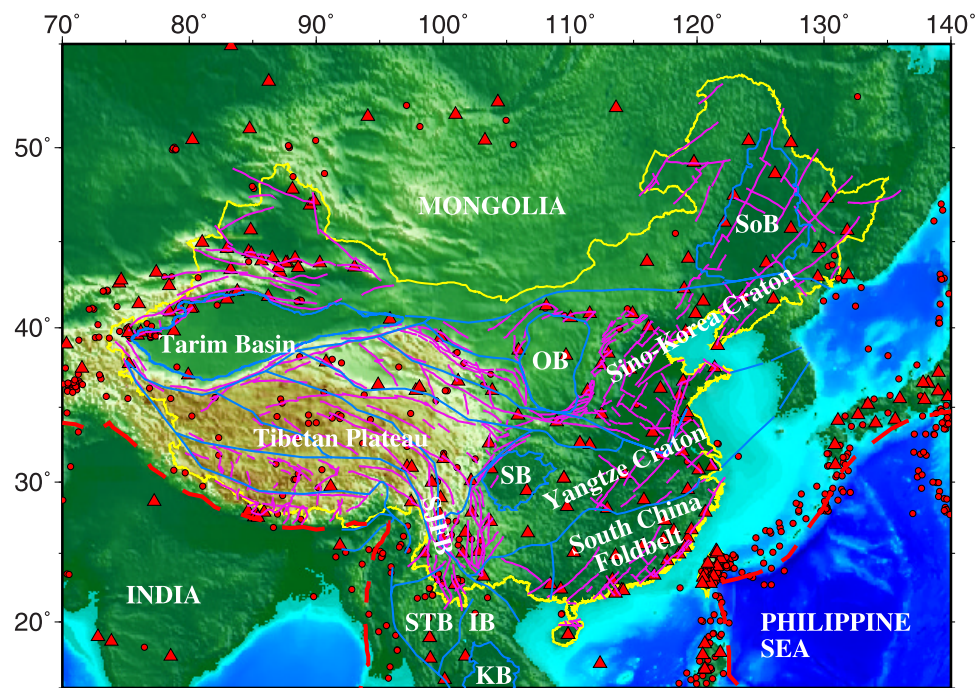


**Figure 1.** The 512 big earthquakes ( $M > 6.0$  from January 1978 to May 2004), 220 stations, active faults and major tectonic boundaries in China and the surrounding area. Earthquake epicenters are shown as red dots, and stations are shown as red triangles. The yellow line shows the boundary of China. Active faults in the China area are shown as purple lines, and tectonic sutures are shown as blue lines, where SoB, Songliao Basin; OB, Ordos Basin; SB, Sichuan Basin; SJFB, Sanjiang Fold Belt; STB, Shan Thai Block; IB, Indochina Block; KB, Khorat Basin.

model [Mooney, 1998] and a  $1^\circ \times 1^\circ$  sediment map [Laske and Masters, 1997]. Although CRUST 2.0 was created by tomographic inversion, there are too few deep seismic soundings (DSSs) to provide enough refraction data for a detailed model. Regional models were constructed by  $P_n$  and/or  $S_n$  tomography [Ritzwoller et al., 2002; Hearn et al., 2004; Liang et al., 2004; Pei et al., 2004; Phillips et al., 2005], from surface waves [Song et al., 1991; Wu et al., 1997; Zhu et al., 2002; Huang et al., 2003; Lebedev and Nolet, 2003], and from  $P$  wave traveltime tomography [Liu et al., 1990]. The model of Liu et al. [1990] was constructed by regional and teleseismic tomography. The maximum and minimum grid spacings in the model of Liu et al. [1990] are  $5^\circ \times 5^\circ$  and  $2^\circ \times 2^\circ$ , respectively, in the horizontal direction and 300 and 45 km in the vertical direction. This model does not include the fine details for local and regional traveltime calculations and precise earthquake locations.

[5]  $P$  wave tomography has been performed in several local regions in China [Zhu et al., 1990; Sun and Liu, 1995; Huang et al., 2002; Xu et al., 2002; Wang et al., 2003; Yu et al., 2003; Huang and Zhao, 2004; Pei et al., 2006]. Xu et al. used  $P$  wave arrival times of local, regional, and teleseismic events recorded by Chinese and Kyrgyzstan seismic networks to tomographically map the crustal and upper mantle velocity structures beneath western China. The grid spacing is  $1.5^\circ \times 1.5^\circ$  in the horizontal direction and about 10 km in the crust and 50 km in the uppermost mantle in the vertical direction. Crustal structures beneath north and east China including Beijing and surrounding regions were obtained by Zhu et al. [1990], Sun and Liu [1995], Yu et al. [2003] and

Huang and Zhao [2004] as the result of their  $P$  wave tomographic studies. Huang et al. [2002] and Wang et al. [2003] inverted the lithospheric structure in southwest China from local/regional arrival time data. Pei et al. [2006] and Li et al. [2006] imaged the mantle beneath East Asia by performing  $P$  wave traveltime tomography using regional and teleseismic events. These models show detailed crustal structures only in a few regions. A detailed map for the whole China area remains to be developed.

[6] A high-resolution three-dimensional (3-D) velocity model of China is necessary to provide accurate traveltimes for reliable determination of earthquake locations. Large-scale models obtained by the teleseismic tomography technique generally cannot resolve vertical variations in the shallow structure. Regional models can be combined in order to cover a large area, but such models cannot guarantee smooth and consistent transitions between different regions. During the last several years, there have been many digital seismic stations installed in the China area (Figure 1). The large database of high-quality recorded arrival times provides an unprecedented opportunity to determine a detailed 3-D crustal structure under the region. Therefore we introduce a method that constructs a 3-D  $P$  velocity model for the whole China area based on observed traveltime data.

[7] The starting model for the tomographic study is a 3-D model created with the adaptive moving window (AMW) method [Sun et al., 2004b] using an extensive catalog of 14 years of earthquake arrival time data. The model assumes a layered crust and a one-layer uppermost mantle at each



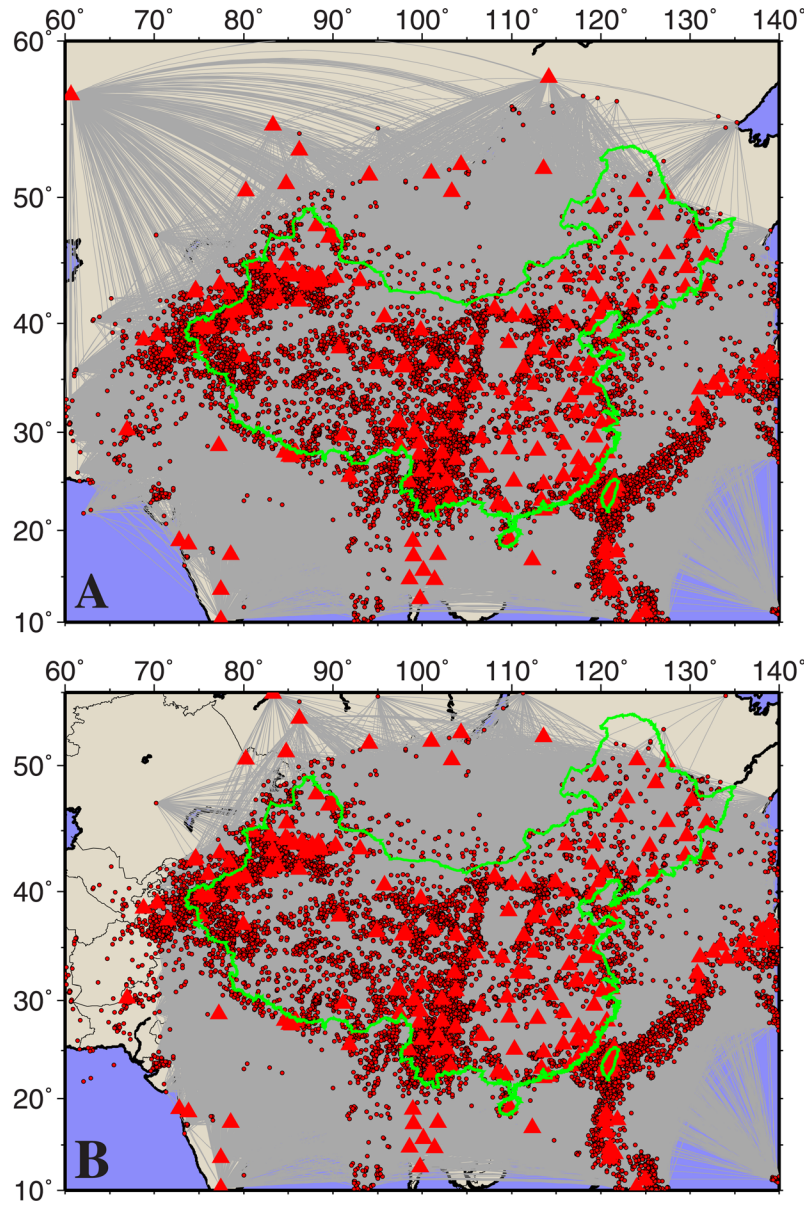


**Figure 2.** (a) The 25,000 earthquakes, 220 stations, and 500,000 ray paths in China and the surrounding area. Earthquake epicenters are shown as black circles, and stations are shown as red triangles. The green line shows the boundary of China. (b) Distribution of seismic stations and epicenters of selected earthquakes. A total of 16,572 events from  $M \geq 3.0$  are selected.

one degree intersection of longitude and latitude. The thickness and body wave velocity of each layer are found from the observed traveltimes. These  $1^\circ \times 1^\circ$  velocity profiles are quilted together with a suitable smoothing to obtain the starting model for the 3-D tomography.

## 2. Traveltime Data and 3-D Tomography

[8] In this study, we use the earthquake phase data (first  $P$  wave arrivals) from January 1990 to December 2003 from the ABCE [Institute of Geophysics, China Seismological Bureau (IG-CSB), 1990–2003]. There are 25,000 earthquakes, 220 stations, and 500,000 ray paths in China and the surrounding area in this database. Figure 2 shows earthquake epicenters, the stations, and the ray paths. We

also incorporated special data such as 129 earthquakes with high-quality records and 3 quarry blast events (ground truth events) from Sichuan Province [Sun *et al.*, 2004a].

[9] Given that the ray coverage is denser in some areas and redundant calculation is involved, we adopted the method described below to assemble the best set of the earthquake data. The study area is divided into parallelepipedic blocks with a spatial size of 10 km (northing)  $\times$  10 km (easting)  $\times$  2 km (depth). Among the earthquakes within each block, we only select the event with the greatest number of first  $P$  wave arrivals and the smallest hypocentral location uncertainty. As a result, our final data set contains 16,000 events with more than 300,000 ray paths. The final ray coverage has a better (more uniform) distribution in the study area (Figure 2b), and it is

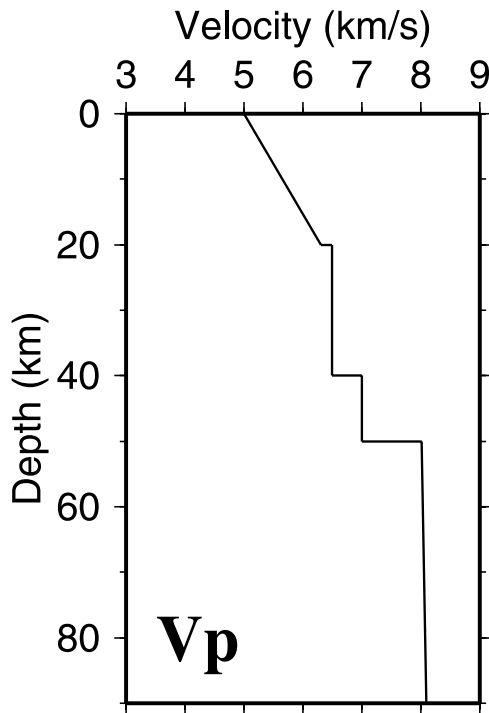


**Figure 3.** Averaged 1-D velocity model used for the tomographic inversion.

therefore more appropriate for tomographic study than the original data set. Since most aftershocks occur in similar locations with smaller magnitudes and tend to produce larger reading errors for the phase arrivals than the main shocks, the final data set contains the least number of aftershocks.

[10] The input and output 3-D models are represented by velocity perturbations relative to an averaged 1-D reference model in the study area. Even though the traveltimes are calculated based on 3-D models, the 1-D reference model significantly influences the final result of the tomographic study because of the linearization process taken in the tomography. An inappropriate initial reference model may not only affect the quality of the three dimensional images by introducing artifacts, but it may also influence the confidence calculations by underestimating the uncertainties of the results [Yu *et al.*, 2003; Kissling *et al.*, 1994]. We inverted the arrival time data in our selected data set for a 1-D velocity model representing the whole study area by minimizing the root-mean-square (RMS) error of the traveltimes. Finally, we obtained the 1-D model shown in Figure 3 which gave the best fit to the observed data. We used this averaged 1-D model as the reference velocity model for our tomographic inversions.

[11] The discontinuities represent known geological boundaries such as the Conrad and the Moho discontinuities. Previous studies were able to map the Moho discontinuity in the study area and revealed its significant lateral depth variations [China Seismological Bureau, 1986; Li *et al.*, 2001; Sun *et al.*, 2004b; Y. Sun *et al.*, The layered crustal structure in China, submitted to *Bulletin of the Seismological Society of America*, 2006]. The Conrad discontinuity is clear only in some regions of the study area, and therefore we only incorporate the Moho discon-

tinuity in this study. The input geometry of the Moho discontinuity was compiled from previous results [Sun *et al.* 2004b]. The Moho is shallower in eastern China, ranging from 30 to 42 km, compared to western China where it is between 50 and 78 km. All the depths are referenced to sea level.

[12] We applied the tomographic method of Zhao *et al.* [1992] for determining the crustal and uppermost mantle velocity structures in China and the surrounding area. Zhao's method, described in detail in several papers [Zhao *et al.*, 1992, 1994; Zhao, 2001], allows 3-D velocity variations everywhere in the model and can accommodate velocity discontinuities. The velocity structure is discretized using a 3-D grid. The velocity perturbation at each point is calculated by linearly interpolating the velocity perturbations at the eight surrounding (adjacent) grid nodes. Velocity perturbations at grid nodes are the unknown parameters for the inversion procedure. To calculate traveltimes and ray paths accurately and rapidly, the pseudobending technique [Um and Thurber, 1987] and Snell's law are used iteratively. Station elevations are taken into account as station corrections when an averaged 4 km/s crustal velocity model was used. The LSQR algorithm [Paige and Saunders, 1982] with a damping regularization is used to solve the large and sparse system of equations. The nonlinear tomographic problem is solved by iteratively conducting linear inversions. At each iteration, perturbations to hypocentral parameters and velocity structure are determined simultaneously. Although we believe that epicentral errors are very small (about 10 km) in the ABCE data set, we have allowed the hypocenters to be relocated in our inversion process in order to solve the inversion problems completely.

### 3. Implementation and Resolution Analysis

[13] From the checkerboard resolution analyses, we adopt a grid spacing of  $1^\circ$  in the horizontal direction, and 10 km in depth (Figure 4). We add grid nodes at depths of 1 km, 2 km,

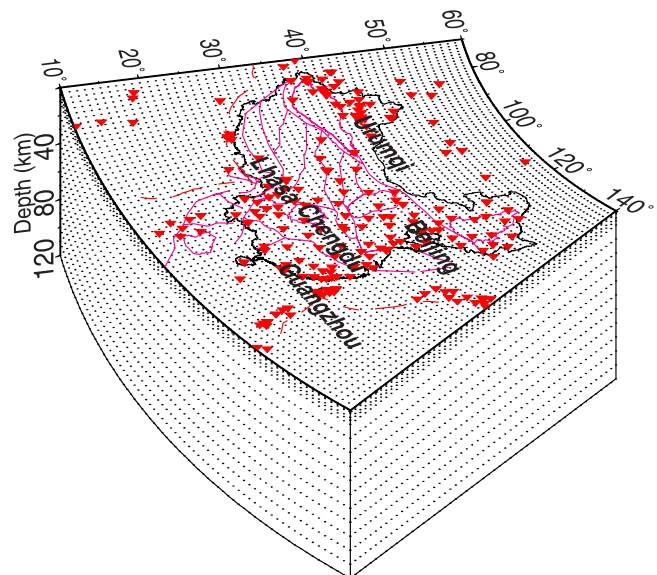


**Figure 4.** Three-dimensional configuration of the grid adopted in the present study.

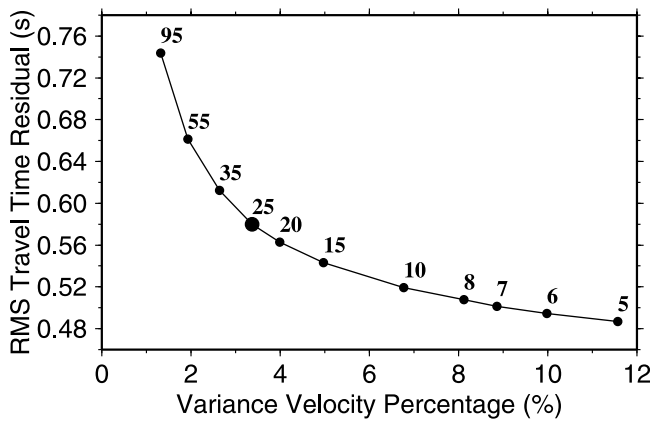


**Figure 5.** Trade-off curve for the variance of the velocity perturbations and root-mean-square traveltime residuals. Numbers beside the black dots denote the damping parameters adopted for the inversions. The largest black dot denotes the optimal damping parameter for the final tomographic model.

5 km, and 7 km to discretize the sediment layer. We chose a damping value of 25.0 from the tradeoff curve (Figure 5) between the traveltime residuals and the model variance by considering the balance between the reduction of traveltime residuals and the smoothness of the 3-D velocity model obtained [Eberhart-Phillips, 1986]. For the inversion with a damping parameter of 25.0, the RMS traveltime residual is reduced from 0.91 s to 0.58 s, and the variance reduction is 57% between the initial and final 3-D models. Figure 6 shows the change in the distribution of traveltime residuals before and after the inversion. Over 80% of the rays have residuals smaller than 0.45 s after the inversion (Figure 6). Figure 6 also shows that the RMS traveltime residual is about 1.2 s if the 1-D reference model is used to calculate the traveltimes. The variance reduction is

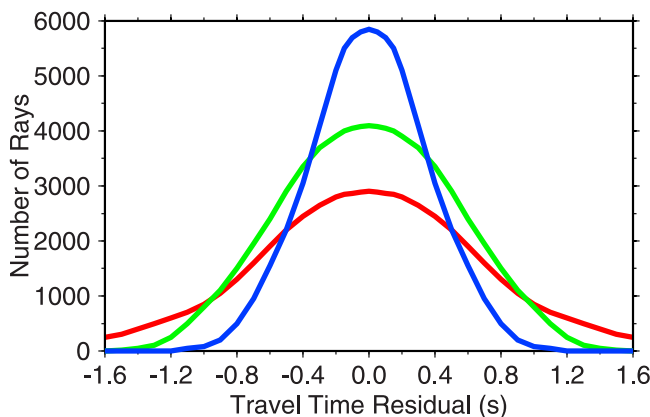


**Figure 6.** Distributions of traveltime residuals. The red line denotes the result for the averaged 1-D model. The green line denotes the result for the starting model (before the inversion). The blue line denotes the result after the inversion.

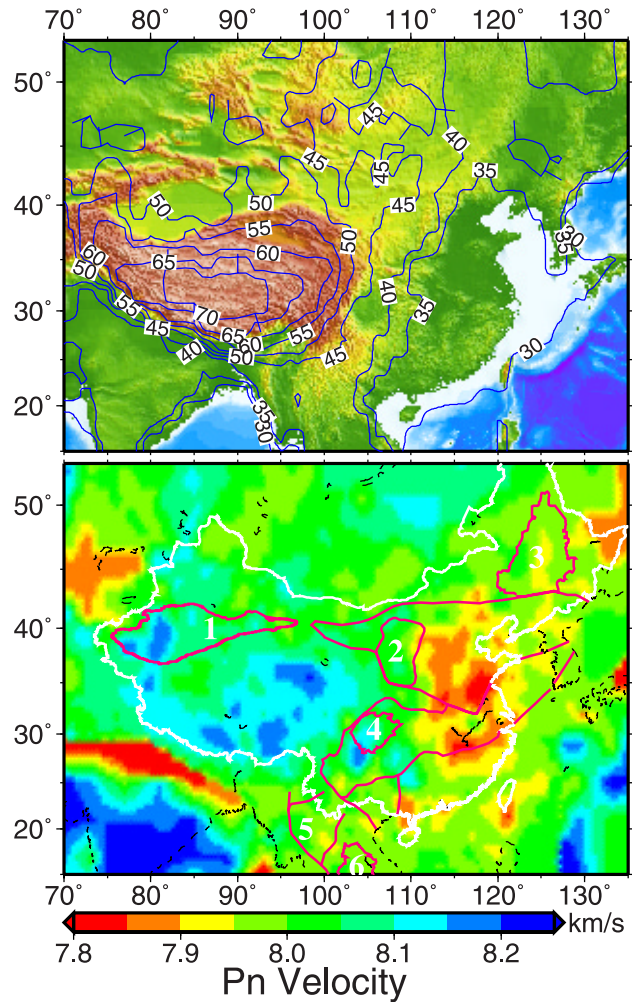


**Figure 7.** Depth distribution of (top) the Moho discontinuities and (bottom) the *Pn* velocities in the study area. The Moho depths are shown in contours. 1, Tarim Basin; 2, Ordos Basin; 3, Songliao Basin; 4, Sichuan Basin; 5, Shan Thai Block; 6, Khorat Basin.

about 70% between the final 3-D model and the averaged 1-D model.

[14] The distribution of hit counts (number of rays passing through each grid node) for each layer [Sun, 2005] shows that most parts of the study area are well sampled by the rays. The Tianshan area, the Sichuan-Yunnan area including eastern Tibet, and southeastern China including Taiwan are the regions with the most ray coverage at all depths. Ray coverage in the crust under north China is also very dense. Intuitively, given such extensive ray coverage, we expect a model with high spatial resolution. We will examine the model resolution in a systematic manner later.

[15] The Moho variations and *Pn* velocities are shown in Figure 7. Figure 8 shows 3-D *P* wave velocity variations at depths of 10, 20, 30, 40, 60, and 80 km. Vertical cross sections of the velocity images along the profiles denoted in Figure 9 are shown in Figures 10 and 11. The tomographic images are shown in areas with hit counts greater than 8.



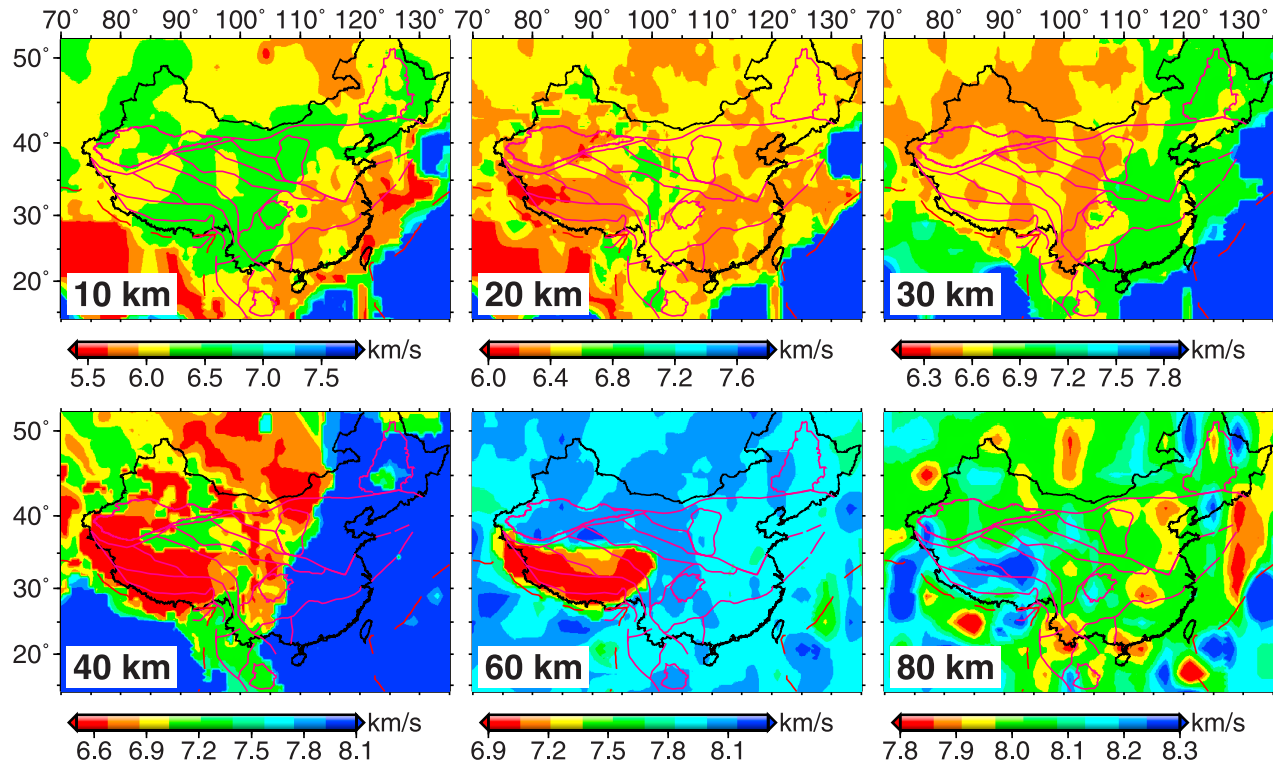


**Figure 8.** *P* wave velocity image at each depth slice. The depth of each layer is shown at the lower left corner of each map.

[16] Before analyzing the results of the tomographic inversion, we perform tests with synthetic data to evaluate the resolution of the tomographic image. We calculate a set of traveltimes by tracing the corresponding rays through a synthetic structure such as checkerboard, then we invert the synthetic data for the velocity structure, and finally we compare the inversion result with the initial synthetic model. To make a checkerboard velocity model, we assign  $\pm 3\%$  velocity perturbations to the 3-D grid nodes. Random errors from a normal distribution with a standard deviation of 0.1 s are added to the synthetic traveltimes calculated from the synthetic models. *Leveque et al.* [1993] showed that in some cases small structures in a checkerboard test can be retrieved effectively while large structures are poorly imaged. To test for such behavior in our tomographic study, we conduct checkerboard tests with different grid spacings of  $1^\circ$ ,  $2^\circ$ ,  $4^\circ$ , and  $8^\circ$ .

[17] Figure 12 shows the input checkerboard and the corresponding resolution test results with grid spacings of  $1^\circ$ . The  $1^\circ$  velocity model is best recovered in the Tianshan, the Sichuan-Yunnan and the southeastern China areas to depths smaller than 40 km. This correlates well with hit count distribution patterns [Sun, 2005]. For depths greater than 50 km, the resolution is high in most of mainland China. While the resolution is high for most Tibetan regions at large depths, part of western Tibet has relatively low resolution. From these resolution tests, we infer that for mainland China and the surrounding area, the tomographic images obtained have a spatial resolution of  $1^\circ$  in the horizontal direction and 10 km in depth, and large-scale structures are well resolved. For the peripheral areas of

Mongolia and India, structure can be resolved at large grid spacing, such as  $8^\circ$ .

## 4. Results and Validation

### 4.1. Results

[18] The 3-D *P* wave velocity model is shown at constant depths in Figure 8. At a depth of 40 km, low-velocity (low-V) zones are visible in the western part of China and high-velocity (high-V) zones exist in the eastern part. A

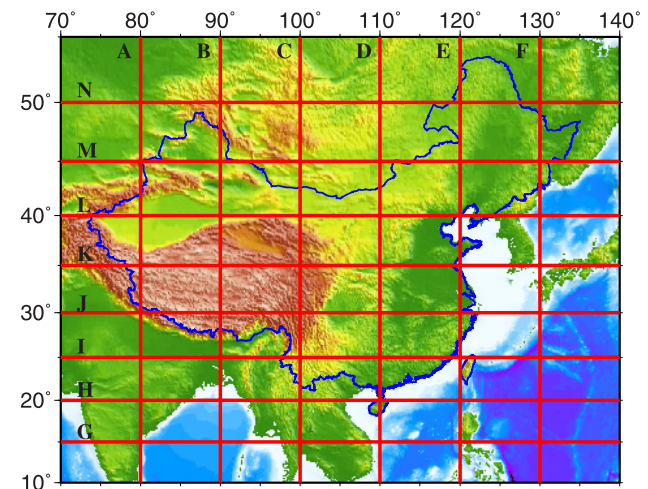


**Figure 9.** Locations of the vertical cross sections shown in Figures 10 and 11.

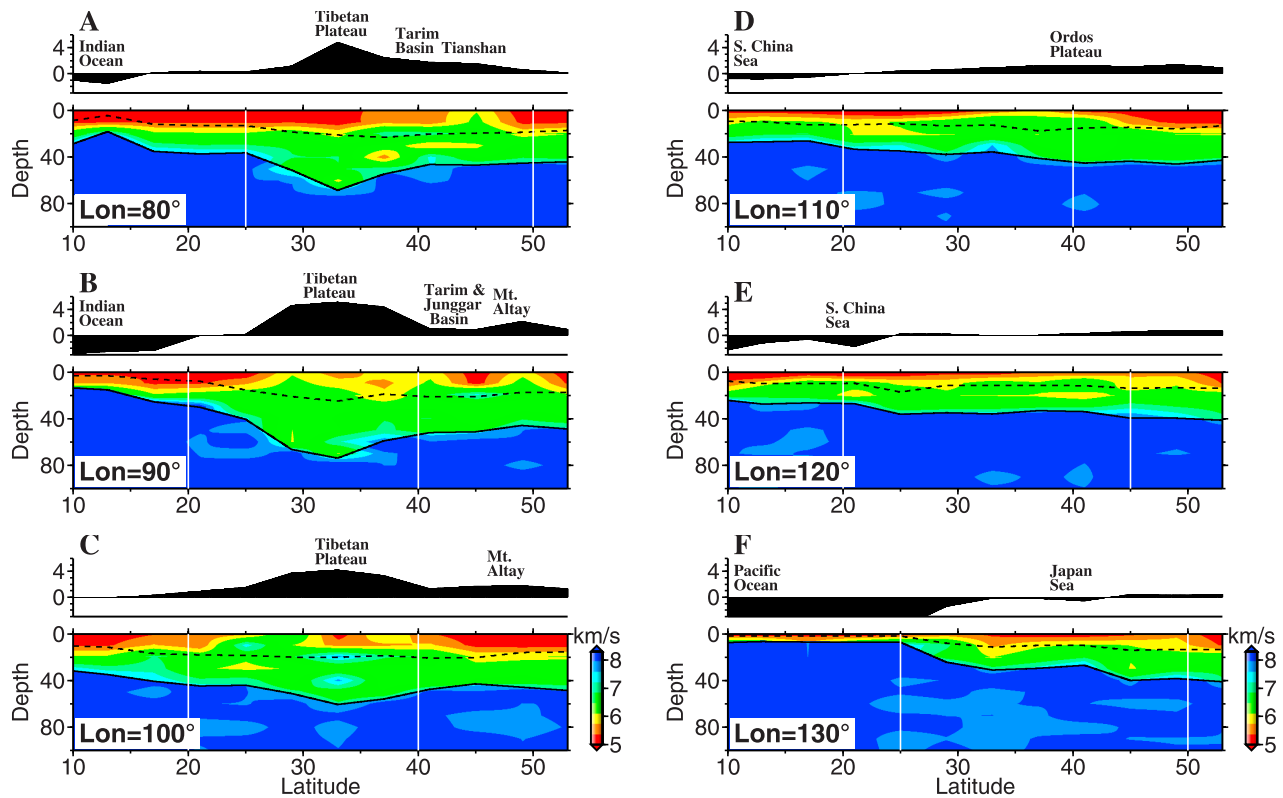


**Figure 10.** Vertical cross sections of *P* wave velocity when the Moho depth variations (Figure 7) are taken into account. Cross sections A, B, C, D, E, and F at the longitudes of 80°, 90°, 100°, 110°, 120°, and 130° are plotted. The surface topography along each profile is shown on the top of each cross section. The black curved lines show the Conrad (dashed) and Moho (solid) discontinuities. Each grid in the region between the two white lines has a ray path hit count of 200 or above.

clear dividing line appears around 105°E separating the east and west seismic zones in mainland China. At a depth of 60 km, the Tibetan Plateau is clearly outlined as a low-*V* zone. At a depth of 80 km, the root of the Tibetan Plateau disappears. High-*V* zones appear in the western and southern part of the Tibetan Plateau. There are a few low-*V* zones sandwiched between the high-*V* zones. The deeper velocity slices (60 and 80 km) with scattered low-*V* zones in eastern China indicate the presence of tectonic extension in the area. These results are consistent with those obtained by a joint inversion of the DSS data from multiple profiles [Li *et al.*, 2001]. Low-*V* zones beneath the Indochina Block including the Khorat Basin in the crust and uppermost mantle are related to intraplate volcanism [Lebedev and Nolet, 2003].

[19] The *P<sub>n</sub>* velocity image has a high resolution in the whole study area (Figure 7). *P<sub>n</sub>* velocities are low at the center of the Songliao Basin, but high under most of the Tarim Basin, the Sichuan Basin and the Ordos Basin. This result is generally consistent with the recent *P<sub>n</sub>* tomography by Pei *et al.* [2004], Liang *et al.* [2004], Hearn *et al.* [2004], and Phillips *et al.* [2005]. Detailed discussion of the *P<sub>n</sub>* structure is given in section 5.

[20] Velocity changes are visible across some features such as the Sanjiang Fold Belt. Velocity anomaly is visible from a depth of 10 km to a depth of 30 km, suggesting that some of the faults may have cut through the crust and reached to the middle or lower crust. No velocity contrast is

visible across most of the faults, particularly in the middle to lower crust, suggesting that most of the faults may be shallow features in the upper crust. It is also possible that our tomographic model has insufficient spatial resolution to image the fault zones.

#### 4.2. Relocation of GT Events

[21] We test our 3-D model by relocating the GT events (which were excluded from the inversion) and comparing the results with known locations. Eleven GT events are the nuclear explosions in northwestern China from 1990 to 1996, recorded by stations in China and the surrounding area. Only *P* wave arrival times are available in the data set. These events are determined independently using both satellite imagery [Fisk, 2002] and seismic data recorded by stations in China and the surrounding area.

[22] The explosions are closely clustered. Table 1 shows the parameters for these nuclear explosions. With our final *P* wave velocity model for the crust and upper mantle in China and the surrounding area, we relocate the GT events using arrival time data recorded at stations within 20° epicentral distance. The relocation errors are also listed in Table 1. The “error” values are the hypocentral difference in kilometers between the reference hypocenters and relocations using the new 3-D *P* wave model, 1-D average China model obtained from the 3-D model, and the AK135 global model.

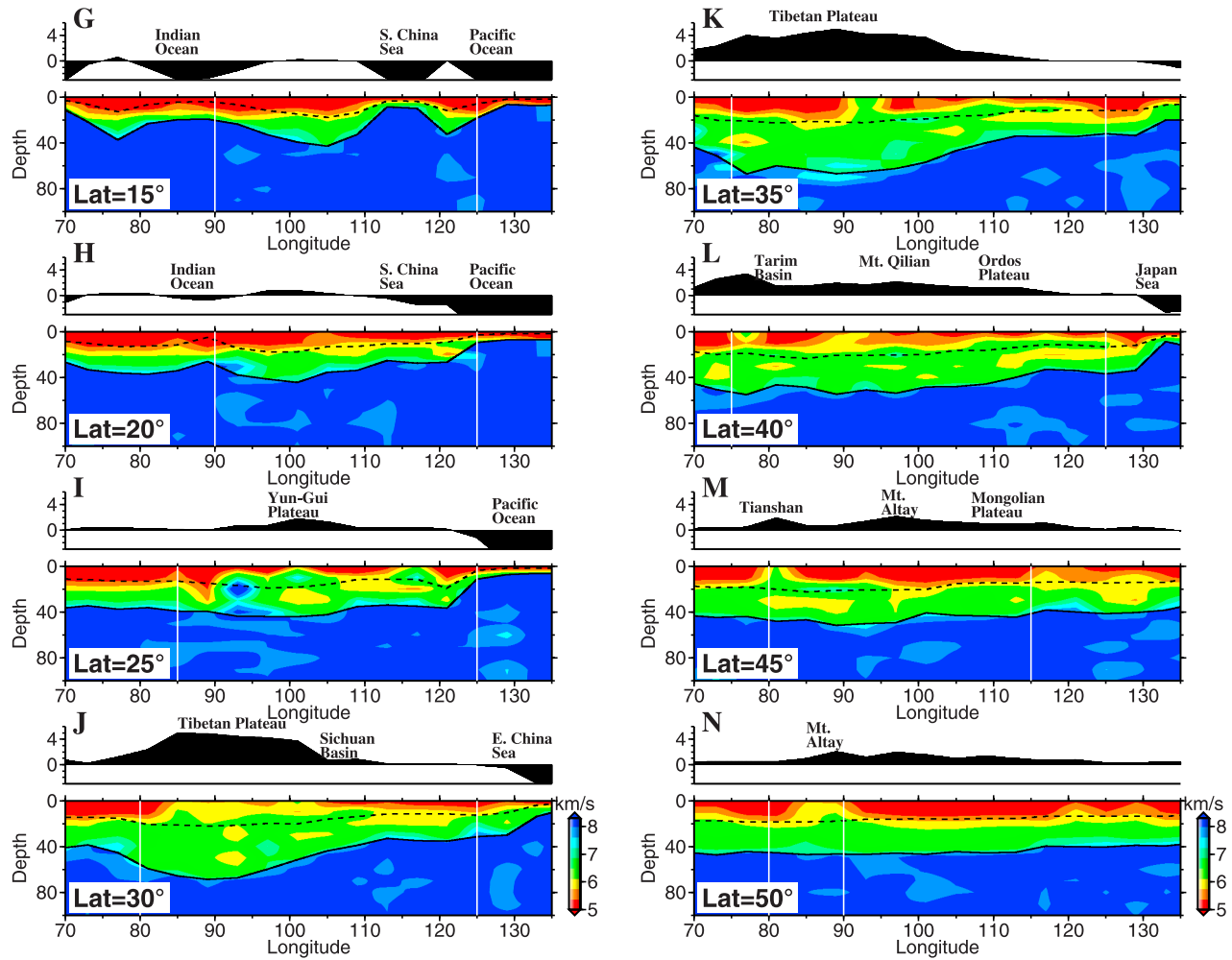


**Figure 11.** Same as Figure 10 except for cross sections G, H, I, J, K, L, M, and N at latitudes of 15°, 20°, 25°, 30°, 35°, 40°, 45°, and 50°.

[23] The averaged hypocentral error of relocation is only 0.7 km with a standard deviation of 0.2 km for our new 3-D *P* wave model. The mean hypocentral misfit is about 10 km if the averaged 1-D velocity in China is used, and the misfit is about 20 km if the global AK135 model is used. Even though the GT events are located in northwestern China with most stations distributed in southern and eastern China, the small relocation errors clearly suggest that an accurate *P* wave velocity model gives good event locations with limited azimuthal coverage.

#### 4.3. Traveltime Validation

[24] Another way of validating velocity model is to compare the observed traveltimes from the GT events and earthquakes with the predicted traveltimes calculated with the new model. The eleven explosions essentially occurred in two testing areas (41.55°, 88.73°) and (41.72°, 88.38°). The distance between these two areas is less than 40 km, which is relatively small compared to the average source-receiver distance of 12° from all the selected stations. Instead of comparing the traveltime residuals at each station from each individual event, we calculate the averaged traveltime residual at each station from all the GT events

(Table 2). We see that both the traveltime residuals and the standard deviations decrease when the models are used in order of AK135, averaged 1-D, the input 3-D, and the final 3-D.

[25] The mean traveltime residual (our final 3-D model) is smaller than 0.6 s when the stations are within 15° epicentral distance from the events. The traveltime residuals increase to about 0.9 s when the stations are about 20° from the events. The larger traveltime residuals observed at greater distances are due to the fact that our final 3-D model is inverted using the arrival times with the source-receiver distance smaller than 15°. The deeper structures (deeper than 200 km) of the model are less constrained by regional arrival time data in our tomographic study. The standard deviations are smaller than 0.2 s. These results clearly confirm that the *P* wave model we obtained from traveltime tomography in the crust and uppermost mantle is accurate.

[26] It is also important to compare the traveltimes from the earthquakes with well constrained hypocenters. Since all explosions (GT events) are located in the northwest part of China, with a 20° limit in epicentral distance from station to event, the model structure in the eastern part of China is not validated by relocating the GT events or comparing the



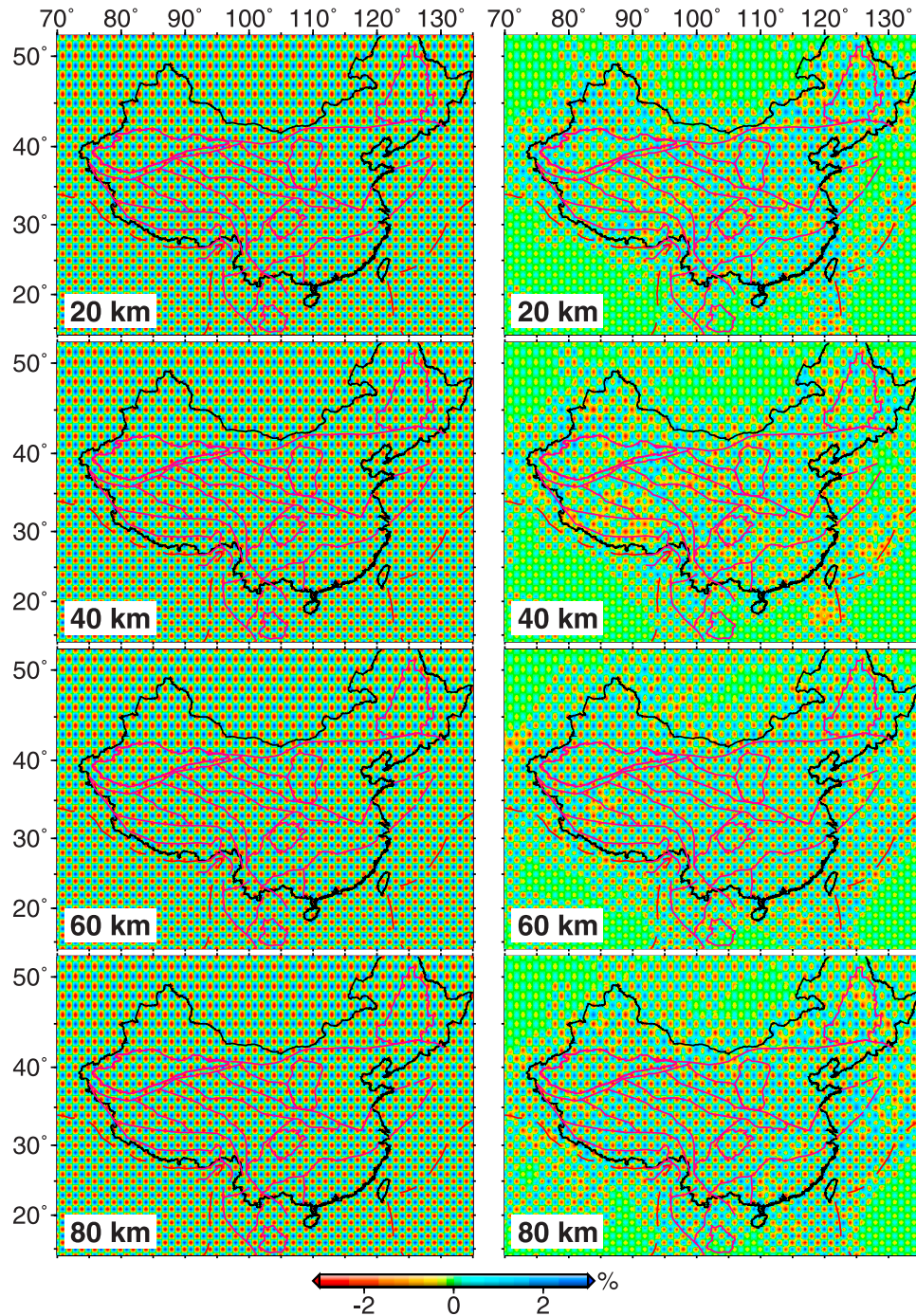


**Figure 12.** (left) Input checkerboard and (right) results when the grid shown in Figure 5 is adopted. The depth of the layer is shown at the lower left corner of each map. Blue and red squares denote high and low velocities, respectively. The velocity perturbation scale is shown at the bottom.

traveltimes from the GT events. To test the eastern China velocity model, we selected one well-located earthquake ( $M$  6.4) in the northern part of China that is recorded by more than 100 stations. The event occurred on 3 May 1996 with the epicenter at (40.72°N, 109.57°E), depth of 28 km and origin time 0332:46.3 UT, given in the ABCE. Our relocation of this event using arrival times from the 3-D velocity model is (40.72°N, 109.58°E) at a depth of 25 km and origin time 0332:45.9 UT. The ABCE data for the event and our relocation are shown in Table 3.

[27] The hypocentral difference between our location and the ABCE location is about 3.5 km, larger than the averaged hypocentral misfit of 0.9 km for the northwestern China GT events, but within the GT5 confidence bounds for this event. The origin time difference is 0.04 sec. The traveltime residuals, between the observed and predicted *P* wave traveltimes within 20° source-station separation, are much smaller using our final 3-D model than AK135. The mean traveltime residual is 1.89 s for AK135 and it is only 0.09 s for our final model. The standard deviation of traveltime

**Table 1.** Eleven GT Events in Northwest China<sup>a</sup>

Event	Date	Time, UT	Latitude, deg	Longitude, deg	Error, km		
					3-D	1-D	AK135
1	6 May 1990	0759:59.25	41.5618	88.7183	0.3	6.2	18.9
2	16 Aug 1990	0459:59.26	41.5392	88.7445	0.9	9.5	23.0
3	21 May 1992	0459:59.06	41.5419	88.7678	0.6	8.7	18.4
4	25 Sep 1992	0800:00.02	41.7167	88.3767	0.8	9.1	17.8
5	5 Oct 1993	0159:57.92	41.5922	88.7035	1.0	9.3	19.1
6	10 Jun 1994	0625:59.46	41.5271	88.7074	0.9	8.1	18.4
7	7 Oct 1994	0325:59.44	41.5741	88.7256	0.7	7.7	19.6
8	15 May 1995	0405:59.38	41.5545	88.7516	0.6	8.8	24.9
9	17 Aug 1995	0059:59.35	41.5402	88.7533	0.7	9.2	18.8
10	8 Jun 1996	0255:59.37	41.5780	88.6875	0.9	9.3	20.1
11	29 Jul 1996	0148:59.62	41.7162	88.3757	0.4	8.4	21.5

<sup>a</sup>The relocation errors (hypocentral) are listed in km. Events are relocated using our new *P* wave model, the averaged 1-D model in China, and the surrounding area and the standard AK135 (global).

residuals is 1.2 s for AK135 and it is 0.49 s for our final model.

## 5. Discussion and Conclusions

[28] Strong *P* wave velocity variations of more than 10% found in the study area indicate the existence of significant structural heterogeneities in the crust and uppermost mantle in this region. At shallow depth (the 10 km slice in Figure 8), velocity images in the North China Block, the South China Block, the Sichuan Basin, the Ordos Basin, the Tarim Basin, and the Tianshan regions exhibit different patterns. In the North China Block, a low-*V* anomaly is found beneath the Songliao Basin and a high-*V* anomaly is imaged beneath the Bohai Gulf region. Low-*V* zones underlie most of the Tianshan region and Tarim Basin though a high-*V* zone exists in the center of the Sichuan Basin. In the South China Block we find a high-*V* anomaly in the south and low-*V* zones in the north. Beneath the mountains surrounding the Ordos Basin in the north, west and east, a high-*V* anomaly is found at the depth of 10 km. The center of the Ordos basin shows a low-*V* anomaly. As a whole, the velocity images of shallow layers correlate well with the surface geology, topography, and lithology.

[29] Our initial *P<sub>n</sub>* velocities were constructed based on the *P<sub>n</sub>* structure of the 1-D Monte Carlo search [Sun *et al.*, 2004b]. Here we compare the *P<sub>n</sub>* velocities obtained by Hearn *et al.* [2004], the 1-D Monte Carlo search, and final 3-D structure (Figure 7). The prominent low *P<sub>n</sub>* zones in eastern China are consistent throughout all the *P<sub>n</sub>* models. Southern and eastern areas of Tibet show a high *P<sub>n</sub>* velocity. We also observe a high *P<sub>n</sub>* velocity beneath the Sichuan Basin, Ordos Basin and Tianshan area. The discrepancies are mostly in the Tibetan region. Hearn *et al.* [2004] observed a high *P<sub>n</sub>* velocity beneath the Qilian and the Kunlun area, though we only observe a high *P<sub>n</sub>* beneath the eastern Qilian in our final model. Some parts of the Kunlun area show high *P<sub>n</sub>* velocity. This discrepancy might be caused by the overaveraging effect of the 1-D inversion. The high *P<sub>n</sub>* in the eastern Tibet is carried over to the western part due to the sparse ray coverage in the western part and very large windows that are selected to provide averaged 1-D profiles in the Monte Carlo inversion.

[30] The Moho discontinuity plays an important role in tomography. The importance of taking into account the Moho depth variations and other discontinuities in the tomographic inversion has also been demonstrated in the earlier studies of the Japan and Tonga subduction zones [Zhao *et al.*, 1992, 1997], southern Carpathians, Romania [Fan *et al.*, 1998], and southwest China [Huang *et al.*, 2002]. When the discontinuity topography is taken into account, ray paths and traveltimes can be computed more accurately, and therefore a better tomographic result is expected. Sun [2005] shows that the final RMS traveltime residual is 0.58 s for the inversion when the Moho topography is considered, 6% lower than the 0.62 s RMS residual with the flat Moho (50 km), the average Moho depth in the study area (Figure 7).

[31] While the Moho depths are fixed as the initial model in our inversion, Sun [2005] conducts an inversion by allowing the Moho depths to change between  $-5$  and  $5$  km of the initial model, and both Moho depths and velocities are unknowns in the inversion. The Moho depth difference is within  $\pm 1$  km and the *P<sub>n</sub>* velocity difference is within  $\pm 0.1$  km/s compared to the reference 3-D model. Along a vertical cross section (profile E in Figure 10) the final velocity difference is within  $\pm 0.1$  km/s in the crust and uppermost mantle. The Moho depth difference along the profile E is within  $\pm 1$  km throughout the cross section.

[32] In summary, our velocity model shows the following features:

[33] 1. The seismic velocity images are characterized by block structures corresponding to geological features bounded by large fault zones. This region consists of a few geological structures: the North China Block including Songliao Basin, the South China Block, the Sichuan Basin,

**Table 2.** Comparison of the Traveltime Residuals Based on Different Models<sup>a</sup>

Traveltime Residuals	Final 3-D	Input 3-D	Averaged 1-D	AK135
Mean, s	[−0.6, 0.6]	[−0.8, 0.8]	[−1, 1]	[−3, 3]
SD, s	[0.05, 0.15]	[0.05, 0.2]	[0.05, 0.3]	[0.1, 0.9]

<sup>a</sup>For each model, the range of the mean and standard deviation (SD) of traveltime residuals at each station are listed. The range of the means and SDs are listed for 50 stations about  $20^\circ$  from the events.



**Table 3.** Comparison of the Hypocentral Parameters of a Well-Constrained Earthquake in Northeastern China<sup>a</sup>

	Origin Time, UT	Latitude, deg	Longitude, deg	Depth, km
ABCE	0332:46.3	40.72	109.57	28
MIT	0332:45.9	40.72	109.58	25

<sup>a</sup>ABCE parameters are obtained from a dense network of local and regional stations and are estimated to be GT-5. MIT parameters are obtained by relocating the event using the new 3-D *P* wave velocity model.

the Tarim Basin, and the Tianshan area. Those areas exhibit different patterns of velocity distribution in the tomographic images. The trend of velocity anomalies is consistent with the trend of regional tectonics.

[34] 2. A clear dividing line along the 105° parallel separates China into a low-*V* zone in the west and a high-*V* zone in the east at a depth of 40 km.

[35] 3. Our tomographic imaging has revealed significant velocity heterogeneities in the middle and lower crust, some of which are consistent with those detected by deep seismic soundings and other geophysical investigations.

[36] 4. *P<sub>n</sub>* velocities are high under southern and eastern Tibet, and under the Sichuan and Ordos basins.

[37] 5. Velocity heterogeneities below Moho at Indochina subduction zone reflect the tectonic history and ongoing subduction.

[38] **Acknowledgments.** This work was supported by the Defense Threat Reduction Agency under contract DTRA01-00-C-0024 and by Air Force Research Laboratory under contract FA8718-04-C-0018. Thanks to Dapeng Zhao and Jianshe Lei in Ehime University, Matsuyama, Japan, for the support on this research. We also thank John Chen and Shunping Pei from Peking University, Beijing, China, for their suggestions and comments. Anca Rosca, Mark Willis, Stephane Rondenay, Burke Minsley, and Maureen Long from MIT; Walter Mooney from USGS; and Charlotte Rowe and Michael Fehler from the Los Alamos National Laboratory provided great help on improving the manuscript. We are greatly indebted to Haijiang Zhang from University of Wisconsin–Madison, two anonymous reviewers, and the Associate Editor for their insightful comments. All the figures in this work are made by using GMT [Wessel and Smith, 1995].

## References

- China Seismological Bureau (1986), *Findings of Exploring the Crust and Upper Mantle Structure of China* (in Chinese), 407 pp., Seismol. Press, Beijing.
- Eberhart-Phillips, D. (1986), Three-dimensional velocity structure in northern California Coast Ranges from inversion of local earthquake arrival times, *Bull. Seismol. Soc. Am.*, **76**, 1025–1052.
- Fan, G., T. Wallace, and D. Zhao (1998), Tomographic imaging of deep velocity structure beneath the eastern and southern Carpathians, Romania: Implications for continental collision, *J. Geophys. Res.*, **103**, 2705–2723.
- Fisk, M. D. (2002), Accurate locations of nuclear explosions at the Lop Nor test site using alignment of seismograms and IKONOS satellite imagery, *Bull. Seismol. Soc. Am.*, **92**, 2911–2925.
- Hearn, T. M., S. Wang, J. F. Ni, Z. Xu, Y. Yu, and X. Zhang (2004), Uppermost mantle velocities beneath China and surrounding regions, *J. Geophys. Res.*, **109**, B11301, doi:10.1029/2003JB002874.
- Huang, J., and D. Zhao (2004), Crustal heterogeneity and seismotectonics of the Chinese capital region, *Tectonophysics*, **385**, 159–180.
- Huang, J., D. Zhao, and S. Zheng (2002), Lithospheric structure and its relationship to seismic and volcanic activity in southwest China, *J. Geophys. Res.*, **107**(B10), 2255, doi:10.1029/2000JB000137.
- Huang, Z., W. Su, Y. Peng, Y. Zheng, and H. Li (2003), Rayleigh wave tomography of China and adjacent regions, *J. Geophys. Res.*, **108**(B2), 2073, doi:10.1029/2001JB001696.
- Institute of Geophysics, China Seismological Bureau (IG-CSB) (1990–2003), Annual bulletin of Chinese earthquakes (ABCE), Seismol. Publ. House, Beijing.
- Kissling, E., W. L. Ellsworth, D. Eberhart-Phillips, and U. Kradolfer (1994), Initial reference models in local earthquake tomography, *J. Geophys. Res.*, **99**, 19,635–19,646.
- Laske, G., and G. Masters (1997), A global digital map of sediments thickness (abstract), *Eos Trans. AGU*, **78**(46), Fall Meet. Suppl., F483.
- Lebedev, S., and G. Nolet (2003), Upper mantle beneath Southeast Asia from *S* velocity tomography, *J. Geophys. Res.*, **108**(B1), 2048, doi:10.1029/2000JB000073.
- Leveque, J., L. Rivera, and G. Wittlinger (1993), On the use of the checkerboard test to assess the resolution of tomographic inversions, *Geophys. J. Int.*, **115**, 313–318.
- Li, C., R. D. van der Hilst, and M. N. Toksöz (2006), Constraining *P*-wave velocity variations in the upper mantle beneath Southeast Asia, *Phys. Earth Planet. Inter.*, **154**, 180–195.
- Li, S., X. Zhang, and Z. Song (2001), Three-dimensional crustal structure of the capital area obtained by a joint inversion of deep seismic sounding data from multiple profiles (in Chinese), *Acta Geophys. Sin.*, **44**, 360–368.
- Liang, C., X. Song, and J. Huang (2004), Tomographic inversion of *P<sub>n</sub>* traveltimes in China, *J. Geophys. Res.*, **109**, B11304, doi:10.1029/2003JB002789.
- Liu, F. T., H. Wu, J. H. Liu, G. Hu, Q. Li, and K. X. Qu (1990), 3-D velocity images beneath the Chinese continent and adjacent regions, *Geophys. J. Int.*, **101**, 379–394.
- Mooney, W. D. (1998), CRUST 5.1: A global crustal model at 5° × 5°, *J. Geophys. Res.*, **103**, 727–747.
- Paige, C., and M. Saunders (1982), LSQR: An algorithm for sparse linear equations and sparse least squares, *Trans. Math. Software*, **8**, 43–71.
- Pei, S., Z. Xu, and S. Wang (2004), Discussion on origin of *P<sub>n</sub>* velocity variation in China and adjacent region (in Chinese), *Acta Seismol. Sin.*, **26**, 1–10.
- Pei, S., Y. Chen, D. Zhao, A. Yin, J. Ning, and X. Chen (2006), Tomographic structure of east Asia and its geodynamic implication, *J. Geophys. Res.*, doi:10.1029/2004JB003332, in press.
- Phillips, W. S., C. A. Rowe, and L. K. Steck (2005), The use of interstation *P* wave arrival time differences to account for regional path variability, *Geophys. Res. Lett.*, **32**, L11301, doi:10.1029/2005GL022558.
- Ritzwoller, M. H., M. P. Barmin, A. Villasenor, A. L. Levshin, and E. R. Engdahl (2002), *P<sub>n</sub>* and *S<sub>n</sub>* tomography across Eurasia to improve regional seismic event locations, *Tectonophysics*, **358**, 39–55.
- Shapiro, N. M., and M. H. Ritzwoller (2002), Monte Carlo inversion for a global shear velocity model of the crust and upper mantle, *Geophys. J. Int.*, **151**, 88–105.
- Song, Z. H., C. Q. An, G. Y. Chen, L. H. Chen, Z. Zhuang, Z. W. Fu, and J. F. Hu (1991), Study on 3-D velocity structure and anisotropy beneath west China from the Love wave dispersion (in Chinese), *Acta Geophys. Sin.*, **34**, 694–707.
- Stevens, J. L., D. A. Adams, and G. E. Baker (2001), Improved surface wave detection and measurement using phase-matched filtering with a global one-degree dispersion model, paper presented at 23rd Seismic Research Review: Worldwide Monitoring of Nuclear Explosions, Natl. Nucl. Secur. Admin., Jackson Hole, Wyo. (Available at <https://www.nemre.nnsa.doe.gov/cgi-bin/prod/researchreview/index.cgi?Year=2001>)
- Sun, R., and F. Liu (1995), Crust structure and strong earthquakes in Beijing, Tianjin and Tanshan area. I. *P* wave velocity structure (in Chinese), *Acta Geophys. Sin.*, **38**, 599–607.
- Sun, Y. (2005), *P*- and *S*-wave tomography of the crust and uppermost mantle in China and surrounding areas, Ph.D. thesis, Mass. Inst. of Technol., Cambridge.
- Sun, Y., S. Kuleli, F. D. Morgan, W. Rodi, and M. N. Toksöz (2004a), Location robustness of earthquakes in Sichuan province, China, *Seismol. Res. Lett.*, **75**(1), 54–62.
- Sun, Y., X. Li, S. Kuleli, F. D. Morgan, and M. N. Toksöz (2004b), Adaptive moving window method for 3-D *P*-velocity tomography and its application in China, *Bull. Seismol. Soc. Am.*, **94**, 740–746.
- Um, J., and C. Thurber (1987), A fast algorithm for two-point seismic ray tracing, *Bull. Seismol. Soc. Am.*, **77**, 972–986.
- Wang, C.-Y., W. W. Chan, and W. D. Mooney (2003), Three-dimensional velocity structure of crust and upper mantle in southwestern China and its tectonic implications, *J. Geophys. Res.*, **108**(B9), 2442, doi:10.1029/2002JB001973.
- Wessel, P., and W. Smith (1995), New version of the generic mapping tools released, *Eos Tran. AGU*, **76**, 329.
- Wu, F. T., A. L. Levshin, and V. M. Kozhevnikov (1997), Rayleigh wave group velocity tomography of Siberia, China, and vicinity, *Pure Appl. Geophys.*, **149**, 447–473.
- Xu, Y., F. Liu, J. Liu, and H. Chen (2002), Crust and upper mantle structure beneath western China from *P* wave travel time tomography, *J. Geophys. Res.*, **107**(B10), 2220, doi:10.1029/2001JB000402.
- Yu, X., Y. Chen, and P. Wang (2003), Three-dimensional *P* wave velocity structure in Beijing–Tianjin–Tangshan area, *Acta Seismol. Sin.*, **25**, 1–14.

- Zhao, D. (2001), New advances of seismic tomography and its applications to subduction zones and earthquake fault zones: A review, *Island Arc*, 10, 68–84.
- Zhao, D., A. Hasegawa, and S. Horiuchi (1992), Tomographic imaging of P and S wave velocity structure beneath northeastern Japan, *J. Geophys. Res.*, 97, 19,909–19,928.
- Zhao, D., A. Hasegawa, and H. Kanamori (1994), Deep structure of Japan subduction zone as derived from local, regional, and teleseismic events, *J. Geophys. Res.*, 99, 22,313–22,330.
- Zhao, D., Y. Xu, D. Wiens, L. Dorman, J. Hilderbrand, and S. Webb (1997), Depth extent of the Lau back-arc spreading center and its relation to subduction processes, *Science*, 278, 254–257.
- Zhu, J., J. Cao, X. Cai, Z. Yan, and X. Cao (2002), High resolution surface wave tomography in east Asia and west Pacific marginal sea, *Chin. J. Geophys.*, 45, 679–698.
- Zhu, L., R. Zeng, and F. Liu (1990), 3-D P wave velocity structure under the Beijing network area (in Chinese), *Acta Geophys. Sin.*, 33, 267–277.
- 
- Y. Sun and M. N. Toksöz, Earth Resources Laboratory, Department of Earth, Atmospheric, and Planetary Sciences, Massachusetts Institute of Technology, E34-566, 42 Carleton Street, Cambridge, MA 02142-1324, USA. (youshun@mit.edu)

# The Layered Shear-Wave Velocity Structure of the Crust and Uppermost Mantle in China

by Youshun Sun, M. Nafi Toksöz, Shunping Pei, and F. Dale Morgan

**Abstract** We present a layered shear-wave velocity structure of the crust and uppermost mantle of China and the surrounding area. We apply an adaptive moving window (Sun, Li, *et al.*, 2004) to construct the *S*-wave velocity model from high-quality body-wave phase data extracted from the *Annual Bulletin of Chinese Earthquakes* (ABCE). More than 350,000 *S*-wave arrivals are used, spanning from 1990 to 2004. The study area is represented by a  $1^\circ$  geographic grid consisting of 2338 points. At each point, 1D *S*-velocity-depth profiles are determined independently from the surface to the uppermost mantle; this is accomplished by performing a Monte Carlo random search of optimum layer parameters (thickness and velocity) via minimizing travel-time misfits for fixed earthquake locations. Each profile contains a four-layer crust and a one-layer uppermost mantle. A final 3D model is obtained by combining and smoothing the 1D models. The obtained *S*-wave model has a good correlation with the previously published *P*-wave model using the same method (Sun, Li, *et al.*, 2004) and reveals key tectonic features such as the low velocity crust beneath Tibet. Our *S*-wave model is generally consistent with the existing regional/local models constructed from body-wave travel-time tomography, and provides more detailed structure in both horizontal and vertical directions compared with the model derived from surface wave inversion. Based on our *P*- and *S*-wave models, the generated synthetic seismograms fit well with the observed seismograms recorded at broadband stations.

*Online Material:* *P*- and *S*-wave velocity models.

## Introduction

The importance of shear-wave velocity is being widely acknowledged in many fields. Compared with compressional-wave velocity, shear-wave velocity is more sensitive to changes in temperature, pressure, composition, water, and volatile content (Goes *et al.*, 2000; Pei *et al.*, 2007). It is therefore of significance to obtain shear-wave velocity structure in tectonically complex areas such as China (Fig. 1). There have been many studies in which *S*-wave velocity models of the crust and upper mantle in China and the surrounding area have been obtained using different approaches. For example, there are several global models covering China and the surrounding areas constructed from surface-wave tomography (e.g., Stevens *et al.*, 2001; Shapiro and Ritzwoller, 2002). The global model CRUST 2.0 (Bassin *et al.*, 2000) was constructed from seismic refraction data. Only *P*-wave velocities were inverted by travel-time tomography, and the *S*-wave velocities in the model are obtained by empirical  $V_P/V_S$  ratios or compiled from other sources. Mantle *S*-velocity models with lateral spatial resolution of  $>200$  km beneath East Asia were obtained from shear and surface wave inversions (Friederich, 2003).

Regional models were constructed by *Sn* tomography (Ritzwoller *et al.*, 2002; Pei *et al.*, 2007), from surface waves (Song *et al.*, 1991; Wu *et al.*, 1997; Xu *et al.*, 2000; Huang *et al.*, 2003; Lebedev and Nolet, 2003), and from receiver functions (Wu *et al.*, 2001; Zou and Chen, 2003; Hu *et al.*, 2005; Xu *et al.*, 2006), respectively. For the whole China area, a detailed shear-wave velocity structure derived from the body-wave travel-time inversion has yet to be done.

In this work, we use shear-wave first arrivals (*Sg* and *Sn*) reported by two sources: (1) in the Annual Bulletin of Chinese Earthquakes (ABCE) compiled by the Institute of Geophysics, China Earthquake Administration (IGCEA), and (2) from regional and provincial networks to generate a 3D *S*-wave velocity model for the crust and uppermost mantle in China by applying the adaptive moving window (AMW) method (Sun, Li, *et al.*, 2004).

## Data and Methods

We used first *S* arrivals extracted from the ABCE for the period of January 1990 to December 2004. This dataset con-



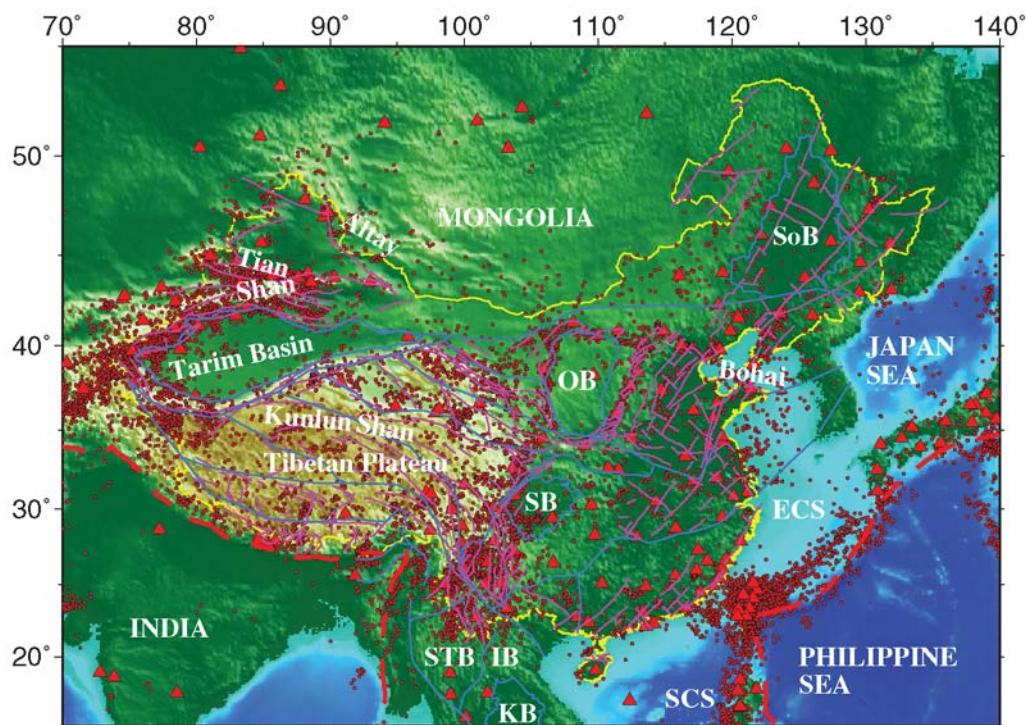


**Figure 1.** The 25,000 earthquakes ( $M > 3.5$  between 1990 and 2004), 220 stations, active faults, and major tectonic boundaries in China and the surrounding area. Earthquake epicenters are shown in red dots, and stations are shown in red triangles. The yellow line shows the boundary of China. Active faults in the China area are shown in purple lines and tectonic sutures are shown in blue lines. Songliao Basin, SoB; Ordos Basin, OB; Sichuan Basin, SB; East China Sea, ECS; South China Sea, SCS; Shan Thai Block, STB; Indochina Block, IB; Khorat Basin, KB.

tains 25,000 earthquakes, 220 stations, and 350,000  $S$ -wave readings in China and the surrounding area. Figure 2a shows the earthquake epicenters, stations, and ray paths in the study area. Figure 2b shows the locations at which the 1D velocity profiles are found using the first arrivals shown in Figure 3.

Earthquake relocations show very minor improvements in epicenter (Sun, Kuleli, *et al.*, 2004; Sun and Toksoz,

2006). Therefore, in this study we use the source locations given by the ABCE and apply the AMW method of Sun, Li, *et al.* (2004) to obtain a 3D  $S$ -wave velocity model in the crust and uppermost mantle beneath China.

We select 2338 points distributed on a  $1^\circ$  grid in the study area (Fig. 2b). We then select a region (window) centered at each point to include the required number of  $S_g$  and

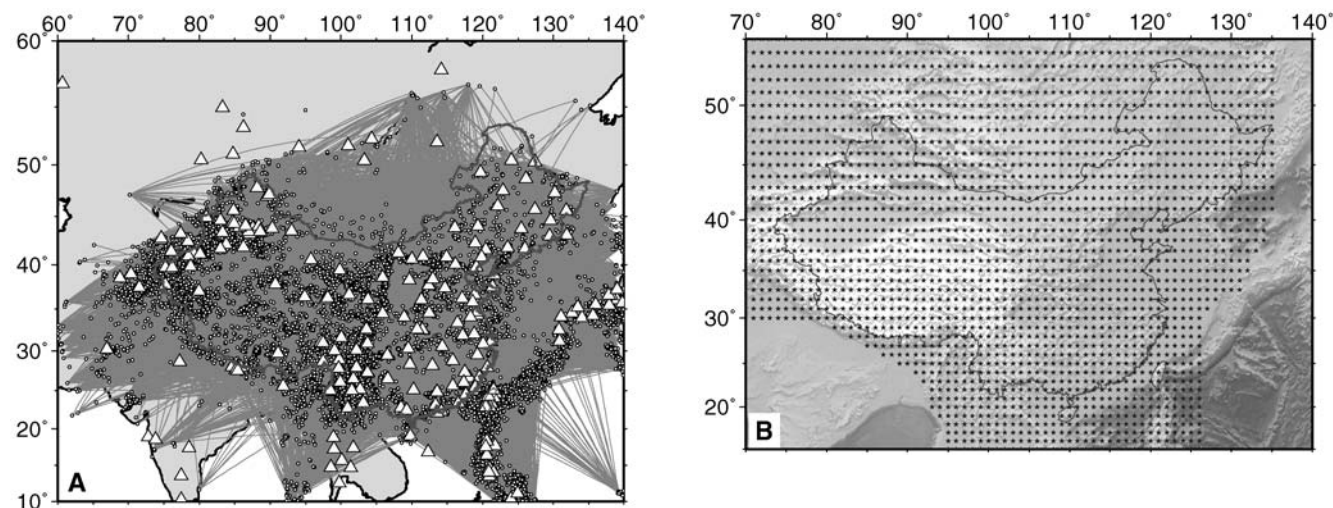


**Figure 2.** (a) Locations of 25,000 earthquakes, dots; 220 stations, triangles; and 350,000 shear-wave ray paths in China and surrounding area. (b) 2338 points (stars) in China and the surrounding area.

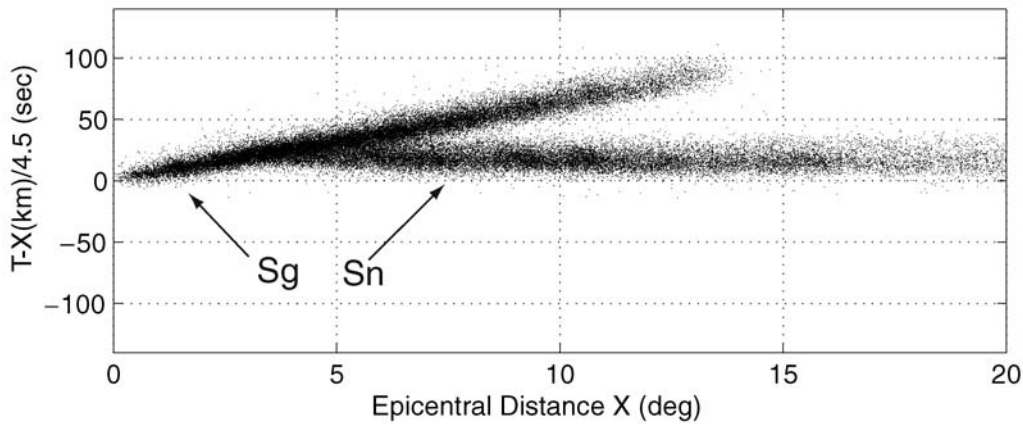


**Figure 3.** The  $S_g$  and  $S_n$  travel-times (reduced) in China within distances of  $20^\circ$ .

$S_n$  ray paths. All the selected ray paths must be entirely contained within the region. In the regions with dense ray coverage, the size of each region starts from  $4^\circ \times 4^\circ$  (latitude and longitude) to guarantee at least 100  $S_g$  and 50  $S_n$  ray paths within the region. In the areas such as Mongolia with sparse ray coverage, the region sizes are increased up to  $15^\circ \times 15^\circ$  so at least 30  $S_g$  and 10  $S_n$  arrivals are included in each region. The maximum source-receiver epicentral distance in each region is  $8^\circ$ . Finally, within each region we apply Monte Carlo searches to invert a 1D layered velocity profile with four layers in the crust and one layer of uppermost mantle by fitting first arrivals ( $S_g$  or  $S_n$ ).

The steps of a Monte Carlo search are as follows:

1. Set parameter ranges.
2. Choose random numbers within parameter ranges for all parameters.
3. Calculate theoretical arrival time.
4. Obtain travel-time residuals ( $\Delta T$ ).
5. Stop if the residual misfit is small or after a maximum number of trials ( $n_{\max}$ ). The residual misfit is measured by the root mean square (rms) error defined as  $\text{rms} = \{\frac{\sum \Delta T^2}{N}\}^{1/2}$ , where  $N$  is the number of observations.
6. Keep parameter sets associated with the smallest residuals.
7. Repeat from step 2 if residuals are large or if  $n_{\max}$  is not reached.

The random search will continue to  $n_{\max}$  or will stop if the rms is smaller than the predefined tolerance  $\varepsilon$ .

There are nine unknowns for each 1D profile (Fig. 4): four crustal layer thicknesses, four shear-wave crustal velocities, and the  $S_n$  velocity in the uppermost mantle. We adopt the top layer (sediment) thickness defined by CRUST 2.0 (Bassin *et al.*, 2000), and the thicknesses of the second (upper) and third (middle) crustal layers from Sun, Li, *et al.* (2004) (this model can be accessed in the electronic edition of *BSSA*). The remaining six unknown parameters are found by random search (Monte Carlo). Based on the previous study by Pei *et al.* (2007), we allow the general Monte

Carlo search for  $S_n$  to range between 4.3 and 4.8 km/sec. The Monte Carlo search range for the fourth layer thickness in the crust is limited to  $\pm 2$  km of the lower crustal thickness found in Sun, Li, *et al.* (2004). The bounds for the four crustal velocities are [2, 3], [3, 3.6], [3.6, 3.9], and [3.9, 4.3] km/sec. Final 1D profiles are chosen with the minimum rms residual of travel time from 100,000 Monte Carlo iterations. Our 3D model is obtained by first resampling all the 2338 1D models to increase sample density by a factor of 5 using linear interpolation, and then by horizontally smoothing the resampled models using a Gaussian function with a half-length of 8 points.

## Results and Validation

### Results

The 3D shear-wave velocity models are shown in Figures 5–7 and can be accessed (E) in the electronic edition of *BSSA*. Depth slices are shown in Figure 5 (right side). The lateral variation of  $S$ -wave velocities exceeds 6% in the study area, indicating strong heterogeneity in the crust

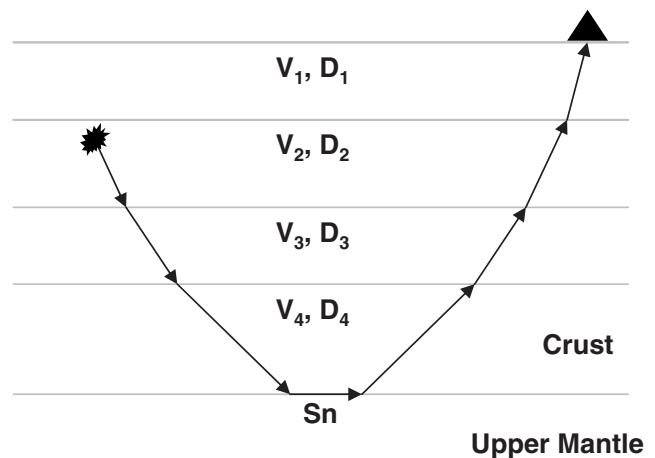


**Figure 4.** Four layers of crust and one layer of uppermost mantle at each location.



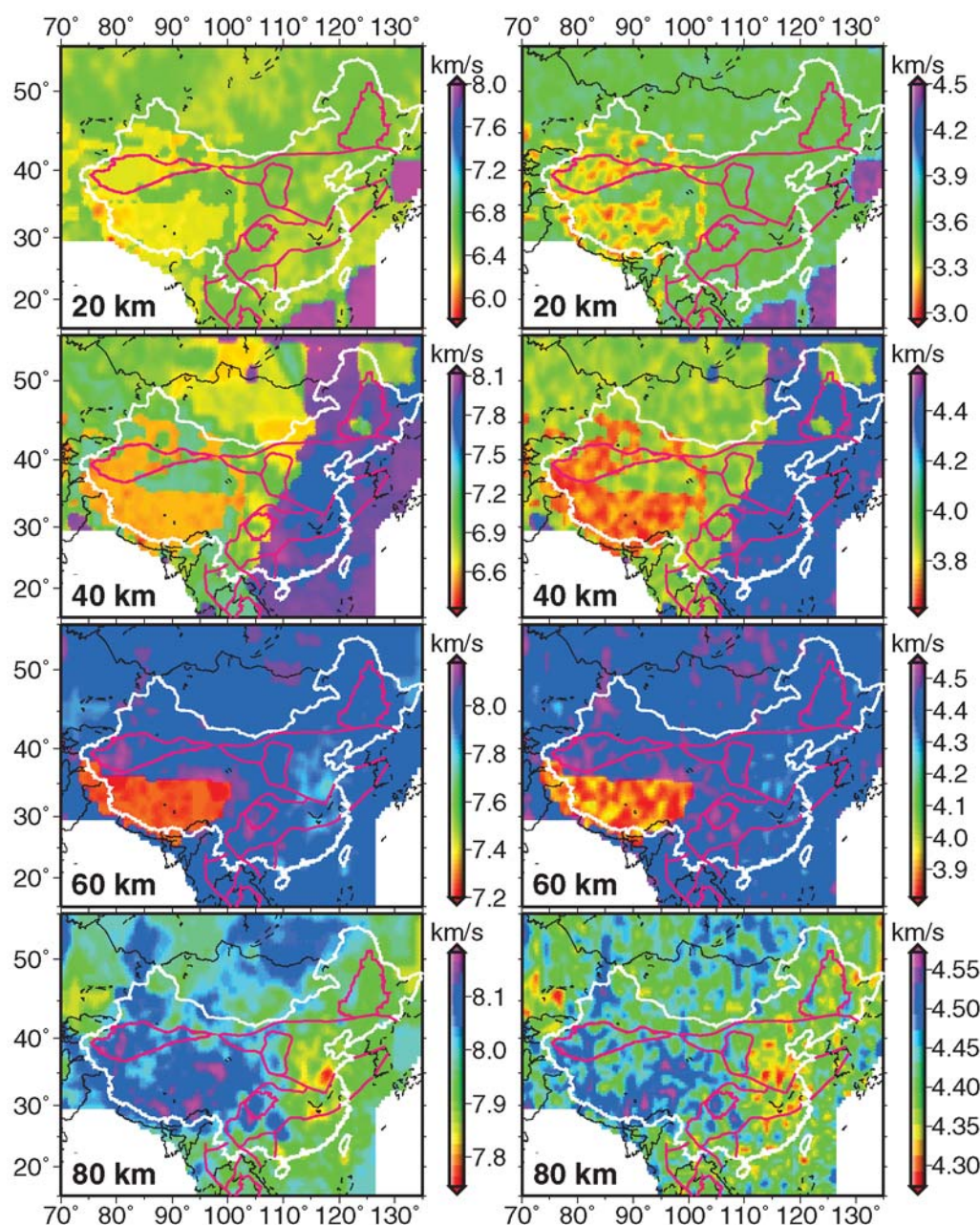


**Figure 5.** Comparison of  $P$ -wave (left) and  $S$ -wave (right) velocity profiles at different depths in the study region. Images are shown in different color scales at each depth.

and upper mantle in this region. There are three prominent features in the model: the thick crust under Tibet with low velocity, the low  $S_n$  velocities in northeast China (rift zone), and the high  $S_n$  velocities under Tibet at 80-km depth (Fig. 5).

In Figure 5, there is a prominent low-velocity zone in the midcrust beneath Tibet at a depth of around 40 km. This feature is consistent with other observations of similar velocity decrease and shear-wave attenuation increase in the mid to lower crust in the same region (Song *et al.*, 1991). Higher velocities under the Sichuan Basin and under Mount Altay

extend into the mantle, as do the lower velocities under the rift system south of the Bohai Bay.

The left side of Figure 5 shows the 3D  $P$ -wave velocity models obtained by an earlier study using our AMW method (Sun, Li, *et al.*, 2004). It is informative to compare this model with the  $S$ -model. We observe a good correlation between the  $P$  and  $S$  velocities under Tibet. Lower velocities in the midcrust appear both in the  $P$  and  $S$  tomograms, though they are more prominent in the  $S$ -model.

$S_n$  velocities and Moho depths are shown in Figure 6. Our  $S_n$  model is similar to the model developed by Pei *et al.*

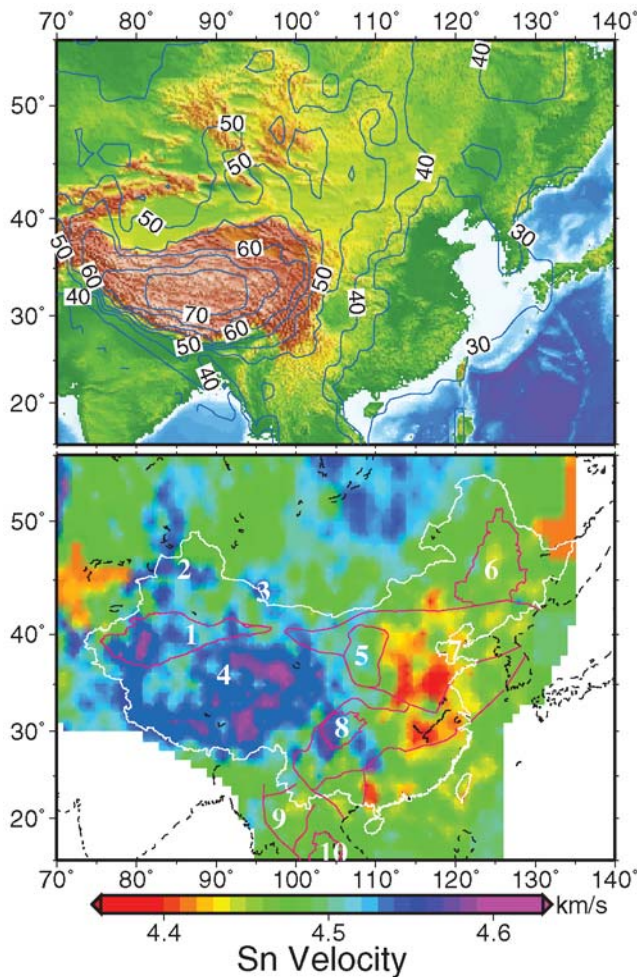


**Figure 6.** Top: Contour plot of Moho depth in China. Bottom:  $S_n$  velocity in China area, where Tarim Basin, 1; Tianshan, 2; Altay, 3; Kunlun, 4; Ordos Basin, 5; Songliao Basin, 6; Bohai Gulf, 7; Sichuan Basin, 8; Shan Thai Block, 9; Khorat Basin, 10.

(2007). Both models exhibit prominent low velocity zones in eastern China. In addition, southern and eastern Tibet clearly show a high  $S_n$ -velocity anomaly. We observe a high  $S_n$  anomaly beneath the Sichuan Basin, Ordos Basin, and the Tianshan area, as well. On the other hand, there are a few minor discrepancies between the two  $S_n$  models. A region of the Kunlun area shows high  $S_n$  velocities in our results, but not in Pei's model. This discrepancy may be caused by the overaveraging effect of our 1D models in the horizontal direction. As a result, the high velocity in eastern Tibet may be carried over due to sparse ray coverage in the western part, which required very large windows to provide averaged 1D profiles in the Monte Carlo inversion.

Our  $S_n$  velocities show very similar patterns to the  $P_n$  velocities previously obtained by Sun, Li, *et al.* (2004). All major spatial features are well correlated. The percentage variation of  $S_n$  velocities is greater than that of  $P_n$ . The amplitude variation of low  $S_n$  velocity is greater than that of  $P_n$  velocity in northeastern China. This may indicate that the

sub-Moho temperature is high in northeastern China because  $S$  velocity is more sensitive to temperature than  $P$  velocity (Goes *et al.*, 2000; Pei *et al.*, 2007).

The Moho depths we obtained show an excellent correlation with the surface topography with high elevation corresponding to a deeper Moho, and Moho depth decreases from west to east in China (Figs. 6 and 7). The large-scale features shown in our Moho depth results are similar to those in the University of Colorado at Boulder (CUB) 1.0 (Shapiro and Ritzwoller, 2002), the Science Applications International Corporation (SAIC)  $1^\circ \times 1^\circ$  (Stevens *et al.*, 2001), and the CRUST 2.0 models (Bassin *et al.*, 2000). Most of the depth discrepancies are only a few kilometers in difference. All four models show deepest Moho (70 + km) at the center of the Tibet plateau, and the shallowest (about 30 km) in the coastal areas around China's continental shelf. The outline of the Tibet plateau is clearly depicted by all models.

In the Tianshan area, the maximum Moho depth in our model is 61 km, which is very close to the 62 km found by Lu *et al.* (2000) from a deep seismic sounding study, and nearly 10-km deeper than the other three models. This discrepancy arises from two factors: (1) the CUB 1.0 and the SAIC  $1^\circ \times 1^\circ$  models were constructed from group- and phase-velocity dispersion measurements of surface waves, and (2) the CRUST 2.0 model was constructed from limited seismic refraction data and was developed from the CRUST 5.1 model (Mooney, 1998) and  $1^\circ \times 1^\circ$  sediment map (Laske and Masters, 1997).

#### Validation

We test our 3D shear-wave model by relocating a ground truth (GT) event in northern China and fitting seismograms along a profile in southern China. The GT event we use is the 1996 Baotou earthquake ( $M$  6.4), recorded by about 100 stations and well located by IGCEA (Sun and Toksoz, 2006). The event occurred on 3 May 1996 with source parameters of ( $40.72^\circ$  N,  $109.57^\circ$  E, 28 km, 0332:46.3 coordinated universal time [UTC]), as detailed in the ABCE. This event is relocated to latitude  $40.71^\circ$  N, longitude  $109.60^\circ$  E, and depth 26 km with an origin time of 0332:46.1 UTC in our 3D model. The hypocentral difference between our location and the ABCE location is about 4 km, well within the GT5 confidence bounds.

In the southern China, we validated our  $S$ -wave velocity model by comparing recorded seismograms with the synthetic ones calculated from our  $P$ - (Sun and Toksoz, 2006) and  $S$ -wave velocity models. We have collected seismograms recorded by the China Digital Broadband Network (CDBN) (Fig. 8) from two events: the Yunnan earthquake (21 July 2003,  $M$  6.0,  $25.99^\circ$  N,  $101.27^\circ$  E, 10 km, 1516:31.3 UTC) and an earthquake near Ishigakijima Island (18 December 2001,  $M$  6.3,  $23.92^\circ$  N,  $122.94^\circ$  E, 33 km, 0402:58.4 UTC). Each event was recorded by up to 47 broadband stations in the CDBN. We selected three profiles in southern China for seismogram fitting (Fig. 8). We then used the discrete wave-



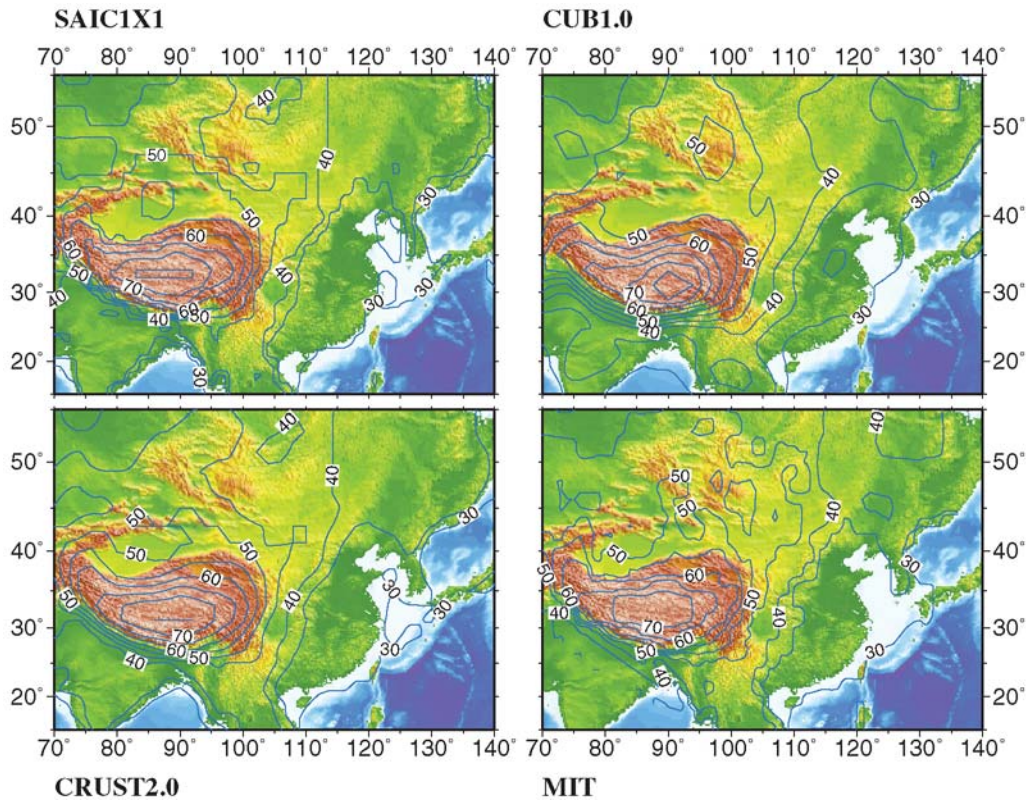


**Figure 7.** Contour comparison of Moho depth. The large-scale features shown in our Moho depth results are similar to those in the CUB 1.0 (Shapiro and Ritzwoller, 2002), the SAIC  $1^\circ \times 1^\circ$  (Stevens *et al.*, 2001), and the CRUST 2.0 models (Bassin *et al.*, 2000). Most of the depth differences are only a few kilometers.

number method (DWM) (Bouchon, 2003) to generate seismograms. The mechanism parameters are provided by Global CMT.

Figure 9 shows the transverse component for both synthetic and observed seismograms for the three selected profiles. The agreement between observed and calculated seismograms from 0 to 1 Hz is good for all profiles (A, B, and C), both for body waves and surface (Love) waves. The amplitude and polarity of Love waves are correctly matched. The first arrivals of *P* and *S* waves match very well with the observed arrival times, and the directions of the particle motion are consistent. This agreement suggests that our *P*- and *S*-wave models are accurate in southern China. Discrepancies between the observed and calculated seismograms are primarily caused by inaccuracies in the source mechanism, the presence of anisotropy, and the reflections of scattered waves, converted waves, and multiples, and due to the fact that the DWM method does not compute the coda waves.

### Analysis and Discussion

As shown in Figure 4, at each point, nine parameters represent a 1D model with a four-layer crust and one-layer uppermost mantle. Five of them are estimated by fitting *S<sub>g</sub>* and *S<sub>n</sub>* arrivals within a window centered at the point. In this section, we discuss three issues: the robustness of the random

search, uncertainty due to the effect of a dipping Moho, and the model resolution and accuracy of the method.

### Robustness of the Monte Carlo Search

For this study, all six parameters are perturbed in each tested model. With the random search method one can be reasonably certain of uniqueness if  $n_{\max}$  goes to infinity and/or  $\epsilon$  goes to zero. The rms error will then move toward the true minimum, and the parameters will move towards the global solution. The question remains as to how we can guarantee the models are the best if the optimal models are obtained by limited iterations ( $n_{\max}$ ) rather than iterating until it approaches infinity.

We selected a few locations in China and searched for 1D profiles with both 100,000 and 50,000,000 trials. The best models found with 100,000 trials are the same as those with 50,000,000 trials. Our selected random searches thus converged at 100,000 trials or fewer.

We estimate the uncertainty due to measurement errors in each final profile by comparing each best model with other suboptimal models (i.e., those with larger rms errors) in the same location. We choose 12 locations that are either  $1^\circ$ ,  $3^\circ$ , or  $10^\circ$  from the center ( $102^\circ$ ,  $35^\circ$ ) of China in both longitude and latitude (Fig. 10). At each location, we selected the 50 best models based on the rms error. We find that

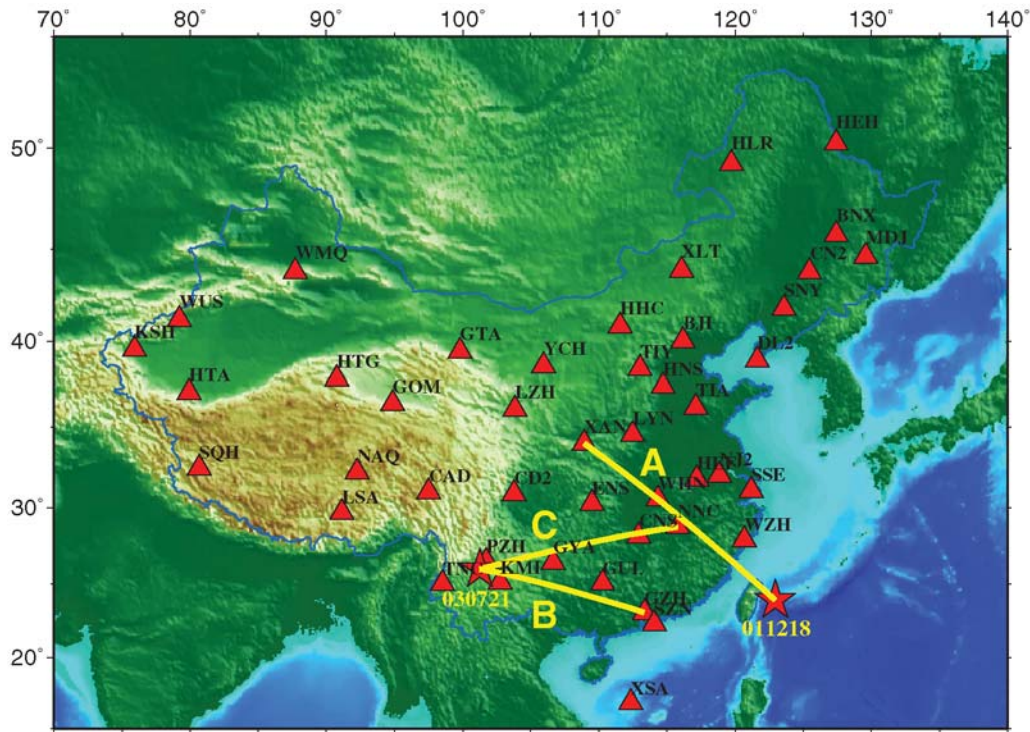


**Figure 8.** The selected three profiles in southern China for fitting seismograms observed from broadband stations. The two events are the Yunnan earthquake (21 July 2003,  $M$  6.0, 25.99° N, 101.27° E, 10 km, 1516:31.3 UTC) and the earthquake near Ishigakijima Island (18 December 2001,  $M$  6.3, 23.92° N, 122.94° E, 33 km, 0402:58.4 UTC). The selected broadband stations are Guangzhou, GZH; Nanchang, NNC; Xi'an, XAN.

at most locations the top 50 models are quite similar to one another, with slightly larger differences in the lower crust. The standard deviation (S.D.) of the velocity in the lower crust is from 0.06 to 0.21 km/sec, while the S.D. range is [0.015, 0.16] in the upper crust and [0.02, 0.11] in the middle crust. The S.D. range for the uppermost mantle is [0.01, 0.03].

#### Uncertainty due to the Effect of Dipping Layers

The best model at each location is obtained by minimizing the RMS travel-time misfit for all observations within the region. From the previous section, we know that the Monte Carlo search fit is very robust when the number of iterations is 100,000 or above. Another important question is what the uncertainty is in each best model due to the dipping layer effect.

Figure 11 shows a two-layer model with a synthetic event on the surface of the earth. The crust and the uppermost mantle are separated by a dipping Moho. There are three parameters to represent the 1D model at the source location: the Moho depth, the averaged crust velocity, and the averaged velocity in the uppermost mantle. We set the Moho depth ( $D$ ) beneath the event to 40 km. The averaged crustal shear velocity ( $V_1$ ) is 3.8 km/sec, and the averaged  $S_n$  velocity ( $V_2$ ) is 4.5 km/sec.

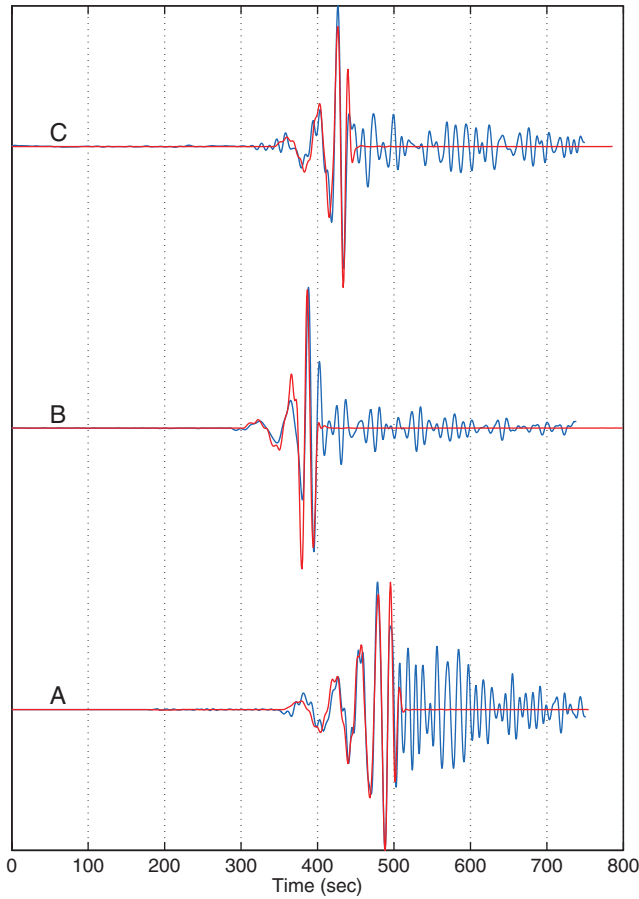
Based on the model shown in Figure 11 with a dipping Moho, we calculate synthetic travel times ( $S_g$  and  $S_n$ ) from the source to stations at epicentral distances of 0–800 km. The stations are 10-km apart on both sides of the event. We then apply the Monte Carlo search method to obtain three optimal parameters of a 1D flat Moho model that minimizes the travel-time misfits. The dipping angle increases from 0° to 30° with a step of 0.5°. We calculate the means and standard deviations at different ranges of dipping angle: [0°, 5°], [5°, 10°], [10°, 15°], and [15°, 30°]. The calculated means of each parameter at all ranges of dipping angles show errors of less than 1% errors compared with the true values.

Table 1 shows the standard deviations of the three parameters in different ranges of the dipping angle ( $\alpha$ ) of the Moho interface. The standard deviations of all the three parameters increase when the dipping angle increases. The estimated crustal velocity carries larger uncertainties than the  $S_n$  velocity. As discussed in Sun, Li, *et al.* (2004), the average dipping angles of the Moho interface in China are smaller than 3° in a region of 4° × 4° or larger. The uncertainties for all three parameters are smaller than 1%.

#### Model Resolution and Accuracy

The 1D velocity profile at each location is found using the travel-time data within the region centered at the location. The size of the region depends on the number of ray paths





**Figure 9.** The observed (blue) and calculated (red) seismograms in transverse direction along profiles A, B, and C shown in Figure 8.

contained in the region. Each 1D profile is an averaged layered model for the selected region. Therefore, the size distribution of the regions determines the resolution of the model image. Smaller region sizes mean higher resolution of the model image, and larger region sizes mean lower resolution of the model image.

Following Sun, Li, *et al.* (2004), we define the accuracy in each region to be the number of selected ray paths divided by the region size. The normalized accuracy represents the inversion resolution in each window. The region-size distribution and spatial resolution (the normalized accuracy) of all

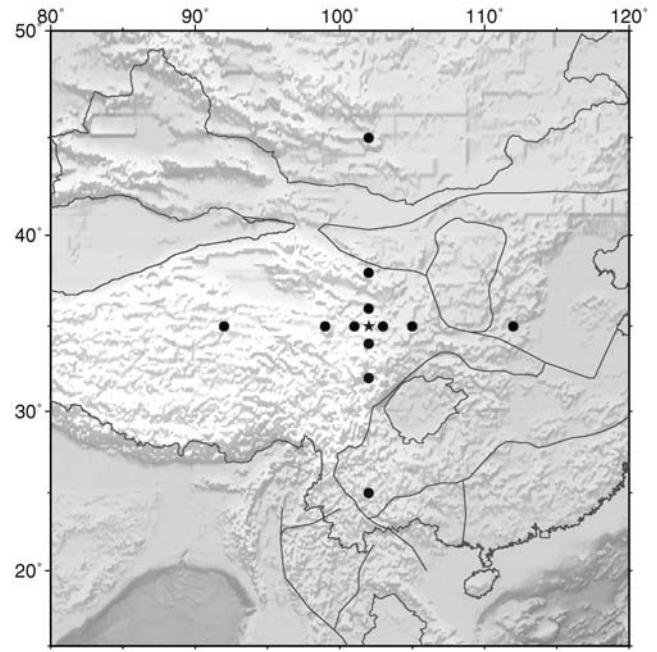


**Figure 10.** Selected locations with 1°, 3°, and 10° distance from the center location (102°, 35°). The center location is shown as a star, and other locations are shown as dots.

2338 points are shown in Figure 12. Nearly 75% of the region sizes are  $8^\circ \times 8^\circ$  or smaller. With relatively coarse ray coverage, areas such as Mongolia and Tibet require larger region sizes. We see a similar pattern between the window-size distribution and the resolution map.

## Conclusions

We used earthquake source locations and arrival times given in the ABCE to invert a large number of 1D shear-wave velocity profiles. We then combined all the 1D models to construct a 3D *S*-wave velocity model. Event location uncertainty does not play a significant role in each 1D model inversion due to the dense ray paths at each selected location (Sun, Li, *et al.*, 2004). Every 1D model is obtained by a Monte Carlo inversion method in a region with a size ranging from  $4^\circ \times 4^\circ$  to  $15^\circ \times 15^\circ$ . Approximately 75% of the region sizes are  $8^\circ \times 8^\circ$  or smaller; however, for areas with coarse ray density, the window size may be as large as  $15^\circ \times 15^\circ$ .

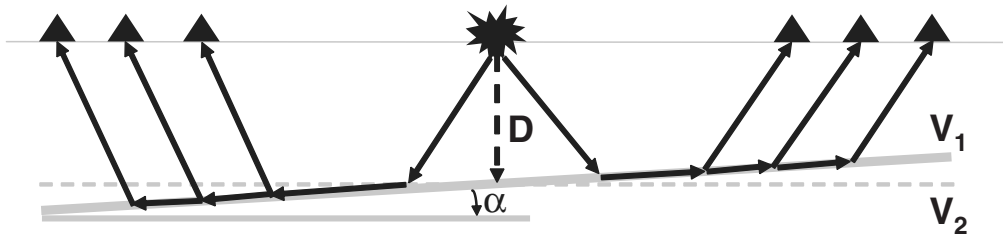


**Figure 11.** A synthetic event on the surface of the earth.  $D$  is the Moho depth at the source location.  $V_1$  is the averaged crustal velocity, and  $V_2$  is the averaged uppermost mantle velocity in the source area.

Table 1

Standard Deviations ( $\sigma$ ) of the Three Parameters ( $D$ ,  $V_1$  and  $V_2$ ) in Different Ranges of the Dipping Angle ( $\alpha$ ) of the Moho

$\alpha$	$\sigma_D$ (km)	$\sigma_{V_1}$ (km/sec)	$\sigma_{V_2}$ (km/sec)
$0^\circ$	0	0	0
$[0^\circ, 5^\circ]$	1	0.1	0
$[5^\circ, 10^\circ]$	2	0.2	0.05
$[10^\circ, 15^\circ]$	3	0.3	0.08
$[15^\circ, 30^\circ]$	4	0.3	0.16

Most areas with coarse ray coverage are located in Mongolia. Within the region centered at each selected location, the 1D velocity profiles represent an average model, while adjacent 1D velocity profiles use data with considerable overlap, and therefore ensure smooth transitions. Moho depths we obtain show excellent correlation with surface topography. In Tianshan, the maximum Moho depth we find in our model is 61 km, about 10-km deeper than those from surface-wave inversion methods, but similar to the results from a local deep-seismic sounding profile. Interfaces found for our  $S_n$  model are more accurate than those from surface-wave inversion.

The 3D  $S$ -wave velocity model obtained by the AMW method follows known tectonic structures and provides accurate body-wave travel times. This model can be used to locate earthquake events, calculate travel times, and generate seismograms. In summary, our shear-wave velocity model exhibits the following features:

1. At the upper crust, down to a depth of 20 km, velocity variations strongly correlate with the major geological features.
2. There is a strong contrast between the eastward and westward regions divided by  $110^\circ$  E longitude. In eastern China, where crustal thickness is about 35 km or less, velocity variations are relatively small. Lower velocities delineate the rift structure of northeast China. In contrast, the region to the west of  $110^\circ$  E longitude shows much more variable crustal velocities. Crustal thickness varies between 35 and 78 km. The roots of prominent features (such as the Tibet, Tarim, Sichuan, and Ordos basins) dominate the subsurface velocity structures.
3. There is a prominent low-velocity zone in the middle crust (around 40-km depth) beneath central Tibet. Shear velocity decreases by as much as 6% relative to the values north of Tibet and the Tarim basin.
4. In general, there is a good correlation between the  $P$ -wave and  $S$ -wave velocity variations; however, the relative magnitudes of the variations (i.e., percentage velocity changes) are different in various regions. For example, the percent shear velocity decrease in the mid-crust under Tibet is twice as large as that of  $P$ -velocity. In the upper mantle, the percent variation of shear velocities is greater than those of  $P$  velocities.

### Acknowledgments

This work was supported by the Defense Threat Reduction Agency under Contract Number DTRA01-00-C-0024 and by the Air Force Research Laboratory under Contract Number fa8718-04-C0018. Thanks to W. Rodi, M. Fehler, C. Rowe, W. Mooney, S. Rondenay, M. Long, X. Campman, B. Minsley, and H. Zhang for their constructive comments and suggestions. The plots shown in this article are plotted in GMT and Matlab.

### References

- Bassin, C., G. Laske, and G. Masters (2000). The current limits of resolution for surface wave tomography in North America, *EOS* **81**, F897.
- Bouchon, M. (2003). A review of the discrete wavenumber method, *Pure Appl. Geophys.* **160**, 445–465.
- Friederich, W. (2003). The  $S$ -velocity structure of the east Asian mantle from inversion of shear and surface waveforms, *Geophys. J. Int.* **153**, 88–102.
- Global Centroid Moment Tensor (CMT) Project catalog search, [www.globalcmt.org/CMTsearch.html](http://www.globalcmt.org/CMTsearch.html) (last accessed December 2007).
- Goes, S., R. Govers, and P. Vacher (2000). Shallow mantle temperatures under Europe from  $P$  and  $S$  wave tomography, *J. Geophys. Res.* **105**, 11,153–11,169.
- Hu, J., Y. Su, X. Zhu, and Y. Chen (2005).  $S$ -wave velocity and Poisson's ratio structure of crust in Yunnan and its implication, *Sci. China Ser. D: Earth Sci.* **48**, no. 2, 210–218.
- Huang, Z., W. Su, Y. Peng, Y. Zheng, and H. Li (2003). Rayleigh wave tomography of China and adjacent regions, *J. Geophys. Res.* **108**, no. B2, 2073, doi 10.1029/2001JB001696.
- Laske, G., and G. Masters (1997). A global digital map of sediments thickness (abstract), *EOS* **78**, F483.
- Lebedev, S., and G. Nolet (2003). Upper mantle beneath southeast Asia from  $S$  velocity tomography, *J. Geophys. Res.* **108**, no. B1, 2048, doi 10.1029/2000JB000073.

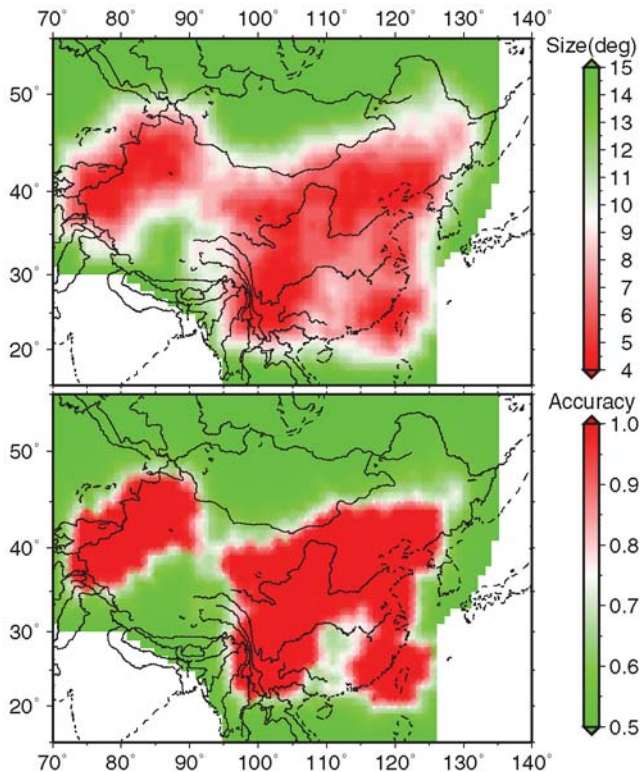


**Figure 12.** Top: Window-size distribution at all 2338 points. Bottom: Resolution (normalized accuracy) at all 2338 points.

- Lu, D., Q. Li, R. Gao, Y. Li, D. Li, W. Liu, and Z. Zhang (2000). A deep seismic sounding profile across the Tianshan Mountains, *Chin. Sci. Bull.* **45**, no. 22, 2100–2106.
- Mooney, W. D. (1998). CRUST 5.1: A global crustal model at  $5^\circ \times 5^\circ$ , *J. Geophys. Res.* **103**, 727–747.
- Pei, S., J. Zhao, Y. Sun, Z. Xu, S. Wang, H. Liu, and C. A. Rowe (2007). Upper mantle seismic velocities and anisotropy in China determined through Pn and Sn tomography, *J. Geophys. Res.* **112**, B05312, doi 10.1029/2006JB004409.
- Ritzwoller, M. H., M. P. Barmin, A. Villasenor, A. L. Levshin, and E. R. Engdahl (2002). Pn and Sn tomography across Eurasia to improve regional seismic event locations, *Tectonophysics* **358**, no. 1–4, 39–55.
- Shapiro, N. M., and M. H. Ritzwoller (2002). Monte Carlo inversion for a global shear velocity model of the crust and upper mantle, *Geophys. J. Int.* **151**, 88–105.
- Song, Z. H., C. Q. An, G. Y. Chen, L. H. Chen, Z. Zhuang, Z. W. Fu, and J. F. Hu (1991). Study on 3-D velocity structure and anisotropy beneath the west China from the Love wave dispersion, *Acta Geophys. Sin.* **34**, 694–707 (in Chinese).
- Stevens, J. L., D. A. Adams, and G. E. Baker (2001). Improved surface wave detection and measurement using phase-matched filtering with a global one-degree dispersion model, in *Proc. of 23rd Seismic Research Review: Worldwide Monitoring of Nuclear Explosions*, Jackson Hole, Wyoming, 2–5 October, 420–430.
- Sun, Y., and M. N. Toksoz (2006). Crustal structure of China and surrounding regions from P wave traveltimes tomography, *J. Geophys. Res.* **111**, B03310, doi 10.1029/2005JB003962.
- Sun, Y., S. Kuleli, F. D. Morgan, W. Rodi, and M. N. Toksöz (2004). Location robustness of earthquakes in Sichuan province, China, *Seism. Res. Lett.* **75**, no. 1, 54–62.
- Sun, Y., X. Li, S. Kuleli, F. D. Morgan, and M. N. Toksöz (2004). Adaptive moving window method for 3-D P-velocity tomography and its application in China, *Bull. Seismol. Soc. Am.* **94**, 740–746.
- Wu, F. T., A. L. Levshin, and V. M. Kozhevnikov (1997). Rayleigh wave group velocity tomography of Siberia, China and vicinity, *Pure Appl. Geophys.* **149**, 447–473.
- Wu, J. P., Y. H. Ming, and C. Y. Wang (2001). The S wave velocity structure beneath digital seismic stations of Yunnan province inferred from teleseismic receiver function modelling, *Chin. J. Geophys.* **44**, 237–243.
- Xu, G., G. Li, S. Wang, H. Chen, and H. Zhou (2000). The 3-D structure of shear waves in the crust and mantle of east continental china inverted by rayleigh wave data, *Chin. J. Geophys.* **43**, 376–384.
- Xu, M., L. Wang, J. Liu, K. Zhong, H. Li, D. Hu, and Z. Xu (2006). Crust and uppermost mantle structure of the Ailaoshan-Red River fault from receiver function analysis, *Sci. China Ser. D: Earth Sci.* **49**, no. 10, 1043.
- Zou, Z., and X. Chen (2003). Mapping the crustal S-wave velocity structure by using the SV component receiver function method, *Acta Seism. Sinica* **16**, 16–25.

Earth Resources Laboratory  
Department of Earth, Atmospheric, and  
Planetary Sciences  
Massachusetts Institute of Technology  
77 Massachusetts Avenue, 54-1820  
Cambridge, Massachusetts 02142  
youshun@mit.edu  
(Y.S., M.N.T., F.D.M.)

Institute of Tibetan Plateau Research  
Chinese Academy of Sciences  
18 Shuangqing Road  
P.O. Box 2871  
Beijing 100085, China  
peisp@itpcas.ac.cn  
(S.P.)

Manuscript received 8 November 2005

## Upper mantle seismic velocities and anisotropy in China determined through Pn and Sn tomography

Shunping Pei,<sup>1</sup> Junmeng Zhao,<sup>1</sup> Youshun Sun,<sup>2</sup> Zhonghuai Xu,<sup>3</sup> Suyun Wang,<sup>3</sup> Hongbing Liu,<sup>1</sup> Charlotte A. Rowe,<sup>4</sup> M. Nafi Toksöz,<sup>2</sup> and Xing Gao<sup>1</sup>

Received 24 March 2006; revised 2 January 2007; accepted 17 January 2007; published 25 May 2007.

[1] We have obtained velocity images of the uppermost mantle beneath China by performing tomographic inversion of both Pn and Sn traveltimes. From the Annual Bulletin of Chinese Earthquakes, 99,139 Pn arrivals and 43,646 Sn arrivals were selected. Pn anisotropy was also obtained simultaneously with Pn velocity. Average Pn and Sn velocities are 8.05 and 4.55 km/s, respectively, and maximum velocity perturbations are about 3–4%. The Pn and Sn velocities are low in eastern China and high in western China. Particularly high velocities are associated with old basins (for example, Tarim, Junggar, Turpan-Hami, Qaidam, and Sichuan) and stable craton (for example, Ordos). Low Sn velocities are found mainly throughout North China. In addition, velocities are relatively low beneath the central Tibetan Plateau and the North-South Seismic Zone (along 103°E). In Tarim and central China where we observe strong anisotropy, the fast Pn velocity directions are consistent with the directions of maximum principal compressive stress as well as directions of crustal movement determined from Global Positioning System. Beneath the India-Eurasia collision zone, the Pn anisotropy direction is parallel to the collision arc and nearly perpendicular to both the direction of maximum compression and crustal movement resulting from pure shear deformation. Both the velocity variations and anisotropy indicate that the Tibetan Plateau was extruded, and the mantle material beneath the plateau has flowed around the East Himalaya Syntax, while the remaining material has diverted northwestward beneath the Tarim Basin.

**Citation:** Pei, S., J. Zhao, Y. Sun, Z. Xu, S. Wang, H. Liu, C. A. Rowe, M. Nafi Toksöz, and X. Gao (2007), Upper mantle seismic velocities and anisotropy in China determined through Pn and Sn tomography, *J. Geophys. Res.*, 112, B05312, doi:10.1029/2006JB004409.

### 1. Introduction

[2] The tectonic differences between eastern and western China are mainly controlled by the India-Eurasia collision and by subduction in the Western Pacific (Figure 1) [e.g., Molnar and Tapponnier, 1975; Tapponnier *et al.*, 1982; Ni and Barazangi, 1984; Molnar *et al.*, 1993; Rowley, 1996; Yin and Harrison, 2000; Tilmann *et al.*, 2003]. These differences have been shown by deep seismic sounding using active sources to image the crustal structure [Li and Mooney, 1998] and by three-dimensional tomographic models of seismic velocity [Liu *et al.*, 2000; Xu *et al.*, 2001; Liu *et al.*, 2001; Zhu *et al.*, 2002; Wang *et al.*, 2003; Sun *et al.*, 2004, 2006; Liu *et al.*, 2005; Sun and Toksöz, 2006].

[3] Pn and Sn velocity variations in the uppermost mantle may provide additional clues to changes in temperature, pressure, composition, water, and volatile content. Furthermore, Pn and Sn velocity variations with azimuth allow us to study the seismic anisotropy of the uppermost mantle, a property that is generally considered to arise from the alignment of aggregate olivine crystals [Ribe, 1992; Silver, 1996]. Thus a study of Pn and Sn velocity variations and Pn anisotropy provides important constraints for the processes of continental deformation and differentiation.

[4] It is well known that clear lateral Pn velocity variations and anisotropy exist in the uppermost mantle [e.g., Hearn, 1996, 1999; Hearn *et al.*, 2004; Mele *et al.*, 1998; Wang *et al.*, 2002; Liang *et al.*, 2004; Pei *et al.*, 2002, 2004a, 2004b; Phillips *et al.*, 2005]. Hearn *et al.* [2004] obtained the shallow and deep Pn velocity variations within the mantle lid in China, via independent inversions for short and long paths, but he did not consider Pn anisotropy in his study. Wang *et al.* [2002] and Liang *et al.* [2004] applied joint Pn velocity and anisotropy inversion to obtain uppermost mantle structure and anisotropy in China. Liang *et al.* [2004] also obtained crustal thickness inferred

<sup>1</sup>Tibetan Plateau Uplift Process and Environment Laboratory, Institute of Tibetan Plateau Research, Chinese Academy of Sciences, Beijing, China.

<sup>2</sup>Earth Resources Laboratory, Massachusetts Institute of Technology, Cambridge, Massachusetts, USA.

<sup>3</sup>Institute of Geophysics, China Earthquake Administration, Beijing, China.

<sup>4</sup>Los Alamos National Laboratory, Los Alamos, New Mexico, USA.



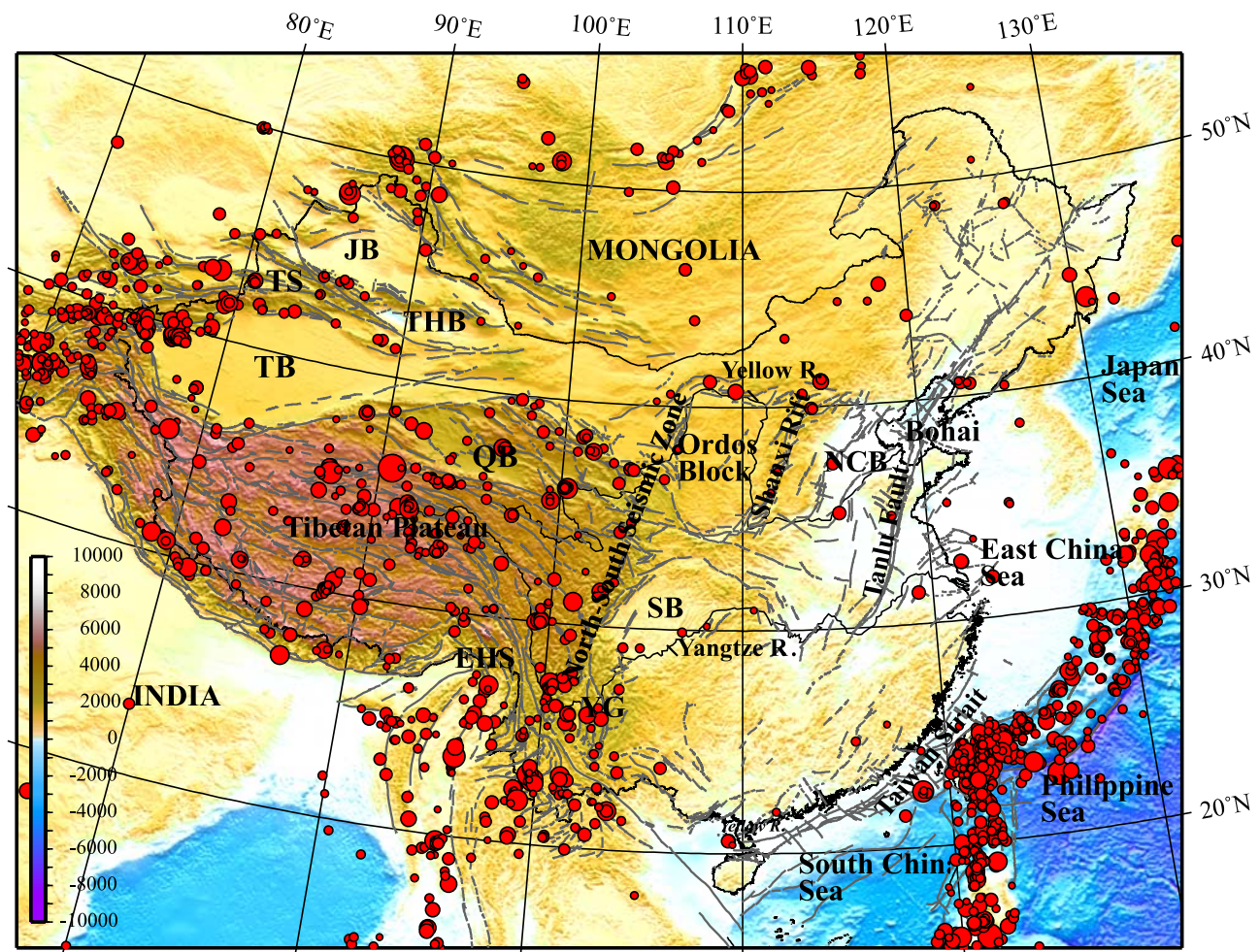


**Figure 1.** Topographic map of China. The color shades indicate elevation. Thin black lines represent active faults. Red circles indicate earthquakes of magnitude >5.0 recorded between 1978 and 2004; circle size is proportional to magnitude. TB, Tarim Basin, TS, Tianshan, JB, Junggar Basin, QB, Qaidam Basin, THB, Turpan-Hami Basin, SB, Sichuan Basin, NCB, North China Basin, EHS, East Himalaya Syntax, YG, Yunnan-Guizhou Plateau.

from station delays. Far less work has been reported with respect to Sn velocity imaging. This dearth of literature on Sn modeling is due to the difficulty in picking the Sn phase and consequently to the small number of Sn phase arrival times reported in seismological bulletins. There are, however, several recent Sn studies in various regions. *Bannister et al.* [1991] obtained a  $\pm 1\%$  variation of S velocity in the uppermost mantle by inverting  $\sim 1500$  Sn traveltimes in Fennoscandia. *Nolet et al.* [1998] calculated Sn velocity in eastern and western North America using only  $\sim 1000$  Sn travel times. *Levshin et al.* [2001] imaged Sn velocity variation ( $4.35\text{--}4.70$  km/s) in the uppermost mantle beneath the Arctic region. In China, *Di et al.* [1999] imaged Sn velocity beneath the Weihe Rift zone based on 1265 Sn travel times.

[5] In this work, we use Pn and Sn arrivals reported in the Annual Bulletin and Preliminary Report of Chinese Earthquakes compiled by the Institute of Geophysics, China Earthquake Administration (IGCEA), plus reports from regional and provincial networks, and arrivals reported by

the International Seismological Centre to construct a tomographic image of Pn and Sn seismic velocity beneath China and surrounding regions. We then examine the geodynamic implications.

## 2. Data

[6] Our study area is defined by  $12^{\circ}\text{--}52^{\circ}\text{N}$  and  $65^{\circ}\text{--}132^{\circ}\text{E}$ . Phase data from the following sources are used: (1) the 1985–1998 Annual Bulletin of Chinese Earthquakes (ABCE) compiled by IGCEA, (2) the 1999–2001 Preliminary Report of Chinese Earthquakes compiled also by IGCEA, (3) the regional seismic networks of 26 provinces, (4) the temporary network of project INDEPTH2 [Nelson et al., 1996], and the Sino-US Joint Seismological Survey [Ding et al., 1993] in Tibet. We have refined the data set by removing repeated and unreliable records and by using only the event parameters given in ABCE, which are more precise than the parameters in provincial reports because the events were relocated using data from all stations in China by IGCEA.



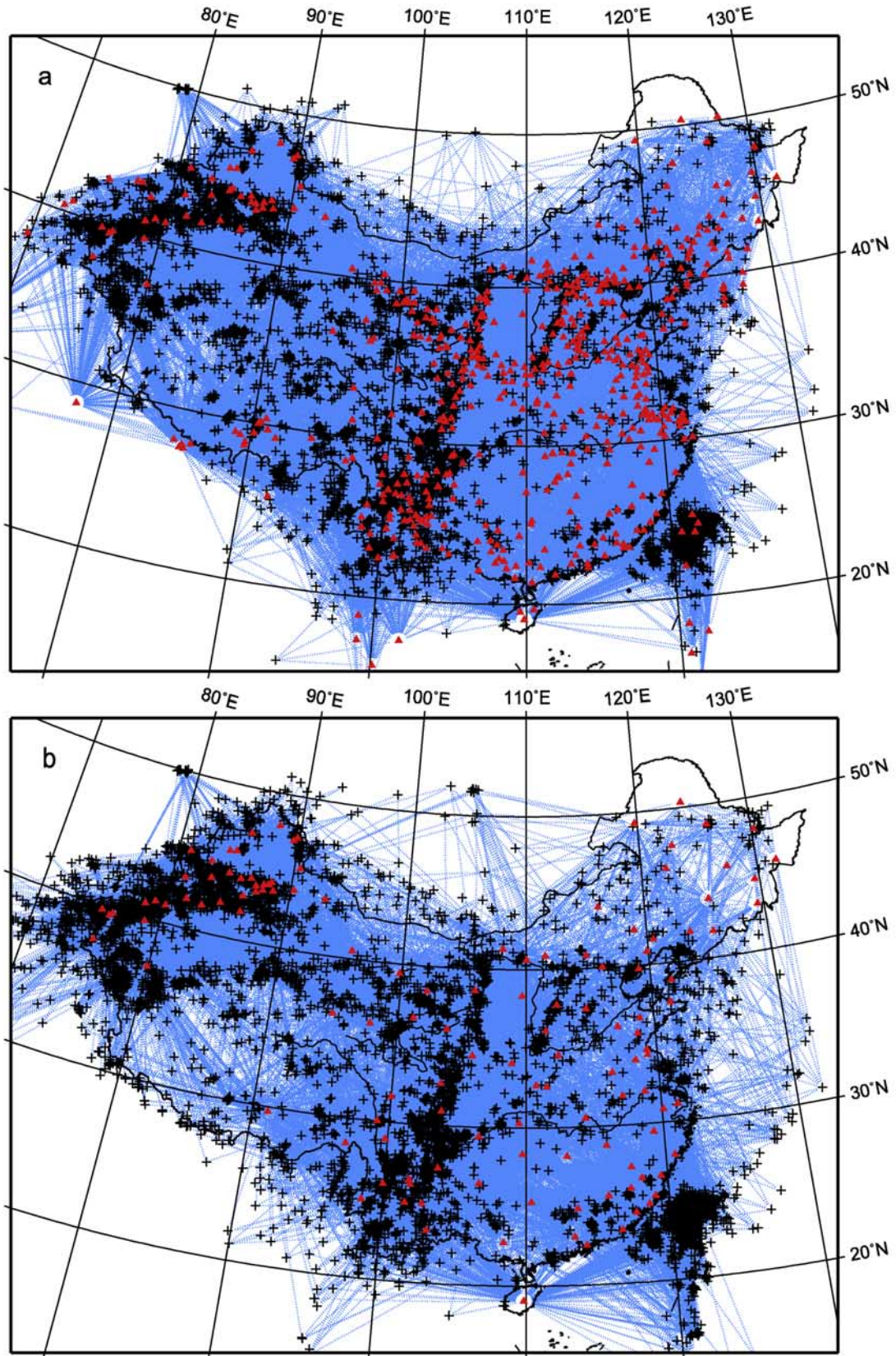


**Figure 2.** Raypath for Pn (a) traveltimes and (b) Sn traveltimes. From 7382 events (crosses) recorded by 575 stations (triangles), 91,139 Pn rays were obtained. From 8782 events recorded by 131 stations, 43,646 Sn rays were obtained. The densest rays are found in Xinjiang, central China, and the Taiwan Strait. Maximum numbers of rays within each cell of 30' by 30' were 3306 and 2741 for Pn and Sn data, respectively.

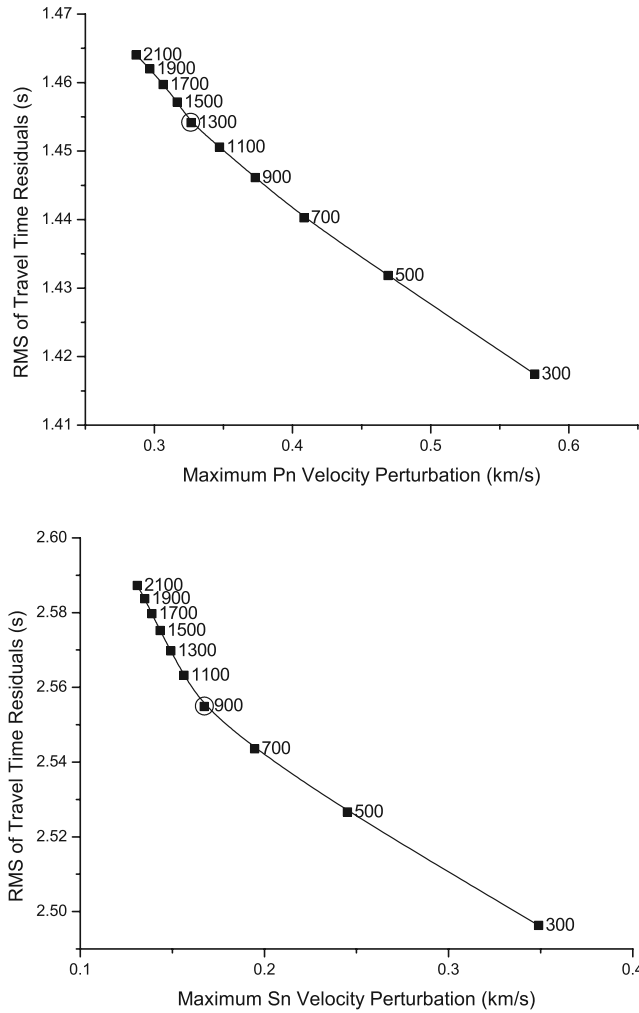


**Figure 3.** Trade-off curves for the maximum velocity perturbations and root mean square value of the traveltime residuals for Pn (above) and Sn (below), separately. Numbers beside the black dots denote the damping parameters adopted for the inversions. The largest black circle denotes the optimum damping parameter chosen for the final tomographic model.

[7] The epicenter distance range of the traveltimes used in this study is  $2^{\circ}$ – $12^{\circ}$  for first P and  $2^{\circ}$ – $15^{\circ}$  for first S. We chose the lower limit to remove Pg and Sg phases and the upper limit to include only the observations along the linear portion of the traveltime curve. Within this distance range, the Pn phases are first arrivals and the Sn phases are first S-wave arrivals. Starting models were obtained by a linear fit to the traveltime, epicentral distance curve. To ensure the data quality, we impose further conditions: each event has at least five Pn and two Sn readings, and each station recorded at least five events. In addition, the traveltime residuals to the fitted line used in this paper are limited to the range of  $\pm 6$  s for Pn and  $\pm 7$  s for Sn because the error in picking the Sn phase is usually larger than Pn. The data set included 91,139 Pn times from 7382 earthquakes recorded by 575 stations (Figure 2a), and 43,646 Sn times from 8782 earthquakes recorded by 131 stations

(Figure 2b). The depth of each event is less than 40 km. Standard deviation of the traveltime residuals is 1.9 s for Pn and 3.3 s for Sn.

### 3. Method

[8] Following Hearn's approach and computation method [Hearn and Ni, 1994; Hearn, 1996], we invert Pn and Sn traveltime residuals for lateral velocity variation and anisotropy within the mantle lid. The Pn and Sn are modeled as refracted rays traveling along the Moho discontinuity (head waves). The variation of seismic velocity within the uppermost mantle is parameterized by subdividing the surface of the uppermost mantle into a two-dimensional grid of  $30' \times 30'$  cells. Pn traveltime residuals are described as the sum of three time terms:

$$t_{ij} = a_i + b_j + \sum d_{ijk}(s_k + A_k \cos 2\varphi + B_k \sin 2\varphi)$$

where  $t_{ij}$  is the traveltime residual for the ray from event  $j$  to station  $i$ ;  $a_i$  is the static delay for station  $i$ , depending on the crustal thickness and velocity beneath the station;  $b_j$  is the static delay for event  $j$ , not only depending on the crustal thickness and velocity beneath the event but also on the event focal depth;  $d_{ijk}$  is the distance traveled by ray  $ij$  in mantle cell  $k$ ;  $s_k$  is the slowness (inverse velocity) perturbation for cell  $k$ ;  $A_k$  and  $B_k$  are the anisotropy coefficients for cell  $k$ ; and  $\varphi$  is the back azimuth angle. The unknown quantities in the equation are  $a_i$ ,  $b_j$ ,  $s_k$ ,  $A_k$ , and  $B_k$ . As a first approximation, seismic anisotropy in the uppermost mantle is assumed to be described by a  $2\varphi$  azimuthal variation. The magnitude of anisotropy for cell  $k$  is given by  $(A_k^2 + B_k^2)^{1/2}$ , and the azimuthal angle  $\theta$  of the fast direction of Pn propagation is given by  $1/2 \arctan(B_k / A_k) + 90$ .

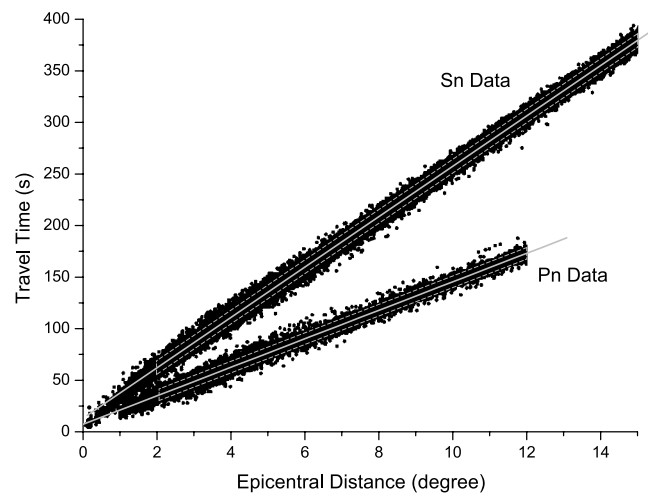


**Figure 4.** First P wave traveltimes and first S traveltimes versus epicentral distance. The data shown within the dashed box outlining the lower fitted line were selected to invert Pn lateral velocity and anisotropy. The average Pn velocity of 8.05 km/s was determined from the slope of this line. The data within the dashed box outlining the upper fitted line represent the Sn arrivals selected to invert for Sn lateral velocity perturbations. The average Sn velocity of 4.55 km/s was determined from the slope of this line.



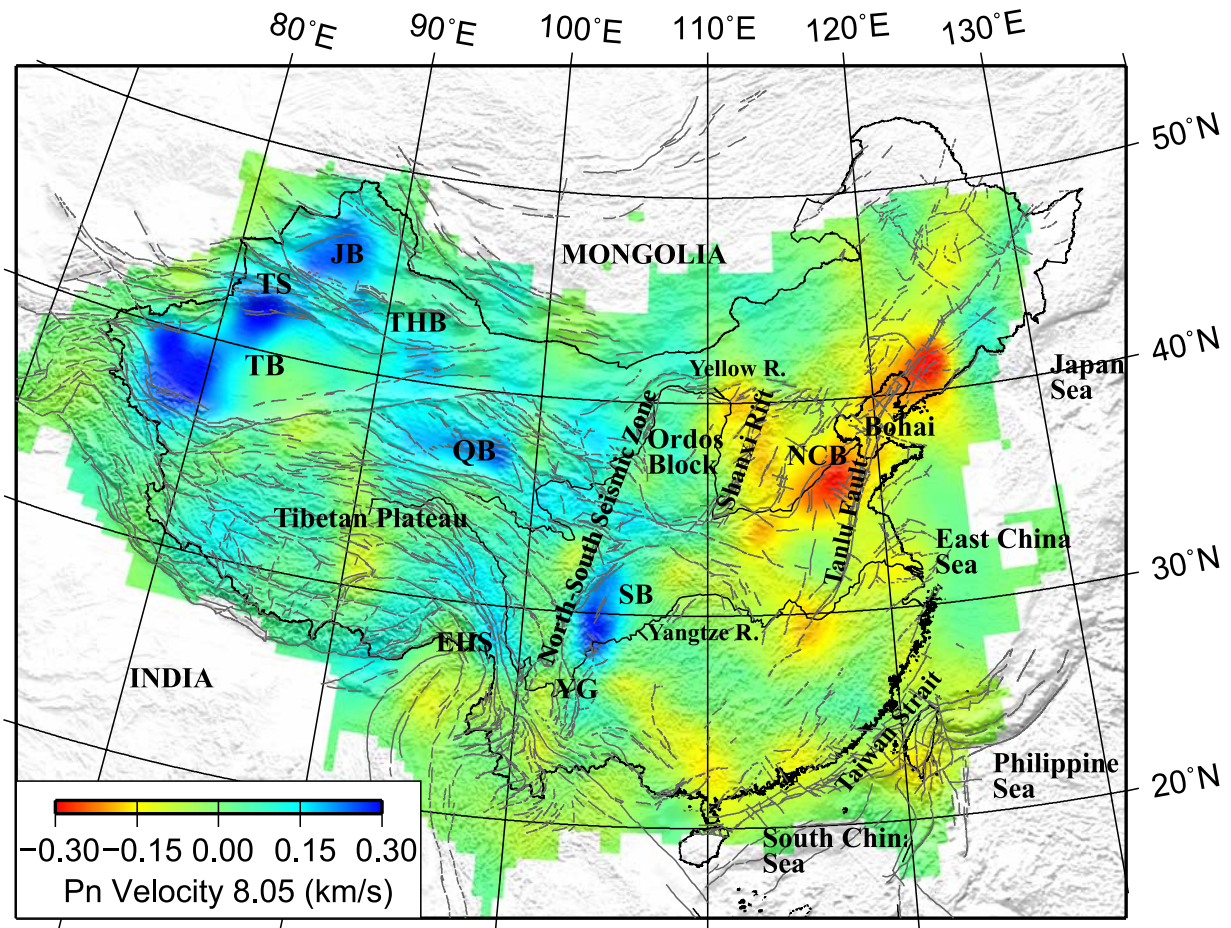


**Figure 5.** Pn lateral velocity variations. Average Pn velocity is 8.05 km/s and perturbation corresponds to color. Red represents velocities lower than the average and blue denotes higher velocities. Thin black lines indicate active faults.

The sum is calculated over all cells through which the ray travels in the uppermost mantle. Further details of the tomography technique used here can be found in the works by *Hearn and Ni [1994]* and *Hearn [1996]*.

[9] A set of Laplacian damping equations regularizes the solution, and two damping constants are separately applied to the unknown slowness and anisotropy coefficients. The two separate damping constants are used to control the smoothness of the velocity image by damping the slowness variations and to control the smoothness of the anisotropy by damping the two anisotropy coefficients. Both damping constants control the trade-off between low uncertainties (high damping) and small resolution width (low damping). The ratio of the two damping constants controls the magnitude of velocity variations and anisotropy variations. A proper pair of damping constants is chosen to balance the uncertainty size and the resolution width. In this approach, the trade-off between velocity and anisotropy variations is a crucial issue, which has been examined by using different combinations of damping parameters for both velocity and anisotropy. We tried different damping constants on the velocity and anisotropy and found higher damping constants creates smoother images, while the ratio of the two damping constants controls the trade-off in structure between the velocity image and the anisotropy image. These images

represent the true solution as seen through different resolution filters in the absence of data error. Differences between the images are primarily in the magnitude of the anisotropy and velocity variations; however, the major patterns found in both the anisotropy and the velocity images are relatively stable with respect to the damping constants. The method of Sn tomography applied in this study is the same as that for Pn tomography, except we do not incorporate the anisotropy into the inversion.

[10] We have performed a series of tests by choosing various cell sizes and different damping constants for the slowness and anisotropy coefficients. The adopted cell size is  $30' \times 30'$ , as stated before, and the damping constants for both slowness perturbation and anisotropy were set to 1300 for Pn and 900 for Sn. The total number of model parameters is 6577 for Pn and 6782 for Sn. We also used the bootstrap technique used by *Hearn [1996]* to assess the robustness of the result. The bootstrap method iteratively resamples the data pool and reruns the inversion using the standard deviation in bootstrapped velocities as proxies for model uncertainty.

[11] Figure 3 shows the trade-off curves for maximum velocity perturbations and root mean square value of the traveltimes residuals. Damping constants control the variance of tomographic velocity perturbations. Small damping

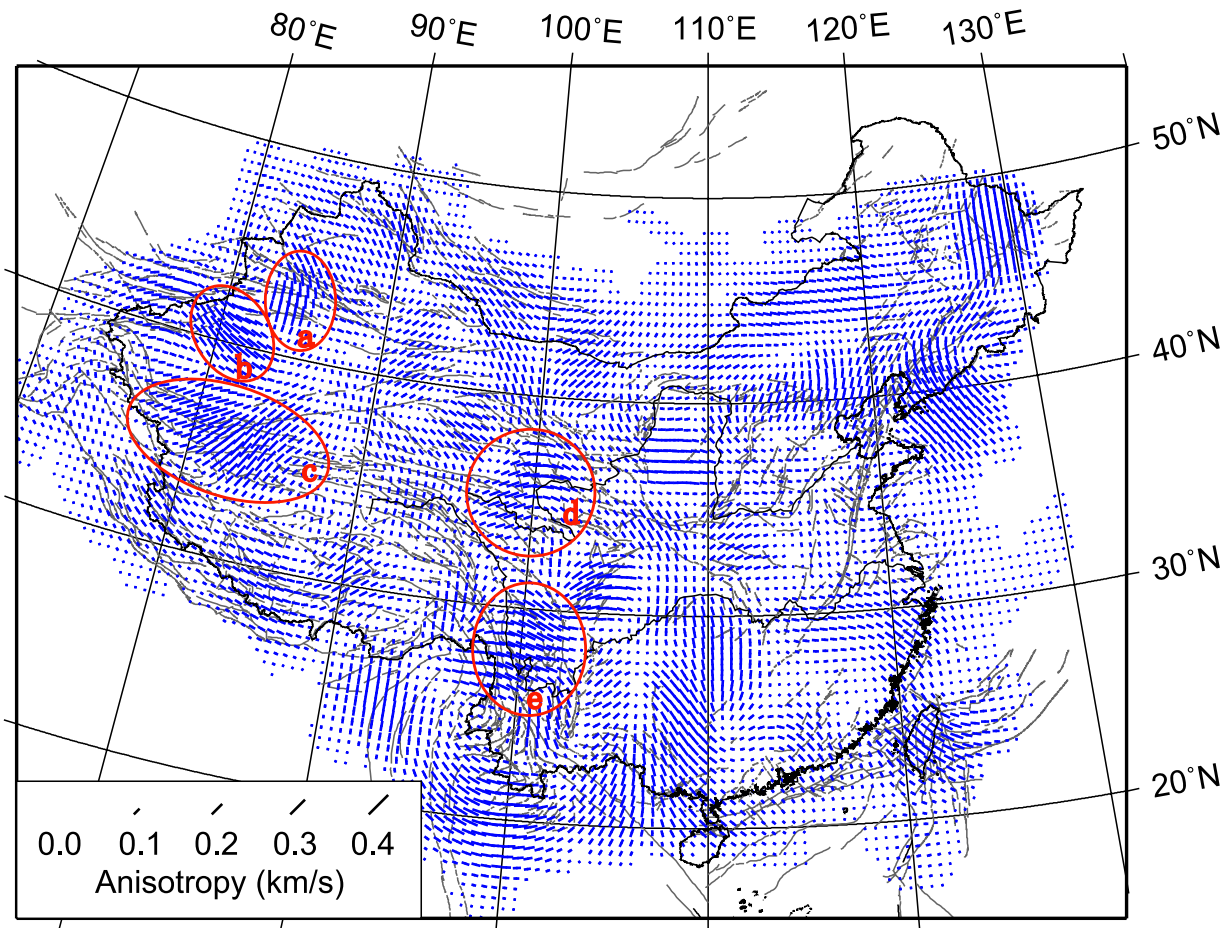


**Figure 6.** Tomographic image of Pn velocity anisotropy. Line segments are drawn parallel to the direction of highest velocity, with their length proportional to the magnitude of anisotropy. Regions exhibiting large anisotropy and possessing dense ray coverage are marked with circles and labeled as a, b, c, d and e.

constants will result in high velocity perturbations and a sharp image, while large damping constants will lead to low velocity perturbations and a smoother image. In general, the damping parameters are chosen as those at the inflection of the curve. We also require that in a small area having anomalously high velocity (i.e., the Tarim basin), the tomographic velocity is close to the average velocity in the anomalous area. In the end, we have chosen damping constants of 1300 for Pn and 900 for Sn.

#### 4. Result

[12] Fitting a straight line to the data set of Pn and Sn traveltimes versus epicentral distance, we obtained an average Pn velocity of 8.05 km/s (Figure 4) and an average Sn velocity of 4.55 km/s (Figure 4). The average P and S velocities within the crust were set to 6.3 and 3.6 km/s, respectively, as determined from Pg and Sg phases. The average P wave velocity of 6.3 km/s is the same as that found in previous research [Hearn *et al.*, 2004; Liang *et al.*, 2004; Li and Mooney, 1998]. The average crustal thickness of 46 km was obtained for our region from the Pn line intercept of 9.1 s (Figure 4), roughly consistent with a 44-km thickness derived from the 14.8-s line intercept of

Sn data (Figure 4). This minor difference is due largely to the different distributions of Pn and Sn rays.

##### 4.1. Pn Velocity and Anisotropy

[13] Pn lateral velocity variations (Figure 5) and anisotropy (Figure 6), station delays (Figure 7), and event delays were obtained by tomographically inverting the Pn travel-time residuals. Relative to the mean value of 8.05 km/s, the Pn velocity perturbations range from  $-0.32$  km/s ( $-4.0\%$ ) to  $0.33$  km/s ( $4.1\%$ ). The average Pn velocity is the same as that found by Hearn *et al.* [2004] and very close to the 8.06 km/s found by Liang *et al.* [2004]. Via 100 bootstrap inversions, we found uncertainties in velocity perturbations for all cells to be less than 0.05 km/s. Average and standard deviation of velocity uncertainties are 0.02 and 0.008 km/s, respectively. The standard deviation of traveltime residuals decreased from 1.9 to 1.45 s, after the inversion.

[14] High velocities dominate in western China. Beneath several large depressed basins, such as the Tarim, Junggar, Turpan-Hami, Qaidam, and Sichuan basins, the velocity perturbation is positive and greater than 0.2 km/s. These basins are surrounded by orogenic belts having low Pn velocity. In northwestern China, the variation of Pn velocity is generally consistent with the velocity distribution at



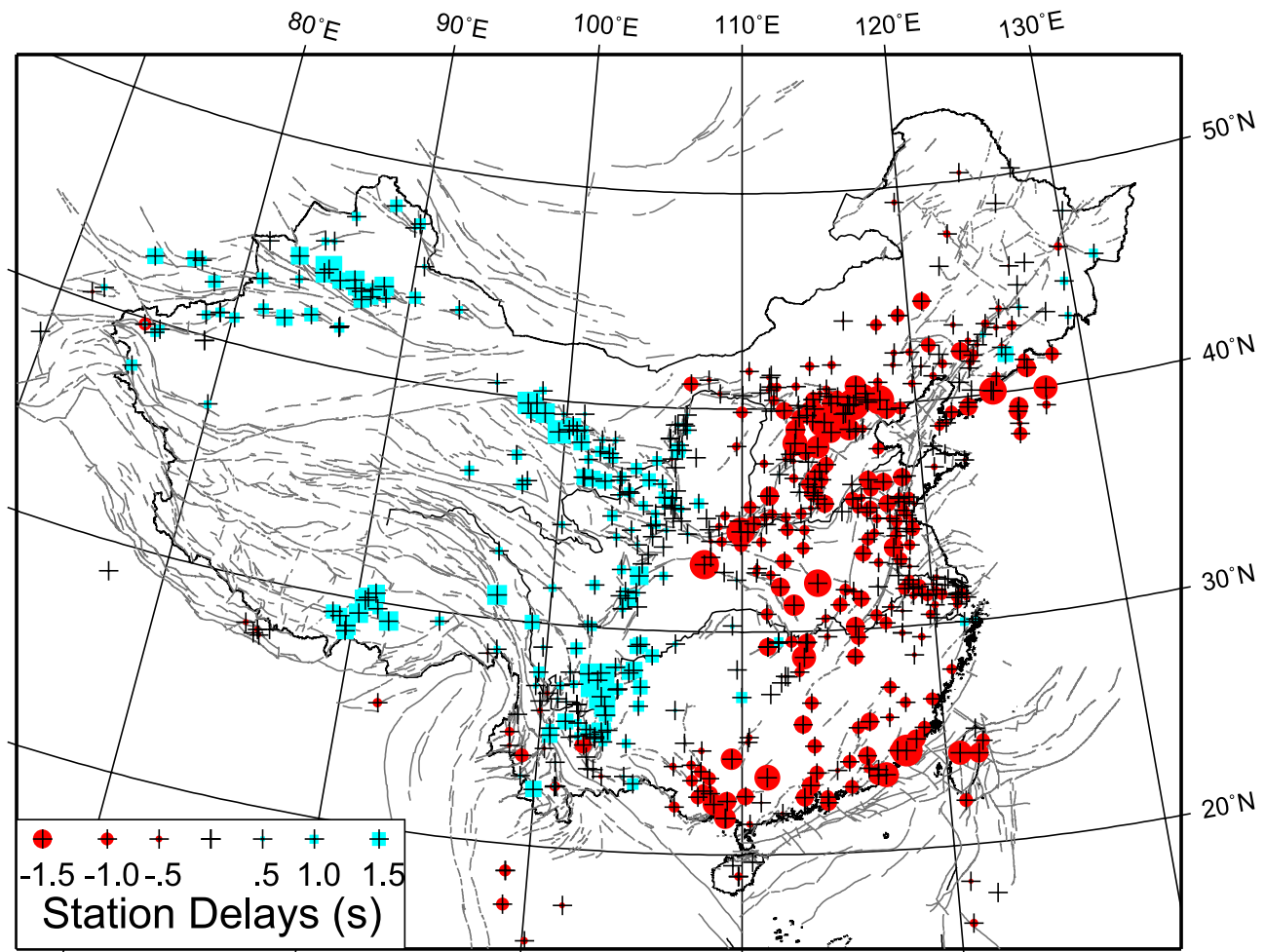


**Figure 7.** Station delays (seconds) for Pn traveltimes. Crosses represent stations. Circles indicate early arrival times, and squares indicate late arrival times, with their sizes proportional to the delay. We find that early arrivals in eastern China, and late arrivals in western China, are due to thin crust in the east and thick crust in the west.

50<sup>+</sup>-km depth given by *Li et al.* [1994] and *Xu et al.* [2001] in their three-dimensional tomographic studies, except for some minor differences at the periphery. In the central Tibetan Plateau, a low velocity Pn anomaly is observed, consistent with that of *McNamara et al.* [1997] and *Phillips et al.* [2005]. This is the same region in which *Barazangi and Ni* [1982] found large Sn attenuation.

[15] In eastern China, relatively low velocities are predominant. The North China extensional basin [*Ye et al.*, 1985] and the area around Bohai Bay exhibit clear low velocities (Figure 5). A low velocity anomaly also exists beneath the Shanxi Rift and North-South Seismic Zone (Figures 1 and 5) as seen by *Phillips et al.* [2005]. The stable Ordos Craton exhibits high velocity. The Pn velocity distribution in eastern China obtained in this study is generally consistent with the P wave velocity variations at 45-km depth given by *Liu et al.* [1989] in their three-dimensional tomographic studies.

[16] Although we have determined Pn anisotropy for all parts of China, we focus our discussion on the region around the Tarim Basin and central China because the ray density there is high (Figure 6). The fast direction of

anisotropy is WNW in the western Tarim Basin (region b in Figure 6), NS in the middle of the Tianshan Mountains (region a in Figure 6), NE in the western edge of Tibet and southern Tarim (region c in Figure 6), NE to E in the north-eastern Tibet (region d in Figure 6), and SE between EHS and the Sichuan Basin (region e in Figure 6). In addition, the fast direction is near EW in the Ordos Block and in the middle of the Sichuan Basin.

[17] Checkerboard tests were conducted to evaluate the effects of ray coverage on spatial resolution. A test checkerboard velocity model was created by assigning sinusoidal velocity and anisotropy anomalies to the cells of the model domain. Maximum sinusoidal velocity and anisotropy are set to a value equal to double the maximum perturbation obtained in the inversion. Synthetic arrival times were calculated for the test model with the same numbers of earthquakes, stations, and raypaths as those used for the tomographic inversion of the real data. These synthetic arrival times were then inverted for velocity and anisotropy using the same algorithm used for the inversion of the real data. Gaussian noise with standard deviation 1.45 s was added to synthetic traveltimes because we conservatively



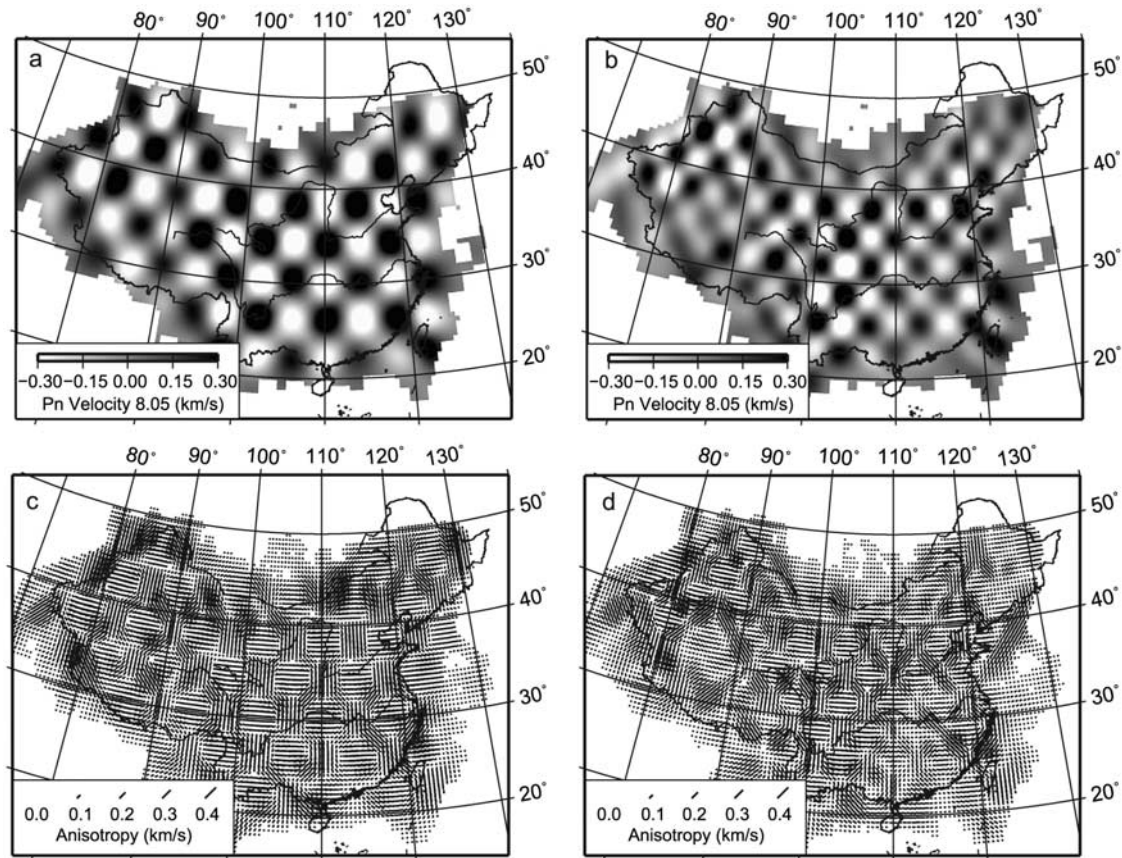


**Figure 8.** Checkerboard tests for Pn velocity with resolutions of (a)  $4^\circ \times 4^\circ$  and (b)  $3^\circ \times 3^\circ$  and for Pn anisotropy resolutions of (c)  $4^\circ \times 4^\circ$  and (d)  $3^\circ \times 3^\circ$ .

assume traveltime residuals after inversion to be noise. Results of the checkerboard test are shown in Figure 8. The spatial resolution is considered to be good for a region in which the checkerboard pattern is recovered. The tests indicate that for most of the studied region,  $3^\circ \times 3^\circ$  cells can be resolved for Pn velocity and  $4^\circ \times 4^\circ$  cells can be resolved for anisotropy. We also tried different cell sizes for the checkerboard test. A smaller cell size yields a comparable result to the  $30' \times 30'$  cells, whereas a larger cell size exhibits a smoother pattern of resolution because of smoothing in neighboring velocity blocks.

[18] Overall, our result is similar to the results of previous studies of Pn velocity and anisotropy [Wang *et al.*, 2002; Hearn *et al.*, 2004; Liang *et al.*, 2004]. Hearn *et al.* [2004] obtained the shallow and deep Pn velocity variations within the mantle lid in China by inverting with shorter raypaths and longer raypaths, separately. His velocity perturbation result for path lengths ranging from  $1.8^\circ$  to  $15^\circ$  is very similar to our result, but our Pn variation is smoother than Hearn's as a result of accommodating the anisotropy in our inversion. Liang *et al.* [2004] applied the same method and obtained similar Pn velocity and anisotropy; differences were only noted at the margin of the model, where the raypath coverage is sparse and results in greater uncertainty. Our inversion has a higher resolution in regions having denser rays and better azimuthal coverage (for example, the Tarim Basin) because we use 50% more Pn data than has been available for previous research.

#### 4.2. Sn Velocity

[19] Figure 9 shows lateral variation of Sn velocity. Relative to the mean value of 4.55 km/s, the Sn velocity perturbations range from  $-0.18$  km/s ( $-4.0\%$ ) to  $0.16$  km/s ( $3.5\%$ ). After 100 bootstrap inversions, the uncertainties in velocity perturbations for all cells are found to be less than  $0.05$  km/s. For 53% of the model region, the uncertainties are less than  $0.02$  km/s.

[20] In general, the Sn velocity image bears a high degree of similarity to the Pn image (Figure 5); velocities are low in eastern China and high in western China. Remarkably high Sn velocity appears mainly in the Tarim, Junggar, Turpan-Hami, Qaidam, and Sichuan basins, and the southern neighboring region. In the region of the Ordos Craton, southern Tibet, and the Taiwan Straits, Sn velocity is also higher than average. In eastern China, low Sn velocity is seen throughout the North China Basin, the region east to Bohai Bay, the Shanxi Rift, and the Tanlu Fault zone. In addition, in the middle and lower reaches of the Yangtze River, the central Tibetan Plateau, and the North-South Seismic Zone, the Sn velocity is slightly low.

[21] Shown in Figure 10 are the associated station delays (Figure 10a) and event delays (Figure 10b). The early arrivals in eastern China and the late arrivals in western China as inferred from station delays can readily be explained in terms of thinner crust in the east and thicker crust in the west, similar to the station delays for Pn traveltimes (Figure 7). Station delays are mainly affected

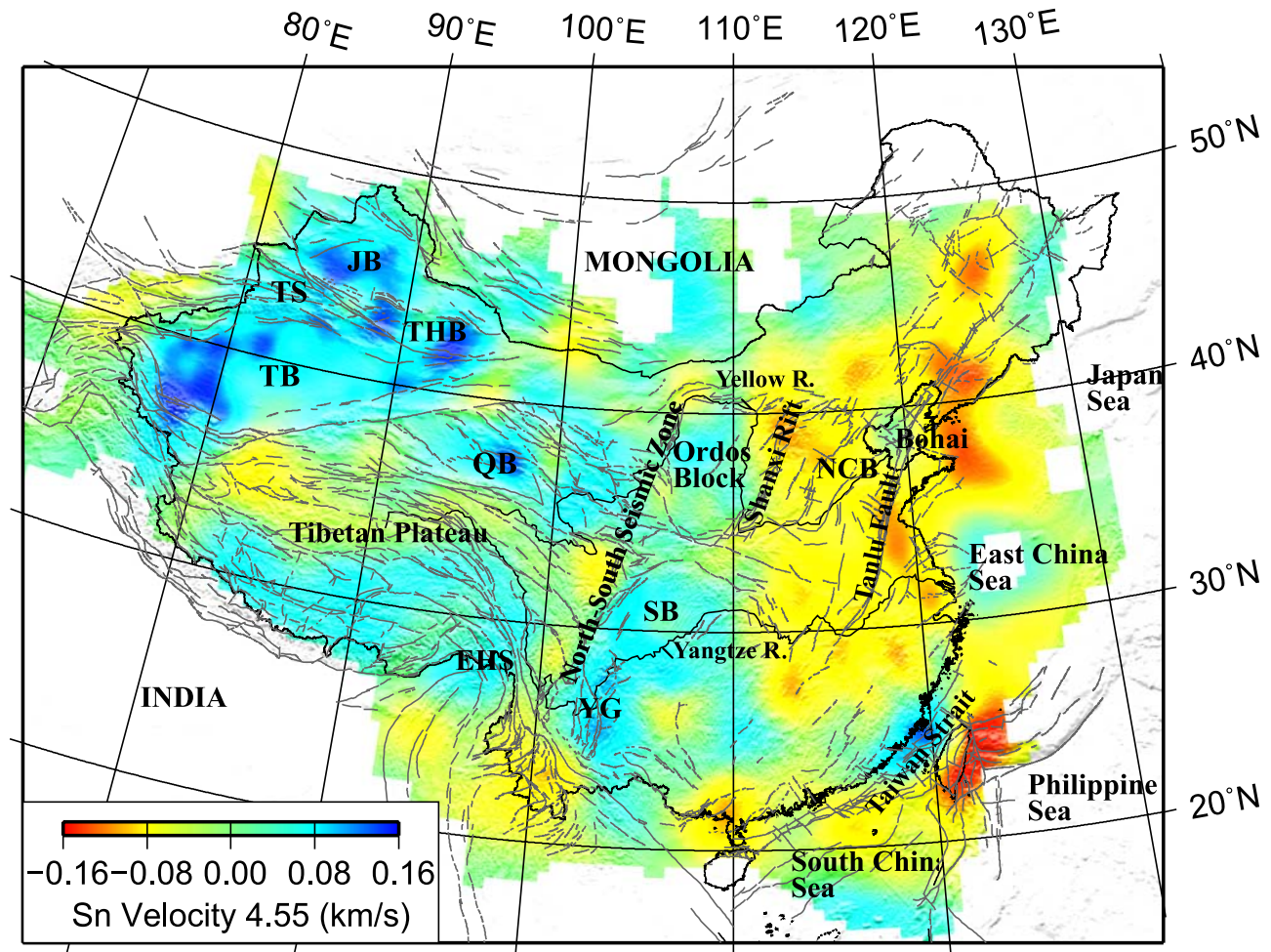


**Figure 9.** Tomographic image of Sn lateral velocity variations. Blue corresponds to high velocity and red to low velocity. The average Sn velocity is 4.55 km/s. Thin black lines represent active faults.

by the variation of crustal thickness beneath the stations. For a mean crustal shear velocity of 3.6 km/s, a 1-s station delay implies increased crustal thickness of 6 km. Event delays are roughly similar to the distribution of station delays, showing the effect of thick crust in the western region and thin crust in the east. Because the event delays depend not only on crustal thickness, but also on the event depths, the event delays show significant variability because of uncertainty in event depth determination.

[22] The standard deviation of traveltime residuals for Sn decreased from 3.3 to 2.55 s after inversion. The same checkerboard test that was used for our Pn analysis was used to assess the resolution of the Sn velocity. Gaussian noise with a standard deviation of 2.55 s was added to synthetic traveltimes. The tests indicate that  $4^\circ \times 4^\circ$  cells can be resolved for most of the region modeled (Figure 11a). For some regions having dense ray coverage, such as the Tarim and Sichuan basins, the resolved cells are as small as  $3^\circ \times 3^\circ$  (Figure 11b).

[23] Overall, the Sn lateral velocity variation is consistent with that of Pn velocity, indicating that Sn and Pn velocities are affected by common factors such as temperature and pressure. A major difference between Sn and Pn velocity variations is observed in North China where the amplitudes

of low Sn velocity variations are greater than those of Pn velocity. Since S velocity is more sensitive to temperature than P velocity [Goes *et al.*, 2000], this may indicate that the sub-Moho temperature is high in North China.

[24] Sun and Toksöz [2006] also obtained Sn velocity through one-dimensional Monte-Carlo inversion [Sun *et al.*, 2004] and three-dimensional tomography [Sun, 2005]. As with our analysis, they found that low Sn velocity exists in eastern China and high Sn velocity exists in the Ordos, Tarim, Qaidam, and Sichuan basins. The two models differ, however, in eastern Tibet, where Sun and Toksöz [2006] obtained a high Sn anomaly there, but we did not. This discrepancy might be caused by the over-averaging effect of the one-dimensional inversion. The high Sn found in eastern Tibet included the effect of high velocity beneath Qaidam and Sichuan basins because very large windows were selected to provide averaged one-dimensional profiles in Sun *et al.*'s Monte-Carlo inversion.

## 5. Discussion

### 5.1. Relationship Between Velocity and Tectonic Activity

[25] The Pn and Sn velocity variations we observed are correlated with levels of tectonic activity (Figures 5 and 9). High velocity is seen in stable, older regions showing little



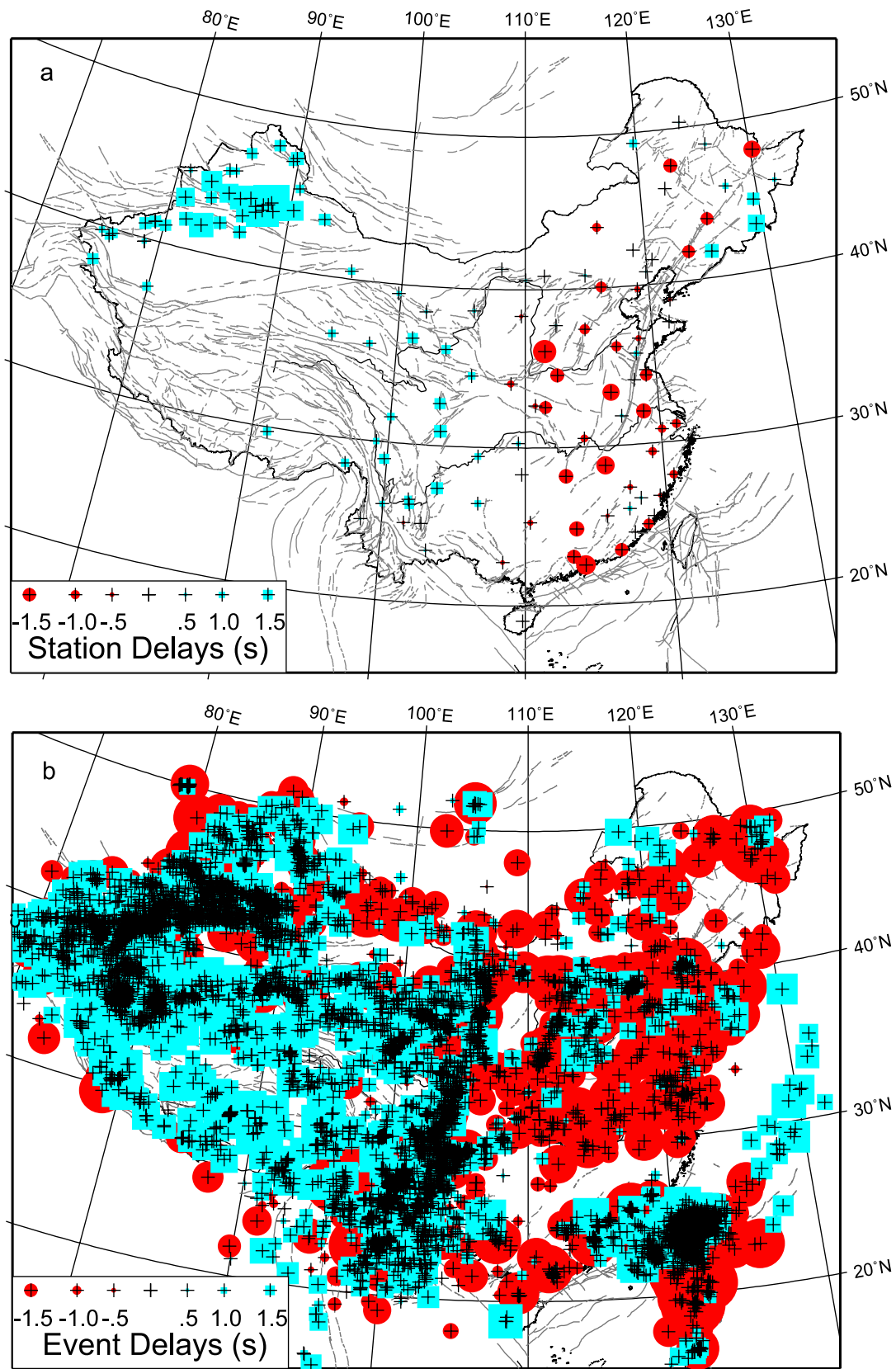


**Figure 10.** (a) Station delays and (b) event delays for Sn traveltimes. The symbols are the same as in Figure 7.

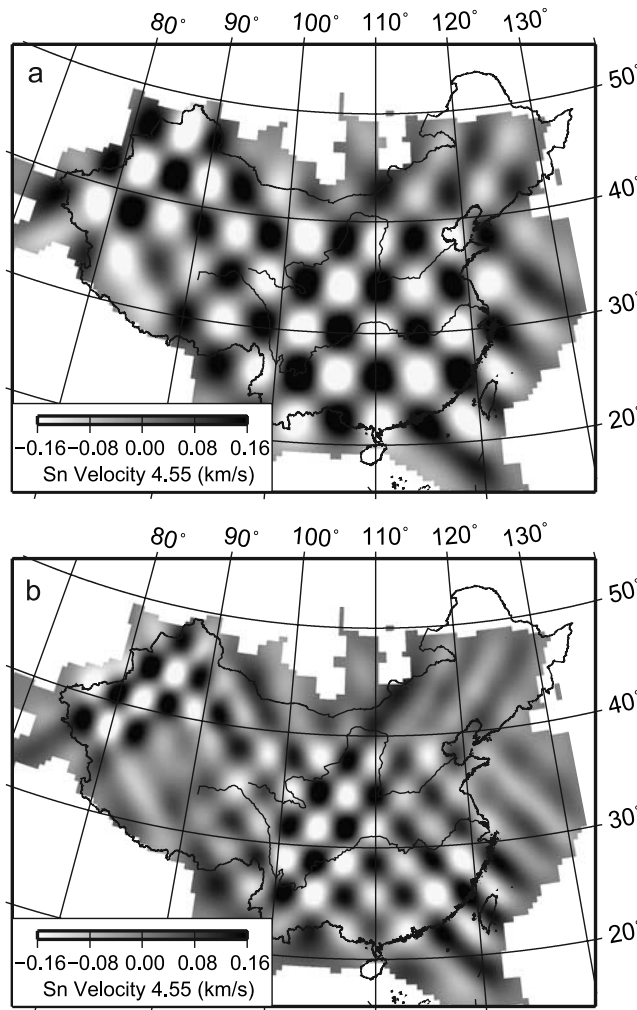


**Figure 11.** Checkerboard tests for Sn velocity resolutions of (a)  $4^\circ \times 4^\circ$  and (b)  $3^\circ \times 3^\circ$ .

recent tectonic activity, such as old basins and cratons, and low velocity often is found in tectonically active regions, such as modern orogenic belts, extensional basins, and volcanic areas.

[26] In the large basins underlain by cratons, such as the Tarim, Junggar, Turpan-Hami, Qaidam, and Sichuan basins, and the Ordos Craton, the velocity is abnormally high. These are cold and old stable geological blocks having insignificant tectonic deformation and weak magmatic activity. The active orogenic belts in western China around these basins, however, exhibit low Pn and Sn velocities, possibly related to strong tectonic deformation. Low velocities throughout the North-China extensional basin [Ye *et al.*, 1985] may be related to crustal thinning and concomitant magmatic activity. Low velocity anomalies along the Shanxi Rift, the Tanlu Fault, and the North-South Seismic Zone may also be associated with strong tectonic activity.

[27] Pn and Sn low velocity regions are generally consistent with the distribution of Cenozoic volcanoes and magmatic rocks [Ma, 1989; Liu, 1999]. There are 29 large Cenozoic volcanoes (or occurrences of volcanic/magmatic rocks) in China (Figure 12), almost all of which reside in low Pn and Sn velocity regions except those marginal regions

of the model having low resolution (1, 4, 5, 6, and 26). Pn and Sn velocity in volcanic regions 20 and 25 (Figure 12) are near average velocity. The consistency implies that the Pn and Sn velocities are closely related to magmatic activity and the temperature in the uppermost mantle.

## 5.2. Validation of Pn Anisotropy

[28] To confirm the anisotropy results presented in this paper, we examined the variations of apparent Pn velocity with azimuth within several selected regions. We calculated the apparent Pn velocity perturbation  $\Delta V$  by the formula

$$\Delta V = -\bar{V}_{\text{mean}}^2 \times \Delta S = -\bar{V}_{\text{mean}}^2 \times t_{\text{res}} / \Delta,$$

where  $t_{\text{res}}$  is the traveltime residual,  $\Delta$  is the epicentral distance,  $\Delta S$  represents the slowness perturbation, and  $\bar{V}_{\text{mean}}$  is the average velocity 8.05 km/s.

[29] We selected 2184 event-station pairs in the Tarim Basin ( $77^\circ$ – $86^\circ$ E,  $37^\circ$ – $42^\circ$ N) and plotted a rose diagram of Pn apparent velocity versus azimuth (Figure 13a). The black line in the rose diagram represents smoothed Pn apparent velocity obtained by averaging over the adjacent 10 points. We then averaged the apparent Pn velocity perturbations in 10-degree bins of azimuth to obtain the results presented in Figure 13b. We found that the fast direction and magnitude of Pn apparent velocity perturbations are WNW and about 0.2 km/s, respectively, which is consistent with the tomographic result (region b in Figure 6). We also found the average Pn apparent velocity in the Tarim Basin to be higher than the average Pn velocity throughout China. The results of Liang *et al.* [2004] do not show clear anisotropy in the western Tarim Basin, perhaps because of sparse ray coverage in their data set. We have obtained much denser ray coverage by including data from the Xinjiang regional seismic network.

[30] We also calculated Pn apparent velocity in two other regions. One is the eastern Tibetan Plateau between EHS and the Sichuan Basin ( $96^\circ$ – $104^\circ$ E,  $25^\circ$ – $31^\circ$ N), where the direction of fast apparent Pn velocity is NW-SE (Figures 13c and 13d), consistent with the inverted fast velocity direction (region e in Figure 6). The other region is the eastern Qaidam Basin ( $95^\circ$ – $102^\circ$ E,  $32^\circ$ – $38^\circ$ N), where the average fast apparent Pn velocity exhibits two dominant directions: a well-defined direction pointing nearly E-W and a less distinct direction near NE-SW (Figure 13e and 13f), while the fast velocity direction of the inverted anisotropy turns from NE-SW to near E-W (region d in Figure 6). The same fast directions were obtained in these two regions by Liang *et al.* [2004].

[31] We conclude from these comparisons that the inverted anisotropy is reliable at least in regions having dense ray coverage. Along the boundary of our study region, the uncertainty of Pn anisotropy is large due to sparse ray coverage and resulting poor azimuthal coverage.

## 5.3. Material Movement in the Uppermost Mantle Beneath the Tibetan Plateau

[32] Pn velocity anisotropy is generally thought to be associated with the preferred alignment of olivine crystals due to creep of material in the uppermost mantle [e.g., Ribe, 1992]. Anisotropy has a close relationship with stress and plate movement. We compare the fast direction of



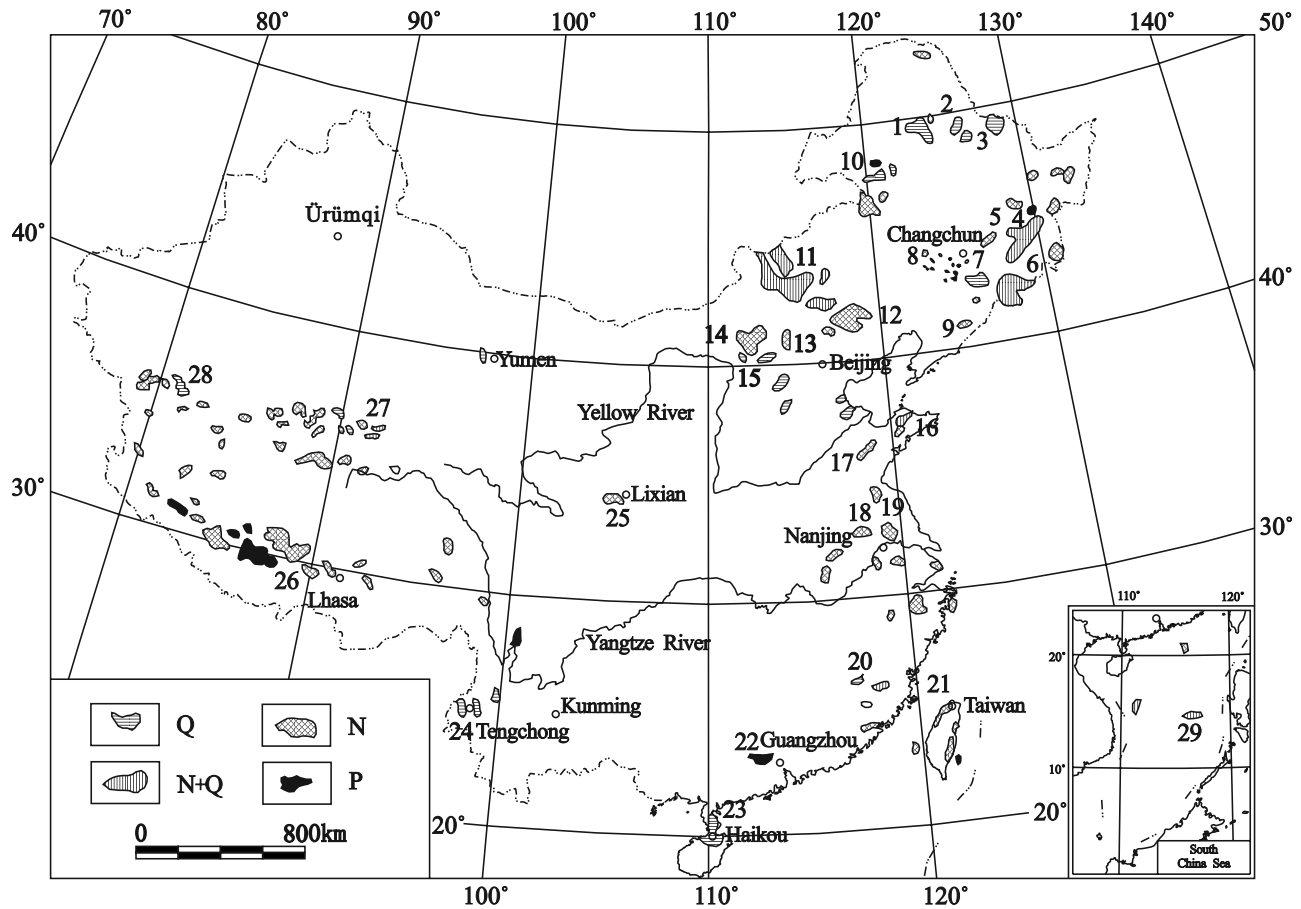


**Figure 12.** Distribution of Cenozoic volcanoes (or volcanic/magmatic rocks) [after Liu, 1999], the numbers indicate places names of Cenozoic volcanoes or magmatic rocks as following: 1. Nuomin, 2. Keluo, 3. Wudalianchi, 4. Jingbohu, 5. Yitong, 6. Changbaishang, 7. Longgang, 8. Shuangliao, 9. Kuandian, 10. Harlahar, 11. Dalainuoer, 12. Weichang, 13. Hannuoba, 14. Jining, 15. Datong, 16. Penglai, 17. Linqu, 18. Jiashan, 19. Liuhe, 20. Mingxi, 21. Taiwan, 22. Sanshui, 23. Leiqiong, 24. Tengchong, 25. Lixian, 26. Gandese, 27. Hoh Xil, 28. West Kunlun, 29. South China Sea.

anisotropy to the principal compressive stress and direction of crustal movement (Figure 14). The maximum principal compressive stress ( $\sigma_1$ ) has been deduced from seismic moment tensors and focal mechanism solutions by Xu [2001]. The crustal movement can be measured by GPS [Wang *et al.*, 2001; Li *et al.*, 2003]. Although the principal stresses calculated this way describe the stress state in the upper and middle crust, they may generally represent the stress state of the lithosphere on a regional scale.

[33] In several regions with well-constrained large anisotropy, the fast Pn velocity directions are consistent with the directions of maximum principal compressive stress as well as directions of crustal movement determined from GPS. For example, in the regions around the East Himalaya Syntax (Figure 14), the directions of maximum principal compressive stress and the directions of crustal movement curl clockwise at the syntax, while the fast directions of anisotropy also generally rotate around the syntax. In western China, i.e., the Tarim, Tianshan, and Junggar regions, the crustal movement direction is NS. The  $\sigma_1$  direction also is near NS with a small swerve in the Tarim, and the Pn anisotropy direction is generally near NS also, with a larger swerve there (Figure 14). The consistency of

the three directions shows that the movement and deformation of the crust and upper mantle in these regions have the same pattern and are thus controlled by the same sources, India-Eurasia collision and mantle convection.

[34] In several other regions, however, the Pn anisotropy direction is almost perpendicular to both  $\sigma_1$  and the direction of crustal movement. For example, beneath the India-Eurasia collision zone of the Tibetan Plateau, the fast Pn anisotropy direction is parallel to the collision arc, and nearly perpendicular to the direction of maximum compression and crustal movement (Figure 14). A similar result was obtained by Liang *et al.* [2004]. The area of anisotropy in the collision zone is about  $10^\circ \times 5^\circ$ , which is much larger than the  $4^\circ$ – $5^\circ$  resolution in this region, thus the tomographic anisotropy can be considered reliable. This anisotropy may be generated under conditions closer to pure shear in a strong collision zone. Under pure shear deformation, the olivine b axes tend to align parallel to the direction of maximum compression [Christensen, 1984; Nicolas and Christensen, 1987; Karato, 1989; Chastel *et al.*, 1993]. The same observation holds for the NW edge of China, in the Qaidam Basin and Yunnan-Guizhou Plateau. In this area, we may be seeing the effect of pure shear deformation, although

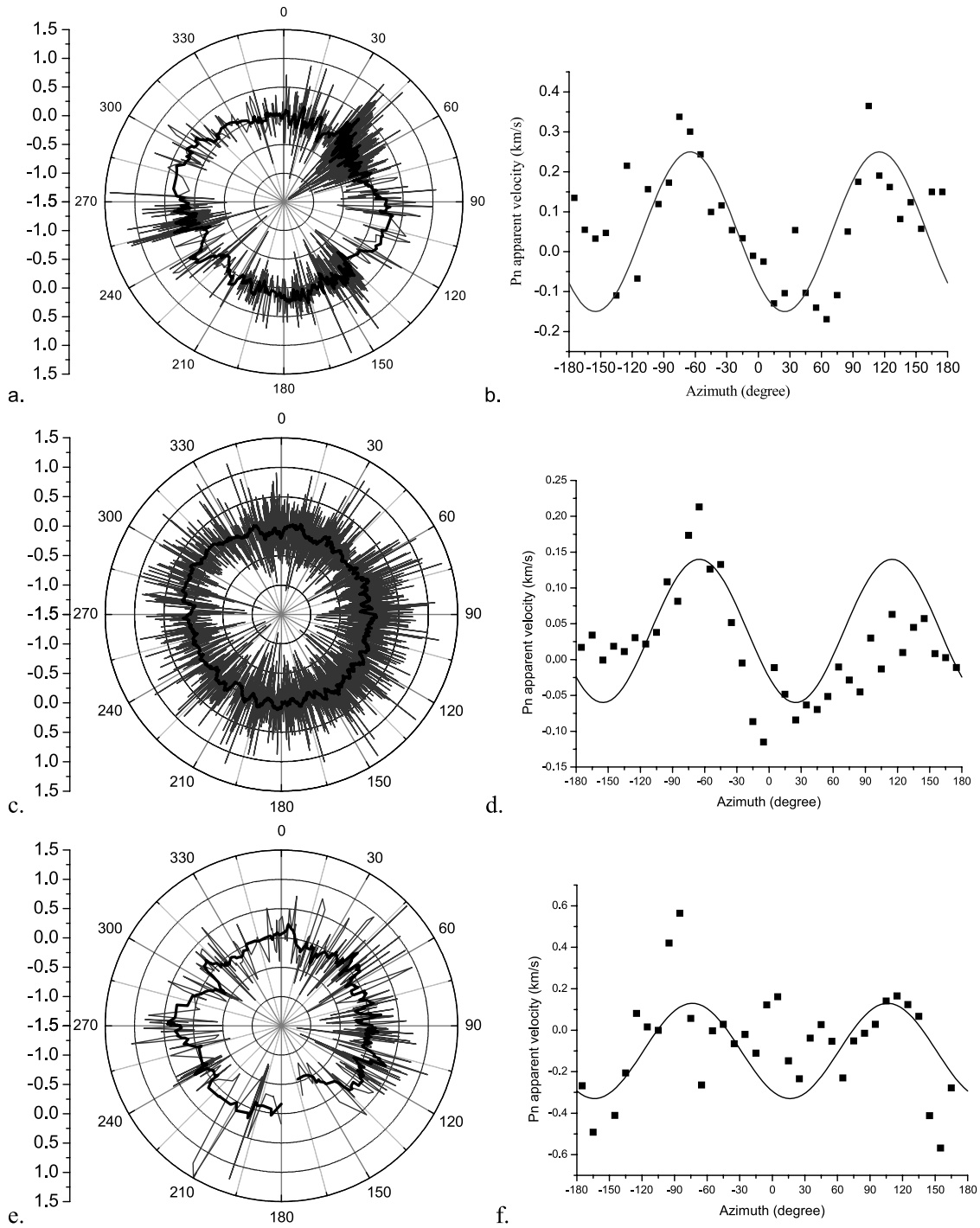


**Figure 13.** Anisotropy of apparent Pn velocity beneath the Tarim Basin, eastern Tibetan Plateau, and eastern Qaidam Basin. (a) Rose-lobed diagram of Pn apparent velocity in the Tarim Basin. The black line in the rose-lobed diagram represents smoothed Pn apparent velocity obtained by averaging the adjacent 10 points. (b) Pn apparent velocity perturbation varying with azimuth. The data points represent average velocity perturbation every 10 degrees, and the solid line is the sinusoidal trend line. Figure 13c and 13d and Figure 13e and 13f are same as Figure 13a and 13b but represent values found beneath the eastern Tibetan Plateau and eastern Qaidam Basin, respectively.

here there are large uncertainties due to the sparse ray and azimuthal coverage; hence, our interpretation is less certain.

[35] On the basis of Pn anisotropy, stress, and GPS observations, we can divide the Tibetan Plateau into three regions to describe material movement in the uppermost

mantle. In the eastern Tibetan Plateau, the material flows clockwise around the East Himalaya Syntax based both on direction of anisotropy and GPS [Wang *et al.*, 2001]. In the western Tibetan Plateau and Tarim, anisotropy implies that the material in the uppermost mantle flows toward the

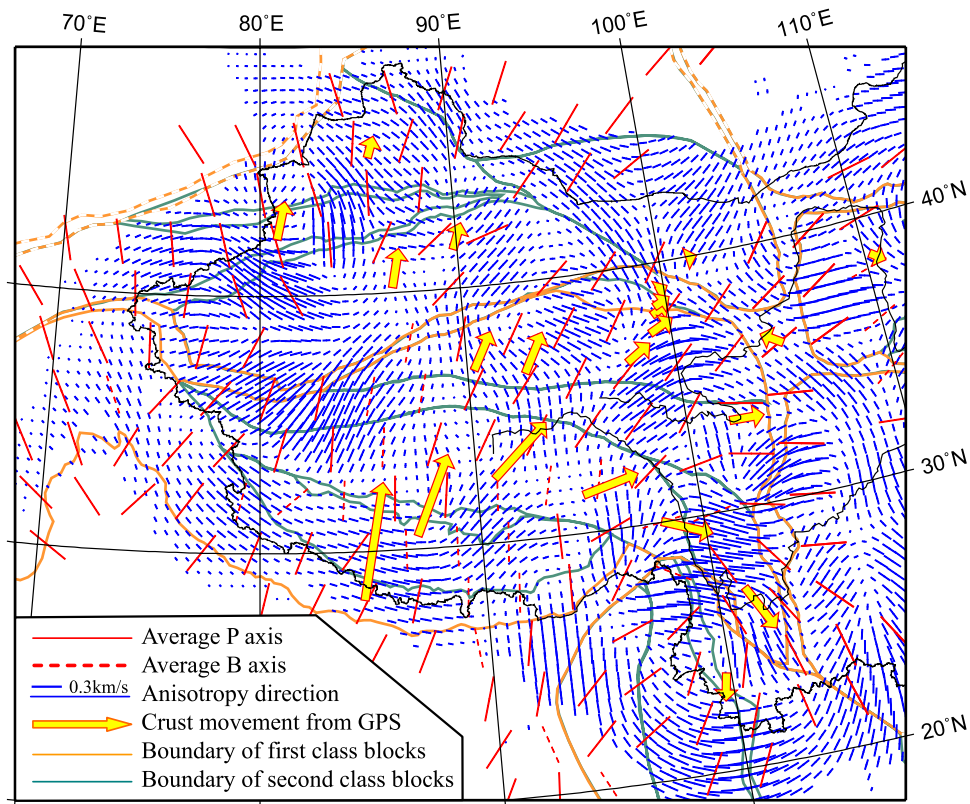


**Figure 14.** Anisotropy, maximum compressive stress, and crustal movement within and around the Tibetan Plateau. Red lines represent average orientation of maximum compressive stress [Xu, 2001] obtained from earthquake focal mechanisms. A dashed line (B axis) is plotted when the P axis is vertical. Yellow arrows represent crustal movement direction of active blocks from GPS [Li *et al.*, 2003]. The boundaries of the blocks are reproduced from Zhang *et al.* [2003].

NE and then turns to NW. In the collision zone, although the absolute material movement is North-South based on GPS studies [Wang *et al.*, 2001], relative movement or deformation of the material within the collision zone appears to be East-West, as indicated by the direction of anisotropy. The resulting extension may give rise to the rift valleys and normal faults having N-S orientations in southern Tibet.

[36] Why would the material in the uppermost mantle move in Tibet? The answer lies in these factors: power source, property of material, and boundary conditions. It is clear that the dynamic power source comes from the collision between the Indian and Eurasian plates. Low Pn and Sn velocities in central Tibet indicate partial melt there, supported also by observations of inefficient Sn propagation [Ni and Barazangi, 1984], low P wave velocity [Tilmann *et al.*, 2003], high Poisson's ratio [Owens and Zandt, 1997], and low resistivity from magnetotelluric data [Unsworth *et al.*, 2005]. The boundary condition is that there are stable blocks around the Tibetan Plateau such as the Tarim, Qaidam, Ordos, and Sichuan basins, having high Pn and Sn velocity. When the Indian plate collided with the Eurasia plate, the molten material was forced upward and displaced outwards [Royden *et al.*, 1997]. The upward flow may give rise to plateau uplift, while the lateral flow might easily change direction when obstructed by the surrounding stable blocks. Part of the lateral flow has curved around the East

Himalaya Syntax, while the remaining material has been diverted northwestward beneath the Tarim Basin.

## 6. Conclusion

[37] We have imaged the Sn velocity structure and re-imaged the Pn velocity structure of China using a large data set augmented with additional Pn traveltime data from provincial seismic networks. We discussed in detail the relationship between velocity variations and tectonic activity, and the relationship between velocity anisotropy and maximum principal compressive stress and present-day crustal motion. We have arrived at the following conclusions:

[38] 1. The average Pn and Sn velocity are 8.05 and 4.55 km/s, respectively. The maximum velocity perturbations are about 3–4%.

[39] 2. Lateral Pn velocity variation is generally consistent with the pattern of the Sn velocity variation. In general, these velocities are low in eastern China and high in western China. Remarkably high Pn and Sn velocities are found beneath the Tarim, Junggar, Turpan-Hami, eastern Qaidam and Sichuan Basins, and the region south of the Sichuan Basin. Beneath the Ordos Craton and Taiwan Straits region, Pn and Sn velocities are also slightly high. Low velocities are seen mainly throughout North China. In the central Tibetan Plateau and the North-South Seismic Zone, Pn and Sn velocities are relatively low.



[40] 3. Pn and Sn velocity variations are related to tectonic activity. High velocities are seen in stable, older regions showing little recent tectonic activity, such as old basins and cratons (for example, the Tarim, Junggar, Turpan-Hami, Qaidam and Sichuan basins, and the Ordos Craton), and low velocities often are found in tectonically active regions, such as modern orogenic belts, extensional basins and volcanic areas (for example, the North-China basin, Shanxi Rift, the Tanlu Fault, and the North-South Seismic Zone). Low Pn and low Sn velocity regions are generally consistent with the surface distribution of Cenozoic magmatic rocks.

[41] 4. In the Tarim and central China, where we observe high anisotropy and we have the benefit of dense ray coverage, we can resolve fast Pn velocity directions that are consistent with the directions of maximum principal compressive stress as well as with directions of crustal movement determined from GPS. Beneath the India-Eurasia collision zone, the Pn anisotropy direction is parallel to the collision arc and nearly perpendicular to both the direction of maximum compression and to crustal movement resulting from pure shear deformation. Both the velocity variations and anisotropy indicate that the Tibetan Plateau was extruded and the mantle material beneath the plateau has flowed around the East Himalaya Syntax, while the remaining material was diverted northwestward beneath the Tarim Basin. This movement arises from the collision between the Indian and Eurasian plates, and the presence of melt material beneath the central plateau, confined by stable blocks surrounding it.

[42] **Acknowledgments.** We sincerely thank Thomas M. Hearn for providing tomographic codes. We also thank Francis T. Wu, Scott Phillips, Anca C. Rosca, and Burke Minsley for their valuable comments in improving the manuscript. We are greatly indebted to two reviewers and the Associate Editor for their insightful comments. This research was supported jointly by the National Natural Science Foundation of China (40674031, 40674073 and 40238059), the Key Project of the National Basic Research Development Plan (G19980407/95-13-02-05), the Talent Project of the CAS (Chinese Academy of Sciences), the Knowledge Innovating Project of the CAS (Grant kzc3-sw-143), the Earth Resources Laboratory at MIT (under contract number FA8718-04-C-0018), and the US Department of Energy (LANL publication LAUR-06-6595).

## References

- Bannister, S. C., B. O. Ruud, and E. S. Husebye (1991), Tomographic estimates of sub-Moho seismic velocities in Fennoscandia and structural implications, *Tectonophysics*, **189**, 37–53.
- Barazangi, M., and J. Ni (1982), Velocities and propagation characteristics of Pn and Sn beneath the Himalayan arc and Tibetan plateau: Possible evidence for underthrusting of Indian continental lithosphere beneath Tibet, *Geology*, **10**, 179–185.
- Chastel, Y., P. Dawson, H. Wenk, and K. Bennett (1993), Anisotropic convection with implications for the upper mantle, *J. Geophys. Res.*, **98**, 17,757–17,771.
- Christensen, N. I. (1984), The magnitude, symmetry and origin of upper mantle anisotropy based on fabric analyses of ultramafic tectonites, *Geophys. J.R. Astron. Soc.*, **76**, 89–111.
- Di, X. L., Z. X. Yuan, and Y. Y. Ding (1999), Seismic velocity image of Moho discontinuity beneath the Weihe fault depression and its adjacent areas obtained by inversion of travel-time data of Sn waves, *Northwest. Seismol. J.*, **21**, 178–182, (in Chinese).
- Ding, Z. F., R. S. Zeng, and F. T. Wu (1993), The Pn wave velocities and the relief of Moho in the Tibetan Plateau, *Acta Seismol. Sin.*, **6**, 317–325.
- Goes, S., R. Govers, and P. Vacher (2000), Shallow mantle temperatures under Europe from P and S wave tomography, *J. Geophys. Res.*, **105**, 11,153–11,169.
- Hearn, T. M. (1996), Anisotropic Pn tomography in the western United States, *J. Geophys. Res.*, **101**, 8403–8414.
- Hearn, T. M. (1999), Uppermost mantle velocities and anisotropy beneath Europe, *J. Geophys. Res.*, **104**, 15,123–15,139.
- Hearn, T. M., and J. Ni (1994), Pn velocities beneath continental collision zones: The Turkish-Iranian plateau, *Geophys. J. Int.*, **117**, 273–283.
- Hearn, T. M., S. Wang, J. F. Ni, Z. Xu, Y. Yu, and X. Zhang (2004), Uppermost mantle velocities beneath China and surrounding regions, *J. Geophys. Res.*, **109**, B11301, doi:10.1029/2003JB002874.
- Karato, S. I. (1989), Seismic anisotropy: Mechanisms and tectonic implications, in *Rheology of Solids and of the Earth*, pp. 393–422, edited by S. Karato and M. Toriumi, Oxford Sci., New York.
- Levshin, A. L., M. H. Ritzwoller, M. P. Barmin, A. Villasenor, and C. A. Padgett (2001), New constraints on the arctic crust and uppermost mantle: surface wave group velocities, Pn, and Sn, *Phys. Earth Planet. Int.*, **123**, 185–204.
- Li, Q., R. F. Liu, A. L. Du, and M. L. Yang (1994), Seismic tomography of Xinjiang and adjacent region, *Acta Geophys. Sin.*, **37**, 311–320, (in Chinese).
- Li, S., and W. Mooney (1998), Crustal structure of China from deep seismic sounding profiles, *Tectonophysics*, **288**, 105–113.
- Li, Y. X., et al. (2003), Movement and strain conditions of active blocks in the Chinese mainland. Science in China (Series D), **33**(Supp.), 65–81, in Chinese.
- Liang, C., X. Song, and J. Huang (2004), Tomographic inversion of Pn travel times in China, *J. Geophys. Res.*, **109**, B11304, doi:10.1029/2003JB002789.
- Liu, F. T., K. X. Qu, H. Wu, Q. Li, J. H. Liu, and G. Hu (1989), Seismic tomography of the Chinese continent and adjacent region, *Chin. J. Geophys.*, **32**, 281–291, (in Chinese).
- Liu, J. Q. (1999), *Volcanos in China*, Science press, Beijing. (in Chinese)
- Liu, F., J. Liu, D. Zhong, J. He, and Q. You (2000), The subducted slab of Yangtze continental block beneath the Tethyan orogen in western Yunnan, *Chin. Sci. Bull.*, **45**, 466–471.
- Liu, J., F. Liu, J. He, H. Chen, and Q. You (2001), Study of seismic tomography in Panxi paleorift area of southwestern China, *Sci. China, Ser. D: Earth Sci.*, **44**, 277–289.
- Liu, Y., X. Chang, J. He, F. Liu, and H. Sun (2005), Three-dimensional velocity images of the crust and upper mantle beneath the North-south zone in China, *Bull. Seismol. Soc. Am.*, **95**(3), 916–925.
- Ma, X. Y. (Eds.) (1989), *Lithospheric Dynamics Atlas of China*, China Cartographic Publishing House, Beijing. (in Chinese)
- McNamara, D. E., W. R. Walter, T. J. Owens, and C. J. Ammon (1997), Upper mantle velocity structure beneath the Tibetan Plateau from Pn travel time tomography, *J. Geophys. Res.*, **102**, 493–505.
- Mele, G., A. Rovelli, D. Seber, T. M. Hearn, and M. Barazangi (1998), Compressional velocity structure and anisotropy in the uppermost mantle beneath Italy and surrounding regions, *J. Geophys. Res.*, **103**, 12,529–12,543.
- Molnar, P., and P. Tapponnier (1975), Cenozoic tectonics of Asia: Effects of a continental collision, *Science*, **198**, 419–426.
- Molnar, P., P. England, and J. Martinod (1993), Mantle dynamics, uplift of the Tibetan Plateau, and the Indian monsoon, *Rev. Geophys.*, **31**, 357–386.
- Nelson, K. D., et al. (1996), Partially molten middle crust beneath southern Tibet: Synthesis of project INDEPTH results, *Science*, **274**, 1684–1688.
- Ni, J., and M. Barazangi (1984), Seismotectonics of the Himalaya Collision Zone: Geometry of the underthrusting Indian Plate beneath the Himalaya, *J. Geophys. Res.*, **89**, 1147–1164.
- Nicolas, A., and N. I. Christensen (1987), Formation of anisotropy in upper mantle peridotites: A review, in *Composition, Structure and Dynamics of the Lithosphere-Athenosphere System*, *Geodyn. Ser.*, vol. 16, edited by K. Fuchs and C. Froidevaux, pp. 111–123, AGU, Washington, D.C.
- Nolet, G., C. Coutlee, and R. Clouser (1998), Sn velocities in western and eastern North America, *Geophys. Res. Lett.*, **25**, 1557–1560.
- Owens, T. J., and G. Zandt (1997), Implications of crustal property variations for models of Tibetan plateau evolution, *Nature*, **387**, 37–43.
- Pei, S. P., Z. H. Xu, S. Y. Wang, and T. M. Hearn (2002), Pn velocity tomography in Xinjiang, China, and adjacent regions, *Chin. J. Geophys.*, **45**, 217–224.
- Pei, S. P., Z. H. Xu, and S. Y. Wang (2004a), Discussion on origin of Pn velocity variation in China and adjacent region, *Acta Seismol. Sin.*, **17**, 1–11.
- Pei, S. P., Z. H. Xu, and S. Y. Wang (2004b), Sn wave tomography of the uppermost mantle beneath the China continent and adjacent regions, *Chin. J. Geophys.*, **47**, 278–284.
- Phillips, W. S., C. A. Rowe, and L. K. Steck (2005), The use of interstation P wave arrival time differences to account for regional path variability, *Geophys. Res. Lett.*, **32**, L11301, doi:10.1029/2005GL022558.
- Ribe, N. M. (1992), On the relation between seismic anisotropy and finite strain, *J. Geophys. Res.*, **97**, 8737–8747.



- Rowley, D. B. (1996), Age of initiation of collision between India and Asia: A review of stratigraphic data, *Earth Planet. Sci. Lett.*, **145**, 1–13.
- Royden, L. H., B. C. Burchfiel, R. W. King, E. Wang, Z. L. Chen, F. Shen, and Y. P. Liu (1997), Surface deformation and lower crustal flow in eastern Tibet, *Science*, **276**, 788–790.
- Silver, P. G. (1996), Seismic anisotropy beneath the continents: Probing the depths of geology, *Annu. Rev. Earth Planet. Sci.*, **24**, 385–432.
- Sun, Y. (2005), P- and S-wave tomography of the crust and uppermost mantle in China and surrounding Areas, Ph.D. thesis, Massachusetts Institute of Technology, Boston.
- Sun, Y., and M. N. Toksöz (2006), Crustal structure of China and surrounding regions from P wave traveltime tomography, *J. Geophys. Res.*, **111**, B03310, doi:10.1029/2005JB003962.
- Sun, Y., X. Li, S. Kuleli, F. D. Morgan, and M. N. Toksöz (2004), Adaptive moving window method for 3D P-velocity tomography and its application in China, *Bull. Seismol. Soc. Am.*, **94**, 740–746.
- Sun, Y., M. N. Toksöz, and F. D. Morgan (2006), The layered crustal structure in China, *Bull. Seismol. Soc. Am.*, in revision.
- Tapponnier, P., G. Peltzer, A. Y. Le Dain, R. Armijo, and P. Cobbold (1982), Propagating extrusion tectonics in Asia: New insights from simple experiments with plasticine, *Geology*, **10**, 611–616.
- Tilmann, F., J. Ni, and INDEPTH III Seismic Team (2003), Seismic imaging of the downwelling Indian lithosphere beneath central Tibet, *Science*, **300**, 1424–1427.
- Unsworth, M. J., A. G. Jones, W. Wei, G. Marquis, S. G. Gokarn, and J. E. Spratt (2005), Crustal rheology of the Himalaya and Southern Tibet inferred from magnetotelluric data, *Nature*, **433**, 78–81, doi:10.1038/nature04154.
- Wang, C., W. W. Chan, and W. D. Mooney (2003), Three-dimensional velocity structure of crust and upper mantle in southwestern China and its tectonic implications, *J. Geophys. Res.*, **108**(B9), 2442, doi:10.1029/2002JB001973.
- Wang, Q., et al. (2001), Present-day crustal deformation in China constrained by global positioning system measurements, *Science*, **294**, 574–577.
- Wang, S. Y., T. Hearn, Z. H. Xu, J. Ni, Y. X. Yu, and X. D. Zhang (2002), Velocity structure of uppermost mantle beneath China continent from Pn tomography, *Sci. China, Ser. D: Earth Sci.*, **45**, 143–150.
- Xu, Z. H. (2001), A present-day tectonic stress map for eastern Asia region, *Acta Seismol. Sin.*, **14**, 524–533.
- Xu, Y., F. T. Liu, J. H. Liu, and R. M. Sun (2001), Seismic tomography beneath the orogenic belts and adjacent basins of northwestern China, *Sci. China, Ser. D: Earth Sci.*, **44**, 468–480.
- Ye, H., K. M. Shedlock, S. J. Hellinger, and J. G. Sclater (1985), The north China basin: an example of a Cenozoic rifted intraplate basin, *Tectonics*, **4**, 153–169.
- Yin, A., and T. M. Harrison (2000), Geological evolution of the Himalayan-Tibetan orogen, *Annu. Rev. Earth Planet. Sci.*, **28**, 211–280.
- Zhang, P. Z., Q. D. Deng, G. M. Zhang, J. Ma, W. J. Gan, W. Min, F. Y. Mao, and Q. Wang (2003), Active tectonic blocks and strong earthquakes in the continent of China, *Sci. China, Ser. D: Earth Sci.*, **46**(Supp.), 13–24.
- Zhu, J., J. Cao, X. Cai, Z. Yan, and X. Cao (2002), High resolution surface wave tomography in east Asia and west Pacific marginal sea, *Chin. J. Geophys.*, **45**, 679–698.

X. Gao, H. Liu, S. Pei, and J. Zhao, Institute of Tibetan Plateau Research, Chinese Academy of Sciences, No. 18, Shunagqing Road, Haidian District, Beijing 100085, China. (peisp@itpcas.ac.cn)

C. A. Rowe, Los Alamos National Laboratory, Los Alamos, NM 87545, USA.

M. Nafi Toksöz and Y. Sun, Earth Resources Laboratory, Massachusetts Institute of Technology, Cambridge, MA, USA.

S. Wang and Z. Xu, Institute of Geophysics, China Earthquake Administration, Beijing 100081, China.

# $M_L$ Amplitude Tomography in North China

by Shunping Pei, Junmeng Zhao, Charlotte A. Rowe, Suyun Wang, Thomas M. Hearn,  
Zhonghuai Xu, Hongbing Liu, and Youshun Sun

**Abstract** We have selected 10,899  $M_L$  amplitude readings from 1732 events recorded by 91 stations, as reported in the Annual Bulletin of Chinese Earthquakes (ABCE), and have used tomographic imaging to estimate the lateral variations of the quality factor  $Q_0$  ( $Q$  at 1 Hz) within the crust of Northern China. Estimated  $Q_0$  values vary from 115 to 715 with an average of 415.  $Q_0$  values are consistent with tectonic and topographic structure in Eastern China.  $Q_0$  is low in the active tectonic regions having many faults, such as the Shanxi and Yinchuan Grabens, Bohai Bay, and Tanlu Fault Zone, and is high in the stable Ordos Craton.  $Q_0$  values are low in several topographically low-lying areas, such as the North China, Taikang-Hefei, Jiangnan, Subei-Yellow Sea, and Songliao basins, whereas it is high in mountainous and uplift regions exhibiting surface expressions of crystalline basement rocks: the Yinshan, Yanshan, Taihang, Qinlin, Dabie and Wuyi Mountains, and Luxi and Jiaoliao Uplifts. Quality-factor estimates are also consistent with  $Pn$ - and  $Sn$ -velocity patterns. High-velocity values, in general, correspond with high  $Q_0$  and low-velocity values with low  $Q_0$ . This is consistent with a common temperature influence in the crust and uppermost mantle.

## Introduction

Seismic travel-time tomography methods have enjoyed great success in the study of tectonic structure, largely because of large travel-time data sets that have been collected from regional event bulletins. Tomography can also be applied to seismic amplitude measurements; however, there are few calibrated data sets of adequate size in routine bulletins. One such data set is from the Annual Bulletin of Chinese Earthquakes (ABCE) compiled by the Institute of Geophysics of the China Earthquake Administration (IGCEA).

The ABCE amplitude data are collected for calculating event magnitudes for the  $M_L$ ,  $m_b$ ,  $m_B$ , and  $M_S$  magnitude scales. Over 100 stations of the Chinese network have been routinely reporting amplitudes for more than a decade. These data not only provide consistent magnitude information but are also valuable for studying regional variations in seismic attenuation.

A large body of research exists studying attenuation in China and surrounding regions using waveforms. Surface waves are often inverted for attenuation (e.g., Romanowicz *et al.*, 1995; Li *et al.*, 2000; Hong *et al.*, 2003; Gung and Romanowicz, 2004; Jemberie and Mitchel, 2004).  $Lg$  wave data have also been applied to attenuation tomography (e.g., Mitchell *et al.*, 1997; Phillips *et al.*, 2000, 2001, 2005; Cong *et al.*, 2003; Taylor *et al.*, 2003; Liu *et al.*, 2004a,b). Body waves have been collected to study attenuation (e.g., Lees and Lindley, 1994; Fan *et al.*, 2001; Rietbrock, 2001). Active seismic data are also useful for estimating attenuation

(e.g., Zhao *et al.*, 2003). Some interesting attenuation research focuses on the Tibetan Plateau (e.g., Feng and Zhou, 1985; Wu and Zeng, 1996; Reese *et al.*, 1999; Fan and Lay, 2002; Xie *et al.*, 2004).

Although some work has been conducted over broad areas to determine an averaged value or range of values for  $Q$ , little has been published using amplitude attenuation to produce detailed images of regionally varying  $Q$ . Tomographic inversion for regional imaging of  $Q$  has been performed in earlier studies using limited waveform data sets (e.g., Haberland and Rietbrock, 2001; Liu *et al.*, 2004b; Phillips *et al.*, 2005a). In this article, we present a study of tomographic attenuation in North China using a large set of amplitude data which were measured originally to calculate  $M_L$  magnitude of local and near regional events.

## Data

Chinese  $M_L$  amplitudes are made following standard seismological practice, and the derived magnitudes are computed using appropriate coefficients for China (ABCE practice). The  $M_L$  magnitude is calculated from the formula  $M_L = \log A\mu + R_6(\Delta)$ , where  $R_6 = 2.46$  for  $\Delta \leq 15$  km and  $R_6 = \log(\Delta) + 0.0013 \Delta + 1.27$  for  $15 \text{ km} < \Delta < 1000$  km (Ge *et al.*, 1987). These  $M_L$  amplitudes are the maximum amplitudes ( $A\mu$ ) measured on the horizontal components of short-period instruments and are used for ray

paths less than 1000 km in length. They are generally measured within the wave train that corresponds to the short-period  $Sg$  wave. At longer distances this is coincident with the longer period  $Lg$  wave train. These waves travel within the crustal wave guide and are thus sensitive to crustal variations in attenuation.

We used the  $M_L$  amplitude data of North China from the ABCE between 1985 and 1995. Most of the data are from seismograms recorded on short-period DD-1 seismographs, whose amplitude response has a frequency band of 0.5 to 20 Hz. At each station, the maximum amplitudes are the averages of the two horizontal components. Although no studies have been published regarding the uncertainties of these measurements, experienced seismologists who have used the data extensively estimate a maximum error for these values of less than 10% (Xu, 2006, personal comm.). This falls within the uncertainty estimates of our inversion, as discussed subsequently. The data were selected using the following criteria: each event was recorded by at least two stations; each station recorded at least five events; the reported period of the  $Sg$  wave at maximum amplitude is between 0.4 sec and 2.0 sec; epicentral distance is between 100 km and 800 km and event depth is less than 30 km. We finally obtained 10,899 amplitude readings from 1732 events recorded by 91 stations, as shown in Figure 1.

### Method

The attenuation of seismic waves between station  $i$  and source  $j$  can be estimated from the amplitude spectrum  $A_{ij}(f)$ , where  $f$  is the frequency at which the amplitude is measured. Amplitude is influenced by several factors: the size of the event, station site and instrument gain, geometrical spreading, and seismic attenuation. With these, the total amplitude can be written as (e.g., Sanders, 1993; Haberland and Rietbrock, 2001):

$$A_{ij}(f) = O_j(f)S_i(f)G_{ij}(R)B_{ij}(f,R), \quad (1)$$

where  $O_j(f)$  represents the event amplitude at frequency  $f$ ,  $S_i(f)$  is the site and instrument gain,  $G_{ij}(R)$  is the geometrical spreading factor at distance  $R$ , and  $B_{ij}(f)$  is seismic attenuation. The event radiation pattern has not been included. However, the maximum amplitude for  $Sg$  is produced by the interference of guided waves originating from many different sectors of the focal sphere, which tends to reduce the effect of the radiation pattern. This is reflected in the relative consistency of  $M_L$  magnitude estimates made at different seismic stations for the same event. We include frequency dependence in all terms except geometrical spreading.

We use a frequency-dependent source spectrum  $O(f)$  (Brune, 1970; Hanks and Wyss, 1972) that can be described by a long-period spectral level  $\Omega_0$  and the corner frequency  $f_c$  as  $O(f) = \Omega_0/(1 + (f^2/f_c^2))$ . The spectral level  $\Omega_0$  is in direct proportion to the seismic moment  $M_0$ . Frequency  $f$  and

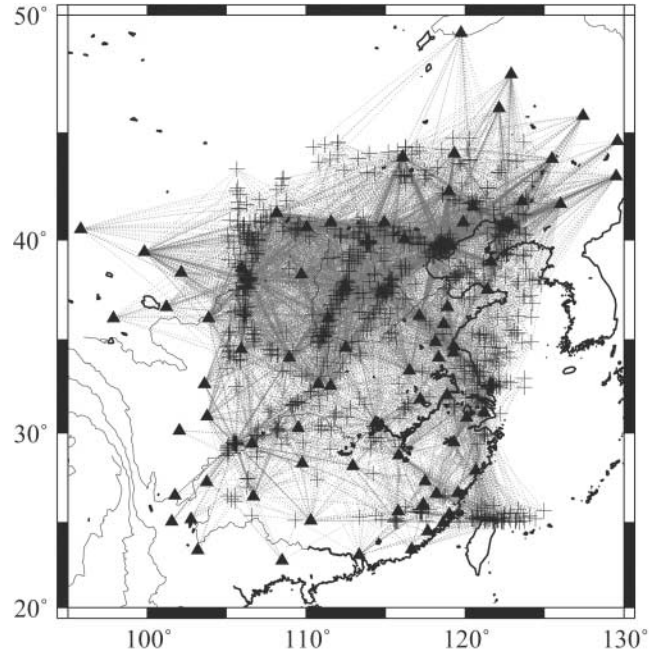


Figure 1. Distribution of ray paths, stations (triangles), and events (crosses). Gray lines represent rays from events to stations. We obtained 10,899 amplitude readings from 1732 events recorded by 91 stations.

corner frequency  $f_c$  can be considered as constants for one event, and frequency  $f$  corresponds to the frequency of the recorded waveform at maximum amplitude of  $Sg$ . We assume source spectrum  $O(f)$  is frequency independent for one event, although it is variable for different events.

The site response,  $S_i(f)$ , includes the effect of instrument gain and site amplification. The spectral dependence of  $S_i(f)$  is unknown, but the  $M_L$  bandwidth is small (0.5 Hz to 2 Hz) and the instrument response is reasonably flat within this range. We therefore assume  $S_i(f)$  is also independent of frequency.

The geometrical spreading (Castro *et al.*, 1996),  $G(R)$ , is considered to be proportional to  $(1/R)^k$ , where  $k$  is the geometrical spreading coefficient, which chiefly depends on wave type.  $k = 1.0$  implies spherical spreading of body waves and  $k = 0.5$  represents cylindrical spreading of  $Lg$  and surface waves.

The attenuation of  $S$  waves,  $B_{ij}(f)$ , is attributed to the quality factor  $Q$ . We assume a frequency-dependent  $Q$  and model it as an exponential decay (e.g., Sanders, 1993; Haberland and Rietbrock, 2001):

$$B_{ij}(f) = \exp\left(-\frac{\pi f R}{vQ}\right) = \exp(-cQ_0^{-1}R), \quad (2)$$

where  $c = \pi f^{1-\eta}/v$ ,  $Q = Q_0 f^\eta$ ,  $v$  is the  $S$ -wave velocity,  $Q_0$  and  $\eta$  are the  $S$ -wave  $Q$  at 1 Hz and its power-law frequency dependence, respectively.



Using equation (2) and taking the natural logarithm of equation (1) yields

$$Y_{ij} = \ln A_{ij}(f) - \ln G_{ij}(R) = a_i + b_j - Q_0^{-1}cR, \quad (3)$$

where the station term is  $a_i = \ln S_i(f)$  and event term is  $b_j = \ln O_j(f)$ . Equation (3) is very similar to the  $Pn$  travel-time equation (Hearn and Ni, 1994), thereby allowing us to resolve lateral variation of  $Q_0$  using the  $Pn$ -tomography method. We first estimate the average  $Q_0$  by fitting the line  $Y - cR$ . We assume that crustal  $S$ -wave velocity is homogeneous, so rays follow a straight line. If we discretize the crust into small 2D cubes of  $X$  km by  $Y$  km, then equation (3) can be rewritten as

$$Y_{ij} = a_i - b_j - \sum_k Q_0^{-1} c R_{ijk}.$$

By subtracting  $Y_{ij}$  from the average model (fitted line), a perturbation equation can be determined as follows:

$$\Delta Y_{ij} = \Delta a_i + \Delta b_j - \sum_k \Delta Q_0^{-1} c R_{ijk}. \quad (4)$$

Equation (4) can be recast as  $\mathbf{A}x = \mathbf{d}$ , where  $\mathbf{d}$  is the data vector,  $x$  is the vector of unknowns, and  $\mathbf{A}$  represents the model parameters. We apply damped LSQR (Paige and Saunders, 1982) with preconditioning to find the least-squares solution. Laplacian smoothing was applied in the inversion (Lees and Crosson, 1989).

## Results

A geometrical spreading coefficient ( $k$ ) of 1.0 is selected, because the standard deviation of the observation residuals ( $\Delta Y_{ij}$ ) in equation (4) is smaller for  $k = 1.0$  than  $k = 0.5$ . We take the average  $Q$ -decay coefficient ( $\eta$ ) of 0.5 (Liu *et al.*, 2003), and the crustal velocity ( $v$ ) of 3.6 km/sec, which was determined from  $Sg$ -wave travel times. By fitting a straight line to the data set of  $M_L$  amplitude ( $Y_{ij}$ ) versus reduced epicentral distance ( $cR$ ) according to equation (3), we obtain an average  $S$ -wave  $Q_0$  of 415 from the slope. We discretize the crust into blocks with cell dimensions of  $15' \times 15'$ , and adopt a damping constant of 1000. The  $S$ -wave  $Q_0$  lateral variations, the station term, and the event term perturbations are obtained by tomographic inversion of the  $M_L$  amplitude residuals after 60 iterations. Figure 2 shows the resulting lateral variations of the  $S$ -wave quality factor  $Q_0$ , which varies from 115 to 715. Blue corresponds to a high-quality factor (low attenuation) and red corresponds to a low-quality factor (highly attenuative crust).

The station term perturbations  $\Delta d_i$  and event term perturbations  $\Delta b_j$  are shown in Figure 3. Negative station term perturbations represent large attenuation beneath the station and positive perturbation represents small attenuation. A station term of 1.0 represents an amplitude gain factor of  $e^{1.0}$  or 2.73. A few stations have gains greater than this, but most

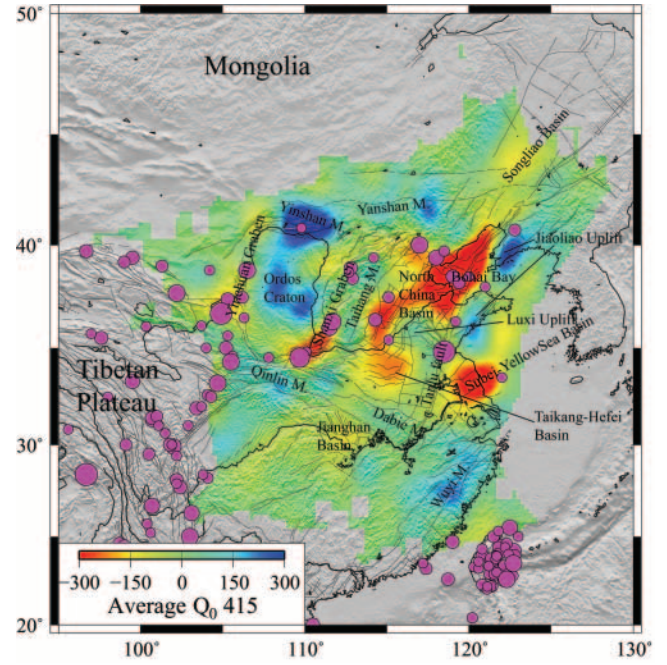


Figure 2. Imaged  $Q_0$  lateral variations. Blue corresponds to a high value and red corresponds to low. Average  $Q_0$  is 415 and varies from 115 to 715. Lines represent active faults; magenta circles represent earthquakes having magnitudes greater than 7.0 (Wang *et al.*, 2003).  $Q_0$  is low in the active tectonic areas with many faults, such as the Shanxi and Yinchuan Grabens, Bohai Bay, and Tanlu Fault Zone.  $Q_0$  is also low in several basins, including the North China Basin, Taikang-Hefei Basin, Jiangnan Basin, Subei-Yellow Sea Basin, and Songliao Basin. High  $Q_0$  occurs both in the stable Ordos Craton and in all mountains and uplift regions where crystalline basement appears at the surface, such as Yinshan, Yanshan, Taihang, Qinlin, Dabie and Wuyi Mountains, and Luxi and Jiaoliao Uplifts.

stations have gains near one. An event term of 1.0 represents a magnitude bias of  $\log_{10} e^{1.0}$  or 0.43 magnitude units. Events with gray squares have larger source sizes than the magnitudes indicated; the discrepancies are caused by the higher attenuation regions shown in Figure 2.

Residuals between  $-2$  and  $+2$  are used in the tomographic inversion. The standard deviation of the residuals is reduced from 0.67 to 0.41 after inversion (Fig. 4). Checkerboard tests were employed to analyze the spatial resolution of our solution. For the given ray paths in this study, theoretical amplitude residuals were calculated for input  $\Delta Q_0$  models with  $\pm 300$  in different square sizes. Gaussian random noise with zero mean and a standard deviation of 0.41 was added to the calculated residuals. Then the synthetic amplitude residuals were inverted to determine whether the squares could be resolved. Figure 5a, b shows checkerboard test models with cell size of  $2^\circ$  by  $2^\circ$  and  $1.5^\circ$  by  $1.5^\circ$ , respectively. The tests indicate that tomogram resolution is on the order of  $2^\circ$  in most regions and  $1.5^\circ$  in the North China



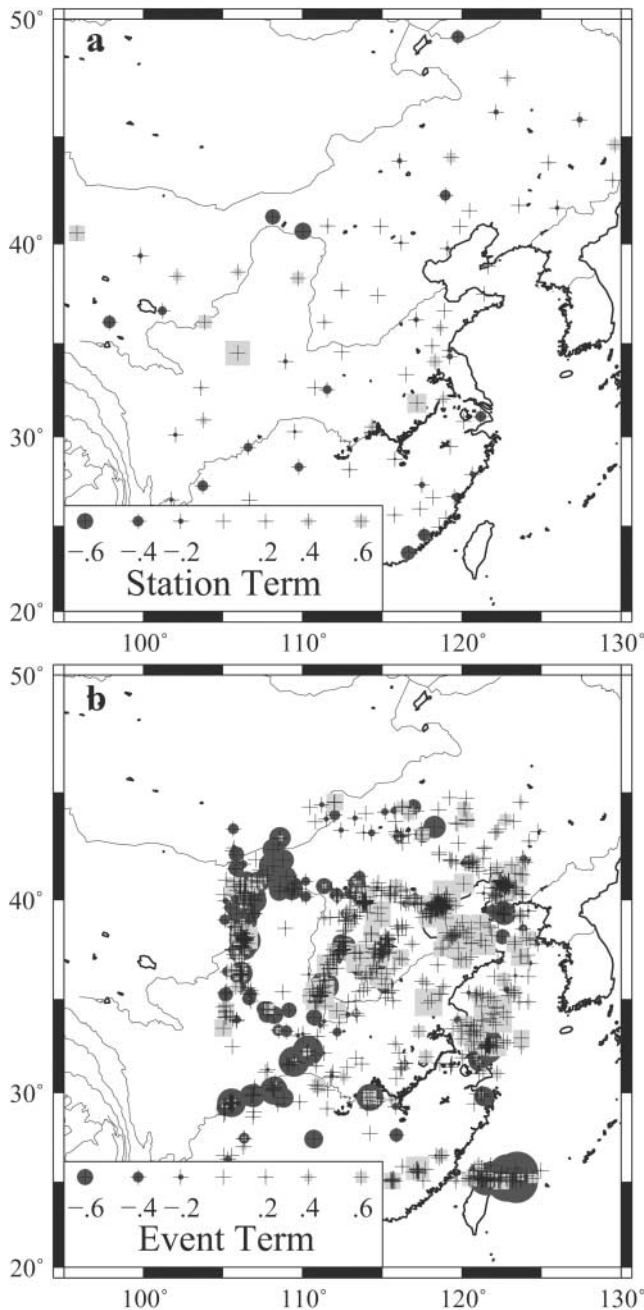


Figure 3. Station term perturbations  $\Delta a_i$  (a) and event term perturbations  $\Delta b_j$  (b). Negative station term perturbations represent large attenuation beneath the station, and positive perturbation represents small attenuation. A station term of 1.0 represents an amplitude gain factor of  $e^{1.0}$  or 2.73. A few stations have gains greater than this, but most stations have gains near one. An event term of 1.0 represents a magnitude bias of  $\log_{10} e^{1.0}$  or 0.43 magnitude units. Events with gray squares have larger source sizes than the magnitudes indicated; the discrepancy arises from rays passing through the higher attenuation regions shown in Figure 2.

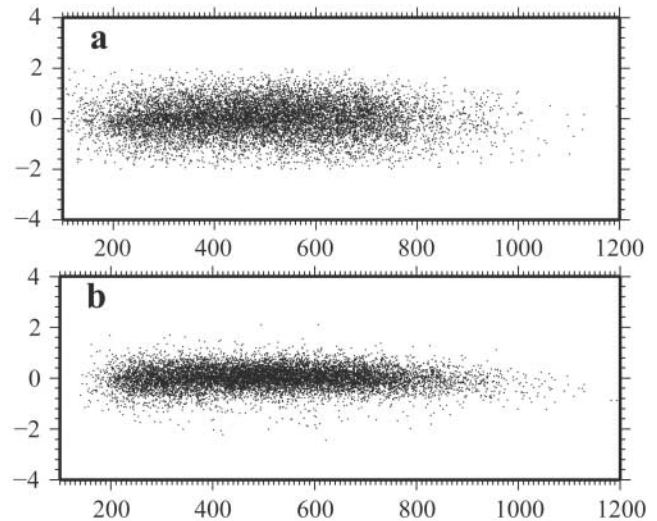


Figure 4. Distribution of amplitude residuals versus reduced epicentral distance ( $cR$ ) before inversion (a) and after inversion (b). Residuals between  $-2$  and  $+2$  are used in the tomographic inversion. The standard deviation of the residuals is reduced from 0.67 to 0.41 after inversion.

Basin. A random error of up to 0.41 can be effectively damped through application of these inversion parameters. Our checkerboard test indicates that the amplitude data errors of 10% have little influence on the resulting  $Q$  values.

### Discussion

Figure 2 shows that the quality factor is consistent with the tectonic structure in North China. Most large earthquakes occur in the low- $Q$  regions, consistent with an intuitive expectation of a strong correlation between greatest seismicity and highly attenuative crust. Low  $Q_0$  follows active tectonic areas having many faults, such as the Shanxi and Yinchuan Graben, Bohai Bay, and Tanlu Fault Zone, whereas  $Q_0$  is high in the stable Ordos Craton. This elevated attenuation can be attributed to the greater scattering and/or absorption in the fractured or faulted zone, compared with intact rocks. At the same time, the  $Q_0$  is consistent with topography in Eastern China.  $Q_0$  is low in some large basins such as the North China Basin, Taikang-Hefei Basin, Jiangnan Basin, Subei-Yellow Sea Basin, and the Songliao Basin. High  $Q_0$  occurs in most mountains and uplift regions where crystalline basement appears at the surface, including the Yinshan, Yanshan, Taihang, Qinlin, Dabao and Wuyi Mountains, Luxi and Jiaoliao Uplifts. Oil and/or gas were found in all basins mentioned previously, and Mesozoic and older rocks are ubiquitous in the mountain areas and uplift regions mentioned (Ma, 1989; Steinshouer *et al.*, 1999). Low  $Q_0$  observed in the basins may result from fluid-filled cracks and pores in the upper crust and deep sedimentary basins. The average depth of earthquakes in our research area is 13 km, and the densest ray coverage is thus within about 6–7 km

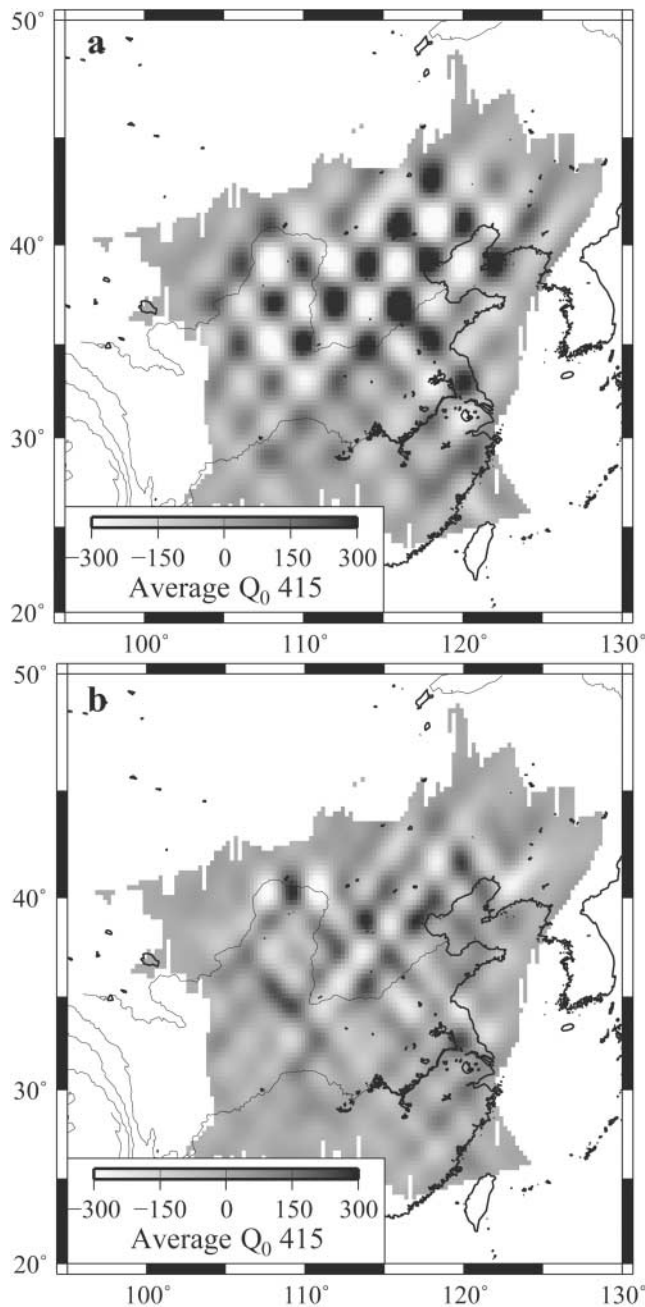


Figure 5. Output quality-factor model created from a checkerboard test model with cell sizes of  $2^\circ$  by  $2^\circ$  (a) and  $1.5^\circ$  by  $1.5^\circ$  (b). Gaussian random noise with zero mean and a standard deviation of 0.41 is added to the calculated residuals. The tests indicate that tomogram resolution is on the order of  $2^\circ$  in most regions and  $1.5^\circ$  in the North China basin.

depth, so the results of the inversion primarily address  $Q_0$  lateral variations within the uppermost 6–7 km of the crust, where oil is typically found. Temperature may also be an important factor in the  $Q_0$  pattern because the Earth's heat flow is high in basins and low in mountains and uplift regions in eastern China (Hu *et al.*, 2001; Wang *et al.*, 2003).

High-attenuation values in the North China Basin were observed by Liu *et al.* (2004b) and Phillips *et al.* (2005a). Our results are consistent with these earlier studies, but provide higher resolution and more detailed information in the North China Basin, Shanxi and Yinchuan Grabens, Ordos Craton, and surrounding regions.

Our estimate of the quality factor is also consistent with previously determined patterns of  $P_n$  (Wang *et al.*, 2003; Hearn *et al.*, 2004; Liang *et al.*, 2004; Sun *et al.*, 2004; Phillips *et al.*, 2005b; Sun and Toksöz, 2006) and  $S_n$  velocities (Pei *et al.*, 2004). High velocity almost always corresponds with high  $Q_0$  and low velocity with low  $Q_0$ , possibly because of common temperature influence in the crust and uppermost mantle.

Most event terms shown in Figure 3 have values between  $-1$  and  $1$  and are geographically correlated. An event term of  $1.0$  corresponds to a  $\log_{10}(2.73) = 0.43$  change in magnitude. This suggests that the  $M_L$  for events in central North China systematically underestimate the event size by almost one-half of a magnitude unit, whereas events in Taiwan, the southeast China coast, and west of Ordos systematically overestimate the size by almost one-half of a magnitude unit.

Station terms vary less than event terms, but some still show values of up to  $1.0$ . A station term of  $1.0$  suggests an amplification gain factor of  $2.73$  for the station because of site response and instrument gains. There are few stations with this amount of amplification; these have only a few data points associated with them. Furthermore, there is no geographical consistency between the station terms. We infer from this that station site amplification for the ABCE is not an important effect.

We analyzed the sensitivity of parameters, such as  $Q$  decay coefficient  $\eta$ , geometrical spreading coefficient  $k$  and  $S$ -wave velocity  $v$ . We found that the pattern of relative  $Q_0$  lateral variations is very stable, although absolute  $Q_0$  may change with different parameters. Less than 20% variation of absolute  $Q_0$  will be produced if  $\eta$  varies between  $0.3$  and  $0.9$ , and  $v$  varies between  $3.3$  and  $3.9$  km/sec.

## Conclusions

This study uses tomographic imaging to investigate crustal attenuation beneath Northern China. Variations in attenuation are large enough that the standard  $M_L$  magnitude calculation can estimate event source size incorrectly by as much as one-half of a magnitude unit. We find that attenuation levels are correlated with regional tectonic structure. High attenuation often occurs in active tectonic areas with significant faulting, whereas attenuation is low in the stable Ordos Craton. The estimate of attenuation shows a close correlation with topography.  $Q_0$  is generally low in basins, whereas high  $Q_0$  mostly occurs in mountains and uplift regions where crystalline basement appears at the surface. It is possible that low  $Q_0$  in basins is caused by fluid in the upper crust, high heat flow, and/or deep sediment in basins,

whereas high  $Q_0$  in the mountains and uplift regions results from the presence of old, dense, competent rock and low heat flow. The quality factor is also consistent with  $Pn$ - and  $Sn$ -velocity patterns. High velocity generally corresponds with high  $Q_0$  and low velocity with low  $Q_0$ , possibly because of a common temperature influence in the crust and uppermost mantle.

### Acknowledgments

We sincerely thank Guomin Zhang, Jie Liu, and Shenghong Tai for their support and helpful suggestions to this study. We also thank Jonathan Ajo-Franklin, Margaret Benoit, Xander Campman, and Burke Minsley for their valuable comments in improving the manuscript. We are grateful to Anton M. Dainty and an anonymous reviewer for their constructive comments and suggestions. This research was supported jointly by the Talent Project of the Chinese Academy of Sciences (CAS), the Knowledge Innovating Project of the CAS (Grant No. kzcxs3-sw-143), the Earth Resources Laboratory at Massachusetts Institute of Technology (under Contract No. FA8718-04-C-0018), and Los Alamos National Laboratory, U.S. Department of Energy, as Publication No. LAUR-06-2435.

### References

- Brune, J. N. (1970). Tectonic stress and the spectra of seismic shear waves from earthquakes, *J. Geophys. Res.* **75**, 4997–5009.
- Castro, R., F. Pacor, A. Sala, and C. Petrungaro (1996). S wave attenuation and site effects in the region of Friuli, Italy, *J. Geophys. Res.* **101**, 22,355–22,369.
- Cong, L. L., J. F. Hu, Z. W. Fu, Y. B. Wen, G. F. Kang, and X. P. Wu (2003). Distribution of Lg coda Q in the Chinese continent and its adjacent regions, *Science in China Ser. D* **46**, 529–539.
- Fan, G., and T. Lay (2002). Characteristics of Lg attenuation in the Tibetan Plateau, *J. Geophys. Res.* **107**, no. B10, 2256, doi 10.1029/2001JB000804.
- Fan, J. C., S. L. Li, X. L. Lai, and H. Z. Deng (2001). Three-dimensional Q structure in Jiashi earthquake region of Xinjiang region, *Acta Seism. Sinica* **24**, 573–581 (in Chinese).
- Feng, R., and H. N. Zhou (1985). Crustal Q structure beneath the Tibetan Plateau, *Chin. J. Geophys.* **28** (Suppl.), 174–184 (in Chinese).
- Ge, H. C., C. Z. Huang, P. Y. Ye, and Z. F. Lu (1987). Lg magnitude determination for the eastern six provinces of China (part I): method and results, *Acta Seism. Sinica* **9**, 37–51 (in Chinese).
- Gung, Y., and B. Romanowicz (2004). Q tomography of the upper mantle using three-component long-period waveforms, *Geophys. J. Int.* **157**, 813–830.
- Haberland, C., and A. Rietbrock (2001). Attenuation tomography in the western central Andes: a detailed insight into the structure of a magmatic arc, *J. Geophys. Res.* **106**, 11,15–11,167.
- Hanks, T. C., and M. Wyss (1972). The use of body-wave spectra in the determination of seismic-source parameters, *Bull. Seism. Soc. Am.* **62**, 561–589.
- Hearn, T. M., and J. Ni (1994). Pn velocities beneath continental collision zones, the Turkish-Iranian plateau, *Geophys. J. Int.* **117**, 273–283.
- Hearn, T. M., S. Wang, J. F. Ni, Z. Xu, Y. Yu, and X. Zhang (2004). Uppermost mantle velocities beneath China and surrounding regions, *J. Geophys. Res.* **109**, no. B11301, doi 10.1029/2003JB002874.
- Hong, X. H., J. S. Zhu, J. M. Cao, and Z. Q. Xu (2003). Tomography of 3-D S-wave quality factor of the crust and upper mantle in China, *Chin. J. Geophys.* **46**, 642–651 (in Chinese).
- Hu, S. B., L. J. He, and J. Y. Wang (2001). Compilation of heat flow data in the China continental area (3rd edition), *Chin. J. Geophys.* **44**, 612–626 (in Chinese).
- Jemberie, A. L., and B. J. Mitchell (2004). Shear wave Q structure and its lateral variation in the crust of China and surrounding regions, *Geophys. J. Int.* **157**, 363–380.
- Lees, J. M., and R. S. Crosson (1989). Tomographic inversion for three-dimensional velocity structure at mount St. Helens using earthquake data, *J. Geophys. Res.* **94**, 5716–5728.
- Lees, J. M., and G. T. Lindley (1994). Three-dimensional attenuation tomography at Loma Prieta: Inversion of  $t^*$  for Q, *J. Geophys. Res.* **99**, 6843–6863.
- Li, G. P., G. M. Xu, E. G. Gao, and Y. Xu (2000).  $Q_\beta$  Tomography under the crust and upper mantle in Eastern China, *Acta Seism. Sinica* **22**, 73–81 (in Chinese).
- Liang, C., X. Song, and J. Huang (2004). Tomographic inversion of Pn travel times in China, *J. Geophys. Res.* **109**, B11304, doi 10.1029/2003JB002789.
- Liu, J., S. H. Zheng, and Y. L. Huang (2003). The inversion of non-elasticity coefficient, source parameters, site response using Genetic Algorithms, *Acta Seism. Sinica* **25**, 211–218 (in Chinese).
- Liu, J. H., F. T. Liu, X. W. Yan, Y. Xu, and T. Y. Hao (2004a). A study of Lg attenuation in North China—the measurement of Lg coda Q, *Chin. J. Geophys.* **47**, 822–831 (in Chinese).
- Liu, J. H., F. T. Liu, X. W. Yan, Y. Xu, and T. Y. Hao (2004b). A study of Lg coda attenuation beneath North China: seismic imaging of Lg Coda  $Q_0$ , *Chin. J. Geophys.* **47**, 1044–1052 (in Chinese).
- Ma, X. Y., ed. (1989). *Lithospheric Dynamics Atlas of China*, China Cartographic Publishing House, Beijing (in Chinese).
- Mitchell, B. J., Y. Pan, J. Xie, and L. Cong (1997). Lg coda Q variation across Eurasia and its relation to crustal evolution, *J. Geophys. Res.* **102**, 22,767–22,779.
- Paige, C. C., and M. A. Saunders (1982). LSQR, An algorithm for sparse linear equations and sparse linear system, *ACM Trans. Math. Software* **8**, 43–71.
- Pei, S. P., Z. H. Xu, and S. Y. Wang (2004). Sn wave tomography of the uppermost mantle beneath the China continent and adjacent regions, *Chin. J. Geophys.* **47**, 278–284.
- Phillips, W. S., H. E. Hartse, S. R. Taylor, and G. E. Randall (2000). 1 Hz Lg Q tomography in central Asia, *Geophys. Res. Lett.* **27**, 3425–3428.
- Phillips, W. S., H. E. Hartse, S. R. Taylor, A. A. Velasco, and G. E. Randall (2001). Application of regional phase amplitude tomography to seismic verification, *Pure Appl. Geophys.* **158**, 1189–1206.
- Phillips, W. S., H. E. Hartse, and J. T. Rutledge (2005a). Amplitude ratio tomography for regional phase Q, *Geophys. Res. Lett.* **32**, doi 10.1029/2005GL023870.
- Phillips, W. S., C. A. Rowe, and L. K. Steck (2005b). The use of interstation P wave arrival time differences to account for regional path variability, *Geophys. Res. Lett.* **32**, L11301, doi 10.1029/2005GL022558.
- Reese, C. C., R. R. Rapine, and J. F. Ni (1999). Lateral variation of Pn and Lg attenuation at the CDSN station LSA, *Bull. Seism. Soc. Am.* **89**, 325–330.
- Rietbrock, A. (2001). P wave attenuation structure in the fault area of the 1995 Kobe earthquake, *J. Geophys. Res.* **106**, 4141–4154.
- Romanowicz, B. (1995). A global tomographic inversion model of shear attenuation in the upper mantle, *J. Geophys. Res.* **100**, 12,375–12,394.
- Sanders, C. O. (1993). Local earthquake tomography: attenuation theory and results, in *Seismic Tomography: Theory and Practice*, H. Iyer and K. Hirahara (Editors), Chapman and Hall, New York, 676–694.
- Steinshouer, D. W., J. Qiang, P. J. McCabe, and R. T. Ryder (1999). Maps showing geology, oil and gas fields, and geologic provinces of the Asia pacific region, *U.S. Geol. Surv. Open-File Rept.* 97-470F.
- Sun, Y., and M. N. Toksoz (2006). Crustal structure of China and surrounding regions from P-wave travel-time tomography, *J. Geophys. Res.* **111**, B03310, doi 10.1029/2005JB003962.
- Sun, Y., L. Xu, S. Kuleli, F. D. Morgan, and M. N. Toksoz (2004). Adaptive moving window method for 3-D P-velocity tomography and its application in China, *Bull. Seism. Soc. Am.* **94**, 740–746.
- Taylor, S. R., X. Yang, and W. S. Phillips (2003). Bayesian Lg Attenuation Tomography Applied to Eastern Asia, *Bull. Seism. Soc. Am.* **93**, 795–803.

- Wang, S. Y., Z. H. Xu, and S. P. Pei (2003). Velocity structure of uppermost mantle beneath North China from Pn tomography and its implications, *Sci. China Ser. D* **46** (Suppl.), 130–140.
- Wu, J. P., and R. S. Zeng (1996). Inversion of Q value structure beneath the Tibet plateau, *Acta Seism. Sinica* **18**, 208–214 (in Chinese).
- Xie, J., R. Gok, J. Ni, and Y. Aoki (2004). Lateral variations of crustal seismic attenuation along the INDEPTH profiles in Tibet from Lg Q inversion, *J. Geophys. Res.* **109**, B10308, doi 10.1029/2004JB002988.
- Zhao, J. M., X. K. Zhang, H. Z. Deng, and J. Zhang (2003). Q value structure of the upper crust along the geoscience transect from Baicheng to Da Qaidam, *Chin. J. Geophys.* **46**, 725–735.

Institute of Tibetan Plateau Research  
Chinese Academy of Sciences  
Beijing 100085, China  
(S.P., J.Z., H.L.)

Los Alamos National Laboratory  
Los Alamos, New Mexico 87545  
(C.A.R.)

Institute of Geophysics  
China Earthquake Administration  
Beijing 100081, China  
(S.W., Z.X.)

New Mexico State University  
Physics Department  
Las Cruces, New Mexico 88003  
(T.M.H.)

Earth Resources Laboratory  
Massachusetts Institute of Technology  
Cambridge, Massachusetts 02139  
(Y.S.)

Manuscript received 21 January 2006.





# Constraining *P*-wave velocity variations in the upper mantle beneath Southeast Asia

Chang Li<sup>\*</sup>, Robert D. van der Hilst, M. Nafi Toksöz

*Department of Earth, Atmospheric, and Planetary Sciences, Massachusetts Institute of Technology,  
77 Massachusetts Ave., Cambridge, MA 02139, USA*

Received 16 May 2005; received in revised form 26 September 2005; accepted 26 September 2005

## Abstract

We have produced a *P*-wave model of the upper mantle beneath Southeast (SE) Asia from reprocessed short period International Seismological Centre (ISC) *P* and *pP* data, short period *P* data of the Annual Bulletin of Chinese Earthquakes (ABCE), and long period *PP*-*P* data. We used 3D sensitivity kernels to combine the datasets, and mantle structure was parameterized with an irregular grid. In the best-sampled region our data resolve structure on scale lengths less than 150 km. The smearing of crustal anomalies to larger depths is reduced by a crustal correction using an a priori 3D model. Our tomographic inversions reveal high-velocity roots beneath the Archean Ordos Plateau, the Sichuan Basin, and other continental blocks in SE Asia. Beneath the Himalayan Block we detect high seismic velocities, which we associate with subduction of Indian lithospheric mantle. This structure is visible above the 410 km discontinuity and may not connect to the remnant of the Neo-Tethys oceanic slab in the lower mantle. Our images suggest that only the southwestern part of the Tibetan plateau is underlain by Indian lithosphere and, thus, that the upper mantle beneath northeastern Tibet is primarily of Asian origin. Our imaging also reveals a large-scale high-velocity structure in the transition zone beneath the Yangtze Craton, which could have been produced in multiple subduction episodes. The low *P*-wave velocities beneath the Hainan Island are most prominent in the upper mantle and transition zone; they may represent counter flow from the surrounding subduction zones, and may not be unrelated to processes beneath eastern Tibet.

© 2005 Elsevier B.V. All rights reserved.

**Keywords:** *P*-wave tomography; Crustal correction; Upper mantle; SE Asia

## 1. Introduction

Southeast Asia is a tectonically diverse and active region. Continental collision in the west and eastward retreating slabs of subducting lithosphere in the east set up a large-scale clockwise rotation (black arrows in Fig. 1). The major large-scale features produced by the collision and post-collisional convergence of the Indian

and Eurasian plates include the Tibetan Plateau, where the continental crust has approximately doubled in thickness (Molnar and Tapponnier, 1975; Tapponnier et al., 2001; Rapine et al., 2003). Offshore, oceanic lithosphere is predominantly of early Cenozoic age, and there is ongoing subduction of the Pacific, Philippine Sea, and Indo Australian plates beneath Eurasia (van der Hilst et al., 1991; Fukao et al., 1992; Widiyantoro and van der Hilst, 1996) with eastward slab roll back since Oligocene times (van der Hilst and Seno, 1993; Northrup et al., 1995). Between these active plate boundary zones the continental lithosphere was subjected to extension during early Cenozoic time (Tapponnier and Molnar, 1977;

<sup>\*</sup> Corresponding author. Tel.: +1 617 324 0268;  
fax: +1 617 258 9697.

E-mail address: [changli@mit.edu](mailto:changli@mit.edu) (C. Li).

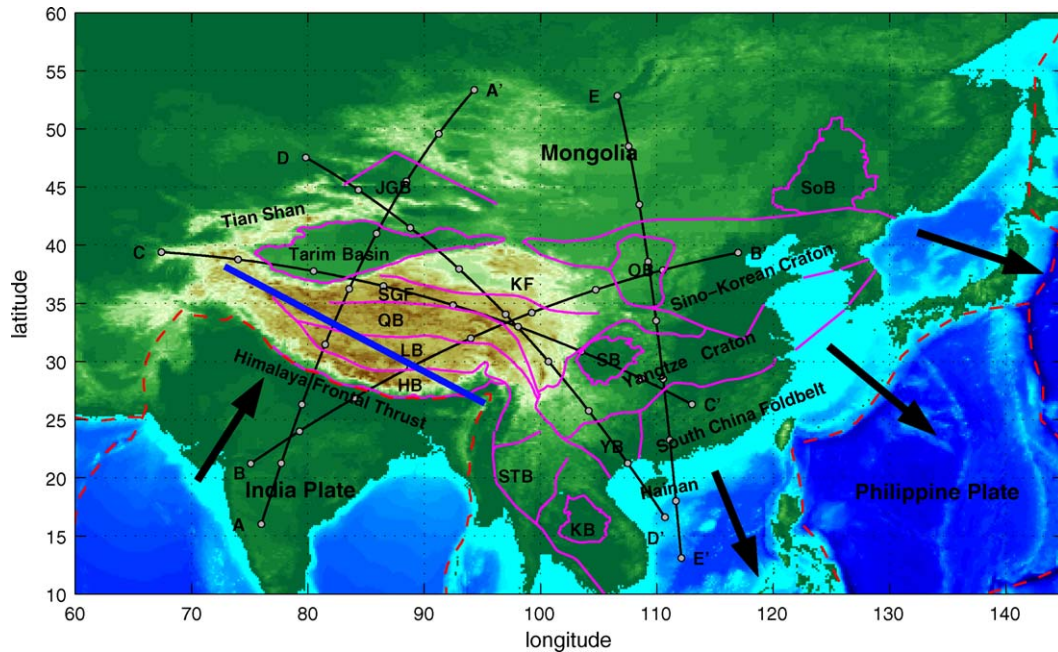


Fig. 1. The main tectonic elements in the SE Asia. The dashed red lines are plate boundaries, according to NUVEL-1 (DeMets et al., 1990). The thick purple lines denote main tectonic structures, where SoB–Songliao Basin, OB–Ordos Basin, SB–Sichuan Basin, KB–Khorat Basin, STB–Shan Thai Block, YB–Youjiang Block, JGB–Junggar Basin, SGF–Songpan Ganzi Foldbelt, QB–Qiangtang Block, LB–Lhasa Block, HB–Himalayan Block, KF–Kunlun Fault (modified from Li, 1998 and Tapponnier et al., 2001). Black arrows show the continental collision in the west and slab roll back in the east set up the clockwise rotation for the SE Asia. The blue thick line shows the horizontal limit of the Indian lithospheric mantle beneath the Tibetan plateau. The positions of five cross-sections in Fig. 9 are shown by black lines with grey dots.

Zhang et al., 1984; Li, 1998). The extensional features are usually regarded in the context of the Indian–Eurasian collision (Molnar and Tapponnier, 1975). However, both the collision and the subduction processes, along with their impact on mantle (return) flow beneath the region, must be taken into account in order to obtain a complete understanding of the dynamics and the tectonic evolution of SE Asia. It can be expected that this complex tectonics has produced significant structural heterogeneity in the upper mantle. Understanding this relationship is the main long-term objective of our study; here we present preliminary results of seismic travel time tomography.

Southeast Asia is characterized by relatively high levels of seismicity, but the distribution of seismological stations from which data are openly available is rather sparse (red triangles in Fig. 2). This puts restrictions on the type of seismic imaging that can be performed and the scale of the structure that can be resolved. Surface wave tomography studies show pronounced high-velocity continental roots beneath several Precambrian tectonic units (e.g., Ordos Plateau, Songliao Basin, Sichuan Basin) of SE Asia (Lebedev and Nolet, 2003; Debayle et al., 2005; Lebedev et al., 2005) and a seismically fast Indian lithosphere under southeastern Tibet

(Friederich, 2003). These features can also be inferred from global shear-wave velocity models (e.g., Trampert and Woodhouse, 1995; Ekström et al., 1997; Shapiro and Ritzwoller, 2002). However, the relatively low frequency of surface wave data put limits the structural wavelengths that can be resolved in the upper mantle.

In regions with good data coverage short-period travel times can provide higher resolution than the surface wave inversions. A number of *P*-wave tomographic studies have concentrated on complex morphology of the subducting oceanic lithospheric slabs beneath the western Pacific, the Philippine Sea, and Indonesia (e.g., van der Hilst et al., 1991; Fukao et al., 1992; Widiyantoro and van der Hilst, 1997). Using data from temporary seismic arrays, receiver function studies have focused on the crust and shallow mantle beneath central Tibet (e.g., Kind et al., 1996; Kosarev et al., 1999; Kind et al., 2002). Regional and local *P*-wave tomography has focused on the crust and uppermost mantle (e.g., Sun et al., 2004; Hearn et al., 2004; Liang et al., 2004; Huang et al., 2002; Wang et al., 2003). Global tomography has long been inadequate for detailed studies of the upper mantle beneath China and the broad realm of continental collision. In part this is due to the paucity of data

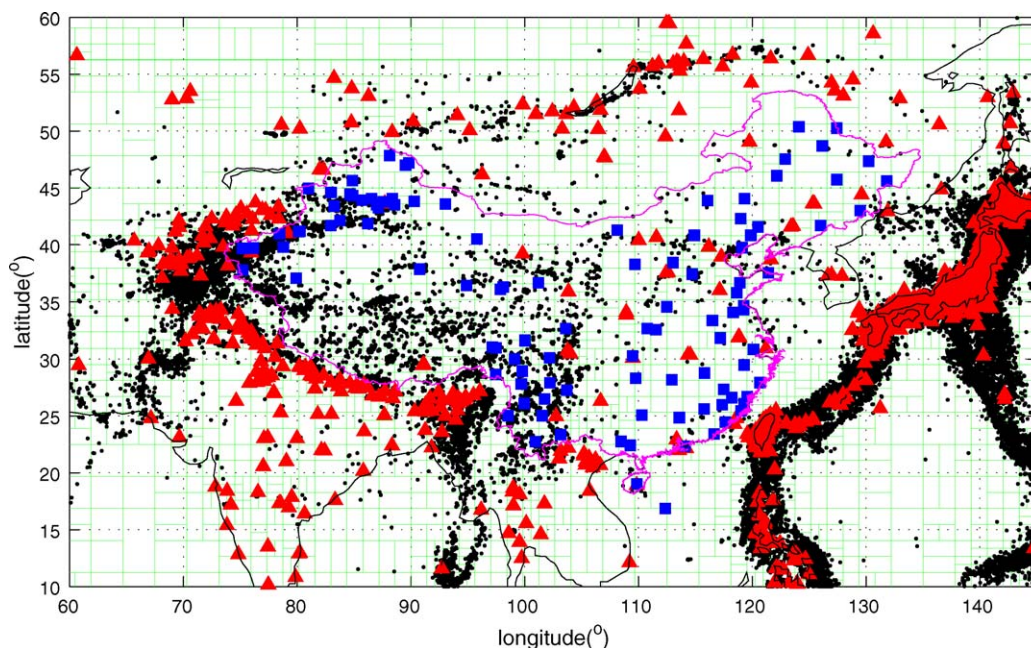


Fig. 2. The distribution of stations and earthquakes (black dots) in Southeast Asia and the irregular grids at 200 km depth. The irregular grid, depicted here with thin green lines for 200 km depth, allows us to resolve the fine structure in regions of dense sampling. Blue squares depict 107 stations of ABCE from which data were not previously reported to ISC. Red triangles depict the 1223 EHB stations in the area of interest, of which 44 stations are located in the mainland China.

from the numerous stations in China. But this situation is changing. There are promising signs that data from Chinese networks may become more openly available, and also data from temporary arrays will continue to fill in gaps in data coverage. For example, data from arrays deployed by MIT in collaboration with the Chengdu Institute of Geology and Mineral Resources (CIGMR), and by Lehigh University – CIGMR (Sol et al., 2004) are now being processed and will soon be incorporated into the inversions.

With a better  $P$  wave velocity model of the upper mantle beneath Southeast Asia we hope to answer specific questions, for instance: How far does the Indian lithospheric mantle underthrust beneath the Tibetan plateau? What is the relationship between recent tectonic processes and structures deeper in the mantle? Which structures in the transition zone (TZ) are related to the underthrusting of Indian lithosphere and which are due to the subduction of the Pacific, Philippine Sea, and Indo-Australian plates? To improve the tomographic images of mantle structure in this region we (i) combine  $P$  data from the Annual Bulletin of Chinese Earthquakes (ABCE) (a national earthquake catalog compiled by the Institute of Geophysics, China Seismological Bureau),  $P$  and  $pP$  data from Engdahl et al. (1998), and  $PP$ - $P$  differential travel time data from Bolton and Masters (2001);

(ii) use an irregular grid parameterization to enhance local parameter estimation; and we (iii) correct for the large regional variations in crustal structure using an a priori 3D crustal model. As regards the latter, we present a simple approach that reduces artifacts caused by errors in the a priori crust models.

The results presented here are a subset of the new  $P$ -wave global model; compared to our previous results – see, for instance, Kárason and van der Hilst (2001) – the use of an irregular grid, the addition of  $PP$ - $P$  and ABCE ( $P$ ) data, and the crustal corrections combine to provide more detail in the upper mantle region of our current interest. The global model will be presented elsewhere (van der Hilst, Li, and Kárason, in preparation) but is freely available upon request.

## 2. Data

The travel time data used in our study comes from three sources. The first is the International Seismological Centre (ISC) data that have been reprocessed by Engdahl et al. (1998) (hereinafter referred to as EHB). Engdahl et al. used arrival times reported to the ISC and calculated travel-time residuals using a non-linear process earthquake relocation and phase re-identification scheme. In our global inversion we used



ca. 9,400,000  $P$  and 680,000  $pP$  EHB residuals of well-constrained regional and teleseismic earthquakes that occurred between 01/01/1964 and 15/09/2004.

As a consequence of many Chinese stations not reporting to ISC the station coverage of EHB is not very good in SE Asia, especially in China. In order to improve data coverage, we augmented the EHB data with Annual Bulletin of Chinese Earthquakes (ABCE) data. This database contains nearly 670,000  $P$ -wave travel time residuals from 220 stations in China and surrounding areas. Combining datasets has to be done with care. Relative to the *ak135* reference velocity model (Kennett et al., 1995), the ABCE residuals have an offset of more than 2 s. There are two contributions to this baseline problem. One is the effect of crustal structure in the region. If the crust is thicker than that of the reference model the arrival time will be greater than the reference travel time, resulting in positive travel time residuals. For example, the 0.5 s offset at Lhasa station is most likely due, in part, to the thick crust of Tibet. We account for this in the inversion. The second and larger effect concerns the source locations used in the EHB and ABCE catalogs; they can differ substantially, in particular for events in the Wadati-Benioff zones beneath the north-west Pacific island arcs. Calculating the ABCE residuals with respect to the EHB hypocenters reduces the baseline to less than 0.2 s. Prior to inversion we eliminated data for the 113 ABCE stations that are already included in EHB. The study area comprises 1223 EHB stations (44 of which are mainland China, red triangles in Fig. 2) and 107 Chinese ABCE stations that have not been reported to ISC (blue square in Fig. 2).

The subset of the global model presented here also includes  $\sim 22,000$   $PP$ - $P$  low frequency differential times measured by waveform cross-correlation (Bolton and Masters, 2001). We account for sensitivity to structure away from the optical ray path with 3D Fréchet derivatives (sensitivity kernels) estimated from single forward scattering; for details see Káráson (2002) and van der Hilst et al. (in preparation). For the spatial resolution sought here these low frequency data may seem superfluous, but the  $PP$ - $P$  differential times constrain large wavelength variations in the region under investigation.

### 3. Methodology

#### 3.1. Adaptive grid

Uneven data coverage can produce significant lateral variation in resolution of tomographic models. We mitigate effects of uneven data coverage by means of an adaptive parameterization based on the sampling density

of the high-frequency data (Abers and Roecker, 1991; Bijwaard et al., 1998; Káráson and van der Hilst, 2000). Each block in the grid used in the inversion consists of one or more base blocks of  $45 \text{ km} \times 0.7^\circ \times 0.7^\circ$ . The total number of free parameters (that is, the sampled irregular blocks and the event relocation parameters) is slightly less than 0.5 million. As an example, Fig. 2 (green lines) displays the irregular grid at 200 km depth. The relatively fine grid near the subduction zones of the Indian and Philippine Sea plates, the Sichuan Basin, and Tian Shan suggests that in these regions we can image finer structures. In contrast, the grids beneath Mongolia, the Tarim Basin, and the center of Philippine Sea is relatively coarse, which, of course, limits the spatial resolution beneath these regions.

For the calculation of the sensitivity matrix associated with short period data we use a high-frequency approximation and trace optical rays (in the radially stratified reference model). We use weighted composite rays (Káráson and van der Hilst, 2001) to better balance the sampling and further reduce the size of the sensitivity matrix. Because of noise in the data, we apply norm and gradient damping: norm damping favors a result that is close to the reference model and thus tends to minimize the amplitude of the model, while gradient damping reduces the differences between adjacent blocks and thus produces smooth variations, both laterally and radially. We perform experiments with synthetic data and known input models to find appropriate values for the damping parameters, but the choice of the parameters remains subjective. In our inversions, the norm damping is small. We use the iterative method LSQR (Paige and Saunders, 1982) to minimize

$$\varepsilon = \|Am - d\|^2 + \lambda_1 \|Lm\|^2 + \lambda_2 \|m\|^2, \quad (1)$$

where  $A$  is the sensitivity matrix,  $d$  is the vector of travel time residuals, and  $m$  is the vector of model parameters (which include slowness perturbations and hypocenter mislocations).  $L$  is a smoothing operator, and  $\lambda_1$  and  $\lambda_2$  are the weights for gradient and norm damping, respectively. The results presented here were obtained after 200 iterations, but for LSQR most of the convergence is achieved within a small number of iterations:  $\sim 98\%$  of the total variance reduction is obtained within the first 25 iterations. In order to visualize the values determined for the irregular blocks we projected and interpolated them on a regular ( $0.5^\circ \times 0.5^\circ \times 50 \text{ km}$ ) grid.

#### 3.2. Crust correction

The small incidence angles of the  $P$ -waves may combine with strong crustal heterogeneity to cause

crustal anomalies to be ‘smeared’ (mapped) to larger depths in the model. This could be a significant problem if the actual crust is very different from that in the 1D reference model, as is the case here. Application of crustal correction in global surface wave tomography is common practice, see, e.g., [Boschi and Ekström \(2002\)](#), but such corrections are not yet routinely considered in regional and global travel time tomography.

In SE Asia, the lateral variation in crustal thickness is considerable. For instance, crust of the Tibetan plateau is

at least 70 km thick compared to just several kilometers for the oceanic crust in the Philippine Sea ([Fig. 3a](#), from (59°E, 35°N) to (134°E, 14°N)). As an estimate of the 3D crustal structure we embed the regional model by [Sun et al. \(2004\)](#) into the global CRUST 2.0 ([Bassin et al., 2000](#)), calculate the difference in wavespeed with respect to *ak135*, and project this a priori crustal model onto our grid ([Fig. 3b](#)). In order to evaluate if and how this crustal heterogeneity would “smear” into the model if unaccounted for, we use a resolution experiment with synthetic data. The response to such a crustal model,

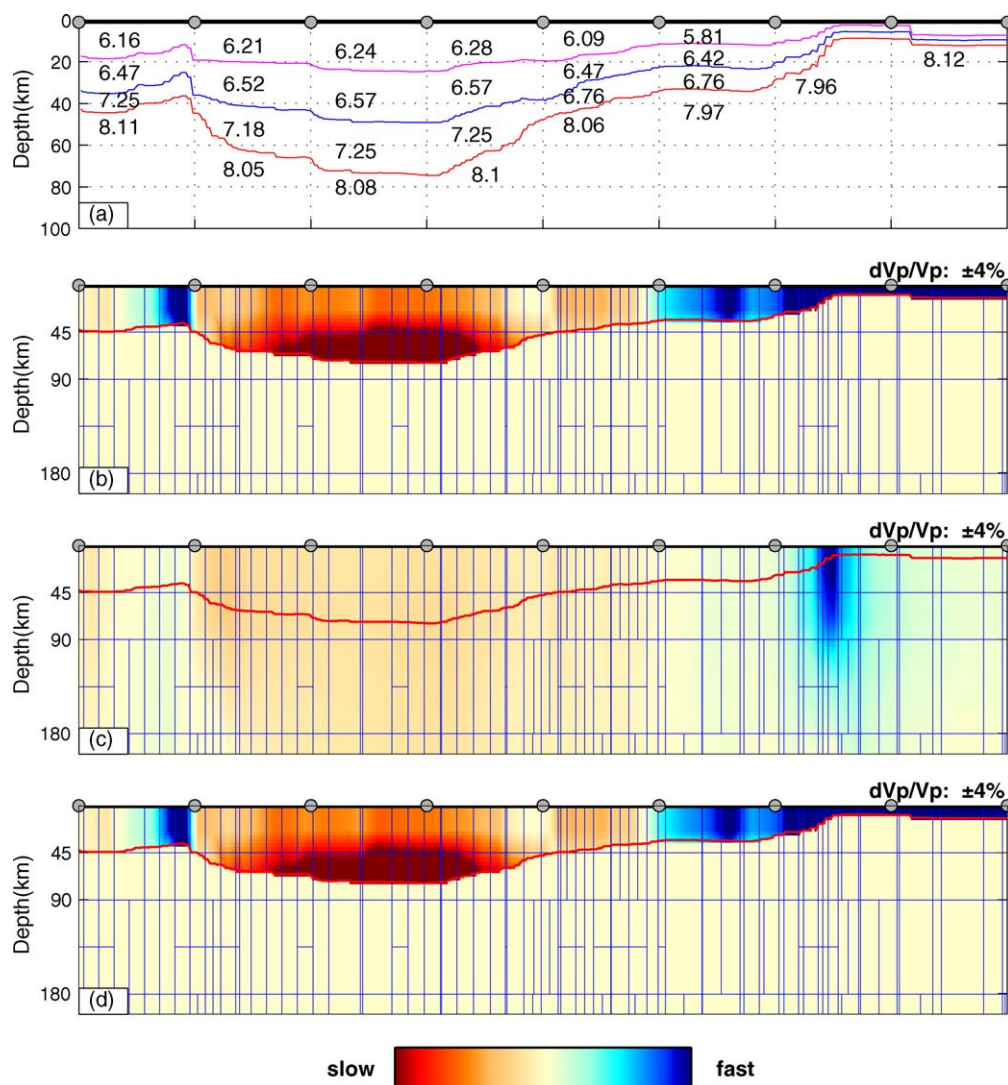


Fig. 3. Regularization for 3D crust. (a) Three layers of crust through the Tibetan plateau and Philippine Sea (from (59°E 35°N) to (134°E 14°N)). *P* wavespeeds of input model (in km/s) for each layer is shown. (b) Vertical projection of 3D crust on irregular grid. (c) The recovery model using same inversion scheme and sampling as in the construction of the final model. (d) The recovery model using the regularization in the model space for crust. After regularization, the big velocity variation of the crust can be confined in crustal blocks. Moho depth (red line) and irregular grid (blue line) are shown in b, c, and d.

including all its artifacts, is shown in Fig. 3c. Obviously, the crust cannot be resolved by the data used, and crustal structure may be smeared to depths of at least 200 km. Moreover, the retrieved anomalies are much smaller than those in the input models. We try to remedy this with a crustal correction.

Crustal corrections can be done in several ways. One could calculate travel times through the 3D crustal model, subtract these from the observed times, ray-trace to the bottom of the 3D crust, and then solve for the structure beneath the crust while leaving the crustal model unchanged (e.g., Waldhauser et al., 2002; Weidle and Widiyantoro, 2005). While straightforward and intuitive, without an explicit method for confining crustal anomalies to the crust, the relatively large anomalies of the 3D crust can still smear into the upper mantle. Moreover, artifacts due to errors in the crustal models are not mitigated. A practical drawback is that later data addition and (crustal) model updates require repeated ray tracing, which comes at considerable computational cost. Furthermore, calculating explicit time corrections is not straightforward for phases with complicated sampling properties, such as *PP*.

In view of these disadvantages, we correct for crustal structure by means of regularization; this is accomplished through a simple modification of (1):

$$\varepsilon = \|AM - d\|^2 + \lambda_1 \|LM\|^2 + \lambda_2 \|M\|^2 + \lambda_3 \|C - M_c\|^2, \quad (2)$$

where  $C$  is the a priori 3D crustal model and  $M_c$  is the crustal part of the model space  $M$ . We determine  $\lambda_3$  through tests with synthetic data. Through such regularization in the model space we can balance the crust and upper mantle contribution to misfit  $\varepsilon$  and recover the a priori crustal model (Fig. 3d). Later addition of data sets does not require further calculations since all is accounted for in the model space.

These methods of crust correction produce the same result, but because of the ease of implementation we use the regularization approach for the inversions discussed below.

## 4. Results

### 4.1. Model improvements

The addition of the ABCE data and the correction for the crust improve the 3D mantle model (Fig. 4). For 60 and 200 km depth, Fig. 4A (1 and 2) depicts the model derived from the EHB and PP data. The addi-

tion of the ABCE data, and concomitant adjustment of the grids, increases our ability to resolve the small-scale structure (Fig. 4B1 and B2). In the mainland of China, where the extra ABCE stations are located, more detail is recovered than before. For example, we now begin to observe a high-velocity structure beneath the eastern part of the Sichuan Basin and the Songliao Basin and a low velocity structure beneath the Songpan Ganzi Foldbelt (Fig. 4B1 and B2). As expected, outside the mainland of China, for instance beneath the Indian continent and the Philippine Sea, the improvements are small. The crustal thickness of central Tibet ( $\sim 70$ – $90$  km) differs significantly from the 35 km in *ak135*, but the application of our crust correction reduces the smearing of unresolved shallow structures (compare, e.g., Fig. 4C2 and B2).

### 4.2. Resolution tests

Resolution test with synthetic data confirm that the addition of the ABCE data increases our ability to resolve 3D structure. In Figs. 5 and 6 we show the retrieved structure from a checkerboard resolution test at different depths for box sizes of  $5^\circ \times 5^\circ$  and  $3^\circ \times 3^\circ$ , respectively. The input structure of  $\pm 1\%$  velocity variation (Figs. 5.0 and 6.0) was computed one layer at a time, and noiseless synthetic travel times were created and inverted using the same inversion scheme and sampling (that is, sensitivity matrix) as used in the inversion of the earthquake data. In the shallow mantle, spatial resolution remains a concern. At 200 and 300 km depth the pattern is smeared beneath Philippine Sea, South China Sea, and most of Mongolia, but in areas of our particular interest, such as mainland China, and the Himalayas the recovery is somewhat better (Fig. 6.3 and 6.4). The  $5^\circ \times 5^\circ$  pattern can be recovered beneath China (Fig. 5.1 and 5.2), but smaller anomalies are not likely to be resolved beneath the Tarim Basin and the northern part of Tibet (Fig. 6.1 and 6.2). At depths below 400 km, both the  $5^\circ \times 5^\circ$  and  $3^\circ \times 3^\circ$  input patterns are recovered beneath most parts of our study region (Figs. 5.5–5.9 and 6.5–6.9).

The near vertical incidence of rays reduces the radial resolution in the shallow mantle. The checkerboard tests of two input patterns ( $400 \text{ km} \times 400 \text{ km}$  and  $280 \text{ km} \times 280 \text{ km}$ ) in Fig. 7 help us evaluate the vertical resolution of structure in the five slices that will be discussed later. These slices are about 4000 km long and extend from Earth's surface to 1700 km depth. In general, the recovery of the input models is adequate below 400 km depth. At shallower depth, small-scale structure cannot be recovered well in many areas beneath the study



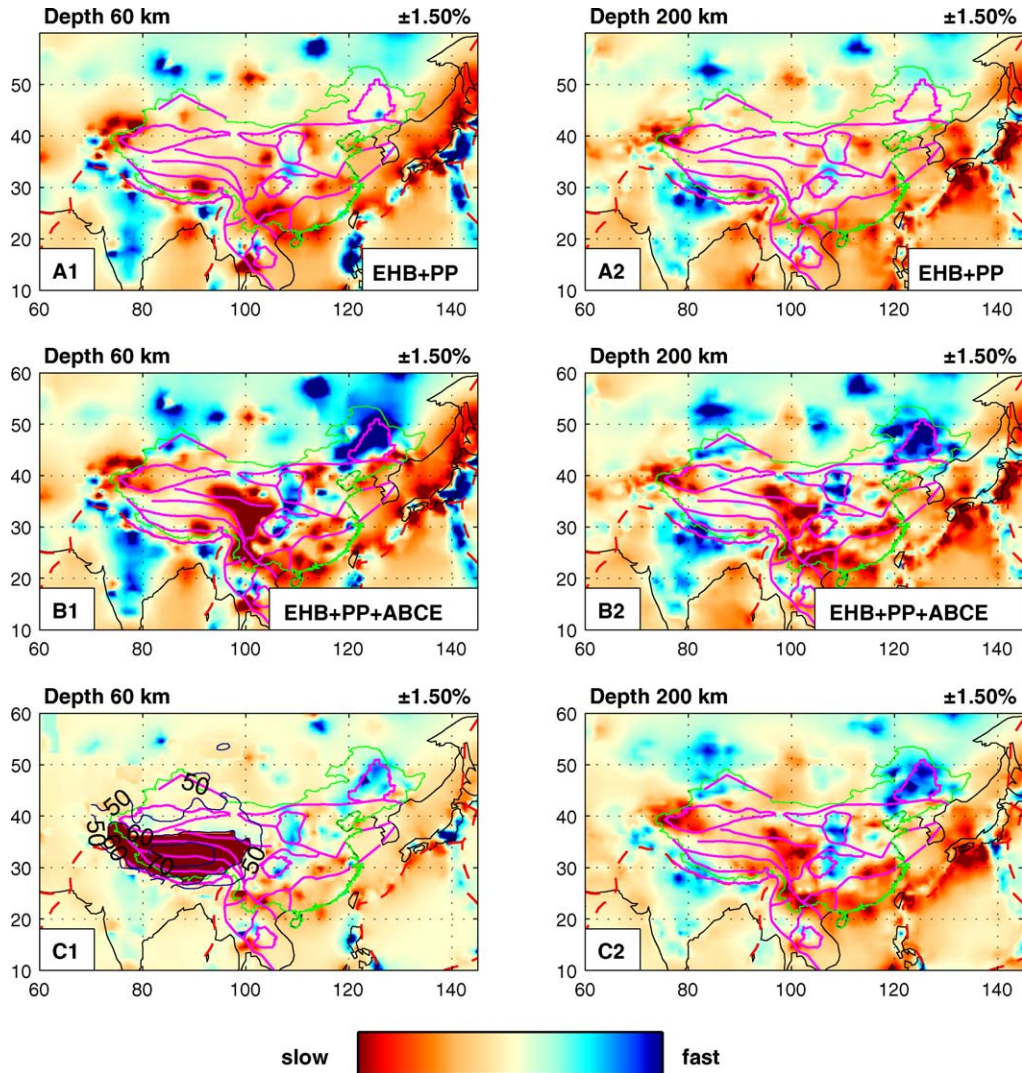


Fig. 4. Effects of data addition and crust correction; for illustration purposes we only display the models at 60 and 200 km depth. (A) Model based on EHB and *PP* data only. (B) EHB + *PP* + ABCE data. (C) EHB + *PP* + ABCE + 3D crust correction. Regularization in the model space not only recovers the big anomaly in the crust, it can also balance the crust and upper mantle to best fit the travel time residuals. C1 depicts the 50, 60, and 70 km depth contours of the 3D crust model used; within these contours the wavespeed is much lower than in the reference values (*ak135*), see Fig. 3b.

region, but larger scale variations can be recovered reasonably well.

From our lateral checkerboard test we conclude that below 200 km depth most of the  $3^\circ \times 3^\circ$  input signal could be recovered, so the average resolution length at these depths is the half of input signal dimension (Lebedev and Nolet, 2003), that is, about 150 km. At shallow depths, the smaller scale pattern is only recovered beneath a few densely sampled regions, such as the Yangtze Craton, the Sino-Korean Craton, and the Himalayas (Fig. 6.1), where we estimate the resolution length to be of the order of 100 km. At the Tarim

Basin and the north part of Tibet, the estimated lateral resolution is ca. 200 km (Fig. 6.2). The vertical resolution length is about 150 km below 400 km depth (Fig. 7).

#### 4.3. Structure of the upper mantle beneath SE Asia

We show the *P*-wave velocity variations in map view from the surface to about 700 km depth (Fig. 8) and in five vertical cross-sections (Fig. 9). For presentation purpose we label the major structures as 1, 2, 3 and so on. The major features of the model are discussed below.



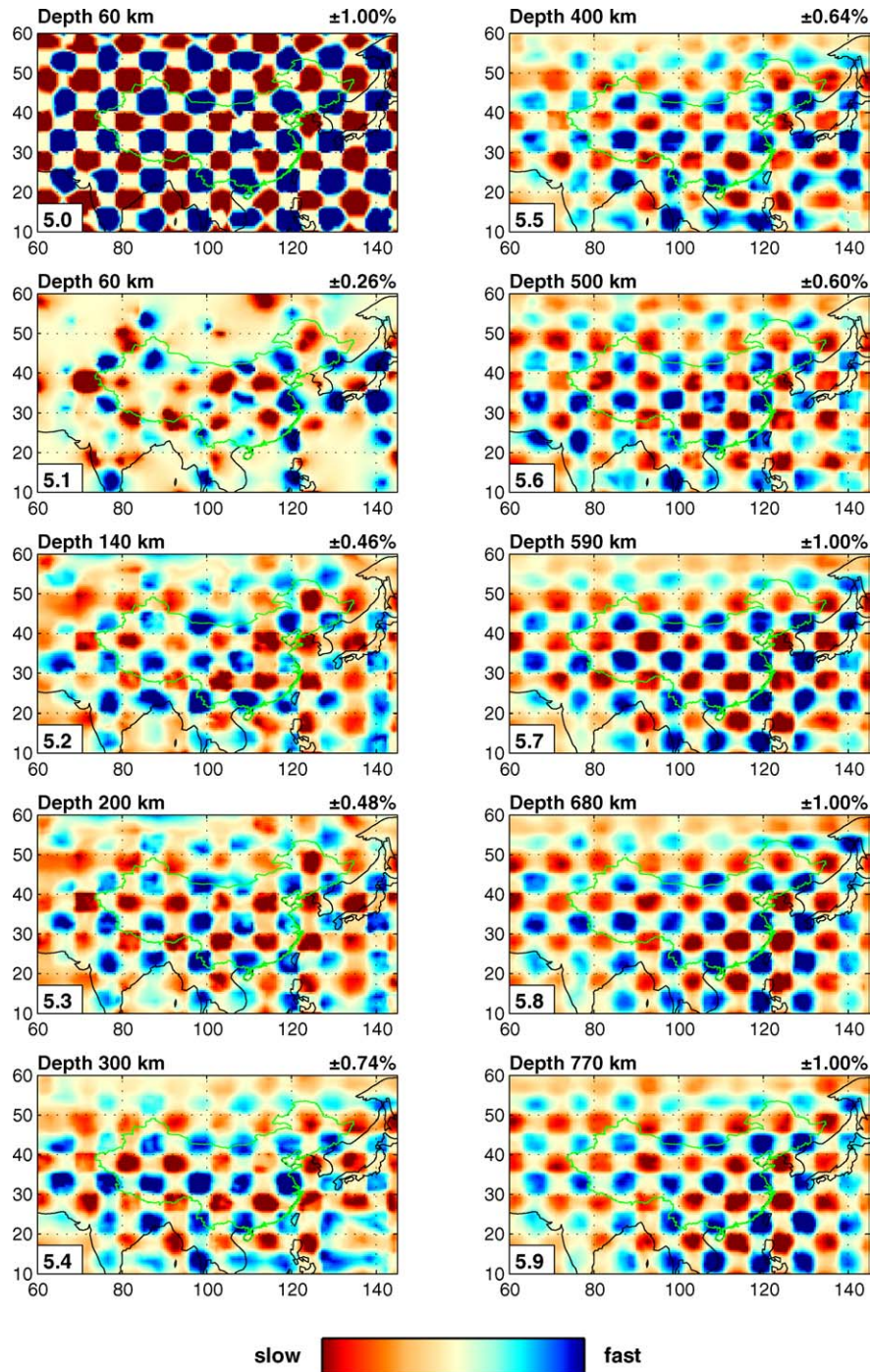


Fig. 5. Checkerboard resolution test for target anomalies at different depths. Input pattern ( $5^\circ \times 5^\circ$ ) is shown in 5.0.

#### 4.3.1. Upper mantle structure beneath India and central Tibet

A pronounced high-velocity anomaly (labeled as 1) is visible to a depth of  $\sim 300$  km beneath the region

of the Precambrian Indian continent (Fig. 8a–d). In cross-section this structure appears to dip northeastward with the flexure starting near the foreland basin about 200 km to the south of the Himalaya Frontal Thrust

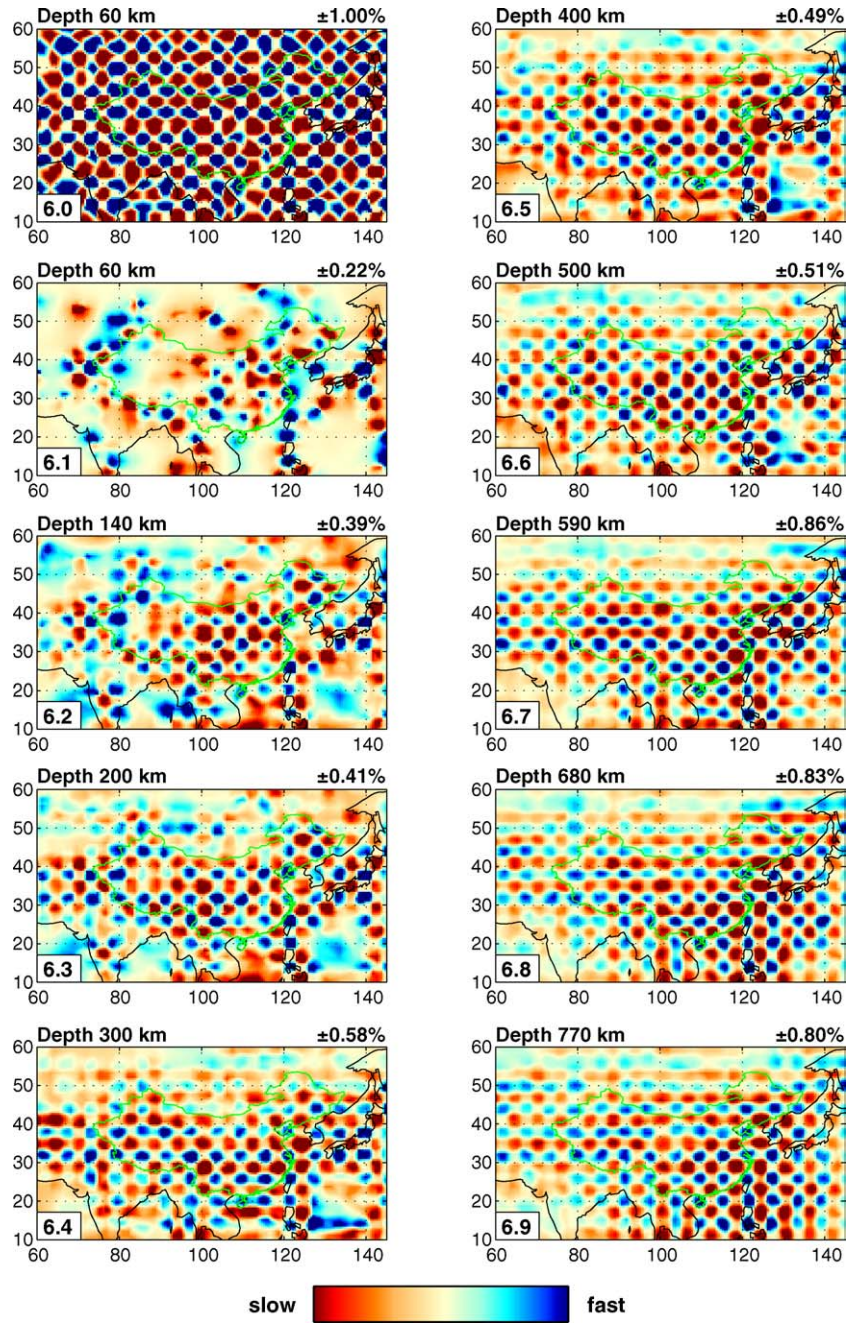


Fig. 6. Checkerboard resolution test for target anomalies at different depths. Input pattern ( $3^\circ \times 3^\circ$ ) is shown in 6.0.

(Figs. 1 and 9a). Even though it is not yet well resolved, we interpret this dipping structure as the subducting slab of Indian continental lithosphere, and perhaps part of the Tethyan oceanic lithosphere in front of it. From Figs. 8b–e and 9a we infer that only the southwestern part of the Plateau, the Himalayan Block and the western Lhasa Block, is directly underlain by the Indian litho-

sphere, the northern limit of Indian lithosphere beneath Tibet is marked by the thick blue line in Fig. 1. Our result is consistent with the image presented by Shapiro and Ritzwoller (2002), but since they used fundamental mode surface waves they could only map the structure to ca. 200 km depth. In our images the dipping structure is detected to at least 400 km depth, and possibly



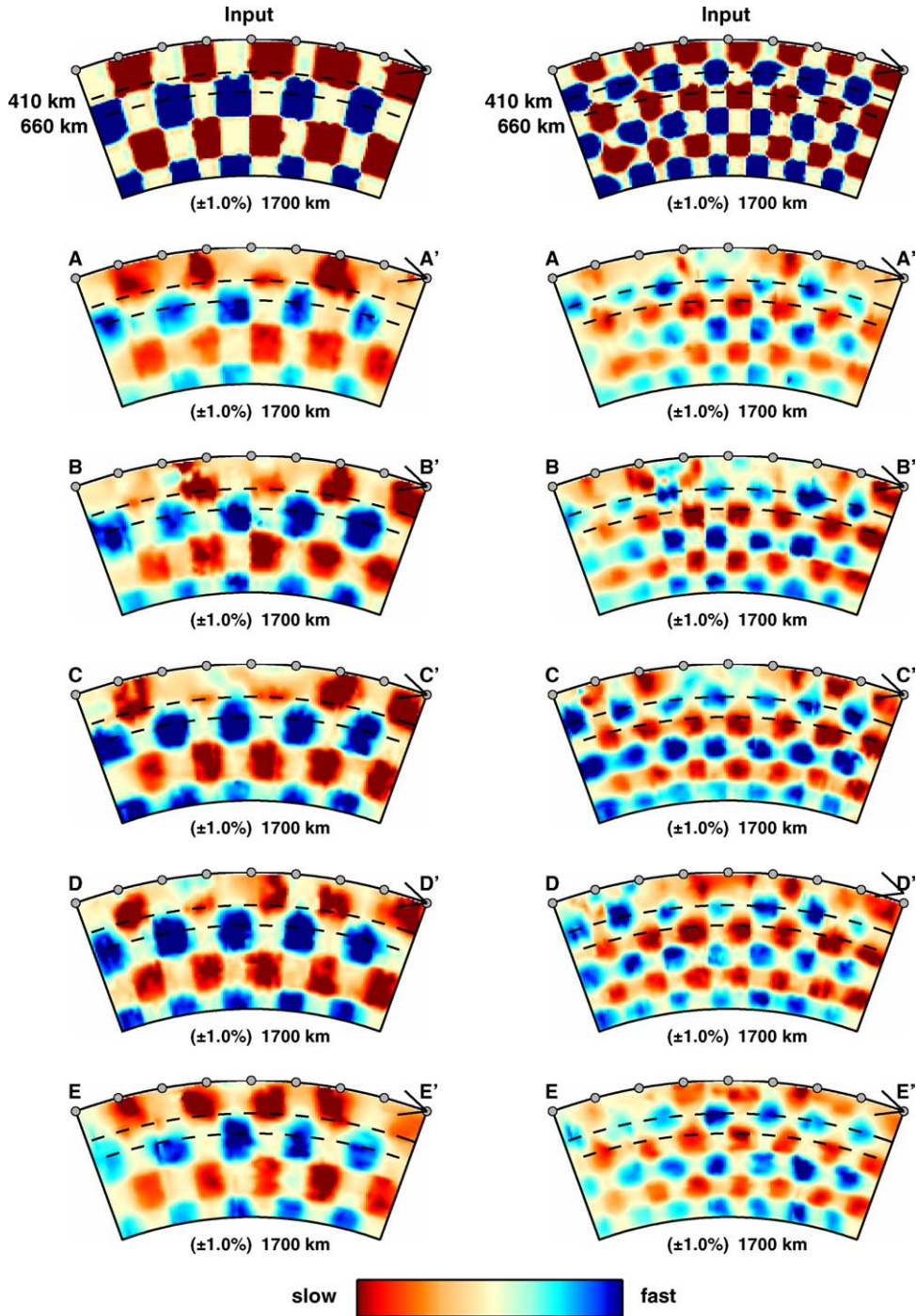


Fig. 7. Vertical checkerboard resolution tests at five slices, as depicted in Fig. 1. For each slice we use the same input pattern (shown at the top) with target anomalies of  $400 \text{ km} \times 400 \text{ km}$  (left) and  $280 \text{ km} \times 280 \text{ km}$  (right).

continues to  $\sim 660 \text{ km}$  depth. At depths greater than about  $660 \text{ km}$  another high-velocity anomaly is observable beneath north-central India (structure 2 in Fig. 8h). In Fig. 9a, this structure extends just near the  $660 \text{ km}$

discontinuity to deep in the lower mantle with a south-dipping angle, where it forms part of the large scale structure that has been interpreted as a remnant slab of late Mesozoic Tethys oceanic lithosphere prior to the

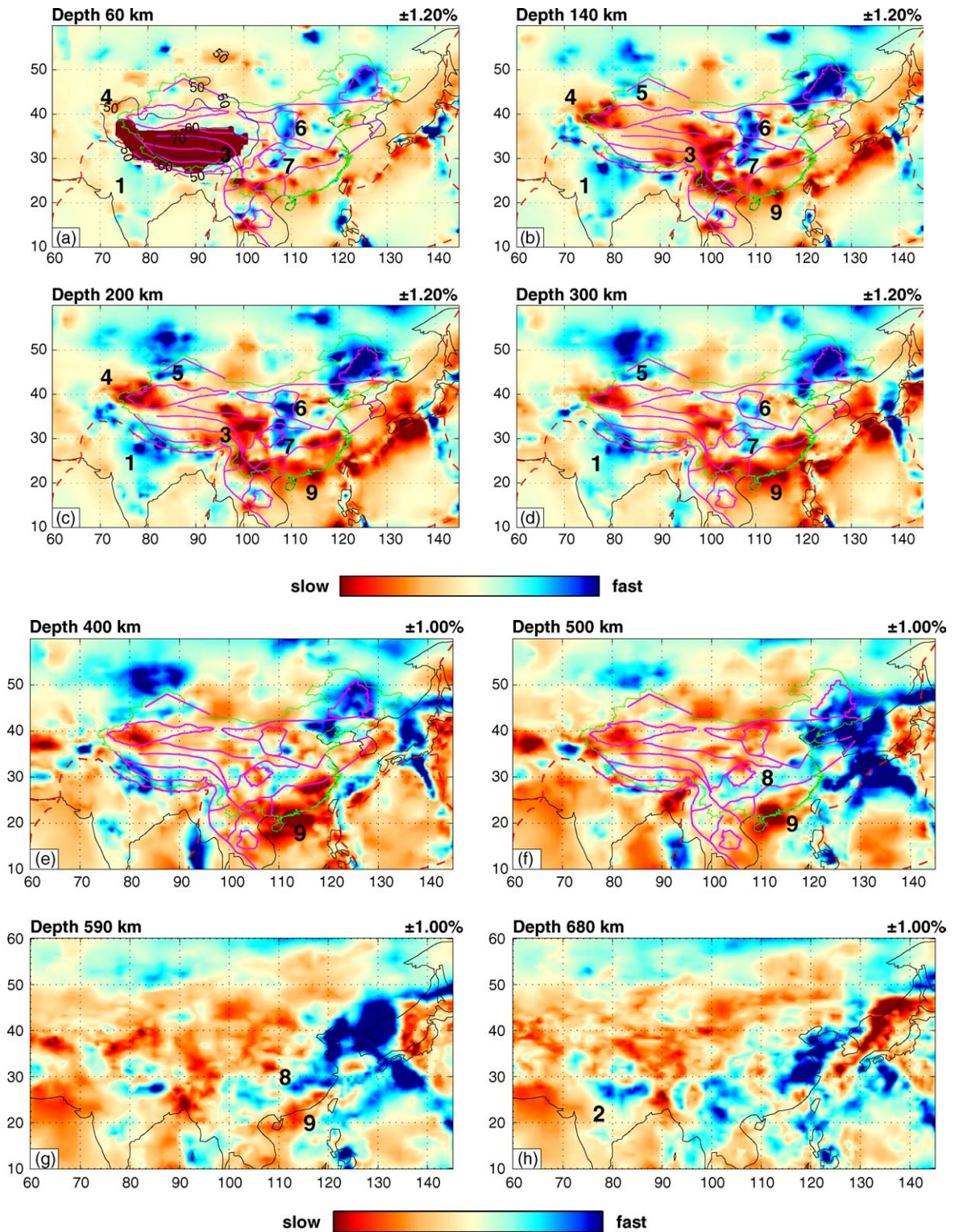


Fig. 8. Lateral  $P$  wavespeeds perturbation at different depths as indicated on the left corner. The blue and red represent fast and slow perturbation, respectively. The perturbation scale is shown on the right upper corner. The significant structures have labeled as 1, 2, 3, etc.



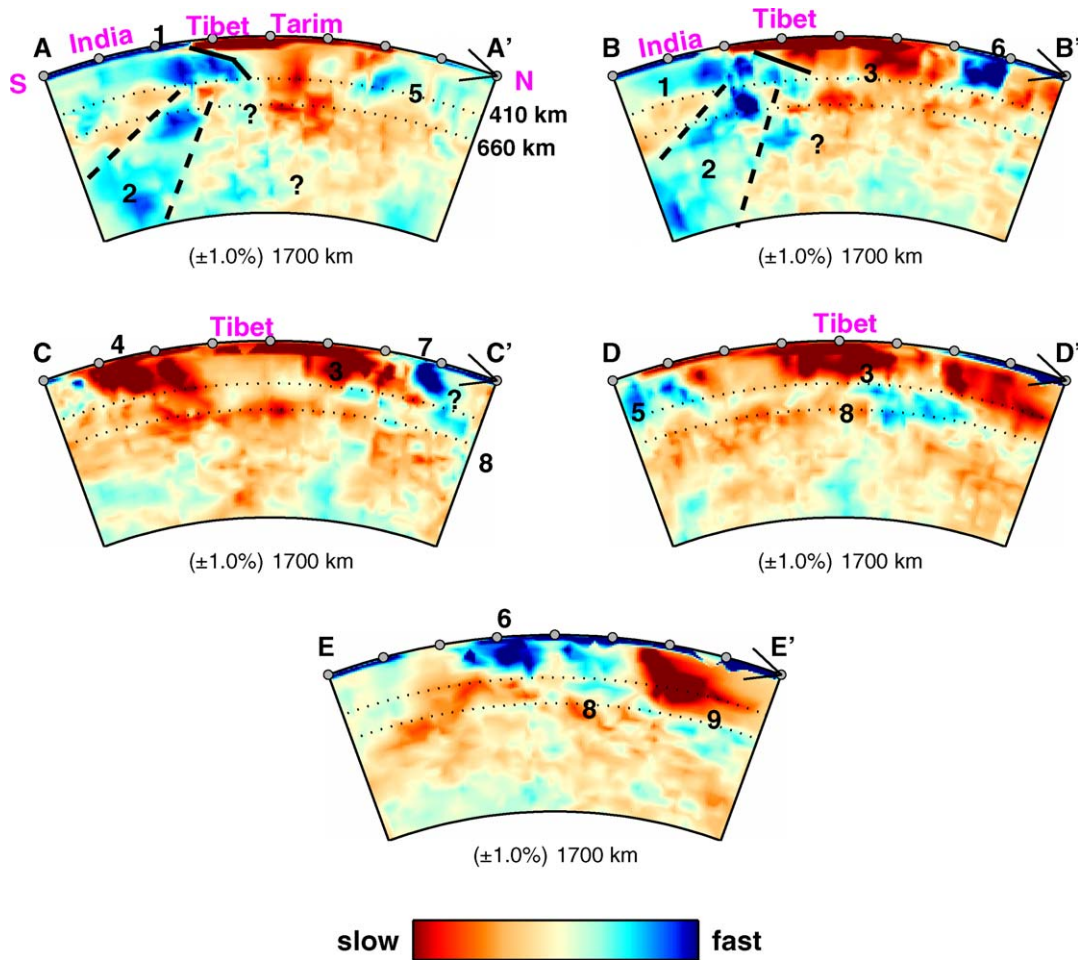


Fig. 9. Vertical cross-sections through some of the main features of the velocity model down to 1700 km depth. The locations of cross-sections AA', BB', CC', DD', and EE' are indicated in Fig. 1.

India-Eurasia collision (van der Hilst et al., 1997; Van der Voo et al., 1999; Replumaz et al., 2004). The spatial resolution of the current data coverage does not yet allow us to establish the structural relationship between the northward dipping structure 1 and the southward dipping structure 2.

#### 4.3.2. Upper mantle structure beneath eastern Tibet

Our results suggest that the shallow mantle beneath the southeastern part of Songpan Ganzi Foldbelt and eastern parts of the Tibetan Plateau is marked by very slow *P* wavespeeds (structure 3 in Fig. 8b). The wavespeeds would be artificially low if the actual crust is even slower than that in the a priori model used, but the resolution of shallow mantle structure is adequate (Fig. 6.2–6.4) so that leakage to large depths is unlikely. The slow velocity structure continues to 300–400 km depth (Figs. 8b–d and 9d). These results suggest that

this slow velocity structure extends beyond the eastern margin of Tibet and to depths well in excess of the thick crust. In fact, our images suggest that these slow structures connect to the slow wavespeeds in the upper mantle beneath South China Sea coast and, in particular, Hainan Island (Fig. 8d–e).

#### 4.3.3. Tian Shan and Tarim basin

Slow velocities beneath the Tian Shan and western part of the Tarim Basin seem to continue to at least 300 km depth (Structure 4 in Figs. 8a–d and 9c). In this depth range, no prominent high wavespeed feature is detected beneath the Tarim Basin, but the resolution beneath Tarim Basin is relatively poor. The shallow mantle beneath the Junggar Basin is marked by high *P* wavespeeds propagation (Structure 5 in Fig. 8b–d). Fig. 9a suggests that this structure may be dipping to the south.

#### 4.3.4. Mantle structure beneath the Archean cratons

Beneath the Sino-Korean Craton the most prominent feature is the high-velocity root extending down to 200 km beneath the Archean nucleus of the Ordos Basin (Structure 6 in Figs. 8a–d and 9b and e). This anomaly seems to be confined within the Ordos Basin boundary. Another high-velocity root, extending down to 200 km, underlies the eastern half of the Sichuan Basin (structure 7 in Figs. 8a–c and 9c). Below 200 km, this high-velocity root fades and changes to slow velocity structures. The resolution in the Sichuan and Ordos Basin is high (Fig. 6.2 and 6.3), so the high-velocity roots are not artifacts. Eastern migration of high-velocity root beneath the Sichuan Basin is probably effected by the collision between Indian and Eurasia plates. A large scale high-velocity anomaly appears in transition zone (410–660 km) beneath the Yangtze Craton (structure 8 in Figs. 8f–g and 9c and d) and the resolution in the transition zone is good (Fig. 6.5–6.8).

#### 4.3.5. South East China, Hainan Island

Beneath Southern and Southeastern China, and beneath Hainan Island, in particular, the  $P$  velocity is very low. At shallow depths the slow anomaly may connect westward, across the Youjiang Block, to the low wavespeeds beneath the Red River fault and the south-eastern part of the Songpan Ganzi Foldbelt (Fig. 8a–c). At larger depth, a pronounced slow velocity feature is

detected beneath the Hainan Island and the southern coast of China (structure 9 in Figs. 8d–g and 9d and e). Near 660 km depth, the wavespeed is not significantly different than the reference wavespeed according to *ak135* (Figs. 8h and 9d and e), in the top of the lower mantle a slow velocity feature appears again. This deeper structure is much weaker than the upper mantle and transition zone anomalies, and it is not distinctly slower than nearby slow anomalies. Other studies have argued for a lower mantle origin of the Hainan structure (e.g., Montelli et al., 2004), but the observations presented here suggest that the most prominent part is confined to the upper mantle and transition zone.

#### 4.4. Comparison to the other global model in the region

The model by Montelli et al. (2004) is more similar to our results than any other  $P$ -models that are publicly available. For this comparison we use their latest model (Montelli et al., in preparation), which has a different crust correction and, therefore, a better upper mantle structure than the one used for their 2004 publication. Fig. 10a and b depicts the anomalies at 140 and 400 km depth, and in Fig. 10c and d we show it for cross-sections BB' and DD'. The long wavelengths patterns agree quite well, although there are substantial differences in amplitude (with our amplitudes almost certainly too low). At

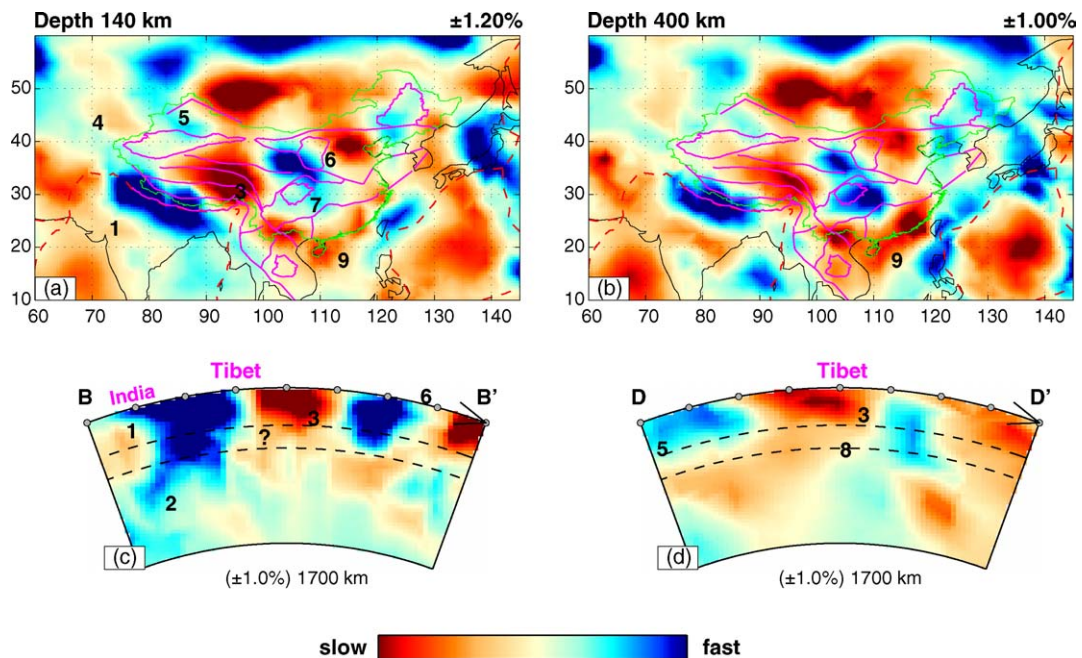


Fig. 10. (a and b) Lateral  $P$  wavespeeds perturbation of model from Montelli et al. (in preparation) at 140 and 400 km depth. (c and d) Vertical cross-sections along BB' and DD'.

shallow depth (Figs. 8b and 10a) we recognize similar fast anomalies beneath the boundary of Indian and Eurasian plates, north-eastern and central China, and to the north of Japan, and slow anomalies beneath the Tibetan Plateau, Hainan Island, and the coast of the South China Sea and to the south of Japan. At larger depth (Figs. 8e and 10b) both models show fast anomalies around western Pacific plate boundaries, but differences occur that could be due to the different types of regularization employed in these studies. These differences merit further investigation, but since our main interest is in the subcontinental mantle this is beyond the scope of this paper. On smaller length scales our model reveals more detail than the model by Montelli et al., which we attribute in part to our use of ABCE data and a higher resolution model for regional variations in crust structure.

## 5. Discussion

### 5.1. The seismic evidence for subduction of Indian lithosphere

The regional tomographic image of the upper mantle beneath central Tibet from the INDEPTH array has revealed a subvertical high-velocity zone from 100 to 400 km depth (Tilmann and Ni, 2003), which has been interpreted as the downwelling Indian lithosphere. This regional image covers the area from 29°N to 33.5°N, and therefore does not completely image the whole underthrusting Indian lithosphere beneath the Himalayan Frontal Thrust and the Tibetan plateau. In our model, the high wavespeeds associated with what is presumably subducted lithosphere is clearly visible beneath the boundary of Indian and Eurasian plates at 140 and 200 km depths (structure 1 in Fig. 8b and c). At larger depths, it trends further northward and mainly underlies beneath the western part of Himalayan Block and Lasha block (Fig. 8d and e). This is also visible in AA' (Fig. 9a). Although the relatively poor resolution beneath the northern Tibet leaves some room for alternate interpretations, our images suggest that the Indian lithosphere subducts from the foreland basin and underlies only the southwestern margin of the Tibet Plateau (thick blue line in Fig. 1), implying that much of the Tibet Plateau is not underlain by Indian but by Asian lithosphere (Tapponnier et al., 2001). This conclusion may be refined by analysis of the data from the MIT-CIGMR and Lehigh-CIGMR arrays, but if confirmed it has important implications for evolutionary models of the Tibetan plateau. The southward dipping high-velocity structure 2 in the lower mantle (Fig. 9a and b), interpreted as Neo-

Tethys oceanic lithosphere (van der Hilst et al., 1997; Van der Voo et al., 1999; Replumaz et al., 2004), seems to be separated from the subducted Indian lithosphere as it sinks below 660 km discontinuity, but this relationship will be subjected to further study.

### 5.2. Fast velocity structure within the TZ (410–660 km) beneath Yangtze Craton

Our images show that there is a significant high-velocity anomaly beneath the Yangtze Craton in the transition zone (structure 8 in Fig. 8f–h, Fig. 9c and d), which spans almost 2000 km from northeast to southwest (Fig. 8f). The high resolution at this depth ensures that this fast velocity anomaly is not artifacts. This large-scale high velocity structure may have a complex origin. The eastern part of these anomalies has been well documented in tomographic studies (e.g., van der Hilst et al., 1991; Fukao et al., 1992) and has been interpreted as “slab deflection” at the 660 km discontinuity as a result of slab roll back oceanward (van der Hilst and Seno, 1993). The strong anomalies in the transition zone east of ~120°E can probably be explained as the subducted ocean lithosphere of the western Pacific and Philippine Sea plates (Fig. 8f and g). It has been suggested that also the western part of the anomaly, between ~100°E and ~120°E, has been produced by subduction. Lebedev and Nolet (2003) interpreted the high S-wave velocity beneath the Sino-Korean Craton as the subducted continental lithosphere of the Yangtze Craton beneath the Sino-Korean Craton. But perhaps the anomaly between ~110°E and ~120°E is related in part to the Philippine Sea subduction and the anomaly between ~100°E and ~110°E might be associated with the eastward subduction of the Indian plate. We thus suggest that the explanation of this transition zone structure may involve other subduction systems than subduction of continental lithosphere alone.

### 5.3. Slow velocity structure beneath Eastern Tibet and South China Sea

In the image of the upper mantle beneath eastern Tibet, the most prominent feature is the large-scale low velocity structure (structure 3 in Figs. 8b and c and 9b–d) in the depth above 200 km. This structure is probably not an artifact of the thick crust since this contribution is corrected for, although it is possible that the crustal velocities are even slower than in the crustal model used for the correction. Preliminary results of receiver function and surface wave analysis of the MIT-CIGMR array data suggest the presence of slow velocity channels in



the crust below the Sichuan and Yunnan provinces (van der Hilst et al., 2005). The location of slow wave propagation also coincided with areas of local volcanism and high heat flow; for instance, the *P* wavespeed beneath the Tengchong volcano (25°N, 98°E), one of the few recently active volcanoes in mainland China, is anomalously low. Interestingly, this is also the area where the lower crust is thought to be sufficiently hot to undergo large-scale horizontal flow (Clark and Royden, 2000).

Our preliminary results suggest that the low wavespeeds are not confined to the crust but extend much deeper into the upper mantle. The slow velocity asthenospheric mantle beneath eastern Tibet is perhaps involved in large-scale extrusion driven by the Indian–Eurasian collision. Alternatively, it may be related to processes further to the southeast. The large low velocity anomaly beneath Hainan Island and the south coast of China extends down to 660 km (structure 9 in Figs. 8c–g and 9d and e) may represent a regional counter flow in response to subduction beneath nearby convergent margins. The images are suggestive of a connection between this structure and those in the shallow mantle beneath eastern Tibet (Fig. 8c). This intriguing spatial relationship is a subject of further study since it may suggest a relationship between the tectonics of eastern Tibet and mantle processes beneath the Hainan Island and South China Sea. If corroborated by further study, this connection would have major implications for our understanding of the geological history of the Tibetan plateau.

## 6. Conclusions

We have combined different seismic data sets and implemented a crustal correction in order to improve the tomographic imaging of the upper mantle beneath SE Asia. The images reveal significant heterogeneity in the upper mantle. First, high-velocity crustal roots (~200 km in thickness) are observed beneath most of the Precambrian Basins (Ordos Basin, Sichuan Basin, and Songliao Basin). Second, our results suggest that only the southwest part of the Tibetan plateau is underlain by lithospheric mantle involved in the subduction of the Indian plate. This implies that most of upper mantle beneath the Tibetan plateau is primarily of Asian origin, in agreement with, for instance, Tapponnier (2001). However, better resolution is required to establish the spatial and temporal relationship between the shallow and deep slabs. Subducted Indian lithosphere is detected to ~400 km depth and may be detached from the sinking ocean slab in the lower mantle. *P*-wave velocity is very slow beneath most of eastern Tibet where the lower crust

is thought to be sufficiently hot to undergo large-scale flow (Clark and Royden, 2000). This slow anomaly may extend across the western boundary of the Yangtze Craton and connect with the low velocity structures deeper in the mantle beneath the Youjiang Block and Hainan Island. If confirmed by further study, our results pertaining to the subduction of Indian lithosphere and the possible connection between shallow mantle structures beneath eastern Tibet and the south coast of China may change views about the tectonic evolution of SE Asia.

## Acknowledgements

We are indebted to Bob Engdahl for his ongoing research on the EHB dataset. We are also grateful to Raffaella Montelli for kindly providing us her new global model and to Youshun Sun for his 3D crust model. We benefited from the constructive discussion with Stéphane Rondenay, Bradford Hager, Leigh Royden, Clark Burchfiel, and Sergei Lebedev. We thank an anonymous reviewer for constructive comments, which have helped us improve the manuscript. This work was funded by NSF grant 6892042 of Collaborative Research in Eastern Tibet and AFRL grant FA8718-04-C-0018.

## References

- Abers, G.A., Roecker, S.W., 1991. Deep-structure of an arc-continent collision: Earthquake relocation and inversion for upper mantle *P* and *S* wave velocities beneath Papua New Guinea. *J. Geophys. Res.* 96, 6379–6401.
- Bassin, C., Laske, G., Masters, G., 2000. The current limits of resolution for surface wave tomography in North America. *EOS Trans. AGU* 81, F897.
- Bijwaard, H., Spakman, W., Engdahl, E.R., 1998. Closing the gap between regional and global travel time tomography. *J. Geophys. Res.* 103, 30055–30078.
- Boschi, L., Ekström, G., 2002. New images of the Earth's upper mantle from measurements of surface wave phase velocity anomalies. *J. Geophys. Res.* 107 (B4), 2059.
- Bolton, H., Masters, G., 2001. Travel times of *P* and *S* from global digital seismic networks: implication for the relative variation of *P* and *S* velocity in the mantle. *J. Geophys. Res.* 106, 13527–13540.
- Clark, M.K., Royden, L.H., 2000. Topographic ooze: building the eastern margin of Tibet by lower crustal flow. *Geology* 28, 703–706.
- Debayle, E., Kennett, B., Priestley, K., 2005. Global azimuthal seismic anisotropy and the unique plate-motion deformation of Australia. *Nature* 433, 509–512.
- DeMets, C., Gordon, R.G., Angus, D.F., Stein, S., 1990. Current plate motions. *Geophys. J. Int.* 101, 425–478.
- Ekström, G., Tromp, J., Larson, E., 1997. Measurements and global models of surface wave propagation. *J. Geophys. Res.* 102, 8137–8157.
- Engdahl, E.R., van der Hilst, R.D., Buland, R., 1998. Global teleseismic earthquake relocation with improved travel times and procedures for depth determination. *Bull. Seism. Soc. Am.* 88, 722–743.

- Friederich, W., 2003. The S-velocity structure of the East Asian mantle from inversion of shear and surface waveforms. *Geophys. J. Int.* 153, 88–102.
- Fukao, Y., Obayashi, M., Inoue, H., Nenbai, M., 1992. Subduction slabs stagnant in the mantle transition zone. *J. Geophys. Res.* 97, 4809–4822.
- Hearn, T., Wang, S., Ni, J., Xu, Z., Yu, Y., Zhang, X., 2004. Uppermost mantle velocities beneath China and surrounding regions. *J. Geophys. Res.* 109 (B11), 301.
- Huang, J., Zhao, D., Zheng, S., 2002. Lithospheric structure and its relationship to seismic and volcanic activity in southwest China. *J. Geophys. Res.* 107 (B10), 2055.
- Kárason, H., van der Hilst, R.D., 2000. Constraints on mantle convection from seismic tomography. In: M.A. Richards, R. Gordon, R.D. van der Hilst (Eds.), *History and Dynamics of Plate Motion*. Am. Geophys. Union, Geophys. Monogr. Ser., 121, 277–288.
- Kárason, H., van der Hilst, R.D., 2001. Tomographic imaging of the lowermost mantle with differential times of refracted and diffracted core phases (PKP Pdiff). *J. Geophys. Res.* 106, 6569–6587.
- Kárason, H., 2002. Constrains on mantle convection from seismic tomography and flow modeling. Ph.D. thesis, MIT.
- Kennett, B.L.N., Engdahl, E.R., Buland, R., 1995. Constrains on seismic velocities in the Earth from travel times. *Geophys. J. Int.* 122, 108–124.
- Kind, R., Ni, J., Zhao, W., Wu, J., Yuan, X., Zhao, L., Sandvol, E., Reese, C., Nabelek, J., Hearn, T., 1996. Mid-crust low velocity zone beneath the southern Lhasa block: Results from the INDEPTH-II earthquake recording program. *Science* 274, 1692–1694.
- Kind, R., Yuan, X., Saul, J., Nelson, D., Sobolev, S.V., Mechie, J., Zhao, W., Kosarev, G., Ni, J., Achauer, U., Jiang, M., 2002. Seismic Images of crust and upper mantle beneath Tibet: evidence for Eurasian plate subduction. *Science* 298, 1219–1221.
- Kosarev, G., Kind, R., Sobolev, S.V., Yuan, X., Hanka, W., Oreshin, S., 1999. Seismic evidence for a detached Indian lithospheric mantle beneath Tibet. *Science* 283, 1306–1309.
- Lebedev, S., Nolet, G., 2003. Upper mantle beneath Southeast Asia from S velocity tomography. *J. Geophys. Res.* 108, 2048–2074.
- Lebedev, S., Nolet, G., Meier, T., van der Hilst, R., 2005. Automated multimode inversion of surface and S waveforms. *Geophys. J. Int.* 162, 951–964.
- Li, Z.X., Tectonic history of the major East Asian lithosphere blocks since the mid-Proterozoic. In: Flower M. et al. (Eds.), *Mantle Dynamics and Plate Interactions in East Asia*, *Geodyn. Ser.*, 27, 211–243.
- Liang, C.T., Song, X.D., Huang, J.L., 2004. Tomographic inversion of Pn travel times in China. *J. Geophys. Res.* 109 (B11), 304.
- Molnar, P., Tapponnier, P., 1975. Cenozoic tectonics of Asia: effects of a continental collision. *Science* 189, 419–426.
- Montelli, R., Nolet, G., Dahlen, F.A., Masters, G., Engdahl, E.R., Hung, S.H., 2004. Finite-frequency tomography reveals a variety of plumes in the mantle. *Science* 303, 338–343.
- Northrup, C., Royden, L., Burchfiel, B., 1995. Motion of the Pacific plate relative to Eurasia and its potential relation to Cenozoic extension along the eastern margin of Eurasia. *Geology* 23, 719–722.
- Paige, C.C., Saunders, M.A., 1982. LSQR: an algorithm for sparse linear equations and sparse least squares. *ACM Trans. Math. Soft.* 8, 43–71.
- Replumaz, A., Kárason, H., van der Hilst, R.D., Besse, J., Tapponnier, P., 2004. 4-D evolution of SE Asia's mantle from geological reconstructions and seismic tomography. *Earth Planet. Sci. Lett.* 211, 103–115.
- Rapine, R., Tilmann, F., West, M., Ni, J., 2003. Crustal structure of northern and southern Tibet from surface wave dispersion analysis. *J. Geophys. Res.* 108 (B2), 2120, doi:10.1029/2001JB000445.
- Shapiro, N.M., Ritzwoller, M.H., 2002. Monte-Carlo inversion for a global shear-velocity model of the crust and upper mantle. *Geophys. J. Int.* 151, 1–18.
- Sol, S.J., Meltzer, A., Zurek, B., Zhang, X., Zhang, J., 2004. Insight into the lithospheric structure and deformation in Eastern Tibet from splitting and travel time variations of core phases, *Eos Trans. AGU*, 85(47), Fall Meet. Suppl., Abstract, T31A-1279.
- Sun, Y., Li, X., Kuleli, S., Morgan, F.D., Toksöz, M.N., 2004. Adaptive moving window method for 3D P-velocity tomography and its application in China. *Bull. Seism. Soc. Am.* 94, 740–746.
- Tapponnier, P., Molnar, P., 1977. Active faulting and tectonics in China. *J. Geophys. Res.* 82, 2905–2930.
- Tapponnier, P., Zhiqin, X., Roger, F., Meyer, B., Arnaud, N., Wittlinger, G., Jingsui, Y., 2001. Oblique stepwise rise and growth of the Tibet Plateau. *Science* 294, 1671–1677.
- Tilmann, F., Ni, J., 2003. Seismic imaging of the downwelling Indian lithosphere beneath central Tibet. *Science* 300, 1424–1427.
- Trampert, J., Woodhouse, J., 1995. Global Phase-velocity maps of Love and Rayleigh waves between 40 and 150 s. *Geophys. J. Int.* 122, 675–690.
- van der Hilst, R.D., Engdahl, E.R., Spakman, W., Nolet, G., 1991. Tomographic imaging of subducted lithosphere below northwest Pacific island arcs. *Nature* 353, 37–43.
- van der Hilst, R.D., Seno, T., 1993. Effects of relative plate motion on the deep structure and penetration depth of slabs below the Izu-Bonin and Mariana island arcs. *Earth Planet. Sci. Lett.* 120, 395–407.
- van der Hilst, R.D., Widiyantoro, S., Engdahl, E.R., 1997. Evidence for deep mantle circulation from global tomography. *Nature* 386, 578–584.
- van der Hilst, R.D., Chen, Z., Li, C., Lev, E., Xu, L., Yao, H., 2005. Crust and Upper Mantle Structure Beneath Sichuan/Yunnan Provinces, SW China: Preliminary Results of a Joint MIT-CIGMR Broad-Band Seismometry Project. *Trans. Am. Geophys. Un. Spring Meeting*, Abstract, S41A-01.
- Van der Voo, R., Spakman, W., Bijwaard, H., 1999. Tethyan subducted slabs under India. *Earth Planet. Sci. Lett.* 171, 7–20.
- Waldhauser, F., Lippitsch, R., Kissling, E., Ansorge, J., 2002. High-resolution teleseismic tomography of upper-mantle structure using an a priori three-dimensional crustal model. *Geophys. J. Int.* 150, 403–414.
- Wang, C.Y., Chan, W., Mooney, W., 2003. Three-dimensional velocity structure of crust and upper mantle in southwestern China and its tectonic implications. *J. Geophys. Res.* 108 (B9), 2442, doi:10.1029/2002JB001973.
- Weidle, C., Widiyantoro, S., CALIXTO Working Group, 2005. Improving depth resolution of teleseismic tomography by simultaneous inversion of teleseismic and global P-wave travel time data: application to the Vrancea region in Southeastern Europe. *Geophys. J. Int.* 162, 811–823.
- Widiyantoro, S., van der Hilst, R.D., 1997. Mantle structure beneath Indonesia inferred from high-resolution tomographic imaging. *Geophys. J. Int.* 130, 167–182.
- Widiyantoro, S., van der Hilst, R.D., 1996. Structure and evolution of lithospheric slab beneath the Sunda arc, Indonesia. *Science* 271, 1566–1570.
- Zhang, Z.M., Liou, J.G., Coleman, R.G., 1984. An outline of the plate tectonics of China. *Geol. Soc. Am. Bull.* 95, 295–312.

# Surface-wave array tomography in SE Tibet from ambient seismic noise and two-station analysis – I. Phase velocity maps

Huajian Yao,<sup>1</sup> Robert D. van der Hilst<sup>1</sup> and Maarten V. de Hoop<sup>2</sup>

<sup>1</sup>Department of Earth, Atmospheric, and Planetary Sciences, Massachusetts Institute of Technology, Cambridge, MA, 02139, USA. E-mail: [hjyao@mit.edu](mailto:hjyao@mit.edu)

<sup>2</sup>Center for Computational and Applied Mathematics, Purdue University, West Lafayette, IN, 47907, USA

Accepted 2006 March 30. Received 2006 March 30; in original form 2006 February 1

## SUMMARY

Empirical Green's functions (EGFs) between pairs of seismographs can be estimated from the time derivative of the long-time cross-correlation of ambient seismic noise. These EGFs reveal velocity dispersion at relatively short periods, which can be used to resolve structures in the crust and uppermost mantle better than with traditional surface-wave tomography. We combine Rayleigh-wave dispersion estimates from EGFs and from traditional two-station (TS) analysis into a new approach to surface-wave array tomography with data from dense receiver arrays. We illustrate the methodology with continuous broad-band recordings from a temporary seismographic network on the southeastern part of the Tibetan plateau, in Sichuan and Yunnan provinces, SW China. The EGFs are robust under temporal changes in regional seismicity and the use of either ambient noise (approximated by records without signal from events with magnitude  $m_b \geq 5$  or 4) or surface wave coda produces similar results. The EGFs do not strongly depend on the presence of large earthquakes, but they are not reciprocal for stations aligned in the N–S direction. This directionality reflects the paucity of seismicity to the north of the array. Using a far-field representation of the surface-wave Green's function and an image transformation technique, we infer from the EGFs the Rayleigh-wave phase velocity dispersion in the period band from 10–30 s. A classical TS approach is used to determine Rayleigh-wave phase velocity dispersion between 20–120 s. Together, they constrain phase velocity variations for  $T = 10$ –120 s, which can be used to study the structure from the crust to the upper mantle. Beneath SE Tibet, short and intermediate period (10–80 s) phase velocities are prominently low, suggesting that the crust and upper mantle beneath SE Tibet is characterized by slow shear wave propagation.

**Key words:** array tomography, empirical Green's functions, phase velocity, SE Tibet, surface waves, two-station method.

## 1 INTRODUCTION

Surface-wave tomography based on ballistic waves propagating from a source to multiple receivers has provided important information about the 3-D shear wave velocity structure in the upper mantle both on a global (Trampert & Woodhouse 1996; Shapiro & Ritzwoller 2002, to name but a few) and regional (e.g. Zielhuis & Nolet 1994; Simons *et al.* 2002; Huang *et al.* 2003) scale. In these studies, depth resolution is obtained from (fundamental and/or higher mode) group or phase velocity dispersion, with the low-frequency component constraining deeper structures than the high-frequency ones. Accurate imaging of the shallow part of the lithosphere, including the crust, is of particular interest for understanding the relationships between mantle dynamics and geologic processes at or near the surface. Unfortunately, if one considers surface-wave dispersion along source–receiver paths, the resolution of structure in the relevant depth range is often limited by: (1) scattering at the short-period part ( $T < 30$  s) of the waveforms; (2) inadequate path

coverage due to the uneven distribution of seismic sources and receivers; (3) insufficient information about the seismic source; and (4) uncertainties about the spatial characteristics of the surface-wave sensitivity kernel (e.g. Spetzler *et al.* 2002; Yoshizawa & Kennett 2002; Zhou *et al.* 2004).

Recent studies show that surface-wave Green's function between two seismograph stations can be estimated from the long-time cross-correlation of coda waves (Campillo & Paul 2003) and ambient seismic noise (Shapiro & Campillo 2004; Shapiro *et al.* 2005; Sabra *et al.* 2005a). The surface-wave periods considered in these studies are shorter than those that can (reliably) be used in traditional analyses of source–receiver propagation. Moreover, measurements can, in principle, be made for any pair of receivers within seismograph arrays, and the dense path coverage thus produced enables high-resolution surface-wave tomography (Shapiro *et al.* 2005; Sabra *et al.* 2005b). Previous studies used group velocity dispersion extracted from the noise cross-correlation function (Shapiro & Campillo 2004; Shapiro *et al.* 2005)—hereinafter referred to as



NCF—or from its time derivative, the empirical Green's function (Sabra *et al.* 2005a,b)—hereinafter EGF. Theoretically, the time derivative of the NCF is equivalent to the Green's function except for a frequency-dependent amplitude factor (Lobkis & Weaver 2001; Weaver & Lobkis 2004; Roux *et al.* 2005), but in contrast to the real Green's functions, which are by definition reciprocal and independent of the seismic source, the EGFs that are estimated from actual coda waves or ambient seismic noise may be time asymmetrical due to the inhomogeneous distribution of noise sources and attenuation (Paul *et al.* 2005; Sabra *et al.* 2005a).

Group dispersion measurements rely on amplitude information and may, therefore, be affected by distortion of the amplitude spectrum of the EGF. The phase information in EGFs estimated from the NCF is, however, theoretically the same as that of the real Green's function. In this paper we demonstrate that accurate phase velocity dispersion measurements can be obtained from the EGF by using the far-field representation of the surface-wave Green's function and an image transformation technique.

Traditional global and regional surface-wave tomography relies on relatively long period data and assumes integration over wave paths—or finite frequency kernels—between source and receivers that are often many thousands of kilometres apart. Such approaches cannot fully exploit the potential data redundancy (and resulting spatial resolution) provided by dense receiver arrays. In principle, better spatial localization can be obtained with the classical two-station (TS) method (Knopoff *et al.* 1966), which measures phase-velocity dispersion between two stations in the intermediate and longer periods range using cross-correlation. For example, Passier *et al.* (1997) use the TS approach to SKIPPY array data in Australia. Brisbane & Stuart (1998) invert shear wave velocity structure beneath North Island, New Zealand, from Rayleigh-wave interstation phase velocities. Recently, Yao *et al.* (2005) introduce an image transformation technique to measure interstation phase velocity dispersion and presented Rayleigh-wave phase velocity maps from 15 to 120 s in western China and adjacent regions.

Here we explore how the Rayleigh-wave phase velocity dispersion data from the Green's function and the TS methods can be integrated into a method for high-resolution surface-wave array tomography of continental lithosphere. We show applications to data from a temporary array of 25 broad-band seismometers operated by MIT and CIGMR (Chengdu Institute of Geology and Mineral Resources) on the southeastern Tibetan plateau, in Sichuan and Yunnan provinces, SW China (Fig. 1). We carry out the analysis up to the construction of phase velocity maps for surface-wave periods of 10–120 s. The inversion for and interpretation of shear heterogeneity in the crust and upper mantle beneath the study region will be presented elsewhere (Yao, Beghein, Van der Hilst, in preparation, 2006).

## 2 EMPIRICAL GREEN'S FUNCTION (EGF)

We calculate EGFs from continuous vertical component seismograms recorded from 2004 April to July. The instrument response has been removed from all the data prior to cross-correlation. We conduct several experiments to test the robustness of the EGFs for temporal variations and directionality of the 'noise' signals. First, we compare EGFs calculated for different time periods. Second, we compare the EGFs reconstructed from data in different frequency bands and discuss the effects of the spatial distribution of the 'noise' sources. Third, we calculate EGFs from ambient seismic 'noise' using records in which signal from known earthquakes (considering

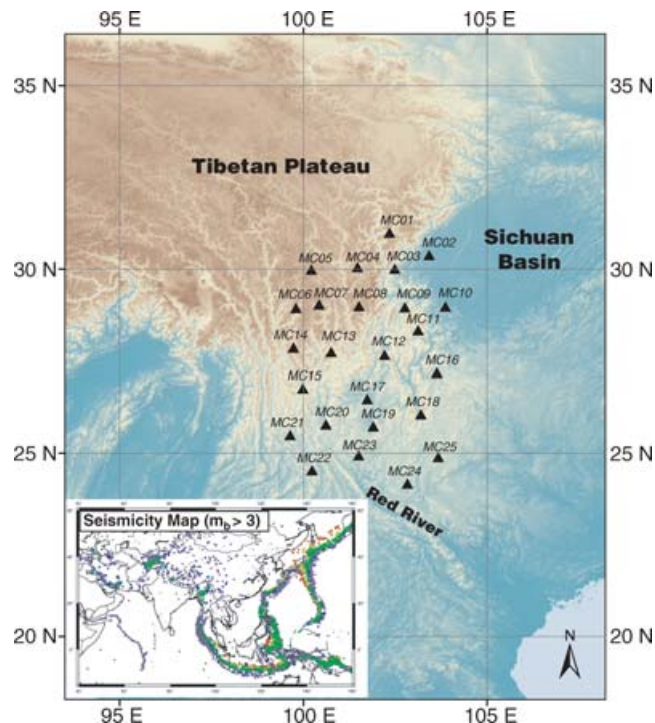


**Figure 1.** The location of 25 stations of the MIT-CIGMR array. The inset (lower left): epicenter of earthquakes with  $m_b > 3$  that occurred in 2004 (Engdahl *et al.* 1998).

different magnitude cut-offs) is suppressed. Fourth, for comparison, we also calculate EGFs explicitly from the surface-wave coda. In this paper we use the term 'noise' rather loosely either for scattered waves or for the parts of the records that are not directly related to (known) large events. In the latter case, 'noise' may contain signal from background seismicity, not just microseismic activity.

### 2.1 Noise correlation

Previous studies (Lobkis & Weaver 2001; Weaver & Lobkis 2004; Roux *et al.* 2005; Sabra *et al.* 2005a) have demonstrated that EGFs obtained from the noise cross-correlation function (NCF), by taking the time derivative, are equivalent to real Green's function except for a frequency-dependent amplitude correction. For hypothetical seismograph stations at position A and B, the relationship between the NCF,  $C(t)$ , the EGF,  $\hat{G}(t)$ , and the real (unknown) Green's function,  $G(t)$ , can be represented as

$$\frac{dC_{AB}(t)}{dt} = -\hat{G}_{AB}(t) + \hat{G}_{BA}(-t) \approx -G_{AB}(t) + G_{BA}(-t). \quad (1)$$

Here, the approximation indicates that the EGF,  $\hat{G}(t)$ , may differ from the exact Green's function,  $G(t)$ , because of effects of anelasticity and specific spatial distribution and spectral properties of the (ambient) noise (Roux *et al.* 2005; Paul *et al.* 2005). Later in this section we will illustrate some of these effects, but for notational simplicity we will drop the distinction of  $\hat{G}$  and  $G$ . In eq. (1),  $G_{AB}(t)$  is the actual Green's function at receiver B for a fictitious (point) source located at A, and  $G_{BA}(-t)$  is the time-reversed Green's function at A for a fictitious (point) source at B. In view of causality,  $G_{AB}(t)$  contributes at  $t \geq 0$  and  $G_{BA}(-t)$  contributes at  $t \leq 0$ . Furthermore,  $C_{AB}(t)$  is the approximate cross-correlation function between

the two stations given by

$$C_{AB}(t) \approx \int_0^{t_C} v_A(\tau) v_B(t + \tau) d\tau, \quad (2)$$

where  $v_A(t)$  and  $v_B(t)$  are the continuously recorded, but time-windowed broad-band data at stations A and B, respectively, and  $t_C$  is the total cross-correlation time (i.e. observation time).

The  $\pi/2$  phase shift between EGF and NCF does not influence estimates of the group velocity between points A and B: indeed, some studies use NCFs (Shapiro & Campillo 2004; Shapiro *et al.* 2005), whereas others prefer to use EGFs because the time derivation enhances the higher frequencies (Sabra *et al.* 2005a,b). The change in amplitude spectrum may, however, affect the group velocity measurements. In contrast, phase velocities do not depend on the amplitude information, but ignoring the phase shift produces an error, which becomes significant if the interstation distance AB is comparable to or less than the wavelengths considered. In this study, we compute the phase velocities from the EGFs.

## 2.2 Temporal variations from microseisms and scatter

To test the robustness of the EGFs we compute them for different time periods: for this purpose, we arbitrarily choose the months of 2004 April, May, June, and July. In a first set of experiments, we use a (generous) group-velocity window ( $2\text{--}10 \text{ km s}^{-1}$ ) to mute the wave trains from earthquakes with  $m_b \geq 6$  (that is, in the corresponding group-velocity window we set the amplitude to zero) in order to approximate cross-correlations from ambient ‘noise’ (which includes signal that is not directly related to large events). We follow Campillo & Paul (2003) and Shapiro & Campillo (2004) to compute for every possible station pair the NCF by one-bit cross-correlation of the vertical component seismograms which are both band-pass filtered in the period bands 10–60 s. We do this for each month separately. The time  $t$  in eq. (2) is from  $-t_m$  to  $t_m$ ;  $t_m = \Delta/v_m$ , with  $\Delta$  the interstation distance and  $v_m$  the minimum group velocity, which is set to be  $1.5 \text{ km s}^{-1}$ . Figs 2(a) and 3 show, for different station pairs, that the EGFs constructed from recordings in the different months are similar to one another.

## 2.3 Directionality and amplitude spectrum

Theoretically, the Green’s functions  $G_{AB}(t)$  and  $G_{BA}(-t)$  should be each others reciprocal. However, EGFs may become one sided due to preferred directions to noise sources, for example, the ocean microseisms in the study by Sabra *et al.* (2005a). For our study, Figs 2(a), 3(a), (c) and (d) reveal a clear directionality: the EGFs for station pairs lining up in N–S direction are one sided whereas the stations lining up in E–W direction are much more symmetric (e.g. Fig. 3b).

In order to investigate if this difference depends on frequency, for station pair MC04–MC23 we compute EGFs in different period bands (10–20, 20–30, 30–40, and 40–60 s) (Fig. 4). In the period bands 10–20 s (Fig. 4a) and 20–30 s (Fig. 4b) the EGFs are one sided and stable over the 4 months. However, in the period bands 30–40 s (Fig. 4c) and 40–60 s (Fig. 4d) the EGFs do not show the one-sided feature and the different months yield different results. Similar frequency dependencies are observed for other station pairs.

The EGFs in the period bands 10–20 s (Fig. 4a) are very similar to those for 10–60 s (Fig. 2a). Amplitude spectra, shown in Fig. 5 for April, reveal that the dominant frequency band of the EGFs is

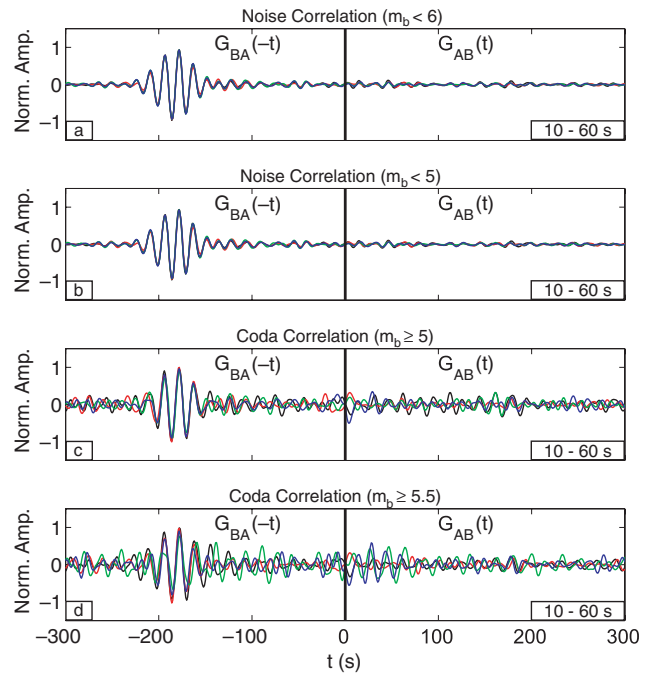


**Figure 2.** EGFs in the period bands 10–60 s from one-bit cross-correlation of vertical component ambient seismic noise (a, b) and surface-wave coda (c, d) of the two-station pair MC04–MC23 for 4 months in 2004 (black—April, red—May, green—June and blue—July). The right half ( $t > 0$ ) and the left half ( $t < 0$ ) of each plot represent the EGF from MC04 (source) to MC23 (receiver) and the EGF from MC23 to MC04, respectively. For (a), using a group-velocity window, wave trains from earthquakes with  $m_b \geq 6.0$  are muted for both stations before the cross-correlation, and the same for (b) but with  $m_b \geq 5.0$ . For (c) only surface-wave coda from earthquakes with  $m_b \geq 5.0$  are kept for the cross-correlation and the same for (d) but with  $m_b \geq 5.5$ . ‘Norm. Amp.’ on the vertical axis means ‘normalized amplitude’.

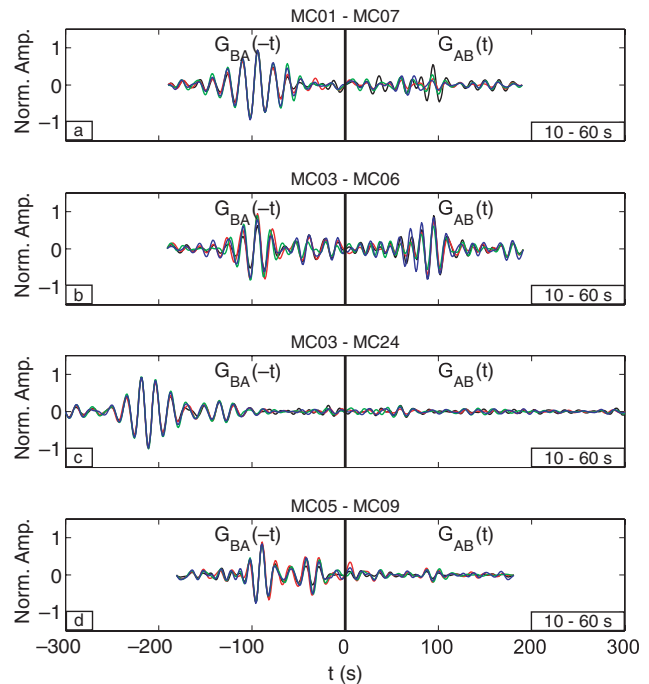


**Figure 3.** EGFs (normalized amplitude) from the cross-correlation of ambient seismic noise of different station pairs in the period bands 10–60 s for 4 months in 2004 as in Fig. 2(a).

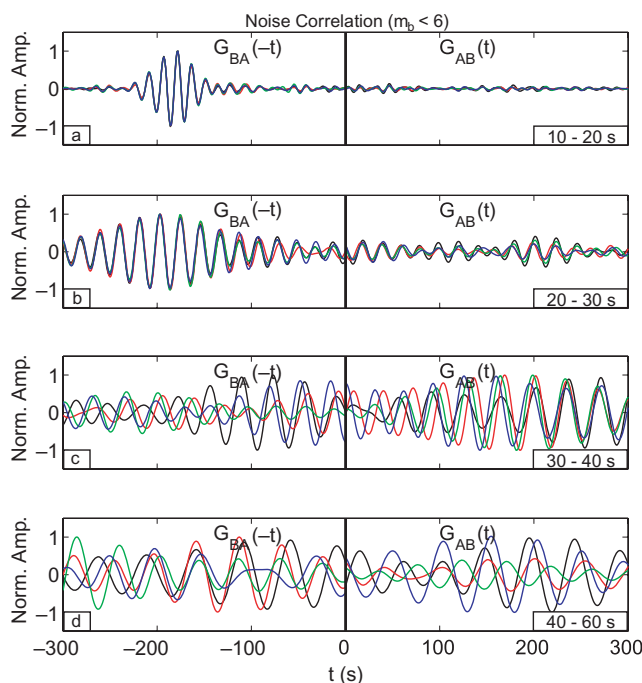


**Figure 4.** EGFs (normalized amplitude) from the cross-correlation of ambient seismic noise of the two-station pair MC04-MC23 for 4 months in 2004 as in Fig. 2(a) but in different period bands: (a) 10–20 s; (b) 20–30 s; (c) 30–40 s; and (d) 40–60 s.

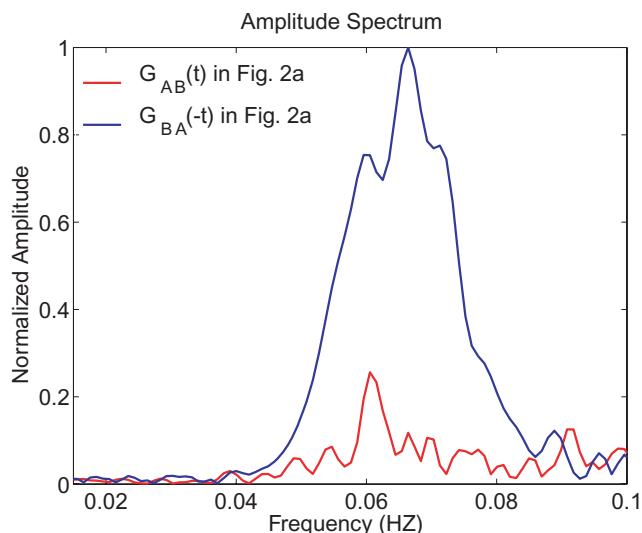


**Figure 5.** Amplitude spectrum of the EGF of the two-station pair MC04-MC23 for 2004 April (black waveform in Fig. 2a): blue line for the left part of the EGF and red line for the right part of the EGF.

~0.08–0.05 Hz (i.e. ~12–20 s) and that their energy is very low at frequencies less than 0.04 Hz (or periods larger than 25 s). The latter may explain the instability of the EGFs observed in Figs 4(c) and (d); the low-frequency waves do not create coherent waves between the station pair. It seems reasonable to assume that the one-sided feature (that is, the failure of reciprocity) in EGFs for the N–S direction is primarily due to the significant lack of seismicity north of the array (Fig. 1, inset), in combination with interstation scattering. However, it is not obvious why the expression of this is so different in the intermediate or longer period bands ( $T > 30$  s), and the part of the

data that contributes to the EGFs at periods larger than 30 s should be investigated further.

## 2.4 Effects on EGFs of specific earthquakes and noise signals

By definition, a Green's function represents the solution due to a point source and is unrelated to the actual source. This is not, generally, true for EGFs. Indeed, because uneven regional distribution of background seismicity can produce directionality of the EGFs (see above), we should investigate if the presence of large earthquakes can produce bias. For that purpose, we compute EGFs, for  $T = 10$ –60 s, after muting signal related to (known) earthquakes with  $m_b \geq 5$  (instead of the  $m_b \geq 6$  used in the experiment described above). The results, shown (again) for station pair MC04-MC23 (Fig. 2b), are almost the same as for input data void only of the signal due to larger earthquakes (Fig. 2a). Tests with magnitude cut-off at 4 or 3 give similar results, which implies that the effect on EGFs from specific earthquakes is small compared to the contributions from microseismicity and ambient noise.

## 2.5 EGFs from surface-wave coda

It has been demonstrated that the diffusive character of coda waves due to multiple scattering in the lithosphere can be used to estimate the Green's functions between two seismic stations (Campillo & Paul 2003; Paul *et al.* 2005). Therefore, complementary to calculating EGFs from background seismic noise (approximated by the muting of signal from large earthquakes), we calculate them (again with one-bit cross-correlation) from the coda of the surface waves due to large earthquakes. For this purpose we mute much of the data and only keep the surface-wave coda (in the group velocity window  $1.5$ – $3$  km s $^{-1}$ ) from larger earthquakes with  $m_b \geq 5$ . The EGFs estimated from the surface-wave coda (Fig. 2c) are almost the same (in the surface-wave part) as the EGFs from ambient seismic noise (previous section), but they become increasingly unstable when the magnitude cut-off increases and when, as a consequence, the number of data decreases (Fig. 2d). Similar to the EGFs from ambient seismic noise (Figs 2a and b), the EGFs from coda correlation (Fig. 2c, d) also show time asymmetry due to the predominant directions in the source distribution (Paul *et al.* 2005).

## 3 PHASE VELOCITY DISPERSION FROM EGFs

Previous studies estimated group velocity dispersion from NCFs (Shapiro & Campillo 2004; Shapiro *et al.* 2005) or EGFs (Sabra *et al.* 2005a,b). Here we demonstrate that phase velocity dispersion can be calculated from the EGF through the use of a far-field representation of the surface-wave Green's function and an image transformation technique (Yao *et al.* 2005). In the far field, the time harmonic wave of the Green's function for the surface-wave fundamental mode at frequency  $\omega$  is given by (Dahlen & Tromp 1998)

$$\text{Re}\{G_{AB}(\omega) \exp(-i\omega t)\} \approx (8\pi kS)^{-1/2} \cos\left(k_{AB}\Delta - \omega t + \frac{\pi}{4}\right), \quad (3)$$

where  $k_{AB} = \frac{1}{\Delta} \int_0^\Delta k d\Delta = \frac{\omega}{c_{AB}}$  is the average wavenumber between 'source' A and receiver B,  $c_{AB}$  is the average phase velocity,  $\Delta$  is the surface distance traversed by the arrival under consideration between 'source' A and receiver B,  $S$  is the geometrical spreading



for surface waves such that  $S \rightarrow \sin(\Delta/R)$  ( $R$  is the radius of the Earth) towards the source, and  $\frac{\pi}{4}$  is remnant of the asymptotic expansion of the Legendre function. We require  $\Delta$  to be at least three wavelengths ( $\lambda$ ) in order to satisfy the far-field approximation. When the phase traveltimes  $t$  satisfies

$$k_{AB}\Delta - \omega t + \frac{\pi}{4} = 0; \quad (4)$$

it will correspond to one peak in the harmonic wave of Green's function. At that point the average phase velocity  $c_{AB}$  at frequency  $\omega$  can be calculated by

$$c_{AB}(T) = \frac{\Delta}{t - T/8}, \quad (5)$$

where  $T = 2\pi/\omega$  is the corresponding period. With the far-field limitation, we require

$$c_{AB} \cdot T = \lambda \leq \Delta/3. \quad (6)$$

For each station pair, eq. (6) determines the largest period to be considered; effectively it produces denser path coverage at shorter periods than at longer periods. For multiresolution imaging this has the attractive property that path coverage will be densest for the shortest period waves considered.

We now illustrate how to extract the phase velocity dispersion curve from the EGF using the far-field approximation and an image

transformation technique. First, we band-pass filter the EGFs at central periods from 10 to 60 s, with 1 s intervals and a pass-band width of 0.4 s. (We remark that for non-symmetric correlation functions the side with the larger amplitude is used as the EGF for subsequent analyses—for example, the left side of Fig. 2a.) Then, we construct a time-period ( $t - T$ ) image (e.g. Fig. 6a) for the surface-wave part (determined by a group-velocity window, for example, 2.5–5 km s<sup>-1</sup>). Each column of the  $t - T$  image represents an amplitude normalized EGF filtered at certain period  $T$  (the black trace in Fig. 6(a) is for  $T = 20$  s). On the  $t - T$  image the frequency dependence is readily observed; notice, for instance, the increase of the phase traveltimes with decreasing period (Fig. 6a).

Each column of the  $t - T$  image (e.g. the black trace in Fig. 6a) is then transformed to a velocity-coordinate waveform (black trace in Fig. 6b) using eq. (5) and a spline interpolation in order to get an evenly spaced velocity coordinate and to keep the amplitude information unchanged upon transformation. Thus, a peak point at the filtered EGF (e.g.  $P$  in Fig. 6a) will have the same phase velocity as that of the corresponding peak at the transformed waveform (e.g.  $P^*$  in Fig. 6b). We use this procedure to transform the  $t - T$  image to a velocity-period ( $c - T$ ) image (Fig. 6b). On the  $c - T$  image the dispersion curve can be easily identified and automatically picked, and the  $2\pi$  ambiguity in phase velocity measurement is well resolved. This image transformation technique, introduced by Yao *et al.* (2005) to measure phase velocities for the TS method,

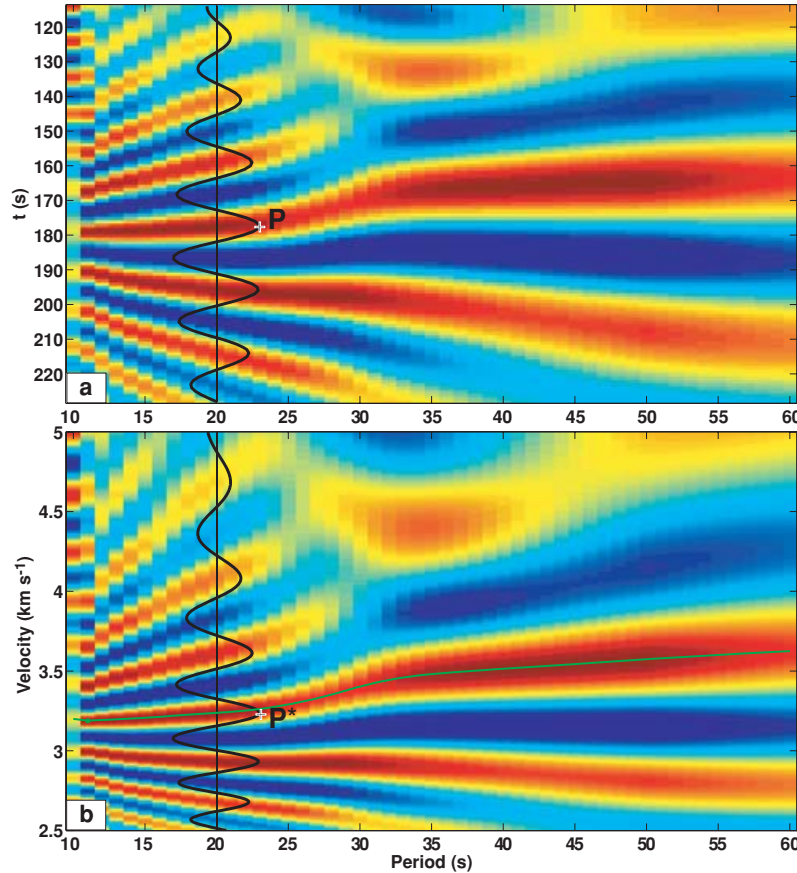


**Figure 6.** Phase velocity dispersion measurements from the EGF of MC23-MC04 in 2004 April: (a) time-period ( $t - T$ ) image by narrow band-pass filtering the EGF; the black waveform is the normalized EGF filtered at the central period  $T = 20$  s, which corresponds to the column at the  $T = 20$  s on the  $t - T$  image; (b) velocity-period ( $c - T$ ) image and phase velocity dispersion measurements (solid green line); the black waveform, which corresponds to the column at the  $T = 20$  s on the  $c - T$  image, is the transformed velocity coordinate waveform from the waveform in (a) using eq. (5) and a spline interpolation. Red and blue on (a) and (b) represent the peak and trough of the wave trains, respectively. The peak point  $P$  at the waveform in (a) is transformed to the peak point  $P^*$  at the waveform in (b).



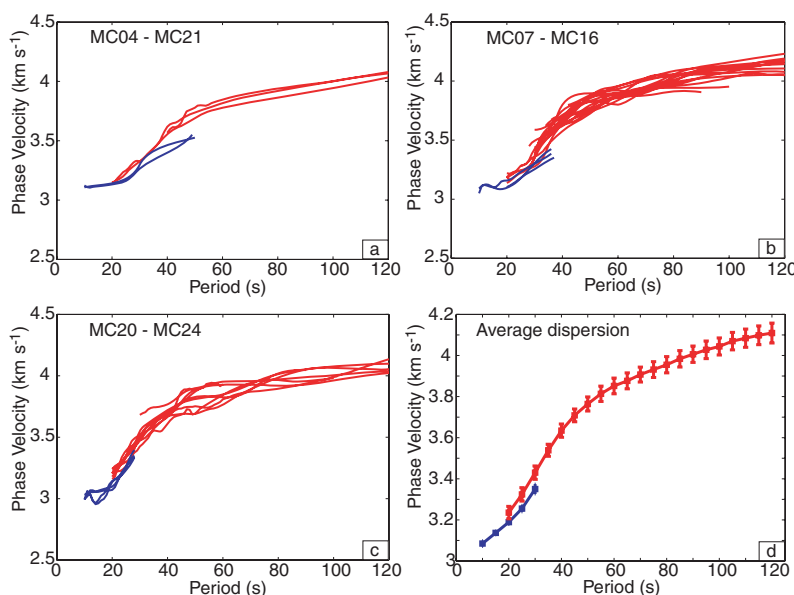


**Figure 7.** Rayleigh-wave phase velocity dispersion measurements from the EGF and TS analysis: (a–c) Rayleigh-wave phase velocity dispersion curves of different two-station paths from the EGF analysis for different months (blue lines) and from the TS analysis for different earthquakes (red lines); (d) average Rayleigh-wave phase velocity dispersion curve and the average standard errors for the studied area from the EGF analysis (blue line and error bars in the period bands 10–30 s) and from the TS method (red line and error bars in the period bands 20–120 s).

greatly enhances the efficiency and reliability of phase velocity measurements. Compared to the measurement of the group traveltime (i.e. the time of the (broad) peak at the envelope) that is needed to determine the group velocities (e.g. Shapiro & Campillo 2004; Sabra *et al.* 2005a), the measurement of the peak traveltime for the phase velocities appears to be more accurate.

We infer the Rayleigh-wave phase velocity dispersion (e.g. blue lines in Figs 7a, b and c) for  $T = 10$ –50 s from vertical component EGFs for all possible two-station paths for the 4 months considered. Recall that the maximum period for the phase velocity measurement of each station pair is set by eq. (6) and, thus, the distance between the pair of receivers considered. For each path we calculate the average phase velocity and its standard error at each period. Finally, we obtain the average phase velocities for the array area (with the corresponding standard errors) by averaging the phase velocity (and its standard error) for all paths (Fig. 7d). The standard errors are quite small (about  $0.01 \text{ km s}^{-1}$  at 10–20 s,  $0.015 \text{ km s}^{-1}$  at 25 s, and  $0.024 \text{ km s}^{-1}$  at 30 s), which shows that EGFs from one-bit cross-correlation of 1 month of ambient seismic noise can give precise phase velocity measurements at the relatively short periods considered here (i.e. 10–30 s). For the phase velocity maps presented in the next section we do not use EGF-derived phase velocity measurements at the periods larger than 30 s because at longer periods the EGFs are less robust, in part because the far-field approximation (6) and the lateral extent of the array limit the number of data at those periods.

## 4 PHASE VELOCITY MAPS

### 4.1 Phase velocity maps from EGFs

We use the technique by Tarantola & Valette (1982) and Tarantola & Nercissian (1984) to invert the phase velocity dispersion measurements from EGFs to obtain the Rayleigh-wave phase velocity variation at different periods. We first obtain the phase slowness (the inverse of the phase velocity) maps by minimization of the cost

function

$$\Phi(\mathbf{s}) = (\mathbf{t} - \mathbf{t}_{\text{obs}})^T \mathbf{C}_D^{-1} (\mathbf{t} - \mathbf{t}_{\text{obs}}) + (\mathbf{s} - \mathbf{s}_p)^T \mathbf{C}_M^{-1} (\mathbf{s} - \mathbf{s}_p); \quad (7)$$

from this we calculate the phase velocity distribution. In eq. (7),  $\mathbf{s}$  is the 2-D phase slowness model,  $\mathbf{s}_p$  is the *prior* 2-D phase slowness model,  $\mathbf{t}_{\text{obs}}$  is the vector of observed phase traveltimes (the  $i$ th component is given by  $(\mathbf{t}_{\text{obs}})_i = \Delta_i/c_i$ ,  $i$  runs through all combinations AB, see eq. 5),  $\mathbf{t}$  is the predicted phase traveltime from the phase slowness model  $\mathbf{s}$ ,  $\mathbf{C}_D$  is the data covariance matrix describing the data uncertainties, and  $\mathbf{C}_M$  is the *prior* model covariance function.

The predicted phase traveltime for the  $i$ th path is determined by  $t_i = \int_0^{\Delta_i} s d\Delta$ , where the integral is along the great-circle path and  $\Delta_i$  is the interstation distance. The region under study is parametrized by means of  $0.5^\circ \times 0.5^\circ$  grid points. The phase slowness  $s$  at any point in the inversion area is determined from the values at four surrounded grid points using bilinear interpolation. The *prior* model covariance function  $\mathbf{C}_M(r_1, r_2)$  represents the covariance between model estimates at  $r_1$  and  $r_2$ :

$$\mathbf{C}_M(r_1, r_2) = \sigma_s^2 \exp\left(-\frac{(r_1 - r_2)^2}{2L^2}\right), \quad (8)$$

where  $\sigma_s = \sigma_c/c_0^2$  represents the *prior* slowness uncertainty,  $\sigma_c$  is the *prior* phase velocity uncertainty with respect to the homogenous starting model with phase slowness  $1/c_0$ , and  $L$  is the correlation length of the model. We set  $\sigma_c$  to  $0.15 \text{ km s}^{-1}$ , and  $c_0$  is the average phase velocity (at a certain period) in the region. On the basis of results from resolution tests, we choose the correlation length  $L$ , which determines the smoothness of the phase slowness maps, to be 100 km.

In order to investigate whether the phase velocity measurements from different months influence the inversion results, we invert the phase velocities at  $T = 10$  s of each of the 4 months under consideration to obtain the Rayleigh-wave phase velocity maps for the four separate months using a homogeneous starting model. The results (Fig. 8) are quite similar to one another, which confirms the stability of the EGFs with regard to temporal variations in regional

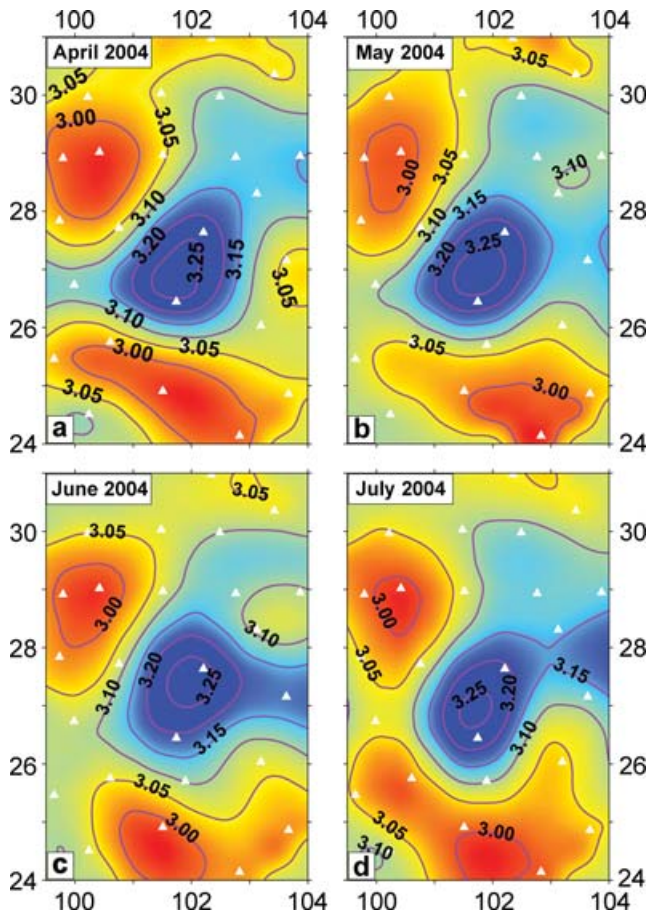


**Figure 8.** Comparison of inverted phase velocity maps at period  $T = 10$  s for four different months from the EGF analysis. White triangles show station location. The contour values are Rayleigh-wave phase velocities ( $\text{km s}^{-1}$ ). Red and blue represents lower and higher velocity, respectively.

(micro-)seismicity. Subsequently, we use the phase velocities for each path averaged over the 4 months to obtain the phase velocity maps at 10, 15, 20, 25 and 30 s. Figs 9(a)–(c) shows the path coverage for the averaged dispersion data at  $T = 10, 20$ , and 30 s. At 10 s the number of averaged phase velocity measurements is 267, which is close to the maximal number (300) of two-station measurements for a seismic array with 25 stations. A series of checkerboard resolution tests suggests that in much of the area under study the horizontal resolution of the phase velocity maps derived from the EGFs is  $\sim 100$  km (Fig. 10b). Figs 11(a)–(c) show examples of phase velocity maps at  $T = 10, 20$ , and 30 s.

We evaluated the reliability of the phase velocity measurements from EGFs by a comparison with group velocities. Ignoring the distortion of the amplitude spectrum, we use a frequency–time analysis to measure from EGFs the group velocities in the period band 10–30 s. Using  $g = d\omega/dk = c + k \cdot dc/dk$ , with  $c$  and  $g$  the phase and group velocities, respectively, we then predict  $c$  from the measured  $g$ . The average absolute discrepancy between  $c$  thus inferred and the phase velocities measured directly from EGFs gradually increases from  $\sim 0.01$   $\text{km s}^{-1}$  at  $T \sim 10$  s to  $\sim 0.04$   $\text{km s}^{-1}$  at  $T \sim 30$  s, which for our study region is about an order of magnitude smaller than the observed variation ( $\sim 0.3$ – $0.4$   $\text{km s}^{-1}$ , Figs 11(a)–(c)). Compared to the average phase velocities inferred directly from EGFs (Fig. 7d), the average phase velocities derived from the group velocities are  $0.01$ – $0.02$   $\text{km s}^{-1}$  higher in the period band 20–30 s, which may

indicate that at these periods the phase velocity measurements are slightly underestimated (by about  $\sim 0.3$ – $0.6$  per cent). The discrepancy increase with increasing period, suggesting that phase velocity measurements at shorter periods (10–20 s) are more reliable than at relatively longer periods ( $T > 20$  s), in accord with Fig. 7(d).

#### 4.2 Phase velocity maps from two-station (TS) method

We use a TS method (Yao *et al.* 2005) to measure Rayleigh-wave fundamental-mode phase velocity dispersion in the period bands 20–120 s. We assume surface-wave propagation along a great-circle path between earthquake and station. For each two-station dispersion measurement, in order to suppress the influence of the structure between the earthquake and the station nearest to it, we require that the earthquake and the station pair considered are (approximately) on the same great circle path, with the maximum two deviation angles ( $\alpha$  and  $\beta$  in Fig. 12a) each less than  $3^\circ$ . The average phase velocity of the two-station path is then approximated by

$$c(T) \approx \frac{\Delta_2 - \Delta_1}{\Delta t(T)}, \quad (9)$$

where  $c(T)$  is the phase velocity at period  $T$ ,  $\Delta t(T)$  is the phase traveltime at period  $T$  estimated from cross-correlation of narrow band-pass filtered waveforms at central period  $T$  at the two stations,<sup>1</sup>  $\Delta_2$  is the distance from the earthquake to the farthest station, and  $\Delta_1$  is the distance to the nearest station. For a small difference in propagation distance, a small error  $\delta t$  in the measurement of  $\Delta t(T)$  will cause a considerable error in the phase velocity measurements, in particular at longer periods. For example, if  $\Delta_2 - \Delta_1 = 200$  km,  $\Delta t = 60$  s at  $T = 20$  s (i.e.  $c \sim 3.33$   $\text{km s}^{-1}$ ),  $\Delta t = 48$  s at  $T = 100$  s (i.e.  $c \sim 4.17$   $\text{km s}^{-1}$ ), and  $\delta t = 1$  s, the relatively error in the phase velocity measurement  $\delta c/c = \delta t/\Delta t$  is  $\sim 1.7$  per cent at  $T = 20$  s and  $\sim 2.1$  per cent at  $T = 100$  s. In order to make reliable measurements at relatively longer periods, we require  $\Delta_2 - \Delta_1$  to be at least half of the wavelength ( $\lambda = c(T) \cdot T$ ); here we refer to this as the half-wavelength criterion. Consequently, the available phase velocity measurements decrease as the period increases (Figs 9d–j), which yields a relatively high path density at the shorter periods and lower path density at the longer periods. Note that this has an effect similar to the effect of the far-field approximation described above.

In this way, we obtain about 600 phase velocity dispersion curves for  $T = 20$ – $120$  s from about 160 earthquakes with  $5.0 \leq M_w \leq 7.0$  and depth  $< 100$  km from 2003 October to 2004 September (Fig. 13). Fig. 14 shows an example of phase velocity measurements using the image transformation technique. Red lines in Figs 7(a)–(c) show the extracted dispersion curves for three two-station paths from different earthquakes. Phase velocity dispersion measurements for the same two-station path are averaged to make 158 average dispersion curves within the period bands 20–120 s, and the standard errors of the phase velocities are calculated for paths with at least two measurements. The average phase velocities (red line in Fig. 7d) and the corresponding standard errors (red error bars in Fig. 7d) for  $T = 20$ – $120$  s are then obtained by averaging all the phase velocity measurements and the standard errors for each period. The standard error increases with increasing period mainly

<sup>1</sup> We note that, formally speaking, the measurement yielded by time domain cross-correlation is not the traveltime proper and should be interpreted with the appropriate finite frequency sensitivity kernel (see, e.g. Dahlen *et al.* 2000; De Hoop & Van der Hilst 2005).

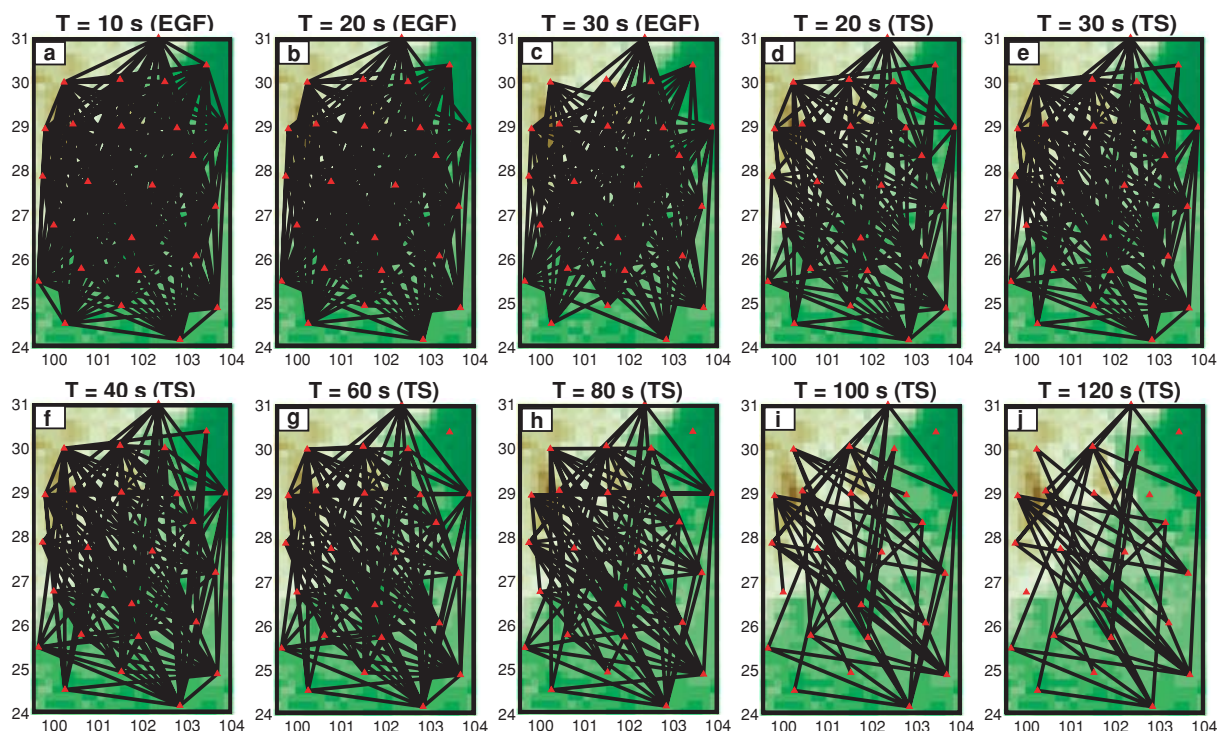


**Figure 9.** Path coverage of Rayleigh-wave phase velocity measurements at different periods: (a–c) for the EGF analysis using the average phase velocity dispersion data over 4 months for each path; (d–j) for the TS method using the average phase velocity dispersion data over different earthquakes for each path. Red triangles show the location of stations. This figure demonstrates that the path coverage is densest where it is needed most, namely, at short periods, whereas the coverage for lower frequency data (which constrain the longer wavelength structures) is much sparser.

due to the decrease of the interstation phase traveltime  $\Delta t(T)$ . At the short and intermediate periods (20–80 s), the standard error is about  $0.03\text{--}0.04\text{ km s}^{-1}$ . However, the standard error increases to  $\sim 0.05\text{ km s}^{-1}$  at 120 s. The standard error given here are lower estimates because we do not consider errors from other sources, for example, scattering, off-great-circle propagation, etc.

The path coverage of the average phase velocity measurements at different periods, shown in Figs 9(d)–(j), is quite good at periods 20–80 s but only about 40 measurements could be made at longer periods (100–120 s) due, in part, to the half wavelength criteria and, in part, to the relatively poor data quality at these long periods. We use the same inversion scheme as described in Section 4 to produce phase velocity maps for  $T = 20\text{--}120\text{ s}$ , except that we set the correlation length  $L$  to 100 km at 20–60 s, to 150 km at 65–80 s, and to 200 km at 85–120 s in view of the fact that the physical resolution is limited by the predominant wavelengths considered. The phase velocity maps at 20, 30, 40, 60, 80, 100 and 120 s are shown in Figs 11(d)–(j). The lateral resolution of these maps is about 100–200 km at 20–60 s (Figs 10c and e) and 200–300 km at 65–120 s (Fig. 10f).

### 4.3 Wave speed variations beneath SE Tibet and SW China

In a separate study (Yao *et al.* 2006) the phase velocity maps will be inverted for 3-D shear wave velocity structure of the crust and upper mantle. Here we merely make some first order observations. In the entire frequency band considered here, high phase velocities mark the (north)eastern part of the array area, close to the Sichuan Basin. In contrast, phase velocity maps at short and intermediate pe-

riods ( $T = 10\text{--}80\text{ s}$ ), shown in Figs 11(a)–(h), exhibit a pronounced low-velocity structure in the northwestern part of the array area (SE Tibet), which suggests a low shear wave velocity structure in the crust and upper mantle. At  $T = 100\text{--}120\text{ s}$  this low-velocity anomaly is mapped further South (Figs 11i and j). These results are—at least qualitatively—consistent with the finding from traveltime that  $P$ -wave propagation is anomalously slow in the upper mantle beneath SE Tibet and the Red River area (Li *et al.* 2006), which may be of relevance for geodynamical models of lower or middle crustal flow as suggested by Royden *et al.* (1997) and Beaumont *et al.* (2004).

## 5 DISCUSSION: COMPARISON OF THE EGF AND TS RESULTS

Phase velocity dispersion measurements were obtained from the EGF and TS analysis in different period bands. The phase velocities at the relatively short period bands (20–30 s) are similar for both methods (Figs 7a, b and c), but the discrepancies become larger ( $>2$  per cent) at periods larger than 30 s (e.g. Fig. 7a). The average phase velocities from the EGF analysis are  $0.046\text{ km s}^{-1}$ ,  $0.069\text{ km s}^{-1}$ ,  $0.080\text{ km s}^{-1}$  lower than the results from the TS method at 20, 25, and 30 s, respectively. Note that these differences exceed the uncertainties for either method which suggests that the discrepancy may be systematic. Comparison of the phase velocity maps at 20 s (Figs 11b and d) and 30 s (Figs 11c and e) shows that the overall low- and high-velocity features are quite similar but that the TS method gives phase velocities that are about 1–3 per cent higher than the EGF results.

Several factors can contribute to this discrepancy. For the EGF analysis, in addition to the possibility of (slightly) underestimating



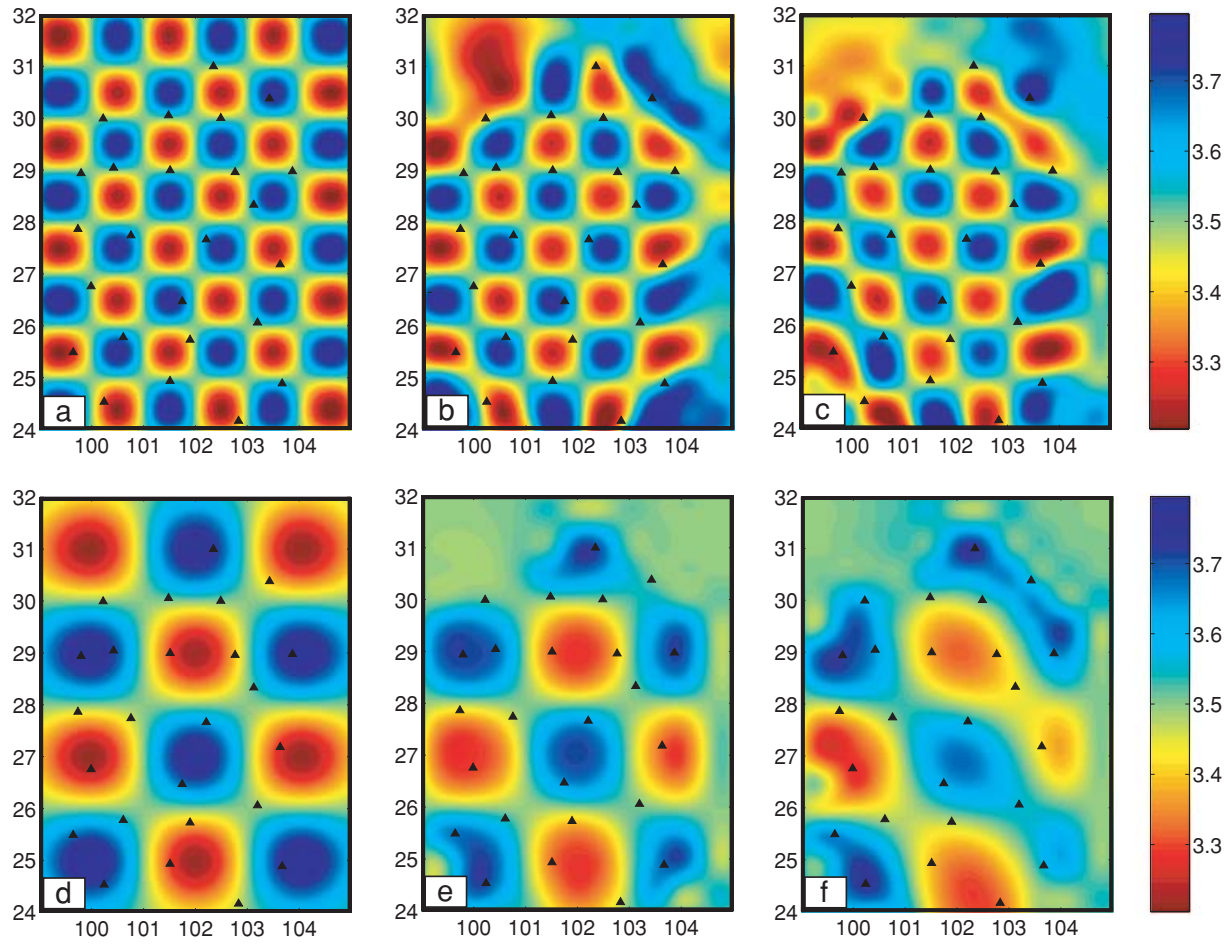


**Figure 10.** Resolution tests: (a) input  $1^\circ \times 1^\circ$  model; (b) recovery of  $1^\circ \times 1^\circ$  model for the path coverage at  $T = 10$  s (EGF) shown as Fig. 9(a); (c) recovery of  $1^\circ \times 1^\circ$  model for the path coverage at  $T = 40$  s (TS) shown as Fig. 9(f); (d) input  $2^\circ \times 2^\circ$  model; (e) recovery of  $2^\circ \times 2^\circ$  model for the path coverage at  $T = 60$  s (TS) shown as Fig. 9(g); (f) recovery of  $2^\circ \times 2^\circ$  model for the path coverage at  $T = 80$  s (TS) shown as Fig. 9(h). Black triangles show the location of stations. The values of the colour bar are Rayleigh-wave phase velocities ( $\text{km s}^{-1}$ ).

the phase velocity measurements (see remarks at the end of Section 4.1), the error in the estimation of interstation phase velocities mainly comes from: (1) incomplete recovery of the Green's function due to the inhomogeneous distribution of the noise sources; and (2) off-great-circle propagation due to interstation velocity anomalies. The first effect is hard to quantify, but the observed stability of the EGFs between 10–30 s suggests that it is relatively small. The second will underestimate interstation phase velocities because the length of off-great-circle paths is always larger than that of great-circle paths (Fig. 12b).

For the TS method there are other sources of inaccuracy. The incoming surface waves are approximated as plane waves. If surface waves propagate along the great-circle path (solid parallel lines with arrow in Fig. 12c), the interstation phase velocity ( $c_{gc}$ ) is estimated by  $c_{gc} \approx (\Delta_2 - \Delta_1)/\Delta t \approx d_{A'B}/\Delta t$ , where  $\Delta_1$ ,  $\Delta_2$ , and  $\Delta t$  are the same as those defined in eq. (9), and  $d_{A'B}$ , the difference in great-circle propagation distance between two stations, is the distance of the solid line  $A'B$  in Fig. 12(c). When the incoming surface wave (dashed parallel lines with arrow in Fig. 12c) deviates from the great-circle propagation path with angle  $\theta$  (defined in Fig. 12c), the interstation phase velocity of this off-great-circle propagation ( $c_{ogc}$ ) is estimated by  $c_{ogc} \approx d_{A''B}/\Delta t$ , where  $d_{A''B}$ , the difference in off-great-circle propagation distance between two stations, is the

distance of the dashed line  $A''B$  in Fig. 12(c). Therefore, the ratio  $c_{ogc}/c_{gc} = d_{A''B}/d_{A'B} = \cos(\beta + \theta)/\cos \beta$ , where  $\beta$  is the deviation angle in Fig. 12(c) which is same as that in Fig. 12(a). For a very small angle (in our study  $\beta \leq 3^\circ$ ), the ratio  $c_{ogc}/c_{gc}$  is less than 1 almost for all  $\theta$  except in a very small range  $-2\beta \leq \theta \leq 0^\circ$  (Fig. 15), which indicates that the interstation phase velocity measurements based on the approximation of great-circle propagation will commonly give a higher estimation (e.g. if  $\beta = 0^\circ$ , the phase velocity is  $\sim 1.5$  per cent higher estimated when  $\theta = 10^\circ$  as shown in Fig. 15).

Other reasons for the frequency-dependent discrepancy of phase velocities between the two methods include the fact that the surface-wave sensitivity zone in the TS method is much larger than the zone of sensitivity to structure in the case of the EGF analysis as shown in Fig. 12(d), especially at longer periods (Yoshizawa & Kennett 2002; Spetzler *et al.* 2002; Zhou *et al.* 2004). In contrast, the measurements from the EGF analysis are only sensitive to heterogeneity in a very narrow zone between the two stations (Fig. 12d), which provides a much higher resolution of the structure along the two-station path. Most earthquakes used for the TS analysis are located to the southeastern direction of the array (Fig. 13); the broader sensitivity kernel for the TS method mainly samples areas with relatively high velocities (e.g. Sichuan basin), whereas wave speeds under the array are mainly slow. This would result in a higher estimation of phase



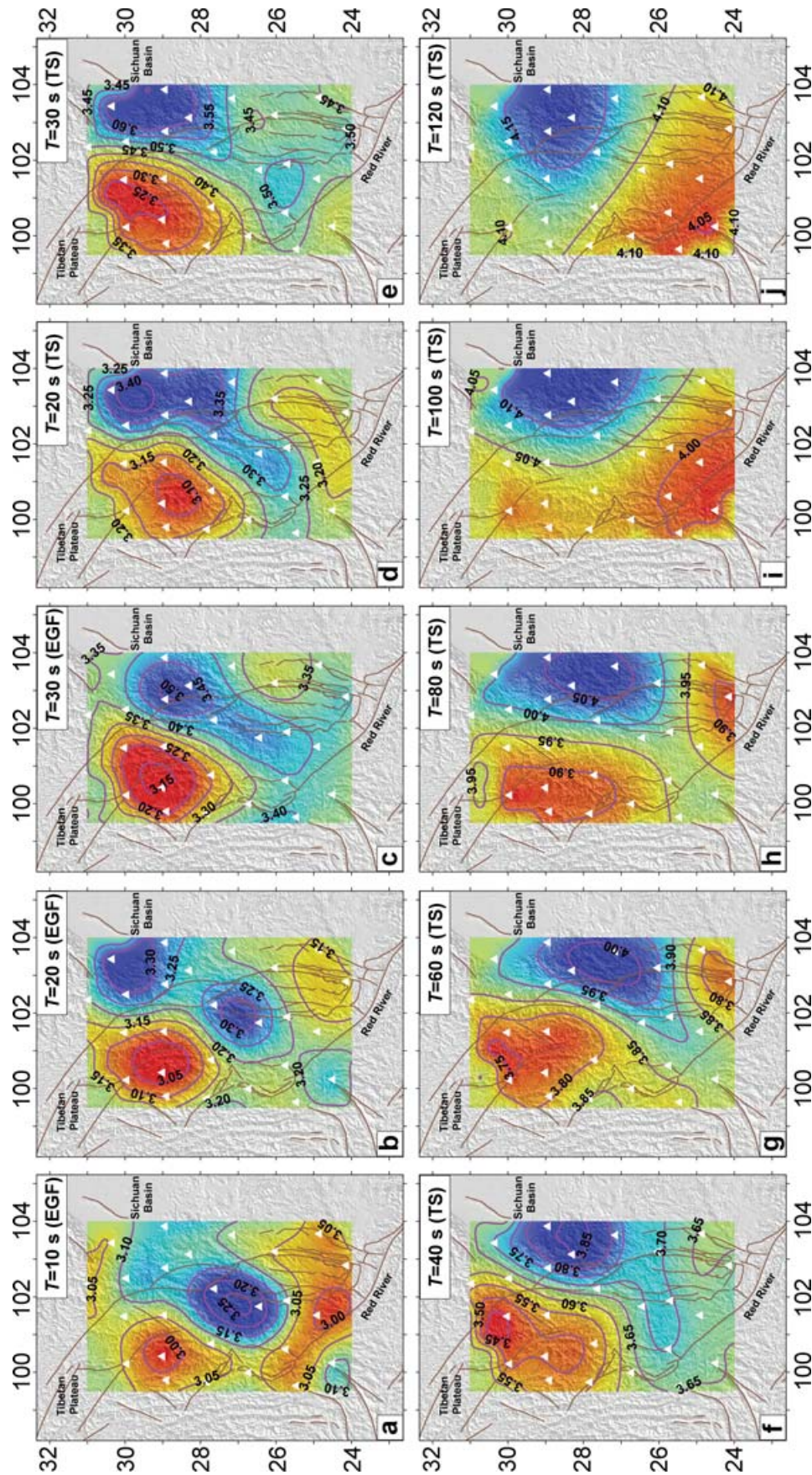
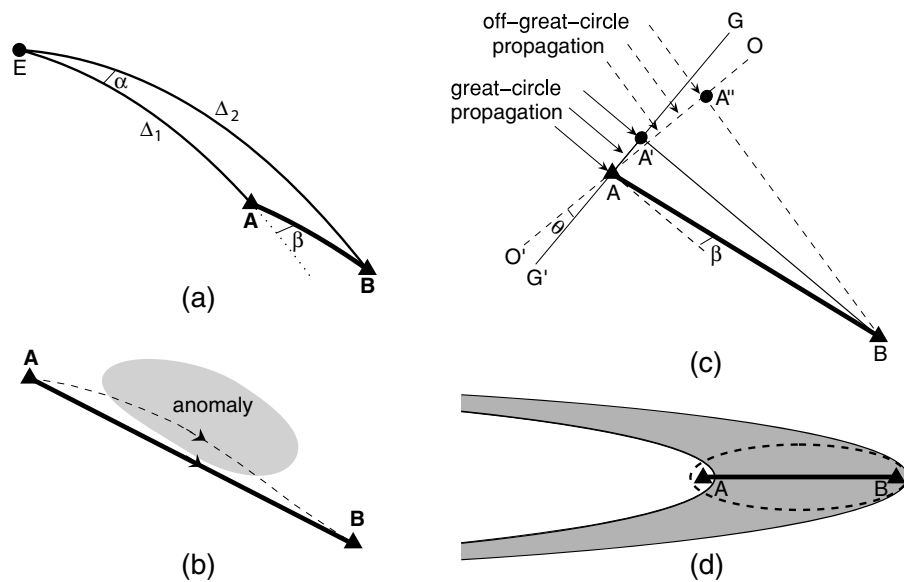
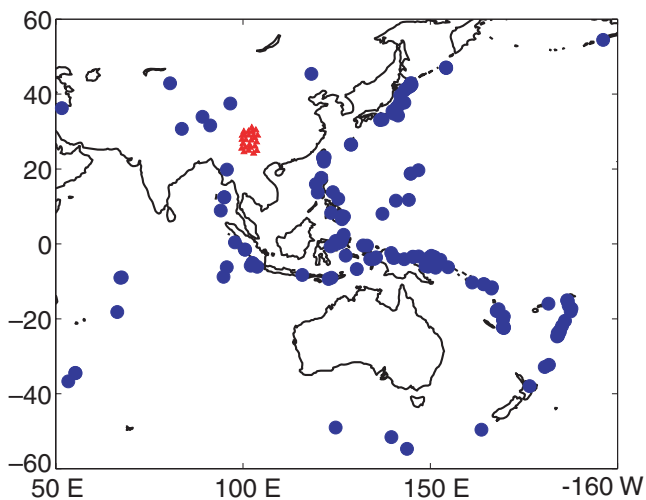


Figure 11. Rayleigh-wave phase velocity maps at different periods (10–120 s): (a–c) are the inversion results (10–30 s) from the TS method; (d–j) are the inversion results (20–120 s) from the TS method. Black triangles show station locations. The corresponding path coverage maps are shown in Fig. 9. The contour values are Rayleigh-wave phase velocities ( $\text{km s}^{-1}$ ). Red and blue represents lower and higher velocity, respectively. Brown lines depict the major faults in the studied area.



**Figure 12.** (a) Illustration of two deviation angles  $\alpha$  and  $\beta$  defined in the TS method:  $\alpha$  is the azimuthal difference of the earthquake (E) to the two stations (A and B, with A nearest to the earthquake);  $\beta$  is the azimuthal difference between the earthquake (E) to the station A and the station A to the station B. The solid lines are all great-circle paths and the dashed line is the extended great-circle path from E to A.  $\Delta_1$  is the great-circle distance between E and A and  $\Delta_2$  is the great-circle distance between E and B. (b) Illustration of off-great-circle propagation of surface waves between source A and receiver B for the EGF analysis. The solid line represents the path of great-circle propagation between two stations A and B; the dashed line is the path of off-great-circle propagation due to the influence of the velocity anomaly region (shaded area). The distance of off-great-circle path (dashed line) is always larger than that of the great-circle path (solid line), which results in a lower estimation of the average phase velocity between two stations because the estimated phase traveltimes from the EGF is the same. (c) Illustration of great-circle propagation (solid parallel lines with arrow) and off-great-circle propagation (dashed parallel lines with arrow) of surface waves for the array TS analysis, where the solid triangles A and B are the two stations, the solid line  $GG'$  is the wave front of great-circle propagating surface waves and is perpendicular to the solid line  $A'B$  with distance (approximately) equal to  $\Delta_2 - \Delta_1$  in (a), the dashed line  $OO'$  is the wave front of off-great-circle propagating surface waves and is perpendicular to the dashed line  $A''B$ , the deviation angle  $\beta$  is the same as that defined in (a), and the off-great-circle angle  $\theta$  is defined as the angle from  $GG'$  to  $OO'$  (clockwise is defined to be positive here). (d) Illustration of surface-wave sensitivity zones for the EGF analysis and the TS method. The shaded area is the sensitivity zone for the TS method, which is much broader than the sensitivity zone (the area inside the dashed ellipse) for the EGF analysis. The solid triangles A and B are the two stations. The solid line is the great circle path between the two stations.



**Figure 13.** The location of earthquakes (blue solid circles) used in the TS method. The red solid triangles show the location of array stations.

velocities from the TS method than from EGF analysis. (NB this effect is likely to be small for low-frequency waves that are primarily sensitive to upper mantle structure.)

In combination, such physical, geometrical, and structural factors explain why, for our study region, the interstation phase ve-

locity measurement from the TS method tends to be higher than that from the EGF analysis because the latter tends to underestimate the average phase velocities while at short period the former may overestimate them.

The EGF analysis can provide more reliable phase velocity measurements at relatively short periods (10–30 s, in this study), but for array tomography studies it becomes less accurate at longer periods because of the use of the far-field approximation. Furthermore, our analysis shows that, for our array, the dispersion measurements become unstable at periods larger than 30 s. In contrast, the TS method can be used to measure phase velocities to much longer periods (e.g. to about 100 s for a two-station path with distance 200 km with the TS method, compared to only ~20 s with the EGF analysis). However, the phase velocity measurements at 20–30 s from the TS method are less reliable mainly due to the effects of strong scattering on the shorter period part ( $T < 30$  s) of the waveform, off-great-circle propagation and much broader sensitivity zone. To exploit the strengths of both methods, we combine the dispersion data from the EGF and TS analysis to construct phase velocity maps in the period bands from 10–120 s, which (in a separate study) we will invert for 3-D shear wave velocity structure of the crust and upper mantle.

## 6 SUMMARY

We have determined EGFs from the cross-correlation of either (monthly) ambient seismic noise or surface-wave coda recorded at



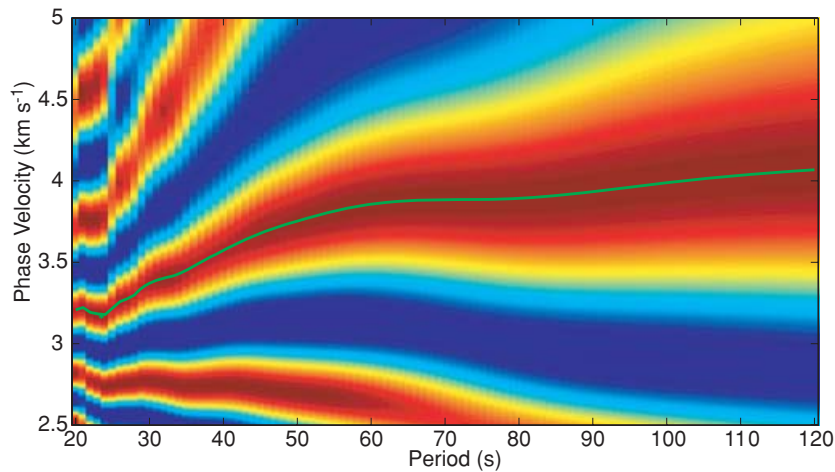


**Figure 14.** Example of extracted dispersion curve (green curve on the  $c - T$  image) for the station pair MC20–MC05 using the TS method based on the image transformation technique. The earthquake locates at  $(-5.8010^\circ, 102.0280^\circ)$  with  $M_w = 5.5$ , depth = 10.0, and source time = 2003/12/24, 11:33:04.36.

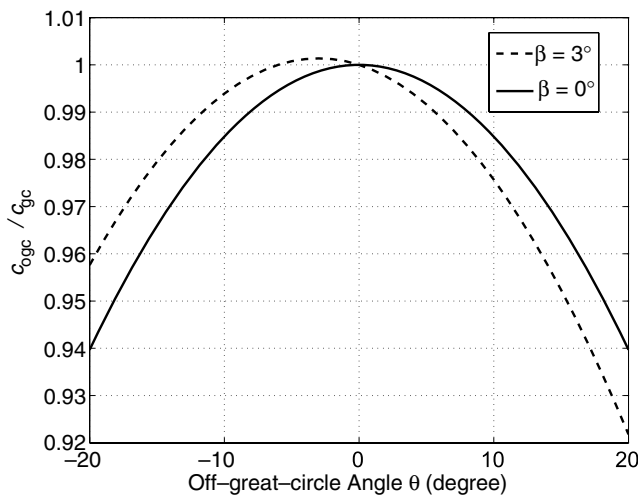


**Figure 15.** The ratio of the interstation phase velocity estimated from off-great-circle propagation ( $c_{ogc}$ ) to the interstation phase velocity estimated from great-circle propagation ( $c_{gc}$ ) at given off-great-circle angle  $\theta$  with the deviation angle  $\beta = 0^\circ$  (solid curve) and  $\beta = 3^\circ$  (dashed curve) as illustrated in Fig. 12(d).

the MIT-CIGMR broad-band network (25 stations) on the southeastern Tibetan plateau in Sichuan and Yunnan provinces, SW China. We used an image transformation technique and a far-field approximation of the surface-wave Green's function to make accurate phase velocity dispersion measurements for relatively short period data ( $T = 10\text{--}30$  s) for all possible two-station combinations in the array. We showed that noise correlations for different months give consistent results, that the EGFs are not biased by individual earthquakes, and that the results from ambient noise or surface-wave coda are very similar. However, the EGFs are time asymmetric (one sided) for stations aligned in the N–S direction, which we attribute to the paucity of seismicity north of the array. For longer periods we have measured interstation phase velocities using classical TS analysis, and the combination of these methods provides dispersion curves and phase velocity maps over a very broad period range ( $T = 10\text{--}120$  s), which can be used for high-resolution tomographic studies of the crust and upper mantle beneath this region.

Application of a far-field approximation (in the case of the EFG analysis) or a half-wavelength criterion (for the TS analysis) produces a situation that is attractive for multiscale surface-wave tomography: the density of path coverage is proportional to the periods under consideration decreases. Tests with synthetic data demonstrate that our array data should be able to resolve heterogeneity on length scales comparable to and larger than the interstation spacing ( $\sim 100$  km and up, for our array). In future studies this will be exploited in multiresolution tomography for isotropic and (azimuthally) anisotropic variations in shear wave speed in the crust and upper mantle beneath SE Tibet.

Phase velocities at short and intermediate periods ( $T = 10\text{--}80$  s) are prominently low in SE Tibet, suggesting that shear wave propagation may be slow in the shallow part of the lithosphere in SE Tibet. Moreover, phase velocities in the entire period band considered here ( $T = 10\text{--}120$  s) are high in the vicinity of the Archean Sichuan craton.

## ACKNOWLEDGMENTS

This work was funded by NSF grant 6892042 of Collaborative Research in Eastern Tibet and AFRL grant FA8718-04-C-0018. We thank Kees Wapenaar (Technical University Delft, The Netherlands), an anonymous reviewer, and Xander Campman (MIT, Cambridge, USA) for their constructive comments, which helped us improve the manuscript.

## REFERENCES

- Beaumont, C., Jamieson, R.A., Nguyen, M.H. & Medvedev, S., 2004. Crustal channel flows: 1. Numerical models with applications to the tectonics of the Himalayan-Tibetan orogen, *J. geophys. Res.*, **109**, B06406, doi:10.1029/2003JB002809.
- Brisbourne, A. & Stuart, G., 1998. Shear-wave velocity structure beneath North Island, New Zealand, from Rayleigh-wave interstation phase velocities, *Geophys. J. Int.*, **133**, 175–184.
- Campillo, M. & Paul, A., 2003. Long-Range correlations in the diffuse seismic coda, *Science*, **299**, 547–549.
- Dahlen, F.A. & Tromp, J., 1998. *Theoretical Global Seismology*, Princeton Univ. Press, Princeton, New Jersey.
- Dahlen, F., Hung, S.-H. & Nolet, G., 2000. Fréchet kernels for finite-frequency traveltimes—I. Theory, *Geophys. J. Int.*, **141**, 157–174.

- De Hoop, M.V. & Van der Hilst, R.D., 2005. On sensitivity kernels for 'wave-equation' transmission tomography, *Geophys. J. Int.*, **160**, 621–633.
- Engdahl, E.R., Van der Hilst, R.D. & Buland, R.P., 1998. Global teleseismic earthquake relocation from improved travel times and procedures for depth determination, *Bull. seism. Soc. Am.*, **88**, 722–743.
- Huang, Z., Su, W., Peng, Y., Zheng, Y. & Li, H., 2003. Rayleigh wave tomography of China and adjacent regions, *J. geophys. Res.*, **108**(B2), 2073, doi:10.1029/2001JB001696.
- Knopoff, L., Muller, S. & Pilant, W.L., 1966. Structure of the crust and upper mantle in the Alps from the phase velocity of Rayleigh waves, *Bull. seism. Soc. Am.*, **56**, 1009–1044.
- Li, C., Van der Hilst, R.D. & Toksoz, M.N., 2006. Constraining P-wave velocity variations in upper mantle beneath Southeast Asia, *Phys. Earth planet. Inter.*, **154**, 180–195.
- Lobkis, O.I. & Weaver, R.L., 2001. On the emergence of the Green's function in the correlations of a diffusive field, *J. acoust. Soc. Am.*, **110**, 3011–3017.
- Passier, M.L., Van der Hilst, R.D. & Snieder, R.K., 1997. Surface wave waveform inversions for local shear-wave velocities under eastern Australia, *Geophys. Res. Lett.*, **24**, 1291–1294.
- Paul, A., Campillo, M., Margerin, L., Larose, E. & Derode, A., 2005. Empirical synthesis of time-asymmetrical Green functions from the correlation of coda waves, *J. geophys. Res.*, **110**, B08302, doi:10.1029/2004JB003521.
- Roux, P., Sabra, K.G., Kuperman, W.A. & Roux, A., 2005. Ambient noise cross correlation in free space: theoretical approach, 2005, *J. acoust. Soc. Am.*, **117**, 79–84.
- Royden, L.H., Burchfiel, B.C., King, R.W., Wang, E., Chen, Z., Shen, F. & Yuping, L., 1997. Surface deformation and lower crustal flow in eastern Tibet, *Science*, **276**, 788–790.
- Sabra, K.G., Gerstoft, P., Roux, P., Kuperman, W.A. & Fehler, M.C., 2005a. Extracting time-domain Green's function estimates from ambient seismic noise, *Geophys. Res. Lett.*, **32**, L03310, doi:10.1029/2004GL021862.
- Sabra, K.G., Gerstoft, P., Roux, P. & Kuperman, W.A., 2005b. Surface wave tomography from microseisms in Southern California, *Geophys. Res. Lett.*, **32**, L14311, doi:10.1029/2005GL023155.
- Shapiro, N.M. & Ritzwoller, M.H., 2002. Monte-Carlo inversion for a global shear-velocity model of the crust and upper mantle, *Geophys. J. Int.*, **151**, 88–105.
- Shapiro, N.M. & Campillo, M., 2004. Emergence of broadband Rayleigh waves from correlations of the ambient seismic noise, *Geophys. Res. Lett.*, **31**, L07614, doi:10.1029/2004GL019491.
- Shapiro, N.M., Campillo, M., Stehly, L. & Ritzwoller, M.H., 2005. High-resolution surface wave tomography from ambient seismic noise, *Science*, **307**, 1615–1618.
- Simons, F.J., van der Hilst, R.D., Montagner, J.P. & Zielhuis, A., 2002. Multimode Rayleigh wave inversion for heterogeneity and azimuthal anisotropy of the Australian upper mantle, *Geophys. J. Int.*, **151**, 738–754.
- Spetzler, J., Trampert, J. & Snieder, R., 2002. The effect of scattering in surface wave tomography, *Geophys. J. Int.*, **149**, 755–767.
- Tarantola, A. & Nercissian, A., 1984. Three-dimensional inversion with blocks, *Geophys. J. R. astr. Soc.*, **76**, 299–306.
- Tarantola, A. & Valette, B., 1982. Generalized nonlinear inverse problem solved using the least squares criterion, *Rev. Geophys. Space Phys.*, **20**(2), 219–232.
- Trampert, J. & Woodhouse, J., 1996. High resolution global phase velocity distributions, *Geophys. Res. Lett.*, **23**, 21–24.
- Weaver, R.L. & Lobkis, O.I., 2004. Diffuse fields in open systems and the emergence of the Green's function, *J. acoust. Soc. Am.*, **116**, 2731–2734.
- Yao, H., Xu, G., Zhu, L. & Xiao, X., 2005. Mantle structure from interstation Rayleigh wave dispersion and its tectonic implication in western China and neighboring regions, *Phys. Earth planet. Inter.*, **148**, 39–54.
- Yoshizawa, K. & Kennett, B.L.N., 2002. Determination of the influence zone for surface wave paths, *Geophys. J. Int.*, **149**, 441–454.
- Zielhuis, A. & Nolet, G., 1994. Deep seismic expression of an ancient plate boundary in Europe, *Science*, **265**, 79–81.
- Zhou, Y., Dahlen, F.A. & Nolet, G., 2004. Three-dimensional sensitivity kernels for surface wave observables, *Geophys. J. Int.*, **158**, 142–168.

